STRESS-DEFECT TRANSPORT INTERACTIONS IN IONIC SOLIDS

A Dissertation
Presented to
The Academic Faculty

By

Narasimhan Swaminathan

In Partial Fulfillment
Of the Requirements for the Degree
Doctor of Philosophy in Mechanical Engineering

Georgia Institute of Technology
May, 2009

STRESS-DEFECT TRANSPORT INTERACTIONS IN IONIC SOLIDS

Approved by:

Dr. Jianmin Qu, Advisor
School of Mechanical Engineering
Georgia Institute of Technology

Dr. David L. McDowell
School of Mechanical Engineering
Georgia Institute of Technology

Dr. Paul A. Kohl
School of Chemical & Biomolecular Engineering
Georgia Institute of Technology

Dr. Ting Zhu
School of Mechanical Engineering
Georgia Institute of Technology

Dr. Meilin Liu
School of Material Science and Engineering
Georgia Institute of Technology

Date Approved: December 11, 2008

To my parents.

ACKNOWLEDGEMENTS

I would like to thank my advisor, Dr. Jianmin Qu for his guidance and insight during the course of my research at Georgia. Tech.. He has been a tremendous source of inspiration not only in the academic research environment but also in time management and discipline (Both at work and working out at the CRC). I have relished my doctoral studies and my life at Tech. as he gave me complete freedom to carry out this research.

I would next like to thank, Dr. Paul A. Kohl, Dr. Meilin Liu, Dr. David McDowell and Dr. Ting Zhu for agreeing to serve in my thesis reading committee.

Dr. Jeffery Donnell has been of immense help in drafting the final form of this thesis. I thank him for proof reading all the chapters carefully and patiently to correct any grammatical errors or modify the manner in which the material is conveyed to make this thesis more readable. Errors despite his sincere efforts are solely my responsibility.

I am grateful to Dr. Ambarish Kulkarni for introducing me to MD and for a few FORTRAN preprocessing and post processing codes that made my life a little easier. I am also thankful to him for the various discussions we had between 3:00 and 3:30 pm almost everyday at the coffee shop. In this regard I would also like to thank Dr. Remi Dingreville for sharing with me his first version of the FORTRAN code to calculate elastic constants. It served as a framework for some of the material involved in this thesis.

I am also thankful to all my friends and colleagues who have been of immense moral support. In particular, I am thankful to Mr. Rajesh Prasannavenkatesan, Mr.Dinesh Bansal, Mr. Aravindhan Ravisekar, Mr.Nikhil Kulkarni, Dr.Vishal Gupta and Mr.Sudhakar Jagannathan for all the fun times we had together. I would also like to thank

my office mates, Mr. Honggang Zhou, Mr. Ryan Austin, Dr. Laurent Capolungo and Miss. Janine Johnson for their support and friendship.

Last but not least, I am thankful to my parents, Mr. T. Swaminathan and Mrs. Jayanthi Swaminathan, to my sister's family, Mr. Sriram Balachandran, Anuradha Swaminathan and Shambavi Balachandran for their unconditional love and support.

TABLE OF CONTENTS

LIST OF TABLES

LIST OF FIGURES

NOMENCLATURE

α	A point defect (*e*- electron, *v*, vacancies, *O*- interstitials, *h*-holes)
$\tilde{\mu}_\alpha$	Electrochemical potential of defect α (J mol^{-1})
μ_α	Chemical potential of defect α (J mol^{-1})
z_α	Equivalent charge of defect α
F	Faradays constant 96485.3399(24) C mol^{-1}
ϕ	Electrostatic potential (V)
V_{OC}	Open circuit voltage (V)
G	Strain energy release rate (J m^{-2})
$\overline{\Pi}$	Internal energy (J)
H	Enthalpy (J)
Γ	Gibbs free energy (J)
$\Im$	Helmholtz free energy (J)
S	Entropy (J K^{-1})
T	Absolute temperature (K)
c_α	Concentration of component α (mol)
ρ_α	Mole fraction of defect α
Γ^0	Gibbs free energy of a perfect crystal (J)
n_α	Numbers of defect α
γ_α	Energy needed to create defect α (J)
Π	Internal energy per unit volume of the natural state (J m^{-3})
k_B	Boltzmann's constant (1.3806503 × 10^{-23} m^2 kg s^{-2} K^{-1})

S_{config} Configurational entropy (J K^{-1})

A Avogadro's number (6.0221415×10^{23})

R Universal gas constant (8.314472 J mol^{-1} K^{-1})

λ_{α} Activity coefficient of defect α

K Equilibrium reaction constant

V_m Molar volume in the natural state (m^3 mol^{-1})

V_m^c Molar volume in the intermediate state (m^3 mol^{-1})

$\boldsymbol{\sigma}$ Cauchy's stress, tensor notation (N m^{-2})

σ_{ij} Cauchy's stress, indicial notation ((N m^{-2})

ε_{ij} Small strain

$\varepsilon_{ij}^{\alpha}$ Chemical eigenstrain due defect α

η_{ij}^{α} Coefficient of chemical expansion for defect α

CCE Coefficient of Chemical Expansion

TCE Thermal Coefficient of Expansion

FEM Finite Element Method

S_{ijkl} Compliance of material (m^2N^{-1})

$s_{ijkl}^{\alpha} = \dfrac{\partial S_{ijkl}}{\partial \rho_{\alpha}}$ Change in the elastic compliance with concentration of defect α (m^2N^{-1})

E Young's modulus (Nm^{-2})

ν Poisson's ratio

u_i Displacement field

$\mathbf{F}$ Material deformation gradient, tensor notation

F_{ij} Material deformation gradient, indicial notation

$\mathbf{f}$ Spatial deformation gradient, tensor notation

f_{ij} Spatial deformation gradient, indicial notation

J=det($\mathbf{F}$) Jacobian of a deformation

δ_{ij} Kronecker delta

$\mathbf{E}$ Lagrange strain, tensor notation

E_{ij} Lagrange strain, indicial notation

$\boldsymbol{\sigma}^{\mathbf{0}}$ First Piola Kirchhoff's stress, tensor notation

σ_{ij}^{0} First Piola Kirchhoff's stress, indicial notation

$\tilde{\boldsymbol{\sigma}}$ Second Piola Kirchhoff's stress, tensor notation

$\tilde{\sigma}_{ij}$ Second Piola Kirchhoff's stress, indicial notation

$\mathbf{F}^{E}$ Elastic deformation gradient, tensor notation

F_{ij}^{E} Elastic deformation gradient, indicial notation

$\mathbf{F}^{c}$ Eigen transformation, tensor notation

F_{ij}^{c} Eigen transformation, indicial notation

$\Delta\rho_{\alpha}$ Deviation in stoichiometry in mole fractions for defect α

ρ_{α}^{0} Stoichiometric concentration of defect α

η_{α} Isotropic CCE for defect α

$\overline{\rho}_{\alpha}$ Concentration of defect α per unit volume of the natural state (mol m^{-3})

$\overline{\rho}_{\alpha}^{c}$ Concentration of defect α per unit volume of the intermediate state (mol m^{-3})

W Strain energy per unit volume of the natural state (J m^{-3})

w Strain energy per unit volume of the intermediate state (J m^{-3})

J^c Jacobian of $\mathbf{F}^c$ ($\det(\mathbf{F}^c)$)

$c^{\alpha}_{ijkl} = \frac{\partial C_{ijkl}}{J^c \partial \rho_{\alpha}}$ Change of elastic stiffness with stoichiometry (N m^{-2})

$\mathbf{\Sigma}$ Eshelby's stress, tensor notation

Σ_{ij} Eshelby's stress, indicial notation

μ^{el}_{α} Elastic contribution to the chemical potential of defect α

m_{α} Mobility of defect α (J^{-1} mol m^2 s^{-1})

$\mathbf{J}_{\alpha}$ Current density of defect α (Amp m^{-2})

δ Non-stoichiometry

$\widetilde{C}_{ijkl}$ Inner elastic constant (N m^{-2})

$\overline{\phi} = \frac{F\phi}{RT}$ Normalized potential

$\in$ Electrical permittivity of the solid (C^2 N^{-1} m^{-1})

LEN Local electroneutrality condition

NPP Nernst-Poisson-Planck

MNPP Modified Nernst Poisson Planck

$\beta = -\frac{\partial E}{\partial \rho_v}$ Change in Young's Modulus with vacancy concentration (N m^{-2})

GDC Gadolinium doped ceria

E^0 Young's modulus at stoichiometry (N m^{-2})

Q Concentration of the immobile defect

a Crack length (m)

$PO_2^{L/R}$ Partial pressure of oxygen at the **L**eft/**R**ight end (atmospheres (atm.))

M Material body force, vector notation, (N m^{-3})

M_i Material body force, indicial notation, (N m^{-3})

$\mathbf{F}^{\mathbf{M}}$ Material force, vector notation, (N)

F_i^M Material force, indicial notation, (N)

$\overline{\phi}^{L/R}$ Non-dimensional electrostatic potential at the **L**eft/**R**ight end

$\rho_\alpha^{L/R}$ Concentration in mole fraction of defect α at the **L**eft/**R**ight end

$K_\sigma^{L/R}$ Stress dependent equilibrium constant at the **L**eft/**R**ight end

$\phi^{L/R}$ Physical electrostatic potential at the **L**eft/**R**ight end (Volts)

L_v / R_v Concentration of vacancies close to the **L**eft/**R**ight boundary

L_ϕ / R_ϕ Non-dimensional electrostatic potential close to the **L**eft/**R**ight boundary

χ Singular perturbation parameter for the NPP/MNPP system

Φ^0 Non-dimensional zeroth order electrostatic potential for the bulk

V^0 Zeroth order vacancy concentration in the bulk

$\overline{E}^0$ Zeroth order electron concentration in the bulk

$\tilde{\phi}^0$ Zeroth order non-dimensional electrostatic potential for the Left boundary layer

$\tilde{v}^0$ Zeroth order vacancy concentration for the Left boundary layer

$\tilde{e}^0$ Zeroth order electron concentration for the Left boundary layer

ψ^0 Zeroth order non-dimensional electrostatic potential for the Right boundary layer

$\overline{v}^0$ Zeroth order vacancy concentration for the Right boundary layer

$\overline{e}^0$ Zeroth order electron concentration for the Right boundary layer

SUMMARY

Ionic solids have gained tremendous importance in recent years due to their roles in energy conversion devices like solid oxide fuel cells, gas separators, oxygen pumps and gas sensors. During their functioning, point defects diffuse through the solid due to an electrochemical potential gradient. In general, the electrochemical potential is considered to be a function of the local concentration of the defects and temperature only, and the non-entropic part of the chemical potential is assumed to be a constant. In addition to thermo-mechanical loads, non-uniform strains due to non-stoichiometry can create mechanical stresses. Thus the prime motivation for this work stems from recognizing that point defect diffusion in the solid occurs under stressed conditions.

The primary objective of this research is to study the extent of stress-defect transport interactions in ionic solids. For this purpose, the first part of this research develops a continuum framework for steady state transport of point defects in a typical oxide ceramic. The main highlight of this framework is the development of the Eshelby stress dependent chemical potential, which is the elastic contribution to the non-entropic part of the chemical potential. The gradient of the Eshelby stress dependent chemical potential is then used to develop a system of governing differential equations that must be solved to address the problem of stress-dependent transport.

The stress dependent electrochemical potential entailed the introduction of two material constants. They are a) the *Chemical Coefficient of Expansion* (CCE) which quantifies the strains induced due to non-stoichiometry and b) a fourth order tensor describing the stoichiometry dependent elastic constants called as the *Open System Elastic Constants* (OSEC). The second part of the research determines these material

properties for Gadolinium doped ceria (GDC) using a combination of molecular simulations and analytical expressions. While the methodology for the determination of CCE is straightforward, the stoichiometry dependent elastic constants pose challenges due to the non-primitive nature of defective GDC lattice. In order to consider the effects of inner elasticity in such non-primitive lattices, a new super cell based approach is presented to calculate the elastic constants. Both CCE and elastic constants are determined for several levels of non-stoichiometry and temperatures.

To study the effect of the interactions on the distribution of point defects, electrostatic potential and the current voltage relationships, a modified form of the Nernst Poisson Planck system of equations (MNPP) is introduced. The 1-D MNPP system contains the effects of both the CCE and the OSEC. The singular nature of the MNPP system rendered direct numerical solutions impossible for the domain under consideration. Hence a combination of the method of matched asymptotic expansions and numerical methods are used to obtain solutions. Differences in the distributions of point defects and electrostatic potentials were observed on solving the MNPP system with and without elasticity effects. This revealed that the interactions between stresses and defect transport existed and could be significant under certain conditions.

Finally, the finite element method was used through a User Element subroutine for ABAQUS, to solve fully coupled stress defect transport equations in a 2D elastic domain with flaws of various configurations. The stresses induced in the vicinity of these flaws were high indicating that premature failure of the component was possible under operating conditions. The strain energy release rates were determined for cracked electrolytes using the material force approach for various values of applied voltages. The

values of these strain energy release rates (G) were also high and indicated the growth of existing cracks in the material. The strain energy release rates were then developed as explicit functions of the electrochemical boundary conditions providing a means to suggest safer operating voltages while functioning of cracked ionic solids in a typical fuel cell environment.

The fusion of the various elements of this thesis provides methodologies and tools to model, study and interpret the consequences of stress-defect transport interactions in ionic solids.

CHAPTER 1. INTRODUCTION

1.1 Motivation

Ionic solids have gained tremendous importance [1] in recent years due to their roles in energy conversion devices such as solid-oxide fuel cells (SOFC) [2], gas separating membranes, gas pumps and sensors [3]. Many of the same figures of merit apply to these different applications, the main ones being, ionic conduction in solid electrolytes for SOFCs, mixed ionic electronic conduction (MIEC) for electrodes [4]. During the functioning of the above mentioned devices charged point defects like vacancies, interstitial ions, electrons and holes diffuse through the ionic solid in a chemical and/or electrical potential gradient. The main motivation for this work stems from the need to identify the dependence of the distribution of the electrochemical field quantities on mechanical stresses and vice versa. Thus diffusion in an electrochemical gradient may create stresses and conversely an applied stress field may cause redistribution/diffusion of point defects in the solid. The proposed research work mainly aims at developing a framework, methodologies and numerical tools to solve problems involving such interactions. The results of this study may then be used to improve analysis techniques used to study the functionality and to enhance the reliability of ionic solids in various applications.

1.2 Ionic solid as an electrolyte

In this thesis an ionic solid, in light of its role as an electrolyte in a fuel cell/gas pump will be studied. In particular Gadolinium doped ceria (GDC) is considered for its

prospective role as an electrolyte in a low temperature SOFC and for its propensity to undergo large chemical expansion. Before introducing various aspects of this research, a brief description of the role of the electrolyte (GDC) and its behavior in the solid state device is in order. A sketch of the typical environment experienced by GDC under normal operating conditions is shown in Figure 1.1. In a fuel cell, the anode is typically exposed to hydrogen (referred to as the low oxygen partial pressure side) while the cathode to air (higher oxygen partial pressure). The anode and cathode are porous materials so as to allow for the fuel and oxygen gas to reach the impermeable electrolyte. At moderate temperatures (~1073K), GDC conducts oxygen ions from the cathode to the anode, due to the presence of oxygen vacancies in its sub-lattice. Conduction of oxygen ions occurs through a vacancy hopping mechanism. At the anode, electrons are released by the oxidation of hydrogen with the formation of water. These electrons move in the external circuit through a load (shown as a light bulb in Figure 1.1 and on reaching the cathode they reduce oxygen gas to form oxygen ions [2]. These oxygen ions are incorporated into the electrolyte through a complex mechanism [5] and are carried to the anode due to the presence of oxygen vacancies.

It is also possible to supply and maintain an external voltage to drive the oxygen gas from a lower partial pressure side to a higher one. Such a set up is now called an oxygen pump. In either case, SOFC or a gas pump, a different partial pressure of oxygen on either side of the electrolyte causes a non-uniform distribution of vacancy concentration within the electrolyte during the functioning of the device.

Thus, clearly the electrolyte's primary function is to conduct ions (oxygen). Certain ionic solids like GDC also conduct a small number of electrons, making them

Mixed Ionic Electronic Conductors (MIEC). The conduction mechanism can also be addressed in terms of the point defects responsible, namely the vacancies. Thus, if the oxygen ions move from the cathode to the anode, the vacancies move in the opposite direction. In this thesis the conduction mechanism is described in terms of the point defect motion.

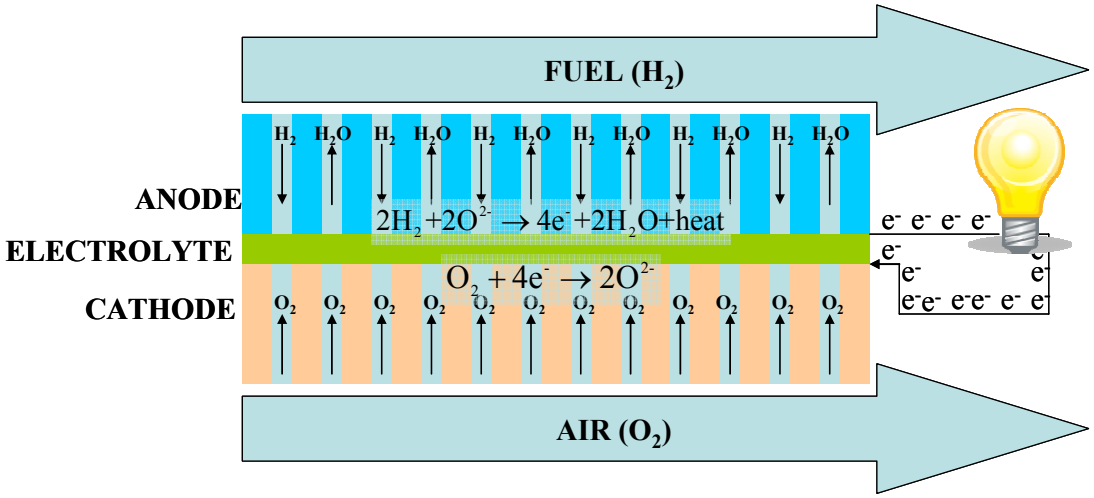

Figure 1.1: Working principle of a solid oxide fuel cell

1.3 Stresses in ionic solids

Diffusion of charged point defects in ionic solids plays a vital role in the conversion of chemical to electrical signals. The diffusivity of these point defects is usually larger at higher temperatures, and because of this the operating temperature of the solid state device is quite high (typically 500°C-1000°C, allowing for internal reforming). This is a primary cause for thermal stresses, especially if the thermal coefficient mismatch between the various cell components is large. The materials used for solid state devices such as solid oxide fuel cells must meet certain stringent and conflicting requirements. For example, the cathode must resist oxidation while the anode must be

resistant to reducing environments. Electrolytes must resist both these extremities in addition to high operating temperatures. Thermal expansion mismatch between the constituent elements also induces stresses [6] in ionic solids during service. In addition to thermo-mechanical stresses, other contributors are also known to be significant. For example, Gadolinium doped ceria (GDC) which is known to be a better ionic conductor at lower temperatures than Yttria stabilized zirconia (YSZ) [7] undergoes volumetric

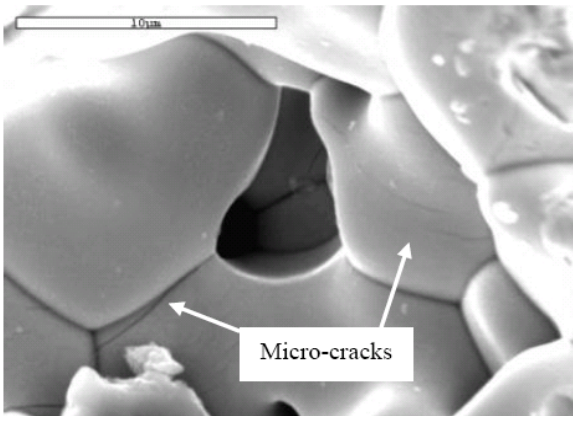

Figure 1.2: Micro-cracks in non-stoichiometric ceria

chemical expansion under reducing environments due to the conversion of Ce^{4+} to Ce^{3+} (a larger ion) [8]. A strain of around 1.5% was reported in [9] when the oxygen partial pressure was 10^{-18}atm. Other ionic solids such as doped Lanthanum Chromite [10, 11] and doped Lanthanum Titanate[12, 13] also show chemical expansion behavior. Local deviations from composition are always present during defect transport and such deviations also create local eigenstrains. When such chemical expansions are not accommodated by appropriate deformation, stresses are induced. Such stresses may be detrimental to the mechanical stability of the ionic solid, and the GDC's propensity to show this behavior makes it an ideal candidate for this research. Figure 1.2 shows cracks observed in a ceria sample which has undergone reduction [14]. In addition to the thermal

and chemical stresses just discussed the ionic solid may also be subjected to surface tractions, like the pressures of the working gases. Thus it is important to first recognize that transport of point defect in ionic solids occurs in the presence of mechanical stresses.

Non-stoichiometry in addition to creating stresses also causes a deviation in the mechanical properties of the material. In a recent article [15] the variation of the Young's modulus of some commonly used electrolytes was investigated. The results of such an investigation are shown in Figure 1.3. It can be seen that the modulus decreases

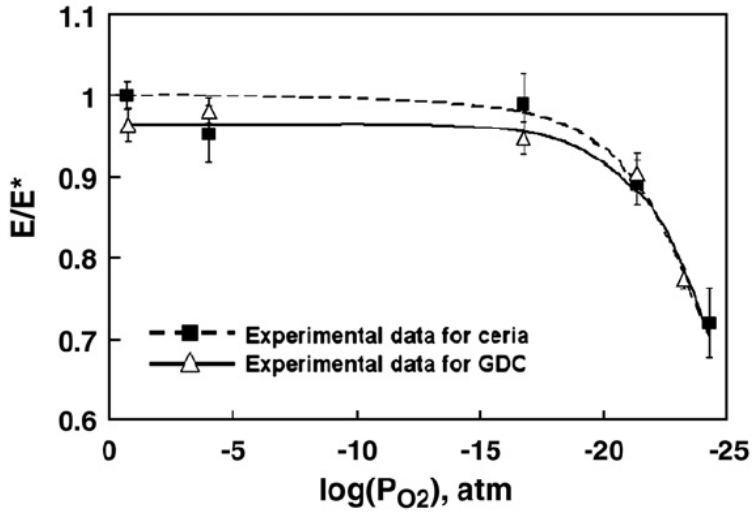

Figure 1.3: Variation of Young's modulus due to non-stoichiometry for some common electrolytes from [15]

significantly for lower partial pressures of oxygen. In addition to variation in elastic modulus it is not difficult to see that other crucial properties of the material, like fracture toughness and strength, may also be dependent on the stoichiometry. In ref.[16] the effects of heat treatment on these properties for ceria was studied. The strength substantially decreased while fracture toughness increased by about 30-40% when the partial pressure was in the 10^{-20} to 10^{-22} atm. range. The reason for such a change in the

toughness was attributed to internal stresses, micro crack toughening and crack deflection mechanisms.

The above paragraph describes how defect transport or non-stoichiometry can cause stresses within the solid and also affect its properties. The converse effect, namely, stresses affecting the chemical nature of the solid or the transport of defects, can also take place. Significant interest in this area has been shown recently. For example in [17, 18], stress-relaxation mechanisms in a thin GDC sample were related to an association-dissociation reaction between the defects. They have suggested that such interactions may pave the way for novel handling of stresses in materials used in electrochemical devices. Thus, the study of stresses affecting the defect transport or chemistry of the solid is not purely academic.

1.4 Research gap

Earlier works that perform failure analysis using numerical methods [19] on ionic solids neglect the effect of electrochemical fields while those that consider the electrochemical fields [20, 21] neglect any mechanical stress effects. Although such interactions may not be very significant for certain ionic solids [22], it may not be true for others [17, 23, 24] as described in section 1.3. Thus the two way interaction that may exist between the electrochemical field quantities and mechanics has not been given much attention, at least with regard to ionic solids. This thesis primarily aims to fill this gap.

The following questions aid in obtaining a better conception of this problem.

1) What are the various field quantities that are of interest in a typical ionic solid?

2) What thermodynamic quantity must be fundamentally modified to consider the interactions among the various fields?

In an ionic solid, the mechanical fields that are of interest are primarily the stresses and strains, at the level of linear elasticity to which we adhere to in this work. These are obtained as solutions to the boundary value problem.

One of the electrochemical fields is clearly the concentration of the charged point defects which are responsible for the conduction. Thermodynamically, it is well known that the electrochemical potential of the defect is the equilibrium governing quantity and is the driving force for defect transport. For species α this is given as [25],

$$\tilde{\mu}_\alpha = \mu_\alpha + z_\alpha F \phi \tag{1.1}$$

where,

μ_α, is the chemical potential of species α and usually depends on the temperature and concentration of the defect species

z_α, is the equivalent charge on species α

F, is the Faraday's constant

ϕ, is the electrostatic potential

Therefore in addition to the concentration of the charged defects, the electrostatic potential must also enter the formulation. The fields that are generally of interest here are therefore the stress, strain, concentration and the electrostatic potential.

The answer to the second question originates in realizing that the forcing term for a change in the concentration of a defect at a continuum point is the electrochemical potential. Thus this factor must be modified to account for the effect of mechanical field quantities on electrochemical fields. Hence, if the electrochemical potentials are known

as a function of stress, the diffusion problem may be solved using these stress dependent potentials to obtain concentration and electrostatic potential distributions. However, due to the coupling between the two fields, equilibrium equations of mechanics must be solved in conjunction with the diffusion problem in order to obtain a complete solution. This makes the problem mathematically non-linear, requiring numerical methods even for simple one dimensional cases [26]. A further complication may be induced due to the dependence on existing stress fields of the Onsager's coefficients (or the coefficient of diffusion) of the general flux/diffusion equations of irreversible thermodynamics [27] this is however not considered in this work.

1.5 Objectives

The main goal of the thesis is to numerically study the interactions between stresses and defect transport in GDC. For this purpose it is clear from section 1.4 that the electrochemical potential of the defect must be first developed as a function of the local stress state. The gradient of this stress-dependent electrochemical potential can then be the driving force for diffusion of point defects. This can then be used to develop a framework, establishing the necessary differential equations and the boundary conditions that need to be solved in order to study the interactions. The solution of the differential equations will give us the necessary distribution of the mechanical and electrochemical field quantities. These distributions can then be compared to the results from the uncoupled case (that uses the stress independent chemical potential). The ensuing differences in these quantities will conclude on the extent of interactions.

In order to achieve the objective, this work takes a four pronged approach involving,

1) Develop a continuum thermodynamic formulation of the stress dependent electrochemical potential and establishing the required coupled differential-algebraic equations to be solved to study interactions between defect transport and mechanics

2) Perform atomistic simulations using Molecular Dynamics (MD) to determine material properties introduced as a result of the developed theory

3) Solve the differential equations for the distribution of the field quantities through analytical and numerical methods

4) Post process the results to quantify other performance related measures of interest

The pictorial representation of the elements of this thesis is shown in Figure 1.4.

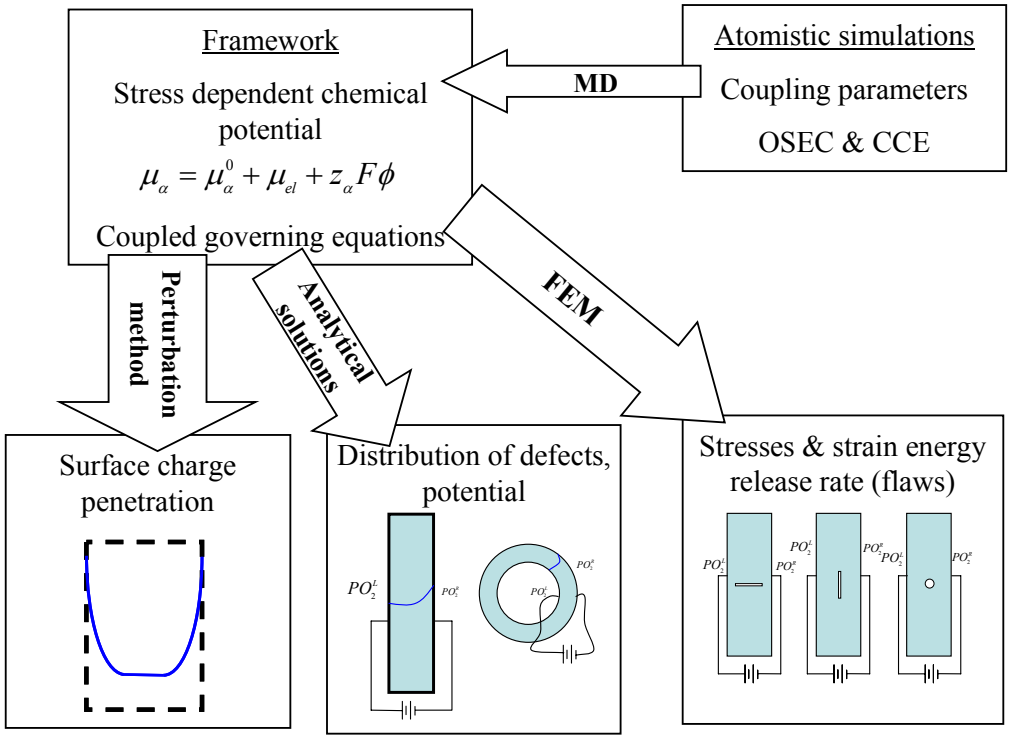

Figure 1.4: Pictorial representation of the elements of this thesis

1.6 Significant contributions in this research

This research addresses the effects of stress on solid state diffusion and hence on the effects of stress-defect transport interaction on the electrochemical and mechanical fields in a solid electrolyte used in solid oxide fuel cell or oxygen pumps. Previous stress analyses on ionic solids generally neglect any concentration dependent eigenstrains, while existing solutions of transport equations pertaining to motion of defects in ionic solids neglect the effects stresses.

The primary significant contribution of this research is the conclusion that the interaction between mechanical and electrochemical field quantities is significant in certain ionic solids. The distribution of the field quantities which are obtained by using the coupled theory show significant variations when compared to distributions obtained from the uncoupled framework. This makes it clear that the current mathematical modeling of transport and mechanical design of ionic solids for applications cannot be carried out independently of each other. Designing ionic solids by considering the interactions as discussed will aid in manufacturing long term mechanically and electrochemically reliable MIECs for use in solid state devices. Secondly, the development of the stress dependent diffusion potential couples solid mechanics and chemistry at a fundamental, thermodynamic level. Due to this, certain quantities of interest in chemistry, like the equilibrium constant for a solid state reaction cannot be a constant through out the solid, for it will depend on the stress state in addition to temperature. Thus this research opens up a relatively less explored interdisciplinary area of electro-mechano-chemistry in association with ionic solids.

Other important contributions include atomistic techniques to determine material properties ensuing from the theoretical development, namely the *Coefficient of Chemical Expansion* (CCE) and the *Open System Elastic Constants* (OSEC). These material properties come naturally from the thermodynamics and are responsible for coupling stresses and defect transport. Although these methods are developed for GDC, they may be applied to other ionic solids of interest as well. The only modification required will be the construction of appropriate crystal structures.

User element subroutine that is developed for the ABAQUS finite element software can solve steady state coupled stress-defect transport equations. This can be used as a starting point by mechanical designers and electrochemists to study the consequences of the interactions on both the mechanical and the electrochemical behavior.

Easy to apply formulas are derived for the strain energy release rate (G) for cracked electrolytes under defect transport conditions. The formulae derived may be expressed entirely in terms of the applied electrochemical loadings (applied voltage, partial pressures of gas etc.). This may prove to be very useful in efforts to establish the severity of flaws in an electrolyte subjected to electrochemical loading conditions. Using this, safe operating voltages may be suggested for specific crack configurations if the critical strain energy release rate values of the concerned material are known.

Grain boundary engineering at both the structural and materials level is proving to be of significant importance in ionic solids. For an example at the structural level, nanocrystalline ceria shows enhanced electronic conductivity over its bulk counterpart [28].On the materials side, composites in which LiI is infiltrated in nanoporous Al_2O_3,

achieve conductivities as high as 10^{-3} S cm^{-1} [29]. Thus nano-structured materials (homogenous or a heterogeneous mixture) show significantly different and useful properties when compared to their macroscopic counterparts [28-34]. In addition to tuning properties by grain engineering, externally applied loads may also prove useful for obtaining new properties in materials with nano-structures. Although the current work does not consider polycrystalline behavior explicitly, the effect of stresses on the surface charge is examined in this work. The results indicate that there is a penetration of charge layer into the material when stress effects are considered. These effects are extremely important and useful especially in nano sized/nano-crystalline materials. The size dependency of the performance in such materials can be easily studied by using the results of this work. In essence the idea that stresses and defect transport interact in ionic materials gives us other methods to tune their properties, like for example by applying external loads.

1.7 Organization of the thesis

A separate chapter devoted to a literature review is not given. This is so because; the thesis involves analysis techniques pertaining to two different length scales, atomistic and continuum. A separate chapter titled "**Literature Review**" discussing material related to both these scales will seem disconnected. Since a separate chapter deals with each aspect of the thesis, the pertinent literature is presented in the chapter itself and is connected to the issue being addressed. Additionally, it is easer to delineate what has been done with regards to a particular research problem and what the contribution of this thesis to the problem will be if the existing literature is discussed in parallel with the contributions. The contents of each chapter are briefly shown in Figure 1.5.

The next chapter (Chapter 2) is devoted to the background material required for reading the thesis. It discusses point defect chemistry, its representations and thermodynamics. The concepts needed for understanding certain nuances associated with the electrochemical potential of point defects in solids is discussed in detail. Also presented is a brief introduction to molecular dynamic (MD) simulations. The required mechanics of materials and finite element background is assumed although some details pertaining to material forces and Eshelby's stress tensor are provided in chapter 6.

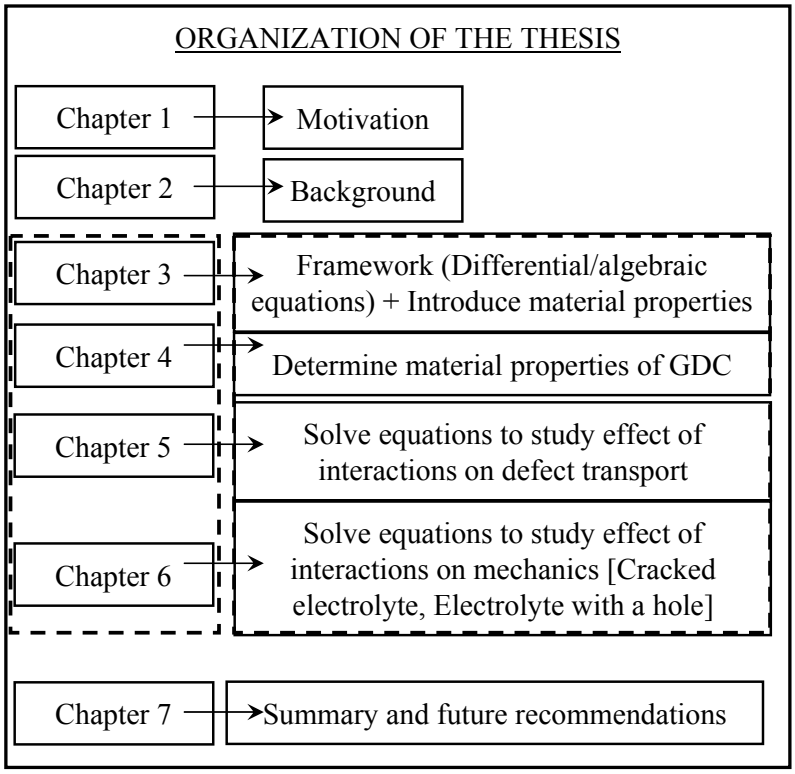

Figure 1.5: Brief depiction of the content of various chapters

Chapter 3 develops the stress dependent electrochemical potential of the point defects. Then it establishes the necessary differential equations and boundary conditions that need to be solved in order to study stress and defect transport interactions in ionic

solids. This is done for a general ionic solid like GDC possessing several kinds of point defects which are typically found in ionic oxides.

The theoretical development of chapter 3 will introduce certain material related properties. These will be obtained for GDC using MD simulations in Chapter 4. In particular, methodologies will be developed to determine the properties, and the values that are obtained will be compared to some recent literature discussing experimental observations. This chapter will also discuss the effect of temperature and defect concentrations on the values of these material constants.

In Chapter 5, the system of equations developed in chapter 4 will be reduced to a one dimensional equation under certain conditions. In particular a thin planar electrolyte and a long tubular electrolyte are considered for the study. The reduction to 1D will allow us to analytically develop solutions to the system of equations and to study the effect of interaction on the distribution of the defects, electrostatic potential, stresses and current voltage relations.

Chapter 6 will discuss the effect of interactions on stress distributions and values of G for certain electrolytes with flaws in them. Particularly cracks of two configurations and an electrolyte with a void is considered for the material in this chapter. A method based on the materials forces approach will be used to calculate G. Error incurred in performing calculations without the interaction between stresses and defect transport will also be quantified. Finally a method to obtain a functional form will be presented to calculate G for the considered crack configurations so that the designers may directly determine the failure criteria of the ionic solid in typical operating conditions. The

functional form will completely depend on the applied electrochemical boundary conditions.

The last chapter (Chapter 7) concludes the thesis with a summary and a listing of the contributions of this research. It also discusses the current state of the art with regard to the size effect in ionic solids, suggests recommendations for future research including some experimental techniques to verify stress defect transport interactions.

CHAPTER 2. BACKGROUND

2.1 Essentials of point defect chemistry

2.1.1 General remarks

As motivated in ref.[35], *The conception that solids have an "inner chemical" life, which makes it possible for us to tune their properties like we do with liquids, is made practical by the existence of point defects in solids.* Point defect centers in solids were introduced by Wagner and Schottky [36, 37]. Defect chemistry not only provides the fundamental understanding of the behavior of point defects, it also enables optimization of solids with regard to technological applications.

There are primarily three kinds of point defects in crystals a) Vacancies –A regular lattice site in the crystal is left unoccupied b) Interstitials – Atoms or Ions are present in usually unoccupied positions and c) Substitutional defects – Regular lattice sites are occupied by foreign or impurity atoms. Usually the concentrations of the point defects are not coupled. However, the situation is different for ionic crystals like GDC, where the atoms are charged. Here, the defects can posses an effective charge relative to the ideal defect free solid. Thus, an interstitial cation is positively charged while a cation vacancy is negatively charged. Unlike line (dislocation) and surface defects (Interfaces), point defects are thermodynamically necessary and are formed on entropic considerations [38], i.e. to attain thermodynamic equilibrium. Point defects created purely by thermal effects are intrinsic while those that are created externally, for example by doping, are extrinsic. Thus, an ionic solid at 0K will be free of any intrinsic point defects.

Point defects are generally quantified by their concentrations in the ionic crystal. In addition to the thermodynamic considerations just mentioned, the electroneutrality of the entire crystal must be considered while determining the concentrations of the point defects in crystals. Hence, the total number of positively and negatively charged equivalents of defects in the crystals must be equal. For example, in the material considered in this thesis, GDC, two forms are used frequently. They are 10GDC ($Ce_{0.9}Gd_{0.1}O_{2-0.05}$) and 20GDC ($Ce_{0.8}Gd_{0.2}O_{2-0.1}$). These materials are formed by doping the parent material CeO_2 with different amounts of Gadolinium atoms. For every two Ce^{4+} atoms replaced by Gd^{3+}, (Substitutional impurity) one positively charged oxygen vacancy (Vacancy) is formed in the oxygen lattice of CeO_2. This is because on doping the lower positive charge on the dopant (Gd^{+3}) when compared host atom (Ce^{+4}), leaves the crystal negatively charged. To compensate, negatively charged oxygen atoms (O^{2-}) can leave the crystal, creating positively charged vacancies. It is the presence of a high concentration of such charged mobile point defects (vacancies in GDC) that make ionic solids suitable for electrochemical applications such as electrodes and electrolytes in solid state devices.

2.1.2 Symbolism of point defects and solid state reactions

Solid state reactions are written in a similar manner to chemical reactions. However, the notation of point defects is different when compared to chemical elements or compounds. Solid state reactions use the Schottky [39] or the Kroger-Vink (KV) [40] notations. Although the Schottky notation is thermodynamically sufficient, it uses the building element [41] formulation which is abstract and difficult to use [38]. In both the notations, in addition to the defective component being addressed, the lattice sites

occupied by the defect together with the charges they posses with respect to a perfect crystal are specified. For a review of Schottky and KV notations please see [42].

The KV notation is used in this thesis because its structural element formulation vividly specifies the creation and annihilation of charged defects. According to the KV notation, $V_M^{\bullet}$ is used to represent a positively charged vacancy at a site which had been occupied by an atom *M*. If an impurity atom *P* is located in the position of a host atom *H* leaving the crystal negatively charged relative to a perfect charge-neutral crystal, it is represented by $P_H^{'}$. Electrons are denoted by e′, while electron holes are represented by $h^{\bullet}$.

A single dot "$\bullet$" represents a single positive charge while a prime " ' " indicates a single negative charge. The charge of an ionic defect is considered with respect to the perfect solid while, electronic defects are indicated with the charges they posses. An atom *M* occupying its lattice site is given by M_M^X with the *X* indicating neutral charge. A vacancy or an ion in an interstitial site may be represented by replacing the suffix *M* by *i*. Thus, the reaction involving the formation of vacancies in GDC, due to doping (see section 2.2.1) may be written in the following form,

$$Gd_2O_3 \xrightarrow{CeO_2} 2Gd_{Ce}^{'} + V_O^{\bullet\bullet} + 3O_O^X \qquad (2.1)$$

where

$Gd_{Ce}^{'}$ represents Gd atom occupying Ce site thus leaving the crystal negatively charged relative to a perfect crystal

$V_O^{\bullet\bullet}$ represents the double positively charged oxygen vacancies

O_O^X represents oxygen atoms in oxygen sites thus having neutral charge.

Thus in formulating solid state reactions in which structural elements take part, one must observe three balances: 1. the material balance (Same kind of atoms must exist on either side of the reaction), 2. the charge balance (Charges must balance on either side, just like any chemical reaction) and 3. the site balance (the ratios to one another of the possible crystallographic sites must be the same on either side).

Although we use the KV notation in this thesis, a brief comment on how it differs from the Schottky notation is in order (see [43] for details). To illustrate we consider the formation of Frenkel [25, 44] defects in AgCl crystal. A Frenkel defect is a disorder where the cation moves to an interstitial position leaving a negatively charged vacancy. The corresponding solid state reaction is written in Schottky notation as,

$$nil \rightleftharpoons Ag^{\bullet} + \left|Ag\right|^{'} \tag{2.2}$$

The same reaction is represented in the KV notation in the following form,

$$Ag_{Ag}^{X} + V_{i}^{X} \rightleftharpoons Ag_{i}^{\bullet} + V_{Ag}^{'} \text{ Or } nil \rightleftharpoons \left(Ag_{i}^{\bullet} - V_{i}^{X}\right) + \left(V_{Ag}^{'} - Ag_{Ag}^{X}\right) \tag{2.3}$$

Comparing Eq. (2.2) and Eq. (2.3) we see that building elements are combinations of structural elements (see Eq. (2.4))

$$\left|Ag\right|^{'} = \left(V_{Ag}^{'} - Ag_{Ag}^{X}\right) \text{ and } Ag^{\bullet} = \left(Ag_{i}^{\bullet} - V_{i}^{X}\right) \tag{2.4}$$

We note that, while the building element combination ($|Ag|^{'}$) may be added to or removed from the solid independent of other building elements, the structural elements may not. This is true because it is impossible to remove silver atoms from the crystal without creating vacancies in the silver lattice. It is this property of a structural element (indirectly reflecting the lattice constraint in the solid) which requires the introduction of the diffusion and virtual electrochemical potentials as will be explained in the next section.

Point defects are also classified as simple and complex point defects. Simple defects are isolated structural elements and may interact through coulombic forces forming defect associates in ionic solids [45-48]. These are called complex defects. Associated complexes are commonly known to occur in both GDC and YSZ (Yttria Stabilized Zirconia (YSZ)), both of which are common materials for electrolytes in SOFCs. Complex defects ultimately reduce the overall ionic conductivity of the solid [38]. Such complex defects are usually formed under high concentrations of point defects and need a different treatment. In two recent articles [17] and [18] the effect of stresses on the shift in the equilibrium of such a solid-state reaction involving the formation of complex defects in $Ce_{0.8}Gd_{0.2}O_{1.9}$ (20GDC) has been investigated. This is another example showing the interaction of stress and electrochemical fields. In the proposed research we consider only simple defect chemistry, although the developed framework may be extended to include complex defects as well.

2.2 Thermodynamics of point defects

2.2.1 The chemical potential

A vague discomfort at the thought of the chemical potential is still characteristic of a physics education. This intellectual gap is due to the obscurity of the writings of J. Willard Gibbs who discovered and understood the matter 100 years ago. - C. Kittel; Preface to his book: Introduction to Solid State Physics.

Physically, chemical potential (or electrochemical potential for a charged component in an electric field) is a quantification of how much a particular component is "disliked" under conditions of constant values of certain state variables and the concentration of all other components [38]. Mathematically, the electrochemical potential

of a certain chemical component is the partial derivative of the free energy with respect to the concentration of that component, keeping other state variables together with the concentration of all the other components as a constant. Those state variables that are kept constant, depend on the free energy chosen [27, 42]. Most generally we may write the electrochemical potential of a component β $\left(\tilde{\mu}_\beta\right)$ as,

$$\tilde{\mu}_\beta = \left(\frac{\partial \Pi}{\partial c_\beta}\right)_{S,l_i,c_{\alpha\neq\beta}} = \left(\frac{\partial H}{\partial c_\beta}\right)_{S,L_i,c_{\alpha\neq\beta}} = \left(\frac{\partial \Im}{\partial c_\beta}\right)_{T,l_i,c_{\alpha\neq\beta}} = \left(\frac{\partial \Gamma}{\partial c_\beta}\right)_{T,L_i,c_{\alpha\neq\beta}} \tag{2.5}$$

where

Π is the internal energy

H is the enthalpy

$\Im$ is the Helmholtz free energy

Γ is the Gibb's free energy

S is the entropy

T is absolute temperature

L_i's are the work coefficients (like pressure, stress, electric field, magnetic field strength)

l_i's are work co-ordinates (like volume, strain, electric polarization and magnetic polarization)

c_β is the concentration of the component β

At this point we note that the chemical and the electrochemical potential differ by the additive term $z_\alpha F\phi$ as indicated in Eq. (1.1). Henceforth, until stated otherwise, we will discuss the chemical potential only and understand that if the defects have net

charges, the electrochemical potential can be obtained by adding the term $z_\alpha F\phi$ to the chemical potential.

The virtual nature of the chemical potential of individual structural elements is apparent from the definition of structural and building elements explained in the previous section. The chemical potential of a structural element cannot be physically realized, as it is impossible to change its concentration without changing the concentration of other structural elements. This is because of the network requirement of the solid [49], according to which the concentration of the structural elements are not independent. For this reason, the associated chemical potentials of the individual structural elements are termed as virtual chemical potentials [49]. The physically realizable chemical potentials are those of the building elements as they inherently the contain network requirement of the solid. This is illustrated and explained in considerable detail in the subsequent sections.

2.2.2 Statistical mechanics of point defects

Consider a diatomic crystal (MO) which allows vacancies in both its cationic (M) and anionic (O) lattices. For illustration purposes only, we can imagine that the M atoms and O atoms can leave the crystal to go into the surrounding gas MO(g) with the creation of vacancies in both the lattices. For simplicity let us consider a case where the defects are neutral. The free energy (Γ) of the imperfect crystal at a given temperature and pressure, can be written as a deviation from the free energy of the perfect crystal (Γ^0) in the following form,

$$\Gamma = \Gamma^0 + n_{V_M^X}\gamma_{V_M^X} + n_{V_O^X}\gamma_{V_O^X} - TS_{config} \tag{2.6}$$

where

$n_{V_M^X}\gamma_{V_M^X}$ is the energy needed to create $n_{V_M^X}$ vacancies in the cationic lattice

$n_{V_o^X}\gamma_{V_O^X}$ is the energy needed to create $n_{V_O^X}$ vacancies in the anionic lattice

S_{config} is the configurational entropy associated with creating the defects and is given as [50],

$$S_{config} = +k_B \ln \Omega_{V_M^X} + k_B \ln \Omega_{V_O^X} \tag{2.7}$$

In Eq. (2.7), $\Omega_{V_M^X}$ and $\Omega_{V_O^X}$ represent the total number of complexions possible while arranging the vacancies in the cationic and anionic lattices and k_B is the Boltzmann's constant. If $n_{M_M^X}$ and $n_{O_O^X}$ represent the total number of cations and anions in the defective crystal, then we may write,

$$n_{M_M^X} + n_{V_M^X} = N_M \tag{2.8}$$

$$n_{O_O^X} + n_{V_O^X} = N_O \tag{2.9}$$

where N_M and N_O represent the total number of cationic and anionic lattice sites in the crystal. For the diatomic lattice considered, $N_M = N_O = N$. The number of complexions is nothing but the number of ways one can arrange N lattice points, taken, $N_M - n_{V_M^X}$ ($N_O - n_{V_O^X}$) at a time. This is given from basic combinatorics as,

$$\begin{aligned} \Omega_{V_M^X} &= \frac{N!}{n_{V_M^X}!\left(N - n_{V_M^X}\right)!} \\ \Omega_{V_O^X} &= \frac{N!}{n_{V_O^X}!\left(N - n_{V_O^X}\right)!} \end{aligned} \tag{2.10}$$

Using Stirling approximation, to write, $\ln K! = K \ln K - K$ (where K is a large number), we obtain the configuration entropy as,

$$S_{config} = k_B N_M \ln\left(\frac{N}{N - n_{V_M^X}}\right) - k_B n_{V_M^X} \ln\left(\frac{n_{V_M^X}}{N - n_{V_M^X}}\right)$$
$$k_B N_O \ln\left(\frac{N}{N - n_{V_O^X}}\right) - k_B n_{V_O^X} \ln\left(\frac{n_{V_O^X}}{N - n_{V_O^X}}\right) \tag{2.11}$$

The chemical potential of the defects is obtained by direct differentiation of Eq. (2.7) after substituting for S_{config} from Eq. (2.11).

$$\mu_{V_M} = \frac{\partial \Gamma}{\partial c_{V_M^X}} = A \frac{\partial \Gamma}{\partial n_{V_M^X}} = A\left[\gamma_{V_M^X} + k_B \ln\left(\frac{n_{V_M^X}}{N - n_{V_M^X}}\right)\right]$$
$$\mu_{V_O} = \frac{\partial \Gamma}{\partial c_{V_O^X}} = A \frac{\partial \Gamma}{\partial n_{V_O^X}} = A\left[\gamma_{V_O^X} + k_B \ln\left(\frac{n_{V_O^X}}{N - n_{V_O^X}}\right)\right] \tag{2.12}$$

Noting that the mole number $c_d = n_d / A$ (where A is Avogadro's number and d represents either, V_M^X ,V_O^X , M or O) and using the relation, $R = k_B A$ (R is the universal gas constant), we obtain the form,

$$\mu_{V_M} = \mu_{V_M}^* + RT \ln\left(\frac{c_{V_M^X}}{c_M - c_{V_M^X}}\right)$$
$$\mu_{V_M} = \mu_{V_M}^* + RT \ln\left(\frac{c_{V_O^X}}{c_O - c_{V_O^X}}\right) \tag{2.13}$$

We see that $\mu_d^* = A\gamma_d$ is a constant. We may write the expressions for the chemical potentials in terms of the mole fractions as well, by diving the terms in the parentheses by the total number of moles of the compound. In the case of the solid MO, this is equal to $c_M \left(= c_O\right)$ and we get,

$$\mu_{V_M} = \mu^*_{V_M} + RT \ln\left(\frac{\rho_{V_M^X}}{1-\rho_{V_M^X}}\right)$$
$$\mu_{V_M} = \mu^*_{V_O} + RT \ln\left(\frac{\rho_{V_O^X}}{1-\rho_{V_O^X}}\right) \quad (2.14)$$

where ρ_d is the mole fraction of the **d**efect V_M^X or V_O^X .

A few comments with regards to the developed chemical potentials are in order.

1) When the mole fraction of the defects is small when compared 1, the chemical potentials take the form,

$$\mu_{V_M} = \mu^*_{V_M} + RT \ln\left(\rho_{V_M^X}\right)$$
$$\mu_{V_O} = \mu^*_{V_O} + RT \ln\left(\rho_{V_O^X}\right) \quad (2.15)$$

It can be seen that this form of the chemical potential is similar to that of a chemical component from traditional chemical thermodynamics. This is the form of the chemical potential that will be used in the thesis.

2) In deriving the expressions for the chemical potential, it was assumed that the energy needed to form a defect γ_d is independent of the number of defects already existing in the solid. This is true only for dilute solutions and is not valid in cases where the concentrations of the defects are in the order of the concentration of the regular lattice sites.

3) It was also assumed in deriving the chemical potential that, the ionic solid is subjected to a constant pressure condition. Thus the elastic energy density is uniform throughout the solid. This need not be the case because stresses resulting from external

thermomechanical loads may be distributed over the solid. Moreover, it was seen in chapter 1 that self stresses arising due to deviation from stoichiometry can also be non-uniformly distributed. Thus, the energy needed to form the defect can depend on the local elastic energy density in the solid. Deriving this dependency is in fact the first portion of this thesis and is discussed in the next chapter.

4) In the expression for the configurational entropy term, defect interactions are not accounted for. If it is known that defect concentrations are large enough to interact, forming associated complexes [44], other methods must be used to include site exclusion effects. This has been done for Ceria and Lanthanum compounds in [51, 52]. In such cases the chemical potentials are generally written as,

$$\begin{aligned} \mu_{V_M} &= \mu^*_{V_M} + RT\ln\left(\rho_{V_M^X}\lambda_{V_M^X}(\rho_{V_M^X})\right) \\ \mu_{V_O} &= \mu^*_{V_O} + RT\ln\left(\rho_{V_O^X}\lambda_{V_O^X}(\rho_{V_O^X})\right) \end{aligned} \tag{2.16}$$

where $\lambda_{V_M^X}$ and $\lambda_{V_O^X}$ are called activity coefficients and are functions of the concentrations. The product, $\rho\lambda$, is in general called activity. In this work we consider only dilute defects, and site exclusion effects are neglected. For such cases the activity coefficient is unity and the activity is simply the concentration of the defects.

5) Interestingly we may differentiate the expression Γ with respect to the concentration of N at constant defect numbers, to get the chemical potential of the monomeric unit MO as,

$$\mu_{MO} = \frac{A\Gamma^0}{c_{MO}} + RT\ln\left(\frac{1}{1-\rho_{V_M^X}}\right) + RT\ln\left(\frac{1}{1-\rho_{V_O^X}}\right) \tag{2.17}$$

clearly, the entropic contributions (the ln terms) are negligible when we consider the dilute case and μ_{MO} scales with the number of monomeric units added. Stated differently the defect concentrations only weakly affect the chemical potential of the monomeric unit MO.

6) We may write the solid state reactions for the example considered resulting in the formation of the vacancies as follows,

$$M_M^X + O_O^X \rightleftharpoons V_M^X + V_O^X + MO(g) \tag{2.18}$$

Rearranging terms we get,

$$nil \rightleftharpoons \left(V_M^X - M_M^X\right) + \left(V_O^X - O_O^X\right) + MO(g) \tag{2.19}$$

The terms $\left(V_M^X - M_M^X\right)$ and $\left(V_O^X - O_O^X\right)$ are the building elements for the defects, and only these combinations are physical quantities. In essence, they emphasize that one can create a vacancy structural element only by removing the atom (another structural element). Thus the chemical potentials $\left(\mu_{V_M} \text{ and } \mu_{V_O}\right)$ derived in this section are for the combinations $\left(V_M^X - M_M^X\right)$ and $\left(V_O^X - O_O^X\right)$ and not for V_M^X and V_O^X, i.e.

$$\begin{aligned} \mu_{V_M} &= \mu_{V_M^X} - \mu_{M_M^X} \\ \mu_{V_O} &= \mu_{V_O^X} - \mu_{O_O^X} \end{aligned} \tag{2.20}$$

These potentials (Eq. (2.20)) must be used to establish chemical equilibrium and as a driving force for diffusion of the defects, and hence they are termed as the diffusion potentials [53]. In simple terms the diffusion potential corresponds to the energy changes associated with an exchange mechanism [54]. The quantities $\mu_{V_M^X}$, $\mu_{M_M^X}$, $\mu_{V_O^X}$ and $\mu_{O_O^X}$ are called the virtual chemical potentials of the structural elements [42, 55-57].

7) Mass action laws are expressions relating the concentration of all species in chemical reactions that are in equilibrium. For a general chemical reaction in equilibrium as in Eq.(2.21), involving several reactants R_i's and products P_i's at different stoichiometric amounts n_i and m_i respectively,

$$n_1R_1 + n_2R_2 + n_3R_3 + \ldots \rightleftharpoons m_1P_1 + m_2P_2 + m_3P_3 + \ldots \tag{2.21}$$

we first write the condition for chemical equilibrium as,

$$\sum_{i=1}^{N} n_i \mu_{R_i} - \sum_{i=1}^{M} m_i \mu_{P_i} = 0 \tag{2.22}$$

We then substitute the expressions for the chemical potentials and obtain the mass action law for the reaction. For the solid state reaction, Eq.(2.19) in our example, this is written as follows,

$$0 = \mu_{V_M} + \mu_{V_O} + \mu_{MO(g)} \tag{2.23}$$

On using Eq.(2.14) we get,

$$0 = \mu^*_{V_M} + \mu^*_{V_O} + \mu_{MO(g)} + RT \ln\left(\frac{\rho_{V_M^X}}{\left(1-\rho_{V_M^X}\right)} \frac{\rho_{V_O^X}}{\left(1-\rho_{V_O^X}\right)} \right) \tag{2.24}$$

This results in,

$$\exp\left(-\left(\frac{\mu^*_{V_M} + \mu^*_{V_O} + \mu_{MO(g)}}{RT} \right) \right) = \frac{\rho_{V_M^X}}{\left(1-\rho_{V_M^X}\right)} \frac{\rho_{V_O^X}}{\left(1-\rho_{V_O^X}\right)} \tag{2.25}$$

The LHS being a constant for given set of conditions, gives,

$$\mathrm{K} = \frac{\rho_{V_M^X}}{\left(1-\rho_{V_M^X}\right)} \frac{\rho_{V_O^X}}{\left(1-\rho_{V_O^X}\right)} \tag{2.26}$$

K is called the equilibrium constant of the reaction and Eq.(2.26) is the mass action law.

If we had used the dilute approximation for the chemical potentials Eq.(2.15), we would obtain,

$$\mathrm{K} = \rho_{V_M^X} \rho_{V_O^X} \tag{2.27}$$

We now note that, the above relation could also have been obtained, if we had naively formulated the mass action law for Eq.(2.18) using virtual chemical potentials of the individual structural elements in the same form as in Eq.(2.15), i.e.,

$$\mu^*_{M_M^X} + RT \ln \rho_{M_M^X} + \mu^*_{O_O^X} + RT \ln \rho_{O_O^X} = \mu^*_{V_M^X} + RT \ln \rho_{V_M^X} + \mu^*_{V_O^X} + RT \ln \rho_{V_O^X} + \mu_{MO(g)} \tag{2.28}$$

But the concentration of the regular sites, $\rho_{M_M^X} = \rho_{O_O^X} \cong 1$ (for dilute case), and rearranging we get back, Eq.(2.27), after recognizing that, $\mu^*_{V_M} = \mu^*_{V_M^X} - \mu^*_{M_M^X}$ and $\mu^*_{V_O} = \mu^*_{V_O^X} - \mu^*_{O_O^X}$. None of the quantities, $\mu^*_{V_M^X}$, $\mu^*_{M_M^X}$, $\mu^*_{V_O^X}$ or $\mu^*_{O_O^X}$ is individually a physical quantity. The appropriate difference is and relates to the energy required to form the defect.

In this thesis, we will consider the solid state reactions and the mass action laws as in Eq.(2.28). In short we will use the definition of the chemical potential in the form as in Eq.(2.15) for all the structural elements in the reaction. Structural elements that are regular sites in the lattice will be assigned an activity of unity while the activity of the defects will be their concentrations in moles per mole of the compound.

8) The change Gibbs free energy may also be written completely in terms of the concentration structural elements of the solid MO under constant temperature and pressure conditions as follows [38, 58-60]

$$\mathrm{d}\Gamma = \mu_{O_O^X} d\rho_{O_O^X} + \mu_{V_O^X} d\rho_{V_O^X} + \mu_{M_M^X} d\rho_{M_M^X} + \mu_{V_M^X} d\rho_{V_M^X} \tag{2.29}$$

Establishing that the total number of cation and the anion sites remains a constant for the solid (network constraint), we have the relations,

$$d\rho_{O_O^X} = -d\rho_{V_O^X} \text{ and } d\rho_{M_M^X} = -d\rho_{V_M^X} \tag{2.30}$$

Using this in Eq.(2.29) we see that,

$$d\Gamma = \left(\mu_{V_O^X} - \mu_{O_O^X}\right) d\rho_{V_O^X} + \left(\mu_{V_M^X} - \mu_{M_M^X}\right) d\rho_{V_M^X} \tag{2.31}$$

$$\frac{\partial\Gamma}{\partial\rho_{V_O^X}} = \left(\mu_{V_O^X} - \mu_{O_O^X}\right) = \mu_{V_O} \text{ and } \frac{\partial\Gamma}{\partial\rho_{V_M^X}} = \left(\mu_{V_M^X} - \mu_{M_M^X}\right) = \mu_{V_M} \tag{2.32}$$

Thus thermodynamics also reveals that the change in concentration of the vacancies is established through the difference in the virtual potentials of the structural elements associated with the appropriate lattices.

It is thus sufficient to express any free energy as a function of the concentration of the defects only and understand to that the partial derivatives with respect to their concentrations represent the diffusion potential of the defects.

With this basic introduction we conclude the essential background needed, on point defect chemistry, its representation and its thermodynamics. In the next section a brief introduction into the theory of Molecular Dynamics simulation is given.

2.3 Molecular dynamics simulations

2.3.1 Introduction

In general three main classes of techniques have been employed in the study of materials at the atomic level: atomistic (static lattice [61] or Molecular Statics (MS)), Molecular Dynamics (MD)[62] and quantum mechanical (ab-initio)[63] methods. Quantum calculations involve the solution to the Schrodinger wave equation or its variations. These calculations typically involve many degrees of freedom which makes

this method computationally inhibitive for study of more than several hundred atoms using modern computers. This is so because the constituent electrons in the system are also considered in these simulations. MS merely uses energy minimization principles to find the equilibrium positions of atoms that are interacting through force fields represented by empirical interatomic potentials. This technique does not simulate the vibration of the atoms about their mean positions which are present at finite temperatures; and hence it represents the system of interest at 0K. MD as opposed to MS, uses classical mechanics (Newton's 2nd law) to determine the equilibrium positions and velocities of atoms in a system at non-zero temperatures [64]. Both MD and MS neglect the explicit effects of electrons and hence are useful for studies where direct electronic effects on physical properties can be neglected. For example: thermal conduction of non-metallic materials is through phonons (unlike metals where it occurs through electrons) or lattice waves. Thus MD can be used to study thermal conductivity of non-metallic materials. The interatomic potential is usually fit to a functional form so as to represent the system of interest as accurately as possible. The accuracy of the interatomic potential chosen, therefore determines the validity of the results of any MD simulation.

To explain the role of interatomic potential in simple terms, we may imagine the heavenly bodies of the universe (galaxies, planets, stars) as atoms. Then the interatomic potential energy is simply the well known gravitational potential energy

$$U_{gravitational} = -\sum_{j=1}^{M}\sum_{i=1}^{N}\frac{G^r m_i m_j}{r_{ij}} \tag{2.33}$$

where

m_i is the mass of the object

r_{ij} is the distance between the atoms

G^r is the universal gravitational constant

The negative sign indicates that the energy decreases when the distances between the concerned objects reduce and hence gravity is an attractive force. The force on an object *i* is the derivative of the gravitational potential energy with respect to the vectorial components of its position, and we get the familiar $1/r^2$ dependent gravitational force.

In MD, the potentials assume more complicated forms. They generally are not dependent on the masses of the atoms (as gravity is a weak force, being several orders of magnitude smaller than the nuclear or electrostatic forces) and can have components that are of attractive and repulsive nature. MD potentials actually represent nuclear forces and are of short range. Thus when two similar atoms are brought too close together, they repel due to electron-electron repulsion (Pauli's exclusion principle). When they are moved apart from each other within a certain distance they attract due to nucleon-electron attraction. Thus, there exists an equilibrium distance where the energy is a minimum. In addition to the short range forces, sometimes it becomes important to consider the long range, non-bonded interaction amongst the constituent atoms. This is, all the more true for ionic solids where the bonding is ionic, meaning bonding is through loss or gain of electrons, giving the atoms a net charge. Hence, the total potential energy of the system is given as a sum of the short range and the long range electrostatic (coulombic) energies. Identifying the various kinds of potentials and the techniques to fit them for materials is a subject of its own and is beyond the scope of this thesis. In this work we use existing interatomic potentials from the literature for the material of interest, GDC, in order to determine the properties which will be introduced in the next chapter. As mentioned, MD

considers the kinetic energy of the vibrating atoms at non-zero temperatures as well. Thus the total energy is actually the sum of the total potential and the kinetic contributions. In essence the problem of MD reduces to that of tracking the evolution of the position and velocities of atoms over time, basically a multi-body dynamics problem.

2.3.2 Statistical mechanics and MD

MD draws its fundamental concepts from the methods of classical statistical mechanics [50]. The theory of statistical mechanics mainly aims to relate the macroscopic thermodynamic properties of materials, such as temperature, pressure chemical potential etc, to the microscopic quantities, the positions and the velocities of the constituent atoms. All the properties of the system are assumed to be only time averages of an otherwise rapidly fluctuating quantity. As the time period of fluctuation is enormously small ($\approx 10^{-15}\,\mathrm{s}$), statistical mechanics invokes ergodicity [65] by employing the concept of ensembles. Ensembles are replicas of the system under consideration, all with the same macroscopic properties, but are different microscopically (the velocities may be distributed differently among the constituent atoms). Thus instead of time averaging, ensemble averages are taken instead. However, MD gives us the trajectories of the atoms and the evolution of their velocities over time; hence the time averages of the properties of interest can be evaluated after a MD run, with importance being given to one important aspect, the initial condition. It was said earlier that MD is nothing but a dynamics problem; thus to solve it, initial positions and the velocities must be specified. But it would be highly unrealistic if the initial microscopic states give different averages of the macroscopic thermodynamic quantity. Hence, an MD simulation has to be carried out for sufficient time so that the velocities and positions are de-correlated from the initial

state (usually in the range of a few pico – nano seconds). By using MD, we may simulate the idealized experiments of thermodynamics and study the system's response. For example, we may simulate a system under constant pressure, temperature and constant number of atoms in order to realize an NPT ensemble. This may then be used to determine the volume of the system under certain applied temperature and pressure. Many numerical advances have been made to realize such ensembles. It is not the subject of this thesis to delve into the intricacies of programming MD. For this we refer the reader to good expositions on the subject through references, [64, 66]. In this work we use MD as a tool to determine the equilibrium configuration of the structure and then we post process the results to obtain the relevant quantities of interest.

With this brief introduction to molecular dynamics we conclude this chapter on the necessary background required to proceed reading the thesis further. In the next chapter, we develop the thermodynamic framework that explicitly delineates the required differential equations to study stress-defect transport interactions after developing the stress dependent chemical potential.

CHAPTER 3. CONTINUUM FRAMEWORK

3.1 Chapter abstract

Pertinent literature associated with this chapter concludes with the identification of the Cauchy's stress dependent chemical potential. However, based on Eshelby's seminal work in 1951 [67] and motivations from a more recent article [68] it is made clear that the elastic contribution to the chemical potential of point defects must come from the Eshelby stress. The crux of this chapter is to derive this dependence. In doing so, two material properties that enable full coupling between defect transport and stresses are introduced. These are the CCE and the variation of elastic constants with vacancy concentration (or more generally non-stoichiometry) (OSEC). The main content of this chapter is then concluded by providing a resume of governing differential and algebraic equations that must be solved to numerically study the stress-defect transport interactions. The boundary conditions to which these differential equations must be subjected to are also provided. The particular kind of defects assumed in this case are the oxygen vacancies, oxygen interstitials, electrons and electron holes which is typical for any oxide ceramic.

3.2 Introduction

3.2.1 Historical to state of the art - Review

The existence of chemical potential in an inhomogeneously stressed solid, for mobile and immobile components was established in [69]. This was done based on thermodynamic arguments; expressions for the chemical potential were developed [70]. Subsequently, [71] investigated the effect of lattice strains, created by defects such as

precipitates and dislocation, on the saddle point energy configuration during diffusion. It was shown by means of detailed calculation that vacancy migration energies may be altered by 10% due to stresses. Therefore it is clear that stress alters defect transport in at least two fundamental ways [71-73]. The drift effect is of thermodynamic origin and is due to the dependence of the chemical potential on stress and to a kinetic effect due to the effect of stress on the migration barrier for diffusion (i.e. the mobility). Since volumetric strains are generated by the formation volume of the defect and by the migration volume, local elastic energy directly affects diffusion. Consequently, both the stress dependent chemical potential and the kinetic parameters governing diffusion should consider the effect of stress on both these volume changes. It could be assumed for the sake of simplicity that the kinetic coefficients of diffusion are not affected by stress and that the volume of defect formation is larger than the volume change that is associated with migration [74]. A recent article [75] has however provided a technique to use atomistic simulations to study the effect of stresses on both the formation and the migration energies.

It was not until the work of Li, Nolfi and Johnson in [76] that the chemical potentials of point defects were applied for diffusional equilibrium of defects in an inhomogeneous stress field. When point defects are considered, as was shown in section 2.2.2 it is the diffusion potential that must be modified to include the effects of stress. The term diffusion potential was coined in ref.[77]. In this work since we consider dilute defect concentration, the terms diffusion potential and the chemical potential can be used interchangeably as was mentioned in section 2.2.2. Although Maxwell's type expressions relating chemical potential, stress, strain and concentration were given in ref. [69] it was

only about seven years later in ref. [78] that the expression was developed for the diffusion potential as a function of the local stress state. These were developed based on the integration of the Maxwell's type expression [58].

Assuming defects similar to those in section 2.2.2 for the MO oxide, the stress dependent diffusion potential for the vacancies in the oxygen and the metal sub-lattices can be given in the following form [78],

$$\mu_\alpha\left(\rho_\alpha,\sigma\right)=\mu_\alpha\left(\rho,0\right)-V_m\eta_{ij}^{\alpha}\sigma_{ij}-\frac{V_m}{2}s_{ijkl}^{\alpha}\sigma_{kl}\sigma_{ij} \tag{3.1}$$

where,

α, is either V_O or V_M

$\mu_\alpha\left(\rho_\alpha,0\right)$, is the stress independent diffusion potential

V_m , is the molar volume of the solid

σ_{ij} , is the Cauchy's stress tensor

$\eta_{ij}^{\alpha}=\frac{\partial\varepsilon_{ij}^{\alpha}}{\partial\rho_\alpha}$, is the *Chemical Coefficient of Expansion* (CCE)

$\varepsilon_{ij}^{\alpha}$, are the eigenstrains due to compositional change of defect species α

$s_{ijkl}^{\alpha}=\frac{\partial S_{ijkl}}{\partial\rho_\alpha}$, is the change in elastic compliance due to a change in concentration of the defect species α

S_{ijkl} is the compliance of the material

ρ_α is the concentration in moles per mole of the compound

From Eq. (3.1) it is clear that the expression for stress dependent diffusion potential entails the introduction of two material parameters η_{ij}^{α} and s_{ijkl}^{α}. η_{ij}^{α} represents the

eigenstrains (or stress free strains) induced due to deviations in local composition; is known as the C*hemical Coefficient of Expansion* (CCE) for species α. CCE is identical to the *Thermal Coefficient of Expansion* (TCE) in the sense that it represents strains per unit change in concentration just as TCE represents strains per unit temperature change. s^{α}_{ijkl} represents the variation of the elastic compliance with composition. It must be noted that, in general the compositional strains follow Vegard's law, which states that strains are linearly related to the deviation in composition through the CCE [79]. It is also clear from the definition of the diffusion potential that these material constants must be associated with the diffusion potential and not the virtual potential of the species.

Expressions such as Eq. (3.1) were developed for metallic systems (alloys) originally in [78] and were extended to nonlinear materials in [80]. Ionic solids were considered to account for charged defects in [81, 82].

There are several applications of the diffusion potential in Eq. (3.1); it can be used to determine the equilibrium concentration distribution of the defects in a solid when it is subjected to a non-uniform stress field [83]. In addition to this it can also be used to study steady state and transient diffusion induced stresses in thin films and in electrolytes [84, 85], by using the gradient of the diffusion potential as the driving force for diffusion. Numerical simulation of kinetic demixing of solids under non-hydrostatic stresses can also be performed using these stress dependent potentials [86]. It is important to note that the chemical potential, in addition to determining diffusional equilibrium of the solid also governs the chemical equilibrium of the solid state reactions [17]. For example, the equilibrium constant of the mass action law, of a chemical reaction is no longer only a function of temperature [27] but is also a function of the stress state. This is hence

another level of coupling between the electrochemical and mechanical fields in the ionic solid. Finally boundary conditions/concentrations are modified by applied tractions, which can also be obtained through the stress dependent diffusion potentials on the boundary chemical reactions. Thus the stress dependent diffusion potential couples the two fields.

Although the discussed diffusion potential is useful for numerically modeling and for studying diffusion-stress coupled problems, some of its features raise questions on its generality. For example, [87] showed that the governing diffusion differential equations and the mechanical equilibrium equations could be decoupled completely under certain conditions. These conditions were; a) isotropic material requiring η to be scalar quantity b) the compliance/stiffness being independent of the composition c) Diffusion (or more generally Onsager's) coefficients being independent of stress and concentration of the specie. The decoupling arises because in an isotropic material (η is a scalar), the elasticity term that governs diffusion is the gradient of the trace of the Cauchy's stress tensor $\left(\nabla\sigma_{ii}\right)$ (see Eq. (3.2))

$$\nabla\mu\left(\rho_\alpha,\sigma\right)=\nabla\mu_\alpha\left(\rho_\alpha,0\right)-V_m\eta^\alpha\nabla\sigma_{ii} \tag{3.2}$$

Using the above equation in a continuity condition [88] for the species α, we get,

$$\frac{\partial\rho_\alpha}{\partial t}=\nabla\bullet D_\alpha\left[\nabla\left(\mu_\alpha\left(\rho_\alpha,0\right)-V_m\eta^\alpha\nabla\sigma_{ii}\right)\right]=D_\alpha\left[\nabla^2\left(\mu_\alpha\left(\overline{\rho}_\alpha,0\right)-V_m\eta^\alpha\nabla^2\sigma_{ii}\right)\right] \tag{3.3}$$

Now it can be easily shown through linear elasticity [88] that,

$$\nabla^2\sigma_{ii}=\frac{-2E}{1-\nu}\nabla^2\sum_\alpha\eta^\alpha\left(\rho_\alpha-\rho_\alpha^0\right)=\frac{-2E}{1-\nu}\sum_\alpha\eta^\alpha\nabla^2\rho_\alpha \tag{3.4}$$

where,

E, is the Young's modulus

ν , is the Poisson's ratio

ρ_{α}^{0} , is the concentration of the species α at stoichiometry

η^{α} , is the chemical coefficient of expansion for species α

D_{α} , is a constant relating the flux of species α and the gradient in the diffusion potential (Defect diffusion coefficient)

Thus the continuity equations may be written completely in terms of concentrations, decoupling the mechanical and the diffusion governing equations. Once the boundary values of the concentrations are prescribed the diffusion problem can be solved completely, independently of the mechanical equilibrium conditions, given by

$$\sigma_{ij,j} = 0 \tag{3.5}$$

It must however be noted that the boundary conditions may still depend on the applied tractions. Although the diffusion problem may be solved independently of the mechanical equilibrium conditions, the solution to the elasticity problem requires knowledge of the concentration profiles. Thus, these equations (3.3) and (3.5) represent a one way coupling between stress and diffusion.

3.2.2 Contribution of current research

In the proposed research the diffusion potential in Eq. (3.1) is only a special case of the more general diffusion potential that is derived in this study based on continuum thermodynamics. The motivation behind the development of an alternative stress dependent diffusion potential is from Eshelby's seminal work on the forces on elastic singularities [67]. Here, he derived the expression for the force on an elastic singularity like a material inhomogeneity in an elastic body. The stresses associated with these forces are called the "Energy Momentum Tensor of Mechanics" or "Eshelby's Stress"[89]. We

will use the term Eshelby's stress (Eshelby stress) in this work. This has received wide spread attention in material mechanics particularly with problems associated with defects and inhomogeneities in continuous media. In our problem, since vacancies and point defects are elastic singularities, it is the Eshelby's stress which should appear as the elastic contribution to the chemical potential and not just Cauchy's stress. Recently Wu [68] has brought this to light with regard to neutral chemical components. In this work, we extend Wu's work to include charged point defects as well. We also show that only under certain conditions of self-stressed diffusion (where non-stoichiometry is the only source of stress) can one use expression (3.2).

The Eshelby's stress tensor, plays two important role in this thesis. First, as just mentioned, it will be elastic contribution to the chemical potential. Secondly, certain balance laws related to the Eshelby's stress tensor will be used to determine the strain energy release rates of cracked electrolyte configurations. The details of the Eshelby's stress tensor are not particularly important in this chapter. Here, we introduce it, as we derive the stress dependent chemical potential from the fundamentals. In chapter 6, while discussing crack driving forces, we explain it in greater detail. For now, it is sufficient to understand that the Eshelby's stress is a function of Cauchy's stress and the strain energy density at a continuum point.

With this motivation we derive the stress dependent diffusion potential and clearly highlight the governing differential/algebraic equations that are to be solved, in order to numerically study the coupled problem.

3.3 Necessary mechanics

3.3.1 Kinematics, stress measures and equilibrium

3.3.1.1 *Deformation*

Consider an ionic solid in equilibrium at a given temperature. It is assumed that at this initial state, the solid is stress-free. By treating the solid as a continuum, the kinematics of the motion of the material particles in the solid can be described by a continuous displacement field **u** given by

$$\mathbf{u} = \mathbf{x} - \mathbf{X} \tag{3.6}$$

where **x** is the position occupied at the current time t by the particle which occupied the position **X** in the initial configuration (t = 0). The Lagrangian and Eulerian descriptions of motion are given by,

$$x_i = x_i(\mathbf{X}, t) \tag{3.7}$$

and

$$X_I = X_I(\mathbf{x}, t) \tag{3.8}$$

Equations (3.7) and (3.8) may be interpreted as a mapping between the initial configuration and the current configuration. The continuum mechanics theory assumes that such mapping is sufficiently smooth (differentiable) and is one-to-one, i.e., the Jacobian (J) given by

$$J = \left| \partial x_i / \partial X_j \right| = \mathrm{Det}[F_{iJ}] = \frac{dV}{dV_0} \tag{3.9}$$

is non-zero. In the above, dV_0 is the representative volume element in the initial reference state and dV is the corresponding volume element the current deformed state.

Partial differentiation of Eq. (3.7) with respect to X_J and Eq. (3.8) with respect to x_j yield, respectively,

$$dx_i = F_{iJ} dX_J \,, dX_I = f_{Ij} dx_j \tag{3.10}$$

where

$$F_{iJ} = \frac{\partial x_i}{\partial X_J} = \delta_{iJ} + \frac{\partial u_i}{\partial X_J} \,,\; f_{Ij} = \frac{\partial X_I}{\partial x_j} = \delta_{Ij} - \frac{\partial u_I}{\partial x_j} \tag{3.11}$$

are called the material deformation gradient tensor and the spatial deformation gradient tensor, respectively. Clearly, we have $f_{Ik} F_{kJ} = \delta_{IJ}$ where δ_{ij} is the Kronecker delta [88]. In the above and the rest of this chapter, repeated Roman (both upper and lower case) subscripts are summed from 1 to 3 according to the summation convention, while Greek subscripts are not summed unless indicated explicitly.

The Lagrangian finite strain tensor is defined in terms of the deformation gradient tensors,

$$E_{IJ} = \frac{1}{2}\left(F_{kI} F_{kJ} - \delta_{IJ}\right) = \frac{1}{2}\left(\frac{\partial u_i}{\partial X_I} + \frac{\partial u_j}{\partial X_i} + \frac{\partial u_k}{\partial X_i}\frac{\partial u_k}{\partial X_j}\right) \tag{3.12}$$

When the displacement gradients are small, i.e., $\left|\partial u_i / \partial X_j\right| \ll 1$ and $\left|\partial u_i / \partial x_j\right| \ll 1$, neglecting the higher order terms leads to

$$E_{ij} = \frac{1}{2}\left(\frac{\partial u_i}{\partial X_j} + \frac{\partial u_j}{\partial X_i}\right) = \frac{1}{2}\left(\frac{\partial u_i}{\partial x_j} + \frac{\partial u_j}{\partial x_i}\right) = \varepsilon_{ij} \tag{3.13}$$

where ε_{ij} is called the infinitesimal strain tensor, and the distinction between the spatial and material descriptions is no longer necessary.

3.3.1.2 ***Stress measures, equilibrium***

The state of stress at a point in a continuum can be represented by the Cauchy stress tensor σ_{ij} in the current (or deformed) configuration. Note that the components of the Cauchy stress tensor are defined as force per unit area in the deformed configuration. The balance of the moment of momentum (Cauchy's second law of motion) dictates the symmetry of the Cauchy stress tensor, i.e., $\sigma_{ij} = \sigma_{ji}$. The equations of equilibrium are given by [88]

$$\frac{\partial \sigma_{ji}}{\partial x_j} + f_i = 0 \tag{3.14}$$

where f_i is the body force per unit volume in the deformed configuration.

Equation (3.14) is valid for any material point within a continuum body. For a material point on the surface (boundary) of the continuum, the following Cauchy formula applies

$$\sigma_{ij} n_j \Big|_S = p_i \tag{3.15}$$

where n_i is the unit outward normal vector of the surface *S* and p_i is the traction vector applied on *S*. Note that p_i is measured as force per unit deformed area.

Further Eq. (3.14) describes the equilibrium of an infinitesimal material element in the deformed configuration. The Cauchy stress tensor is typically written as a function of the Eulerian spatial coordinates x_i. To describe the equilibrium in the initial (undeformed) configuration, the Piola-Kirchhoff stress tensors are introduced.

The first Piola-Kirchhoff stress tensor, σ_{ij}^0, is defined as the actual force in the deformed configuration per unit undeformed area, while the second Piola-Kirchhoff

stress tensor, $\tilde{\sigma}_{ij}$, is defined as a fictitious force in the undeformed configuration per unit undeformed area. The fictitious force here is obtained by transforming the actual force in the deformed configuration back to the undeformed configuration, which is equivalent to pre-multiplying the actual force in the deformed configuration by the spatial deformation gradient tensor f_{Ij}. Hence, the two Piola-Kirchhoff stresses are related by the deformation gradient tensors in the following manner

$$\tilde{\sigma}_{IJ} = f_{Ik}\sigma^0_{Ik} \text{ or } \sigma^0_{Ij} = \tilde{\sigma}_{IK}F_{jK} \tag{3.16}$$

The Piola-Kirchhoff stresses are typically written as functions of the Lagrangian material coordinates X_i. They can be related to the Cauchy stress tensor by

$$\sigma^0_{Ij} = Jf_{Ik}\sigma_{kj},\ \tilde{\sigma}_{IJ} = Jf_{Ik}f_{Jm}\sigma_{km} \tag{3.17}$$

In Eq. (3.17) that $\tilde{\sigma}_{IJ}$ is symmetric while σ^0_{Ij} is generally non-symmetric. It is important to keep in mind that the Piola-Kirchhoff stress tensors are not actual stresses, i.e., they do not exist in the continuum under consideration. They are introduced to simplify the equilibrium equation in the initial configuration, namely,

$$\frac{\partial \sigma^0_{Ji}}{\partial X_J} + f_0 = 0 \text{ or } \frac{\partial\left(\tilde{\sigma}_{JK}F_{iK}\right)}{\partial X_J} + f_0 = 0 \tag{3.18}$$

where f_0 is the body force per unit volume in the initial configuration.

The Cauchy formula given by Eq. (3.15) can also be expressed in the initial configuration as,

$$\sigma^0_{Ji}N_J = F_{iJ}\tilde{p}_J,\ \tilde{\sigma}_{JI}N_J = f_{Ij}p^0_j \tag{3.19}$$

where

$$p^0_j = \frac{dS}{dS_0}p_j,\ \tilde{p}_J = \frac{dS}{dS_0}f_{Jk}p_k \tag{3.20}$$

and dS_0 is an area element in the initial configuration and dS is the same area element in the deformed configuration. Note that p_j is the force acting on the deformed surface per unit deformed area. Therefore, p_j^0 is the force acting on the deformed surface per unit undeformed area, while $\tilde{p}_J$ is a fictitious force acting on the deformed surface per unit undeformed area. This fictitious force is the actual force acting on the deformed surface transformed by f_{Jk}. Neither of p_j^0 and $\tilde{p}_J$ is a real traction vector. They are called pseudo traction vectors, introduced to accommodate the pseudo stress tensors.

For small deformation, i.e., $\left|\partial u_i / \partial X_J\right| \ll 1$ and $\left|\partial u_i / \partial x_j\right| \ll 1$, one can show from Eq. (3.13) that when the same coordinate system is used for both the Lagrangian and Eulerian configurations,

$$F_{ij} \approx \delta_{ij} + \frac{\partial u_i}{\partial X_j} \text{ and } J = \left|\partial x_i / \partial X_j\right| \approx \left|1 + \frac{\partial u_i}{\partial X_j}\right| \tag{3.21}$$

Thus, it follows from Eq. (3.21) that Piola-Kirchhoff stress reduces to the Cauchy stress,

$$\sigma_{ij} = \tilde{\sigma}_{km} = \sigma_{ij}^0 \tag{3.22}$$

for small deformation. Furthermore, the distinction between n_i and N_i, and between dS and dS_0 can also be neglected. Thus, the pseudo traction vector reduces to the Cauchy traction vector as well.

3.3.2 Multiplicative decomposition of F

As discussed in section 1.3, a change of defect concentration from its stoichiometry can cause a volumetric change (deformation) in the ionic solid. If such changes are uniform throughout the solid and the solid is not constrained mechanically the deformation would be uniform and no stress would be generated anywhere in the

solid, though the solid has undergone a volumetric change. Such a homogeneous deformation of the ionic solid from its stoichiometric state to a non-stoichiometric state is inelastic, since no stress is generated. Thus, it is called an eigentransformation after [68]. However, if the solid is constrained mechanically or if the change in defect concentration is not uniform throughout the solid, stresses may be created due to the incompatibility of the eigentransformation. Consequently, elastic deformation has to occur so that the total deformation becomes compatible. Therefore, the total deformation of an ionic solid in its non-stoichiometric state is described by the following multiplicative decomposition of the deformation gradient,

$$\boxed{\mathbf{F} = \mathbf{F}^E \mathbf{F}^c} \tag{3.23}$$

where $\mathbf{F}^c$ represents the eigentransformation due to non-stoichiometry only, and $\mathbf{F}^E$ represents the elastic deformation associated with $\mathbf{F}^c$ so that the total deformation is compatible.

It follows from the first of Eq. (3.12) that the total Lagrange strain can be written as

$$\mathbf{E} = \frac{1}{2}(\mathbf{F}^T\mathbf{F} - \mathbf{I}) = \left(\mathbf{F}^c\right)^T \mathbf{E}^E \mathbf{F}^c + \mathbf{E}^c \tag{3.24}$$

where

$$\mathbf{E}^E = \frac{1}{2}\left[\left(\mathbf{F}^E\right)^T \mathbf{F}^E - \mathbf{I}\right],\ \mathbf{E}^c = \frac{1}{2}\left[\left(\mathbf{F}^c\right)^T \mathbf{F}^c - \mathbf{I}\right] \tag{3.25}$$

are the elastic strain and the compositional strain (eigenstrain), respectively.

Following [68], we will use three configurations as in Figure 3.1 to develop the kinematics of the deformation. The stoichiometric state of the solid at a given

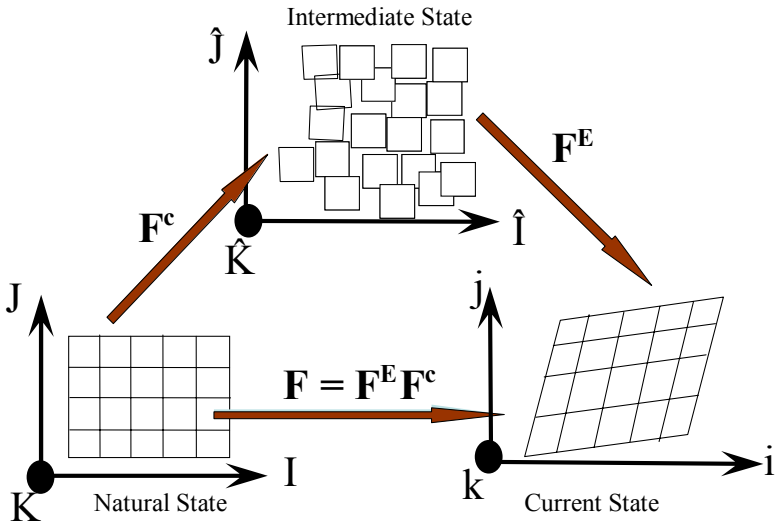

Figure 3.1: Multiplicative decomposition of the deformation gradient

temperature is called the initial or natural state. It is assumed that in the natural state of the solid, there is no stress (residual stress from manufacture etc.). From the natural state, the solid is transformed by the total deformation gradient **F** into its current state. In the current state, both elastic and inelastic deformation, as well as stress, may co-exist. In addition to these two physical states, we introduce an intermediate state. The intermediate state is the one created by transforming the natural state through the eigentransformation $\mathbf{F}^c$. Clearly, the intermediate state is also a stress-free state. One must realize that the intermediate state is not an actual physical state, as the solid is not necessarily continuous in the intermediate state due to the incompatibility of the eigentransformation. The three states are schematically shown in Figure 3.1. The specification of a Cartesian coordinate system to the intermediate state is still questionable [90], and investigation into the

properties of such a space is required. Nevertheless, since such a choice cannot be ruled out by mathematical or physical arguments according to ref. [90], and since it has been used in ref.[68, 91] and many others, we continue to use the Cartesian system for the intermediate state.

For clarity, tensorial quantities associated with the natural, current and intermediate states will be indicated, respectively, by subscripts of upper case Roman letters, lower case Roman letters and upper case Roman letters with a cap. For example, a second order tensor is written as ω_{IJ} in the natural state, ω_{ij} in the current state, and $\omega_{\hat{I}\hat{J}}$ in the intermediate state. Using this convention, we can write the component form of Eq. (3.23) as $F_{iJ} = F^{E}_{i\hat{K}} F^{c}_{\hat{K}J}$, since $F^{c}_{\hat{K}J}$ is the two-point tensor mapping the natural state to the intermediate state and $F^{E}_{i\hat{K}}$ is the two-point tensor mapping the intermediate state to the current state.

3.3.3 Strain energy densities & elastic constitutive equations

If we let the deviation from stoichiometry of defect species α be $\Delta\rho_{\alpha}$, then, to the leading order, the total volumetric change of the solid can be written as a linear function of the deviation of all defects from their stoichiometric values [92]

$$\frac{V^{c}_{m} - V_{m}}{V_{m}} = \sum_{\alpha} 3\eta_{\alpha}\Delta\rho_{\alpha} \tag{3.26}$$

where V_{m} is the molar volume of the solid in its natural state, and V^{c}_{m} is the molar volume of the solid in its intermediate state obtained by mapping V_{m} through the eigentransformation $\mathbf{F}^{c}$, i.e.,

$$V^{c}_{m} = J^{c} V_{m} \tag{3.27}$$

where J^c is related to $\mathbf{F}^c$ through Eq. (3.9) . Clearly V_m^c is a function of the defect concentrations. In Eq. (3.26), $\Delta\rho_\alpha = \rho_\alpha - \rho_\alpha^0$ with ρ_α^0 being the stoichiometric defect concentration for the species α. The constant η_α is called the coefficient of chemical expansion (CCE) of species α. Clearly, when the defect concentration is measured using the molar fraction, the corresponding CCE is dimensionless. It follows from Eq. (3.26) that the CCE can be written as

$$\eta_\alpha = \frac{1}{3}\frac{\partial V_m^c}{V_m \partial \rho_\alpha} \tag{3.28}$$

The CCE is an intrinsic material property. The advantage of introducing such a non-dimensional parameter to characterize the volumetric deformation due to compositional change is obvious. Gadolinium doped ceria (GDC) is known to have high CCE. Equation (3.28) also provides a way to obtain the CCE theoretically (experimentally) by computing (measuring) the molar volume of the ionic solid at different levels of non-stoichiometry.

Next we introduce the molar concentration in the natural and intermediate states by $\overline{\rho}_\alpha = \rho_\alpha / V_m$ and $\overline{\rho}_\alpha^c = \rho_\alpha / V_m^c$, respectively. They are related by the Jacobian

$$J^c = \frac{V_m^c}{V_m} = \frac{\overline{\rho}_\alpha}{\overline{\rho}_\alpha^c} \tag{3.29}$$

In terms of the Jacobian J^c, the eigentransformation induced by defect deviation can be written as

$$F_{iJ}^c = \left(J^c\right)^{1/3} \delta_{iJ} \tag{3.30}$$

Therefore, it can be easily shown that

$$\frac{\partial F_{iJ}^c}{\partial \rho_\alpha} = \frac{1}{3J^c}\frac{\partial J^c}{\partial \rho_\alpha} F_{iJ}^c \tag{3.31}$$

The deformation from the intermediate state to the current state represented by $\mathbf{F}^E$ is an elastic one. The elastic strain energy induced by such an isothermal and isocompositional deformation can be written as a function of the elastic strain $\mathbf{E}^E$, entropy s and molar concentrations $\overline{\rho}_\alpha^c$ of the intermediate state. For convenience, we define $w(\mathbf{E}^E, s, \overline{\rho}_\alpha^c)$ as the elastic strain energy of the current state per unit volume of the intermediate state. Since $\mathbf{E}^E$ is related to $\mathbf{F}^E$ through Eq. (3.25) and $\mathbf{F}^E$ is related to $\mathbf{F}$ and $\mathbf{F}^c$ through Eq., (3.23), $\mathbf{E}^E$ is a function of $\mathbf{F}$ and $\mathbf{F}^c$. Further, the volume elements between the intermediate and the natural states are related through J^c. Therefore, the elastic strain energy density of the current state per unit volume of the natural state can be written as

$$W(\mathbf{F}, \mathbf{F}^c, s, \overline{\rho}_\alpha) = J^c w(\mathbf{E}^E, s, \overline{\rho}_\alpha / J^c) = J^c w(\mathbf{E}^E, s, \overline{\rho}_\alpha^c) \tag{3.32}$$

For future reference, we expand the elastic strain energy density into power series of the defect concentrations. To the leading order, one may write

$$w(\mathbf{E}^E, s, \overline{\rho}_\alpha^c) = w_0(\mathbf{E}^E) + V_m \sum_\beta \Delta\overline{\rho}_\beta^c w_\beta(\mathbf{E}^E) \tag{3.33}$$

where

$$w_0(\mathbf{E}^E) = w(\mathbf{E}^E, s, \overline{\rho}_\alpha^0), w_\beta(\mathbf{E}^E) = \left.\frac{\partial w(\mathbf{E}^E, s, \overline{\rho}_\alpha^c)}{V_m \overline{\rho}_\beta^c}\right|_{\overline{\rho}_\alpha^c = \overline{\rho}_\alpha^0} \tag{3.34}$$

in which $\overline{\rho}_\alpha^0 = \rho_\alpha^0 / V_m$ is the molar concentration of species α at the natural state (stoichiometry). Substituting Eq. (3.33) back to Eq. (3.32) yields the expansion of the elastic strain energy density in the natural state

$$W(\mathbf{F}, \mathbf{F}^c, s, \overline{\rho}_\alpha) = J^c w_0(\mathbf{E}^E) + V_m \sum_\beta \Delta\overline{\rho}_\beta w_\beta(\mathbf{E}^E) \tag{3.35}$$

where Eq. (3.29) has been used to convert the molar concentration in the intermediate state to the natural state.

For linear elastic materials, the elastic strain energy density is given by

$$w(\mathbf{E}^E, s, \overline{\rho}_\alpha^c) = \frac{1}{2} C_{\hat{I}\hat{J}\hat{K}\hat{L}} E^E_{\hat{I}\hat{J}} E^E_{\hat{K}\hat{L}} \tag{3.36}$$

where $C_{\hat{I}\hat{J}\hat{K}\hat{L}}$ is the linear elastic stiffness tensor of the solid at the intermediate state. Therefore, $C_{\hat{I}\hat{J}\hat{K}\hat{L}}$ is a function of the defect concentration. It then follows from Eq.(3.34) that

$$w_0(\mathbf{E}^E) = \frac{1}{2} C^0_{\hat{I}\hat{J}\hat{K}\hat{L}} E^E_{\hat{I}\hat{J}} E^E_{\hat{K}\hat{L}}\,,\; w_\beta(\mathbf{E}^E) = \frac{1}{2} c^\beta_{\hat{I}\hat{J}\hat{K}\hat{L}} E^E_{\hat{I}\hat{J}} E^E_{\hat{K}\hat{L}} \tag{3.37}$$

where

$$C^0_{\hat{I}\hat{J}\hat{K}\hat{L}} = C_{IJKL}\Big|_{\overline{\rho}_\alpha^c = \overline{\rho}_\alpha^0}\,,\; c^\beta_{\hat{I}\hat{J}\hat{K}\hat{L}} = \frac{\partial C_{\hat{I}\hat{J}\hat{K}\hat{L}}}{V_m \partial \overline{\rho}_\beta^c}\bigg|_{\overline{\rho}_\alpha^c = \overline{\rho}_\alpha^0} = J^c \frac{\partial C_{\hat{I}\hat{J}\hat{K}\hat{L}}}{\partial \rho_\beta}\bigg|_{\rho_\alpha = \rho_\alpha^0} \tag{3.38}$$

Clearly $C^0_{\hat{I}\hat{J}\hat{K}\hat{L}}$ is the elastic stiffness tensor of the solid at stoichiometry (represented in the intermediate state). The dependence of the elastic modulus on the defect concentration has been demonstrated experimentally [93] for several ionic solids of practical interest. The tensor $c^\beta_{\hat{I}\hat{J}\hat{K}\hat{L}}$ represents the change in the elastic stiffness with stoichiometry. This dependence will be analyzed in the next chapter using atomistic simulations.

For elastically isotropic materials, the elastic stiffness tensor $C_{\hat{I}\hat{J}\hat{K}\hat{L}}$ can be written as

$$C_{\hat{I}\hat{J}\hat{K}\hat{L}} = \frac{E}{3(1-2\nu)} \delta_{\hat{I}\hat{J}} \delta_{KL} + \frac{E}{2(1+\nu)} \left(\delta_{\hat{I}\hat{K}} \delta_{\hat{J}L} + \delta_{\hat{I}\hat{L}} \delta_{\hat{J}\hat{K}} - \frac{2}{3} \delta_{\hat{I}\hat{J}} \delta_{\hat{K}\hat{L}} \right) \tag{3.39}$$

where E is the elastic Young's modulus and ν the Poisson's ratio; both are functions of defect concentrations. In this case Eq. (3.36) can be recast into

$$w(\mathbf{E}^E, s, \overline{\rho}_\alpha^c) = \frac{E}{2(1+\nu)} E^E_{\hat{K}\hat{J}} E^E_{\hat{K}\hat{J}} + \frac{E\nu}{2(1+\nu)(1-2\nu)} E^E_{\hat{K}\hat{K}} E^E_{\hat{L}\hat{L}} \tag{3.40}$$

When the deformation is small, i.e., $\left|u_{\hat{I},J}\right| \ll 1$ and $\left|u_{i,\hat{J}}\right| \ll 1$, one may neglect the distinction between the Lagrangian and Eulerian frames and use lower case subscripts for all quantities. It thus follows from Eq. (3.21) that the total deformation gradient is given by $F_{ij} = \delta_{ij} + u_{i,j}$, where u_i is the displacement field. The total strain is then given by

$$\varepsilon_{ij} = \frac{1}{2}(F_{ki}F_{kj} - \delta_{ij}) = \frac{1}{2}\left(\frac{\partial u_i}{\partial x_i} + \frac{\partial u_j}{\partial x_i}\right) \tag{3.41}$$

Similarly, the eigentransformation due to compositional change is simplified to

$$F^c_{ij} = (1+\varepsilon^c)\delta_{ij} \tag{3.42}$$

where

$$\varepsilon^c = \sum_\alpha \varepsilon^\alpha = \sum_\alpha \eta_\alpha \Delta\rho_\alpha \tag{3.43}$$

is the compositional strain induced by the deviation of all defect concentrations from their stoichiometric values. The Jacobian is simplified to

$$J^c = \mathrm{Det}\left[\mathbf{F}^c\right] = (1+\varepsilon^c)^3 = 1+3\varepsilon^c \tag{3.44}$$

It then follows from Eq. (3.23) that

$$F^E_{ij} = F_{ik}\left(F^c_{kj}\right)^{-1} = \frac{(\delta_{ij}+u_{i,j})}{1+\varepsilon^c} \approx \delta_{ij} + u_{i,j} - \varepsilon^c\delta_{ij} \ . \tag{3.45}$$

Consequently, it follows from the first of (3.25) that the elastic strain that maps the intermediate state to the current state is given by,

$$E^E_{ij} = \varepsilon^E_{ij} = \frac{1}{2}\left[F^E_{kj}F^E_{kj} - I\right] = \varepsilon_{ij} - \varepsilon^c\delta_{ij} \tag{3.46}$$

This is the small deformation elastic strain. Thus,

$$w_0(\mathbf{E}^E) \approx \frac{1}{2}C^0_{ijkl}\varepsilon^E_{ij}\varepsilon^E_{kl} \ \ w_\beta(\mathbf{E}^E) \approx \frac{1}{2}c^\beta_{ijkl}\varepsilon^E_{ij}\varepsilon^E_{kl} \tag{3.47}$$

In the case of small deformation, the Piola-Kirchhoff stress is the same as the Cauchy stress, i.e., $\tilde{\sigma}_{ij} = \sigma_{ij}^0 = \sigma_{ij}$. So, following Eq. (3.46), we can write the small strain Hooke's law as

$$\tilde{\sigma}_{IJ} = \sigma_{ij}^0 = \sigma_{ij} = C_{ijkl}\varepsilon_{kl}^E = C_{ijkl}\left(\varepsilon_{ij} - \varepsilon^c \delta_{ij}\right) \tag{3.48}$$

For isotropic elasticity this reduces to,

$$\begin{aligned} \sigma_{ij} &= \frac{E}{(1+\nu)}\varepsilon_{ij}^E + \frac{E\nu}{(1+\nu)(1-2\nu)}\varepsilon_{kk}^E\delta_{ij} \\ &= \frac{E}{(1+\nu)(1-2\nu)}\left[\nu\varepsilon_{kk}\delta_{ij} + (1-2\nu)\varepsilon_{ij} - (1+\nu)\sum_\alpha \eta_\alpha \Delta\rho_\alpha \delta_{ij}\right] \end{aligned} \tag{3.49}$$

Consequently,

$$\sigma_{kk} = \frac{E}{(1-2\nu)}\left[\varepsilon_{kk} - 3\sum_\alpha \eta_\alpha \Delta\rho_\alpha\right] \tag{3.50}$$

Before closing this section, we want to mention that it is customary in electrochemistry to define deviation from stoichiometry using molar fraction. For example, the stoichiometric composition of GDC is $Ce_{0.8}Gd_{0.2}O_{1.9}$. The stoichiometric oxygen vacancy concentration in terms of molar fraction is 0.1 or 10%. A deviation of δ from stoichiometric oxygen vacancy concentration is commonly denoted by $Ce_{0.8}Gd_{0.2}O_{1.9-\delta}$. Therefore, the deviation of oxygen vacancy from stoichiometry is

$$\Delta\rho_v = \delta \tag{3.51}$$

Generally speaking, the CCE needs to be measured for a given ionic solid. For example, it is found that [94] the volumetric strain in $Ce_{0.8}Gd_{0.2}O_{1.9}$ is 0.0145 when the oxygen vacancy deviation from stoichiometry is $\delta = 0.12$. Therefore, it follows from Eq. (3.43) - Eq. (3.51) that the CCE due to oxygen vacancy in GDC is $\eta = 0.1208$. Atomistic

calculations [95-97] can also be used to calculate the CCE for a given ionic solid. Results from the atomistic simulations for GDC will be reported in the next chapter.

3.4 Eshelby stress dependent chemical potential

3.4.1 The formulation

As in [78, 81, 82], we consider the internal energy density $\Pi(F_{iJ}, s, \rho_\alpha)$ to be a function of the local entropy density *s*, the total deformation gradient F_{iJ}, and the molar fraction ρ_α of all the structural elements typically present in GDC (oxygen ions, double positively charged oxygen vacancies, double negatively charged oxygen interstitials, holes and electrons and the interstitial vacancies). GDC primarily allows defects in its anionic sub-lattice; therefore we consider deviation in compositions only in the anionic lattice. In fact it is the structural integrity of the cationic lattice that allows us to define continuum quantities like stress, strain displacement field etc. Note that, other free energies may also be used as mentioned in Chapter 2, section 2.2.1 The change internal energy per unit volume in the natural state can be written as [27, 60],

$$d\prod = \sigma^0_{Ji} dF_{iJ} + Tds + \tilde{\mu}_{O_o^x} d\overline{\rho}_{O_o^x} + \tilde{\mu}_{V_o^{\cdot\cdot}} d\overline{\rho}_v + \tilde{\mu}_{V_i^x} d\overline{\rho}_{V_i^x} + \tilde{\mu}_{O_i^{\cdot\cdot}} d\overline{\rho}_O + \tilde{\mu}_e d\overline{\rho}_e + \tilde{\mu}_h d\overline{\rho}_h \quad (3.52)$$

where

$$\sigma^0_{Ji} = \left(\frac{\partial \Pi}{\partial F_{iJ}}\right)_{s,\overline{\rho}_\alpha} \quad T = \left(\frac{\partial \Pi}{\partial s}\right)_{F_{iJ},\overline{\rho}_\alpha} \quad (3.53)$$

are the first Piola-Kirchhoff stress tensor and the absolute temperature, respectively, while $\tilde{\mu}_\alpha$ is the electrochemical potential for the species α. They are the thermodynamic driving forces that cause the changes in deformation, entropy and defect concentrations. Recall that the electrochemical potentials for the electronic species ($\tilde{\mu}_e$ and $\tilde{\mu}_h$) are true

electrochemical potentials while those of the ionic species are not (See discussion in section 2.2.2). Making use of the definition of diffusion potentials one may re-write Eq. (3.52) as

$$d\prod = \sigma_{Ji}^{0} dF_{iJ} + Tds + \sum_{\alpha} \tilde{\mu}_{\alpha} d\overline{\rho}_{\alpha} \tag{3.54}$$

where the sum is carried out for $\alpha = v, O, e, h$ only (only for the defects) and

$$\tilde{\mu}_{v} = \tilde{\mu}_{V_o^{\bullet\bullet}} - \tilde{\mu}_{O_o^{x}} \,,\ \tilde{\mu}_{O} = \tilde{\mu}_{O_i^{\bullet}} - \tilde{\mu}_{V_i^{x}} \tag{3.55}$$

are called the diffusion potentials for oxygen vacancies and oxygen interstitials, respectively. These diffusion potentials and the electrochemical potentials for electrons and holes are related to the internal energy through,

$$\tilde{\mu}_{\alpha} = \left(\frac{\partial \Pi}{\partial \overline{\rho}_{\alpha}} \right)_{F_{iJ}, s, \overline{\rho}_{\beta \neq \alpha}} \,,\ \alpha = v, O, e, h \tag{3.56}$$

As mentioned earlier, for dilute defect concentration we may loosely call the diffusion potentials of the ionic species the electrochemical potentials as well.

An expression of the internal energy is given in [68],

$$\Pi = W(\mathbf{F}, \mathbf{F}^{c}, s, \overline{\rho}_{\alpha}) + \Pi_{0}(s, \overline{\rho}_{\alpha}) \tag{3.57}$$

where $W(\mathbf{F}, \mathbf{F}^{c}, s, \overline{\rho}_{\alpha})$ is the strain energy density given in Eq. (3.32). The function $\Pi_{0}(s, \overline{\rho}_{\alpha})$ is the standard internal energy density when no stresses are present in the ionic solid so that the electrochemical potential of species α at zero stress can be written as,

$$\tilde{\mu}_{\alpha}\left(\rho_{\alpha}, 0\right) = \left(\frac{\partial \Pi_{0}}{\partial \overline{\rho}_{\alpha}} \right)_{F_{iJ}, s, \overline{\rho}_{\beta \neq \alpha}} \,, \alpha = v, O, e, h \tag{3.58}$$

To obtain the stress-dependent electrochemical potential, consider the derivative

$$\left.\frac{\partial W(\mathbf{F},\mathbf{F}^c,s,\overline{\rho}_\alpha)}{\partial \overline{\rho}_\alpha}\right|_{F_{iJ},s,\rho_{\beta\neq\alpha}} = \frac{\partial\left[J^c w_0(\mathbf{E}^E)\right]}{\partial \overline{\rho}_\alpha} + V_m w_\alpha(\mathbf{E}^E) \tag{3.59}$$

In deriving the above, the elastic strain energy expansion (Eq. (3.35)) has been used. The first term on the right hand side of Eq. (3.59) can be further reduced to

$$\frac{\partial\left[J^c w_0(\mathbf{E}^E)\right]}{\partial \overline{\rho}_\alpha} = \frac{\partial\left[J^c w_0(\mathbf{E}^E)\right]}{\partial F^c_{\hat{I}J}}\frac{\partial F^c_{\hat{I}J}}{\partial \overline{\rho}_\alpha} = \left[\Sigma_{IK}\left(F^c_{K\hat{M}}\right)^{-1}\right]\frac{\partial F^c_{\hat{M}I}}{\partial \rho_\alpha} = \frac{V_m \Sigma_{KK}}{3J^c}\frac{\partial J^c}{\partial \rho_\alpha} \quad , \tag{3.60}$$

where

$$\boxed{\Sigma_{IJ} = J^c w_0(\mathbf{E}^E)\delta_{IJ} - \sigma^0_{Im}F_{mJ}} \tag{3.61}$$

is known as the Eshelby stress tensor for dilute defect concentrations. The second equality in Eq. (3.60) is derived in Appendix A. A slightly different version of it can be found in [68]. The third equality in Eq. (3.60) is a direct consequence of Eq. (3.31). Substituting Eq. (3.60) into Eq. (3.59), then into Eq. (3.56), in conjunction with Eq. (3.58), yields the Eshelby stress-dependent electrochemical potential as

$$\tilde{\mu}_\alpha\left(\rho_\alpha,\tau_\alpha\right) = \tilde{\mu}_\alpha\left(\rho_\alpha,0\right) + \mu^{el}_\alpha \tag{3.62}$$

where $\tilde{\mu}_\alpha\left(\rho_\alpha,0\right)$ is electrochemical potential of species α at zero stress and

$$\mu^{el}_\alpha = V_m\tau_\alpha \tag{3.63}$$

$$\tau_\alpha = w_\alpha(\mathbf{E}^E) + \frac{\Sigma_{KK}}{3J^c}\frac{\partial J^c}{\partial \rho_\alpha} \tag{3.64}$$

μ^{el}_α is the effect of elasticity on the chemical potential. This electrochemical potential containing the Eshelby stress appears to be new to the electrochemical literature. For linear elastic and small strain deformation, the Piola-Kirchhoff stress can be replaced by the Cauchy stress. It thus follows from Eq. (3.21) that

$$\sigma^0_{Im}F_{mJ} = \sigma_{im}(\delta_{mj} + u_{m,j}) \tag{3.65}$$

Furthermore, Eq. (3.44) and Eq. (3.47) lead to

$$J^c w_0(\mathbf{E}^E) = \frac{1}{2} C^0_{ijkl} \varepsilon^E_{ij} \varepsilon^E_{kl}, \; w_\alpha(\mathbf{E}^E) = \frac{1}{2} c^\beta_{ijkl} \varepsilon^E_{ij} \varepsilon^E_{kl} \tag{3.66}$$

Consequently,

$$\Sigma_{KK} = J^c w_0(\mathbf{E}^E)\delta_{KK} - \sigma^0_{Km} F_{mK} = \frac{3}{2} C^0_{ijkl} \varepsilon^E_{ij} \varepsilon^E_{kl} - \sigma_{kk} - \sigma_{km} u_{m,k} \tag{3.67}$$

Making use of Eqs. (3.65) , (3.66) and (3.44) in (3.64) yields

$$\boxed{\tau_\alpha = \frac{1}{2} c^\alpha_{ijkl} \varepsilon^E_{ij} \varepsilon^E_{kl} + \left(\frac{3}{2} C^0_{ijkl} \varepsilon^E_{ij} \varepsilon^E_{kl} - \sigma_{kk} - \sigma_{km} u_{m,k} \right) \eta_\alpha} \tag{3.68}$$

Note that $C_{ijmn} S_{mnkl} = I_{ijkl}$, S_{mnkl} is the elastic compliance tensor. Therefore, we can show that

$$c^\alpha_{ijkl} \varepsilon^E_{ij} \varepsilon^E_{kl} = -s^\alpha_{ijkl} \sigma_{kl} \sigma_{ij} \tag{3.69}$$

where

$$s^\alpha_{ijkl} = \left. \frac{\partial S_{ijkl}}{\partial \rho_\alpha} \right|_{\rho_\alpha = \rho^0_\alpha} \tag{3.70}$$

is the variation of the elastic compliance with respect to the defect concentration ρ_α. Therefore, Eq. (3.68)can be rewritten in terms of the Cauchy tensor,

$$\boxed{\tau_\alpha = -\frac{1}{2} s^\alpha_{ijkl} \sigma_{ij} \sigma_{kl} + \left(\frac{3}{2} S^0_{ijkl} \sigma_{ij} \sigma_{kl} - \sigma_{kk} - \sigma_{km} u_{m,k} \right) \eta_\alpha} \tag{3.71}$$

The complete electrochemical potential thus follows from substituting Eq. (3.68) into Eq. (3.62) and realizing that the diffusion potentials at zero stress can be generically written as in section 2.2.2

$$\tilde{\mu}_\alpha(\rho_\alpha, 0) = \mu^*_\alpha + RT \ln(\lambda_\alpha \rho_\alpha) + z_\alpha F \phi, \; \alpha = v, O \tag{3.72}$$

3.4.2 Self stressed diffusion

As pointed out by Wu [68], for problems involving compositional changes, it is usually necessary to keep the higher order term $S^0_{ijkl}\sigma_{ij}\sigma_{kl}$ during linearization. In this particular case, linearization of the full nonlinear expression Eq. (3.64) was carried out by retaining terms linear to $\Delta\rho_\alpha$. In a given ionic solid under small strain deformation $u_{m,k} << 1$, if all the stresses are caused by $\Delta\rho_\alpha$ (self stresses), i.e., $\sigma_{ij} = \sigma^c_{ij} \sim \Delta\rho_\alpha$. Then, $S^0_{ijkl}\sigma_{ij}\sigma_{kl} \sim (\Delta\rho_\alpha)^2$. In this case, $S^0_{ijkl}\sigma_{ij}\sigma_{kl}$ can be neglected and the electrochemical potential reduces to that used by [54, 78, 85], namely,

$$\tau_\alpha = -\sigma_{kk}\eta_\alpha \tag{3.73}$$

However, in many problems, the total stress field is caused by a combination of compositional change and other factors, i.e., $\sigma_{ij} = \sigma^c_{ij} + \overline{\sigma}_{ij}$, where $\overline{\sigma}_{ij}$ is the stress induced by other factors such as thermal stress, applied loads, etc. In these cases, the higher order term becomes linear to $\Delta\rho_\alpha$, i.e., $S^0_{ijkl}\sigma_{ij}\sigma_{kl} \sim \tau_{ij}\Delta\rho_\alpha$; therefore, it cannot be neglected.

3.5 Governing equations

3.5.1 Diffusion of defects

As mentioned in section 3.4.1, we consider a network solid through which the defects diffuse. By a network solid we mean that the solid is non-diffusing, and it does not lose its physical identity by dissolving into the surrounding medium, for example. This enables us to define strain, displacement and stress at a continuum point [78]. The defects are considered as species that simply diffuse through a solid with a solid

framework that does not change. The defect concentrations are defined at a continuum point like stress or strain and are given in moles per mole of the compound.

A gradient in the electrochemical potential of the defects causes the defects to diffuse within the solid. According to non-equilibrium thermodynamics [58], the molar flux of the diffusing mobile defect species α is given by,

$$\mathrm{N}_{\alpha} = -\sum_{\beta} L_{\alpha\beta} \nabla \tilde{\mu}_{\beta} \tag{3.74}$$

where $L_{\alpha\beta}$ are the phenomenological Onsager coefficients. The off-diagonal terms in $L_{\alpha\beta}$ represent the interactions between the various defects. For the four mobile defect species (electrons, electron holes, oxygen interstitials and oxygen vacancies), such interactions are considered negligible in this work. However recent studies have shown that this may not be the case [98] for certain materials. In this study $L_{\alpha\beta}$ is taken as a diagonal tensor, so that current density of a charged species reduces to

$$\mathbf{J}_{\alpha} = -\frac{\rho_{\alpha} D_{\alpha}}{RT} \nabla \tilde{\mu}_{\alpha} \tag{3.75}$$

Where

$$D_{\alpha} = \frac{z_{\alpha} F R m_{\alpha} T}{V_m} \tag{3.76}$$

is the concentration independent part of the diffusion coefficient and ∇ is the spatial gradient operator, and m_{α} is the mobility of the species. Substitution of Eq. (3.62) into Eq. (3.75) leads to

$$\mathbf{J}_{\alpha} = -D_{\alpha}\left(1 + \frac{\partial \ln \lambda_{\alpha}}{\partial \ln \rho_{\alpha}}\right)\nabla \rho_{\alpha} - \frac{V_m \rho_{\alpha} D_{\alpha}}{RT} \nabla \tau_{\alpha} - \frac{z_{\alpha} \rho_{\alpha} D_{\alpha} F}{RT} \nabla \phi \tag{3.77}$$

In deriving the above equation, the following relationship has been used,

$$\nabla \mu_\alpha(\rho_\alpha, 0) = \frac{RT}{\rho_\alpha}\left(1 + \frac{\partial \ln \lambda_\alpha}{\partial \ln \rho_\alpha}\right)\nabla \rho_\alpha \tag{3.78}$$

We note here that, although $L_{\alpha\beta}$ is assumed as a diagonal tensor, the flux of one species may still depend on other species because the function τ_α depends on the total compositional strain, which is dependent on all defects. In other words, compositional strain causes flux interaction among different species. This fact will be seen later in the examples.

The continuity condition for each type of defect leads to

$$\frac{\partial \rho_\alpha}{\partial t} = -\frac{1}{z_\alpha F}\nabla \bullet \mathbf{J}_\alpha \tag{3.79}$$

Combining, Eq. (3.79) for the oxygen ions and oxygen vacancies, and similarly for the electrons and electron holes results in

$$\left(\frac{\partial \rho_O}{\partial t} + \frac{\partial \rho_v}{\partial t}\right) = \frac{1}{2F}\nabla \bullet \left(\mathbf{J}_O + \mathbf{J}_v\right) \tag{3.80}$$

$$\left(\frac{\partial \rho_e}{\partial t} + \frac{\partial \rho_h}{\partial t}\right) = \frac{1}{F}\nabla \bullet \left(\mathbf{J}_e + \mathbf{J}_h\right) \tag{3.81}$$

3.5.2 Boundary and interfacial conditions

The governing equations derived in previous sections are valid within the ionic solid of interest. Defect distributions within the solid depend also on what happens at the boundary of the solid. In this section, appropriate boundary conditions will be developed.

Consider an ionic solid Ω with surface S with outward unit normal vector n_i. Without loss of generality, the total boundary S may be divided into three types, namely, S^f - the portions in contact with a fluid, S^s - the portions in contact with another solid, and S^v - the portions in contact with vacuum. Note that, in general, each type may

contain multiple noncontiguous parts. Furthermore, the boundary conditions to be described consist of three aspects, mechanical, electrical and electrochemical.

3.5.2.1 ***Mechanical boundary conditions***

For a coherent solid-solid interface, the displacement vector and the traction vector must be continuous across the interface,

$$u_i\big|_{S^s} = u_i^s\big|_{S^s}\ ,\ \sigma_{ij}n_j\big|_{S^s} = \sigma_{ij}^s n_j\big|_{S^s} \tag{3.82}$$

where u_i^s and σ_{ij}^s are the displacement vector and stress tensor in the adjacent solid.

For a solid-fluid interface under static equilibrium, the displacement normal to the interface and the normal stress must be continuous across the interface. Further, the shear stress vanishes at the interface. Thus,

$$u_i\big|_{S^f} = u_i^s\big|_{S^f}\ ,\ \sigma_{ij}n_j\big|_{S^f} = p^s n_i\big|_{S^f} \tag{3.83}$$

where p^s is the pressure in the adjacent fluid. On the solid-vacuum interface, either displacement condition

$$u_i\big|_{S^v} = \overline{u}_i \tag{3.84}$$

or the traction condition

$$\boxed{\sigma_{ij}n_j\big|_{S^v} = p_i} \tag{3.85}$$

may be specified, where $\overline{u}_i$ is the prescribed displacement, and p_i is the prescribed traction vector.

3.5.2.2 ***Electrochemical conditions***

3.5.2.2.1 Electrode-Electrolyte interface kinetics

Before we present the electrochemical conditions used in this work, it is important to mention a few points from the theory of electrode kinetics, and the simplifications done in this work for mathematical ease. At the electrode-electrolyte interface, oxidation and reduction reactions take place, Eq.(3.86),

$$\boldsymbol{OX} + \boldsymbol{e} \underset{\textit{oxidation}}{\overset{\textit{reduction}}{\rightleftharpoons}} \boldsymbol{RD} \tag{3.86}$$

where,

OX denotes an oxidized component

RD denotes the reduced component

e denotes an electron

To specify the boundary conditions to the system of defect transport equations developed (Eqs. (3.80) - (3.81)), the kinetics of these reactions must be used. According to Liu, et. al [99], equation of the Butler-Volmer type must be used in conjunction with the governing differential equations of the problem. If this is done, then the concentrations of the various electrochemically active species cannot be specified independently of the applied external voltage at the boundaries. The reaction rate constant would be potential dependent (see [100] for details).

However, to proceed in this manner a detailed understanding of the kinetics of the reactions at the electrode-electrolyte (In the case of SOFC electrolyte, electrode-electrolyte and gas) is required. Although mechanisms are being proposed for the reactions at the gas solid interface in a solid electrolyte (see Eqs. (3.87),(3.89)) [5, 99, 101] the actual mechanisms still remains unclear. Moreover, the gas-solid reactions in

solid electrolytes are multistep processes thus complicating the kinetics even more. Since the main aim of this work is to study the interactions between stresses and defect transport and not the electrode-electrolyte interface kinetics, we assume that the boundary reactions (which are about to be discussed) are in equilibrium (or that the kinetics is infinitely fast). This is done purely for mathematical simplicity so as to allow us to solve the governing differential equations. In a real system, kinetics may play a significant role and must be considered.

3.5.2.2.2 Equilibrium gas-solid reactions

At the solid-gas (or fluid) interface, defects in the solid may react with the species in the gaseous phase. For example, if electrons e' and oxygen vacancies $V_O^{\bullet\bullet}$ are the majority defects in a solid in contact with oxygen gas, then the following redox reaction may take place at the solid-gas interface, see Appendix B,

$$O_O^X(\text{solid}) \underset{\text{reduction}}{\overset{\text{oxidation}}{\rightleftharpoons}} \left\{V_O^{\bullet\bullet} + 2e'\right\}(\text{solid}) + \frac{1}{2}O_2(\text{gas}) \tag{3.87}$$

where the direction of the reaction depends on the oxygen partial pressure $\left(PO_2\right)$ in the gas phase relative to the oxygen concentration in the solid [99]. The corresponding mass action law on the surface of the solid is thus given by

$$\boxed{K_{S1} = \rho_{V_O^{\bullet\bullet}} \rho_e^2 \sqrt{PO_2}} \tag{3.88}$$

Another reaction at the solid-gas interface is the formation of a neutrally charged vacancy through a reaction between interstitial atoms and holes,

$$\left\{O_i^{"} + 2h^{\bullet}\right\}(\text{solid}) \rightleftharpoons V_i^X(\text{solid}) + \frac{1}{2}O_2(\text{gas}) \tag{3.89}$$

The corresponding mass action law on the solid surface can be written as

$$K_{S2} = \frac{\sqrt{PO_2}}{\rho_{O_i^{\cdot\cdot}} \rho_h^{\bullet}} \tag{3.90}$$

In the above, K_{S1} and K_{S2} are the equilibrium constants for the reactions (3.88) and (3.90) respectively. Obviously, the equilibrium constants K_{S1} and K_{S2} are temperature dependent.

When reaction (3.87) is read from right-to-left it represents the entry of oxygen in the form of gas into a vacancy in the solid thus occupying its lattice position. A similar explanation can be given for reaction (3.89) as well.

3.5.2.3 ***Electrical conditions***

To describe electrical boundary conditions, the total surface S is divided into electrically conductive and insulating portions. On the insulating boundary S^i,

$$\mathbf{J}_e \bullet \mathbf{n}\big|_{S^i} = 0 \tag{3.91}$$

On the conductive boundary S^c, one has

$$\tilde{\mu}_e\big|_{S^c} = -FV \tag{3.92}$$

where V is the applied voltage (relative to a reference state). A frequently encountered situation is when two parts of the conductive boundary S_I^c and S_{II}^c are subjected to prescribed voltages V^I and V^{II}, respectively. In this case, the electrical boundary condition for the electrochemical potential can be written as

$$\tilde{\mu}_e\big|_{S_{II}^c} - \tilde{\mu}_e\big|_{S_I^c} = -F(V^{II} - V^I) \tag{3.93}$$

If the conductive boundaries S_I^c and S_{II}^c of the solid are exposed to ideal gas with oxygen partial pressure $P_{O_2}^I$ and $P_{O_2}^{II}$, respectively, then the electrical potential difference across these two parts of the boundary is given by,

$$\phi\big|_{S_{II}^c} - \phi\big|_{S_I^c} = (V^{II} - V^I) + \frac{RT}{F}\ln\left(\frac{\rho_e\big|_{S_{II}^c}}{\rho_e\big|_{S_I^c}}\right) \tag{3.94}$$

3.5.3 Resume of governing equations

In the preceding sections, eight basic field quantities were introduced. They are the four defect concentrations, ρ_e, ρ_h, ρ_v and ρ_O, the electrostatic potential ϕ, and the three displacement components u_i. The equations that govern these field quantities at steady state are highlighted with boxes and the number of the equation is given on the left hand side.

The diffusion equations

1st

$$0 = \frac{-1}{2FRT}\nabla\bullet\left(\rho_O D_O \nabla\tilde{\mu}_O + \rho_v D_v \nabla\tilde{\mu}_v\right) \tag{3.95}$$

2nd

$$0 = \frac{-1}{2FRT}\nabla\bullet\left(\rho_e D_e \nabla\tilde{\mu}_e + \rho_h D_h \nabla\tilde{\mu}_h\right) \tag{3.96}$$

The Poisson equation for the electrostatic potential,

3rd

$$-\kappa_\varepsilon \nabla^2\phi = \frac{F}{\varepsilon_0 V_m}\sum_\alpha z_\alpha \rho_\alpha \tag{3.97}$$

where $F = 9.648\times10^4\,\mathrm{C/mol}$ is the Faraday constant, $\varepsilon_0 = 8.854\times10^{-12}\,\mathrm{farad/m}$ is the electric permittivity of free space, κ_ε is the dielectric constant of the solid, V_m is the molar volume, and z_α is the effective charge of defect α. The sum should include all

point defects in the solid including both mobile and immobile defects. The set of equations (3.95)- (3.97) is often referred to as the Nernst-Poisson-Planck (NPP) system of equations, when the stress independent chemical potentials are used. We will call the system using the stress dependent chemical potentials as the Modified Nernst Poisson Planck system of equations (MNPP). The Poisson equation is of immense importance and creates numerical issues during the solution of the NPP set, especially when the size of the ionic solid is much greater than a characteristic length of the problem, the Debye length. Methods of perturbation analysis prove useful in obtaining solutions to such problems. The details of this issue are dealt with in chapter 5 where the MNPP will be solved using the perturbation method approach.

The three equilibrium equations of mechanics

4th, 5th and 6th

$$\frac{\partial \sigma_{ji}}{\partial x_j} + f_i = 0 \tag{3.98}$$

Mass action laws

The two more algebraic equations are required. They are

7th and 8th

$$\rho_O \rho_v = K_F \text{ and } \rho_e \rho_h = K_e \tag{3.99}$$

The first of (3.99) represents the mass action law for the Frenkel defect reaction (see APPENDIX B),

$$O_O^X + V_i^X \rightleftharpoons O_i'' + V_O^{\bullet\bullet} \tag{3.100}$$

while the second for the electron hole reaction,

$$e' + h^{\bullet} = nil \tag{3.101}$$

and K_F and K_e are the equilibrium constants for the reactions.

These eight equations together with the appropriate boundary conditions presented in the section 3.5.2 constitute the boundary value problem for the mechanical, electrical and electrochemical fields in an ionic solid. Solutions to this boundary value problem provide us with the distribution of charged defects and the deformation/stress induced by the deviation from stoichiometry of these charged defects, as well as the electrostatic potential.

Before concluding this section, we note that, mass action laws for the defect reactions are obtained by equating the chemical potentials that are functions of concentrations only. The equilibrium constants in this case are functions of temperature. For the coupled mechanical and electrochemical field, the chemical potentials become dependent on the stress state and so will the equilibrium constants. Similarly, the boundary conditions will also depend on the mechanical stress acting at the boundary of the solid. The stress dependent chemical boundary conditions are derived in Appendix C.

3.6 Conclusions

In this chapter the Eshelby stress dependent chemical potential is derived and a system of governing equations and associated boundary conditions has been delinated for the coupled mechanical and electrochemical field quantities. Although Eshelby's stress is only a function of the Cauchy's stress and the strain energy density as derived, we have distinguished between the "Cauchy Stress" dependent and the "Eshelby Stress" dependent chemical potentials for the physical significance the Eshelby stress has in domains with singularities (see section 3.2.2). These equations were derived for the ionic solid with four types of majority defects, namely, oxygen vacancies, interstitials, electrons and holes, which are typical in oxide ceramics. Equations for small strain linear

elastic ionic solids were also presented. Solutions to the boundary value problem presented will yield the distributions of defect concentrations, electrostatic potential and the mechanical stresses in the ionic solid.

CHAPTER 4. ATOMISITIC SIMULATIONS

4.1 Chapter abstract

The material properties introduced in chapter 3, namely the CCE and the OSEC that enable full coupling between defect transport and mechanics are determined in this chapter for the materials 10GDC and 20GDC. A combination of analytical and MD simulations is used to determine these parameters.

The determination of the CCE involves comparing the volumes of the MD cells at each non-stoichiometric level to the volume of the stoichiometric cell. It is found that the CCE was constant with temperature and the chemical strains varied linearly with non-stoichiometry validating Vegard's law. The numerical values of the CCE are found to be reasonably close to existing experimental data and in the range of 0.069-0.079 for a wide range of temperatures.

For the determination of elastic stiffness as a function of non-stoichiometry, it is recalled that the analytical expressions obtained from the interatomic potential by application of virtual homogenous strains needed modification on account of a possible inner elastic contribution due to the non-primitive nature of defective GDC crystals. The MD cell is built using a new approach to allow for calculating the inner elastic contributions. The modified expressions are then used to predict the total elastic constants at various temperatures and stoichiometric levels. For GDC it is found that;

1) The elastic constants of the defective structure show a cubic material response.
2) The elastic constants are insensitive to temperature.
3) The inner elastic contribution is negligible.

4) The components C_{11} show a greater variation with non-stoichiometry than any other component (C_{12} or C_{66}).

Once the single crystal elastic constants of GDC are determined, a polycrystalline material response is found by homogenization method for a GDC sample consisting of randomly oriented grains. The isotropic material response of such a polycrystalline material is then quantified using the familiar Young's modulus and Poisson's ratio. It is found that the latter did not vary beyond 4% over the entire range of non-stoichiometry studied. The Young's modulus showed close to a linear variation with a maximum slope of about -200GPa over all the temperatures considered.

Finally a possible reason for the higher variation with non-stoichiometry for C_{11} when compared to C_{12} or C_{66} is given by examining the contributions towards the elastic constants of the short and long range parts of the interatomic potentials. It is found that, for C_{11}, both parts decreased with non-stoichiometry with almost equal slopes, thus causing an overall decrease in the elastic constant. For C_{12} or C_{66}, the short range contribution decreased while the long range increased with non-stoichiometry, with equal slopes negating each others effects and thus negating the effect of non-stoichiometry on C_{12} or C_{66}.

This chapter hence provides the values of the necessary parameters that must be used to together with the framework of the previous chapter to completely describe the interaction between defect transport and mechanics in GDC.

4.2 Introduction

4.2.1 State of the art- Review

Since the advent of modern parallel computing, MD has been used for analyzing solids at the atomic level. Instead of providing a historical review of general applications of MD to solids, in this discussion a short review of some of the applications of MD to determine the properties of ionic solids with defects is presented.

Ionic solids with defects have been analyzed through molecular simulations for several purposes. Some of them are; to calculate defect energies [102], entropies, transport [103-107], mechanical [108] and thermal properties [109]. A review of the several methods for calculating some of these properties can be found in [110]. In addition to the properties mentioned, point defect interactions [111, 112], crystal structure [113] and oxygen diffusion mechanisms [106, 114-116] and diffusion characteristics under different dopant concentrations and types [105, 117-119] have been studied for popular SOFC materials (ex. GDC, YSZ and Lanthanum oxides). Another pertinent article that deserves mention here is ref. [120]. The goal of this article involved determining the cluster configuration of defects in GDC with the least binding energies.

4.2.2 Contribution of current research

In this thesis MD is used as a tool to determine the CCE and the elastic constants for non-stoichiometric GDC. These material properties couple defect transport and mechanics at a fundamental thermodynamic level through the chemical potential as introduced in the previous chapter. The main aspects of the atomistic simulations performed in this work are in order.

4.2.2.1 *CCE*

Although several existing works determine the properties of defective ionic solids as presented in section 4.2.1, there have been none that use MD to determine the CCE. Here, the expansion of the defective MD cells of reduced GDC at specific temperatures is first determined and compared with that of the stoichiometric MD cells at the same temperatures. In this manner any thermal expansion effect is negated. Then, the volumetric strains are calculated at different levels of defect concentrations. This allows us to validate the extent of non-stoichiometry to which Vegards' law might be valid (as it is one of the primary assumptions in the previous chapter), then the CCE is determined accordingly. Although formation volumes of defects can be calculated from some of the methods presented in recent works [121], these are not the same as determining the CCE. Thus, the first aim of this chapter is to present the methodology to determine CCE and apply it to GDC.

4.2.2.2 *Elastic Constants*

Firstly we note that we examine the elastic stiffness tensor C_{ijkl} at various levels of stoichiometry and not the quantity c^{α}_{ijkl} which is the derivative of C_{ijkl} with respect to the concentrations. By doing so we first ensure that it is realistic to assume the elastic constants have a linear variation with stoichiometry. This could be looked upon as validating Vegard's law for the elastic constants (Linear variation of elastic stiffness with non-stoichiometry). The determination of elastic constants for defective lattice structures is not as straightforward as the CCE. Direct MD experiments to obtain stress-strain variation cannot yield the complete stiffness tensor. In this work the method of homogenous strains is used to obtain an analytical expression for the elastic constants

directly from the interatomic potential [122]. For crystals made of one kind of sub-lattice, analytical derivatives of the interatomic potential energy with respect to a virtual homogenous strains yield the elastic stiffnesses (if the effect of temperature is neglected) [65]. The effect of temperature on the elastic constants for materials that exist in the solid state for a wide range of temperature can be assumed to be negligible [123]. If the effect of temperature must be considered, a statistical mechanics approach must be taken and it must account for the thermal vibrations explicitly in the expressions for the elastic constants, as can be seen in references [124, 125]. For solids made of several sub-lattices constituting a heterogeneous system [126], "Inner Elasticity" [127, 128] must be considered. Inner elasticity refers to a contribution to the elastic response of solids from relative displacement arising between the various sub-lattices when the crystal is subjected to a homogenous strain [122]. Such relative displacements occur when the atoms of a particular sub-lattice are not present at a site possessing the inversion symmetry [129] and therefore have to undergo a preferential inner displacement to attain equilibrium for an applied homogenous strain. The effect of inner elasticity comes from the contribution of inner elastic constants to the total elastic constants [128, 130, 131]. In materials like ceria (fluorite structure) which has three kinds of sub-lattices (1 Ceria and 2 Oxygen) [132, 133], and also in doped stoichiometric and non-stoichiometric ceria compounds, it appears that the effects of inner elasticity cannot be neglected.

In other structures with the fluorite structure, such as calcium fluorite (CaF_2), there is experimental evidence of inner displacement [134]. However, because two fluorine sub-lattices move in equal and opposite direction along the body diagonal of the fluorite unit cell, the effective contribution to inner elastic constants is negligible [135].

While the contributions of inner elastic constants to the total elastic constants may turn out to be small for fluorite based structures like GDC or non-stoichiometric GDC, such an assumption is not obvious. This is because the location of oxygen vacancies and the dopant atoms in the crystal may be such that the contribution of inner elastic constants to some, or all of the elastic constants is significant. In this work the total elastic constant of 10 and 20GDC for various vacancy concentrations and temperatures is computed. Following this, the magnitudes of the contributions from inner elastic constants to the total elastic constants are discussed.

Three references [136-138], in which an expression for the non-stoichiometry dependent Young's modulus for GDC was developed from an interatomic potential deserves a mention here. Although the analytical expressions derived there provide a trend in the variation of modulus with stoichiometry, the potential used is not appropriate for ionic solids, especially since it does not account for the coulombic interactions. Further, the model provides values for the Young's modulus but does not consider the general elastic stiffness tensor and also uses experimental results to obtain the elastic modulus at the stoichiometric state. In this work the Buckingham potential with interatomic potential parameters from existing literature is used to calculate the entire stiffness matrix for 10 and 20GDC while considering inner elastic contributions as well. Also reported are the average values of Young's modulus and Poisson's ratio for the materials. Further, the contributions to the elastic stiffness tensor from the interatomic potential and the long range coulombic parts are examined to investigate their variability with vacancy concentrations.

4.2.2.3 *A semi MD approach*

Although MD simulations were used in this work, the fluctuations in the calculations of the various properties were not considered explicitly. The cell vectors (required for the calculation of volumes of the MD cell for the determination of CCE) or the position of the atoms (needed for the calculation of the elastic constants) is obtained by averaging the relevant quantities (volumes and positions) over the production run of the MD simulation. In essence the effects of temperature are considered only to the extent that they affect the final position of the atoms. This makes our approach "*Semi MD*". It was found that the elastic constants of pure ceria were predicted accurately even without the fluctuations being considered. This semi-analytical method has proven to be accurate for computing elastic properties of FCC metals [139].

In the next section, we first present the interatomic potentials used in this study. Then we explain the crystal structure of pure ceria (CeO_2) and we present the methodology to build a non-stoichiometric GDC structure that will allow us to calculate the contribution of inner elasticity to the total elastic constants. Finally, the results for the CCE and elastic constants for non-stoichiometric 10 and 20GDC are given for various temperature and defect concentrations.

4.3 MD simulations

4.3.1 Interatomic potentials & simulation parameters

In this work, we use DL-POLY to perform the MD simulations [140]. Buckingham potential is used according to which the energy due to short range interaction is given by

$$U^{(n)} = A\exp\left(-\frac{r^{mn}}{\rho}\right) - \frac{C}{(r^{mn})^6} \tag{4.1}$$

where r^{mn} is the scalar distance between atom *m* and atom *n*. The parameters A, ρ and C are listed in Table 4.1, where two sets of potential parameters for the pairs Ce^{4+}-O^{2-}, O^{2-}-O^{2-} and Ce^{4+}-O^{2-} are shown.

The first set of parameters of pure ceria is taken from [141]; these are known to predict the lattice parameters, lattice energies, static relative permittivity and high frequency dielectric constant of pure ceria with good accuracy. However, they over predict the elastic constants C_{11} by about 27%, C_{12} by 16% and C_{44} by 50% of pure ceria at its stoichiometric state, when compared to existing experimental data in the literature. Therefore the first set of parameters was used to calculate only the CCE. The second set of potential parameters was taken from [142] to compute the elastic constants as they predict the elastic properties of pure ceria with a good accuracy. The pair potential between Gd^{3+}-O^{2-} were also taken from [48] where they were used to study defect clusters in doped ceria.

As mentioned before, neither potential has been used to predict the CCE. In this work both the potentials were considered and used to calculate the CCE. It was however found that the CCE values matched experimental values with good accuracy only for the first set. Hence only these results are reported in this work.

The cut off radius for the short range forces was set to 16.0Å in all simulations. Further, in addition to the short range interactions, even coulombic interactions exist for the material under consideration (see section 1.3). These electrostatic interactions are computed using Ewald's sum in DL-POLY. The simulated structures also have complete

charges assigned to the specific ions i.e.,+4 or +3 for Ce (depending on whether it is Ce^{4+} or Ce^{3+}), +3 for Gd and -2 for O.

Table 4.1: Interatomic potential parameters for GDC

Ionic Pairs	*A*(eV)		*ρ*(Å)		*C*(eV Å^6)	
	[141], [48]	[142], [48]	[141] ,[48]	[142], [48]	[141] ,[48]	[142], [48]
O^{2-} - O^{2-}	9547.96	9533.421	0.2192	0.234	32.0	224.88
Ce^{4+} - O^{2-}	1809.68	755.1311	0.3547	0.429	20.40	0.0
Ce^{3+} - O^{2-}	2010.18	1140.193	0.3449	0.386	23.11	0.0
Gd^{3+}-O^{2-}	1885.75	1885.75	0.3399	0.3399	20.34	20.34

All simulations were performed in an **NST** (constant stress) ensemble so as to allow for any variation in MD cell shape which may take place due to non-stoichiometry. Further, the total period of equilibration was 3ps, and the production run was carried out for 5ps with a time step of 0.1fs.

4.4 Material system

4.4.1 Pure ceria

Ceria (CeO_2) has a typical fluorite structure (see Figure 4.1) .The fluorite structure can be viewed as three interpenetrating FCC sub-lattices, with the two oxygen sub-lattices shifted by $\pm\frac{1}{4}[111]$ along one body diagonal direction of the cerium sub-lattice[133]. CeO_2 belongs to space group $Fm\bar{3}m$ and has a lattice constant 5.411Å at room temperature. It consists of Ce^{4+} ions forming a face centered cubic configuration which encloses a simple cubic configuration of the oxygen ions. Crystallographically, Ce is located in the Wyckoff position (4a), while the two oxygen ions are in positions (8c). The importance of the Wyckoff position arises in discussing the contribution of the inner elastic constants and is explained in APPENDIX D.

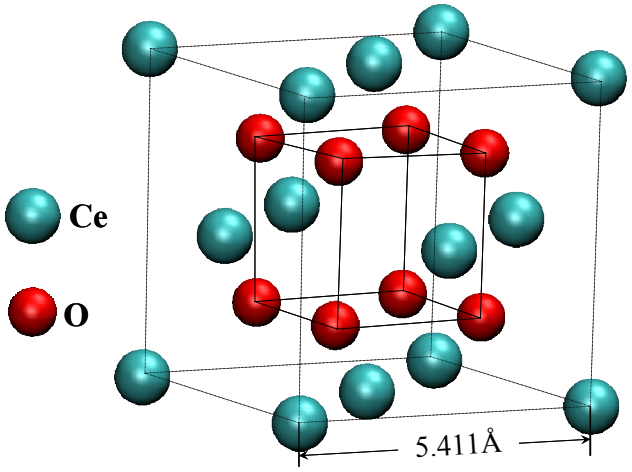

Figure 4.1: Structure of pure ceria

4.4.2 Building non-stoichiometric GDC

Generating the defective lattice from pure ceria is complicated as there are several ways in which it can be done. For determination of CCE or elastic constants of non-stoichiometric 10GDC or 20GDC, oxygen atoms must be removed and Ce^{3+} ions must be introduced to reflect the appropriate level of non-stoichiometry and chemical reduction. This may be done at random for the determination of CCE. However, to determine elastic constants taking into account the inner elastic contributions according to the development in [130], a periodic MD simulation cell is needed. It is also necessary to identify specific sub-lattices in the crystal structure. This may be achieved by using a single unit cell of ceria and by applying periodic boundary conditions. However, the range of vacancy concentration that can be investigated using a single unit cell is severely restricted. For example, a single unit cell of ceria has 4 cerium atoms and 8 oxygen atoms. Even if one oxygen vacancy is created, it amounts to creating vacancy concentration of 0.25 mole fraction. This means that cases of stoichiometric or lower vacancy concentrations cannot

be examined. Thus, a large simulation cell with a sufficient number of atoms has to be created, allowing one to generate a wide range of vacancy concentrations. To this large simulation cell, periodic boundary conditions may be applied to simulate the bulk material. Vacancies may be generated in this large simulation cell randomly by removing appropriate number of oxygen atoms and replacing the necessary number of Ce^{4+} atoms with Gd^{3+} or Ce^{3+}, simulating stoichiometric or reduced material respectively. To illustrate let us suppose that we have *x* number of Ce^{4+} spots and *2x* numbers of O^{2-} spots (this corresponds to pure ceria) in the MD cell. We want to generate a structure corresponding to the formula $Ce_{0.9}Gd_{0.1}O_{2-0.05-y}$. Firstly, we recognize that, this compound is non-stoichiometric 10GDC with y mole fraction of vacancy concentration in excess of the stoichiometric compound ($Ce_{0.9}Gd_{0.1}O_{2-0.05}$). Hence, the total number of oxygen atoms to be removed to create the N_v number of vacancies is,

$$N_v = (0.05 + y)x \tag{4.2}$$

The total number of Ce^{4+} positions to be replaced by Gd^{3+} is given by,

$$N_{Gd^{3+}} = 0.1x \tag{4.3}$$

Further, owing to the reduction we replace $N_{Ce^{3+}}$ of the Ce^{4+} spots with Ce^{3+} atoms such that the system is electrically neutral, in this case it is

$$N_{Ce^{3+}} = 2yx \tag{4.4}$$

The replacement of atoms can be done at random within the MD simulation cell. But by doing so, information regarding the kind or the number of sub-lattices present in the system is lost (disorder [143]). Every atom in the system may be labeled as a sub-lattice, as periodicity is imposed on the entire simulation cell (see Figure 4.2) for

simulating the bulk. But as will be shown, the inner elastic tensors arising in the determination of inner elastic constants become so large that it is computationally very

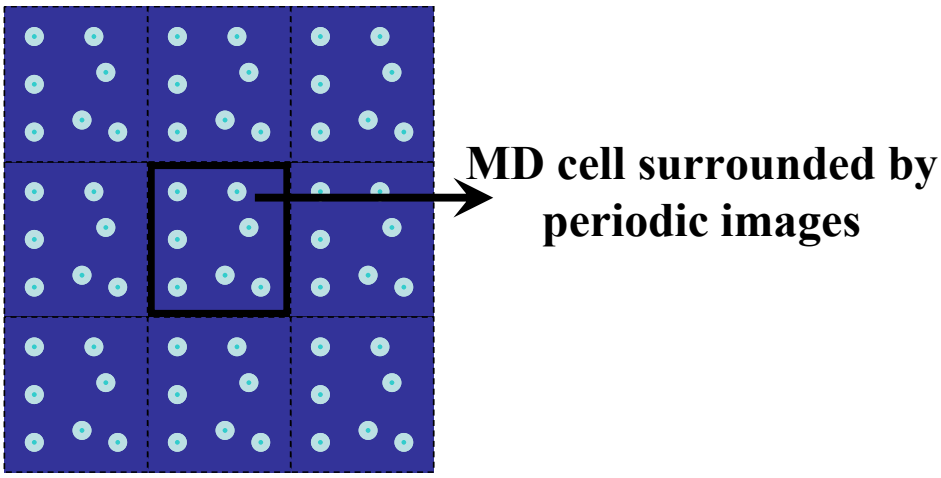

Figure 4.2: MD Cell and its periodic images

inefficient to label all atoms in the system as a sub-lattice. The explanation for this is given in APPENDIX D. Thus, the randomly generated structure (MD cell) can no longer be identified as one that is obtained from a periodic repetition of some unit cell.

To address this disorder problem, a structural theory of anion deficient fluorite structure has been proposed [144]. These methodologies, impose specific restrictions on the modular unit cells that may be used to build the defective unit cell [145]. For example, one of the restrictions is that not more than two anion vacancies may exist in a fluorite module. Such restrictions entail a large number of modules to simulate a bulk defective crystal structure, and they hence cause the size of the MD cell to be very large, increasing the computational time. These techniques are therefore not used in this work. Moreover, the analyses given in these references address undoped oxides only and are not easy to build computationally. Clearly, there is no unique way to generate the defective

structure so that the repeating unit containing certain number of vacancies and other atoms is always identified with a unique space group.

In this work, the methodology to generate the MD simulation cell involves five unit cells of pure ceria with a total of 60 atoms (x=20). Oxygen atoms are removed; Ce^{3+} and Gd^{3+} replace the Ce^{4+} sites, depending on the level of non-stoichiometry that needs to be studied. This we call the *unit cell of the defective structure,* and this will be addressed from now on as the **D-unit cell (Defective unit cell)**. All the atoms forming this unit cell are identified as a sub-lattice (a maximum of 60 sub-lattices can exist, and this corresponds to pure ceria). The created structure is repeated in the X, Y and Z directions and periodicity is imposed to simulate bulk. To this end, we use two unit cells in the [100], ten [010] and [001] directions. The unit cell of the defective structure so formed allows us to create a wide range of non-stoichiometry exactly. The replacement of atoms as required is done at random within the unit cell in the same manner as exemplified by Eqs.(4.2),(4.3) and (4.4). Before proceeding any further we would like to point out four aspects of this method of constructing the defective MD cell:

1) The placement of the 5 unit cells of ceria from which the defective unit cell is created is completely arbitrary.

2) To indicate the number of possible generations for a particular defective crystal, we can look at stoichiometric 10GDC. Here, the removal oxygen to create vacancies may be done in 40 different ways, and replacement of Ce^{4+} with Gd^{3+}, for each of the 40 ways of placing the vacancies, may be done in 190 ways. There are hence, 7600 ways to just generate the stoichiometric 10GDC for one arrangement of the 5 unit cells. For the non-stoichiometric case, there are $\frac{40!}{n!(40-n)!}$ ways to create vacancies (n is the number of

vacancies), for each vacancy distribution, there are 190 and 4845 ways to create the doping for 10 and 20GDC respectively, and for a particular distribution of vacancy, there are $\frac{(20-d)!}{(2n-d)!(20-2n)!}$ ways of replacing Ce^{4+} with Ce^{3+} atoms to generate the reduced state where d=2 for 10GDC and d=4 for 20GDC.

3) The specification that every single atom in the D-unit cell forms a sub-lattice engenders the possibility of the existence of two or more sub-lattices that may not be different. To be very accurate one has to examine the unit cell structure to classify it under a specific point group. Even if this is done, the relaxed state of the crystal structure

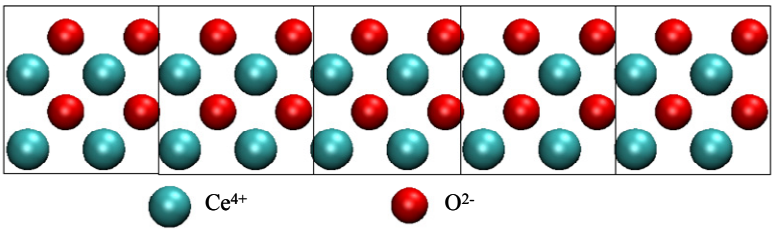

Figure 4.3: Five unit cells of pure ceria

can consist of D-unit cells belonging to a different point group. Therefore, by treating all the atoms in the D-unit cell as individual sub-lattices we allow the crystal structure to evolve during the simulation, as required by energy minimization. The inner elastic constants take their values naturally as required by the relaxed structure, and no prior knowledge regarding possible crystal symmetry is needed.

4) We now note that if the preferred locations of the vacancies with respect to the dopant atoms are known, it is possible to reduce the number of possible generations. However, in this work we assume that any position of vacancy relative to the position of the dopant atom is equally likely.

Clearly, it would be impossible to perform all possible simulations as articulated in point (2). In this work, we examine one particular generation for each defective state, and we also consider that the five unit cells of ceria are placed next to each other as shown in the Figure 4.3. From this, the defective unit cells are created using the procedure just described. The unit cell is then repeated in the X, Y and Z directions as explained previously.

The simulation cell used in this work has x=4000 and corresponds to a total of 12000 atomic spots. The simulations were all carried out for four temperatures 100, 900, 1173 and 1273K for both 10 and 20GDC. The non-stoichiometries examined were δ=0, 0.05, 0.1, 0.15, 0.2 and 0.25 for both $Ce_{0.9}Gd_{0.1}O_{1.95-\delta}$ (10GDC) and $Ce_{0.8}Gd_{0.2}O_{1.9-\delta}$ (20GDC).

4.4.3 Expression for total and inner elastic constants

In this section the formula used to determine the elastic constants is presented and we also discuss the issue of inner elasticity. The detailed derivation of the total elastic constants, comprising of the inner elastic contribution is given in APPENDIX D. Although the derivation there closely follows ref. [146], we feel that the presentation here is slightly more clear with regards to the notation.

As explained in section 4.2.2.2, in those crystals that are primitive (Bravais lattice based crystals) it is not necessary to consider inner elasticity, as there will be no preferential displacement of the sub-lattices with respect to each other on the application of a homogenous strain. In cases where the crystal is non-primitive, inner elasticity has to be accounted for, as the sub-lattices move on application of a homogenous strain. This is shown for two kinds of sub-lattices in Figure 4.4.

On subjecting a primitive crystal (all atoms have inversion as a symmetry element), with N sub-lattices to a homogenous Lagrange strain (**E**), any vector $\mathbf{r^o}$, joining two atoms in the undeformed state, transforms to the deformed state of **r** through the relation,

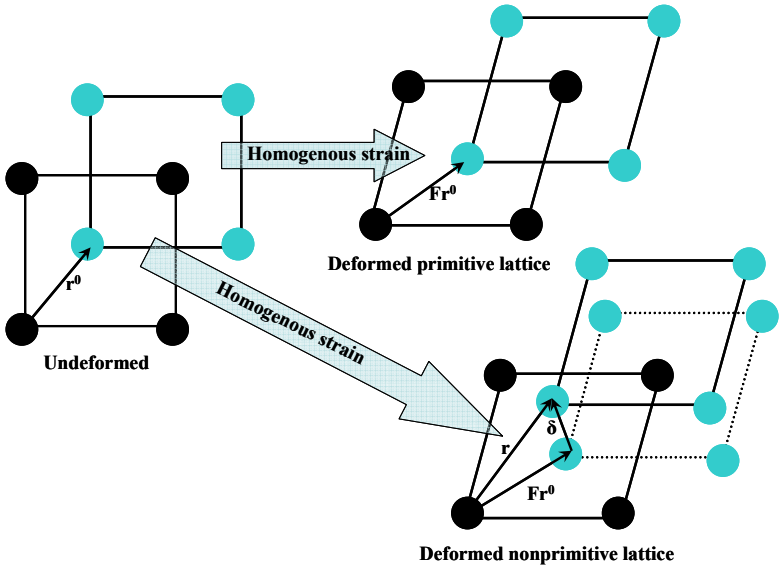

Figure 4.4: Inner displacement of non-primitive crystals

$$r=\mathbf{F}r^{o} \tag{4.5}$$

where,

F is the deformation gradient

$\mathbf{r^o}$ is the position vector between two atoms before deformation

r is the position vector after deformation

The homogenous Lagrange strain is given by,

$$\mathbf{E}=\frac{\mathbf{1}}{\mathbf{2}}\left[\mathbf{F}^{\mathrm{T}}\mathbf{F}-\mathbf{I}\right] \tag{4.6}$$

where, **I** is the identity tensor

If the system is governed by a central kind of interatomic potential (interaction between atoms depends only on the magnitude of distances between the atoms), then the total energy density (u) is given as,

$$u = \frac{1}{2\Omega} \sum_{p=1}^{N} \sum_{\substack{q=1 \\ q \neq p}}^{N} e(r^{pq}) \tag{4.7}$$

Where,

$e(r^{pq})$ is the potential energy due to interaction between atom p and q due to both the short and the Coulombic forces.

r^{pq} is the magnitude of the distance between atom p and q

Ω is the MD cell volume

The elastic constants C_{ijmn} for the primitive lattice system are given using the formulae,

$$C_{ijmn} = \left. \frac{\partial^2 u}{\partial E_{ij} \partial E_{mn}} \right|_{E_{ij}=0} = \frac{1}{4\Omega} \sum_{p=1}^{N} \sum_{\substack{q=1 \\ q \neq p}}^{N} \frac{\partial}{\partial s^{pq}} \left(\frac{1}{r^{pq}} \frac{\partial e(r^{pq})}{\partial r^{pq}} \frac{\partial s^{pq}}{\partial E_{ij}} \right) \left. \frac{\partial s^{pq}}{\partial E_{mn}} \right|_{E_{ij}=0} \tag{4.8}$$

$$C_{ijmn} = \frac{1}{2\Omega} \sum_{p=1}^{N} \sum_{\substack{q=1 \\ p \neq q}}^{N} \left[\frac{1}{\left(r^{pq}\right)^2} \left\{ \frac{\partial^2 e(r^{pq})}{\partial \left(r^{pq}\right)^2} - \frac{1}{r^{pq}} \frac{\partial e(r^{pq})}{\partial r^{pq}} \right\} \right|_{r=r^o} r_i^{o[pq]} r_j^{o[pq]} r_m^{o[pq]} r_n^{o[pq]} \Bigg] \tag{4.9}$$

where

$r_i^{o[pq]}$ refers to the i^{th} component of the position vector from atom p to q at zero strain and

$$s^{ab} = \left[2E_{mn} + I_{mn} \right] r_m^{o[ab]} r_n^{o[ab]} \tag{4.10}$$

is the square of the magnitude of the distance between atom a and b. Eq.(4.9) is the common expression used to determine elastic constants directly from the interatomic potential when inner elasticity can be neglected.

For a non-primitive crystal, preferential displacement of sub-lattices is allowed, Eq. (4.5) is no longer correct, and the following relation must hold (See Figure 4.4),

$$\mathrm{r}^{[ab]} = \mathrm{Fr}^{o[ab]} + \delta^{s_a} - \delta^{s_b} \tag{4.11}$$

Where, δ^{s_a} is read as the relative displacement of sub-lattice to which atom 'a' belongs. The relative displacements are always taken with respect to the reference atom in the N^{th} sub-lattice. We also note that $\delta^{s_a}=0$ if the sub-lattice to which '*a*' belongs is the same as the one to which N belongs. This is true because the atoms belonging to a particular sub-lattice suffer a rigid body preferential displacement with respect to the reference atom.

Using the corrected deformation gradient as in Eq. (4.11), the total elastic constant is given by,

$$C^{\mathrm{T}}_{ijmn} = C_{ijmn} - D^{k}_{ij\alpha} g^{kr}_{\alpha\beta} D^{r}_{\beta mn} \tag{4.12}$$

where, the tensors **D** and **g** are as derived in the appendix from the interatomic potential.

In order to verify the codes written to perform the computations, the internal strain (see APPENDIX D) **P**, of pure fluorite structure (CaF_2) was also computed. It is shown that internal strains suffered by the two oxygen sub-lattices are equal and opposite as required by the fluorite structure [134]. The values of the internal strains of the oxygen sub-lattices are also compared, to data from literature, validating our codes both qualitatively and quantitatively. The details of this calculation are explained in APPENDIX D.

4.5 CCE Results

4.5.1 CCE from MD Simulation

An MD simulation cell was relaxed in a N**S**T (Constant **S**tress) ensemble to allow for any variation in cell shape. After relaxation, the MD cell vectors were examined, and it was concluded that the strain induced as a result of non-stoichiometry was purely volumetric. This is in accordance with experimental evidence[147]. The chemical expansion coefficient was then obtained by comparing the volumes of the relaxed MD simulation cells of non-stoichiometric GDC, to the volume of the cell at stoichiometry. Both volume calculations were done at the same temperature. By comparing the volumes at a constant temperature the effect of thermal expansion was automatically excluded

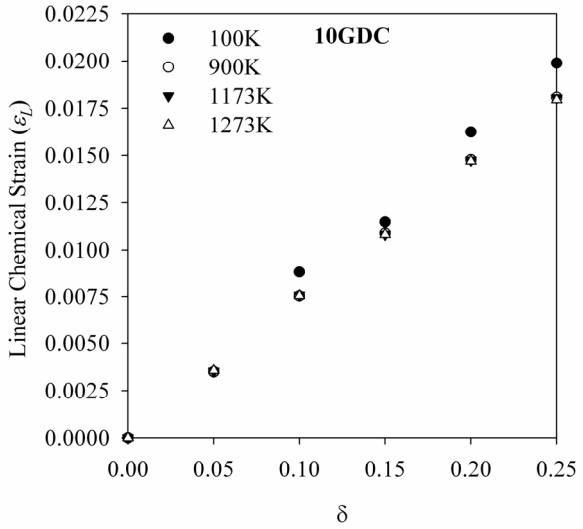

Figure 4.5: Linear chemical strain vs. δ for 10GDC

from the CCE. Once the linear strains $\left(\varepsilon_L = \Delta V / 3V\right)$ are obtained, the CCE for the vacancies can be calculated using the expression,

$$CCE = \eta_v = \varepsilon_L / \delta \tag{4.13}$$

where, ΔV is the change in volume with respect to the volume V at stoichiometry.

Eq. (4.13) however assumes that chemical strains vary linearly with non-

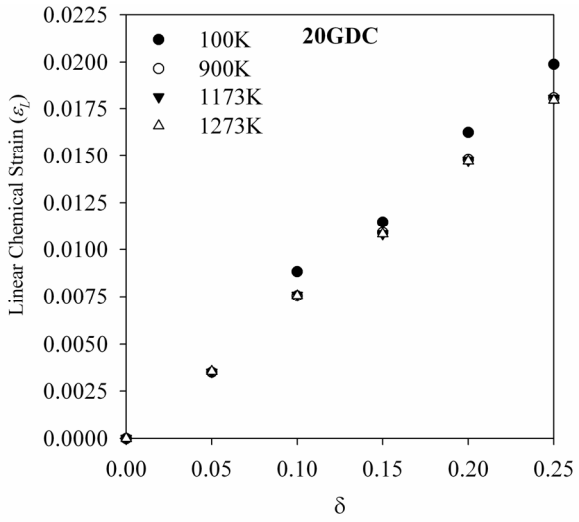

Figure 4.6: Linear chemical strain vs. δ for 20GDC

stoichiometry. To verify this we plotted the linear chemical strains vs. non-stoichiometry. Figure 4.5 shows the plot for 10GDC while Figure 4.6 shows the same result for 20GDC. Clearly the strains vary linearly with non-stoichiometry for all temperatures, thus validating Vegard's law [79] and also corroborating Eq. (4.13). The slopes of the lines may be regarded as CCE for the appropriate compound and temperature. Table 4.2 shows the average CCEs (calculated using Eq.(4.13)) for both 10 and 20GDC for the various temperatures. The CCEs are slightly higher for lower temperatures, suggesting that the effect of temperature on the CCE is to decrease it. Also, the CCE values are higher for 10GDC than for 20GDC concluding that a higher doping concentration reduces the CCE values.

The value of CCE ranges between 0.069-0.079 for all the temperatures and the non-stoichiometry levels examined in this work compare well with recent experimental

studies [148]. Further, it must be mentioned that the standard deviation in the CCE values was 0.0026 and 0.0029 for 10 and 20GDC respectively. For this reason the CCE for GDC may be approximately considered to be in the range of 0.069-0.079 for a wide range of temperatures.

Table 4.2: Average CCE values for 10 and 20 GDC at various temperatures

Temperature K	CCE/10GDC	CCE/20GDC
100	0.0791	0.0765
900	0.07291	0.07093
1173	0.07291	0.0698
1273	0.0729	0.069

4.5.2 Comparison with experiments

To compare the results with experiments, we closely followed reference [137]. In this article the authors have plotted the linear chemical strains vs. the partial pressure of

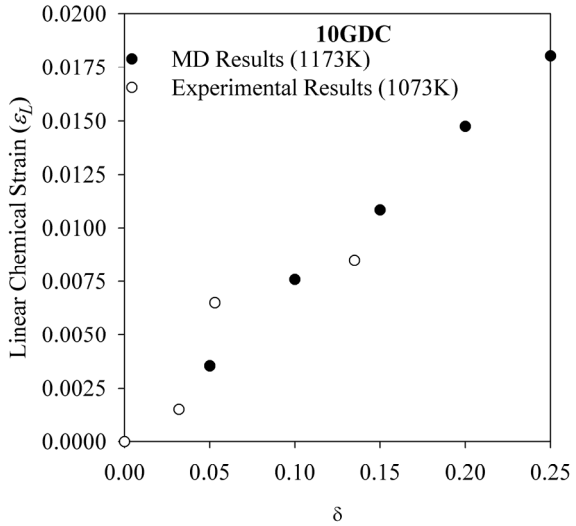

Figure 4.7: Comparison with experiments ref.[137]

oxygen instead of the vacancy concentration. We have compared our results with this data after converting the partial pressure to the vacancy concentration (and hence the

deviation δ) using expression 11 in the reference. Figure 4.7 shows the comparison of linear chemical strains for various values of non-stoichiometry for 10 GDC. Clearly we can see that the MD results match the results from the experiments for lower levels of non-stoichiometry. For larger vacancy concentrations the MD simulations seem to under predict the chemical strains by a maximum of 10%.

4.6 Elastic constants

4.6.1 Single crystal GDC

The single crystal stiffness tensor for the range of non-stoichiometry and temperatures considered are plotted in Figure 4.8. These were calculated based on Eq.(4.12). Although the GDC structures were all constructed from ceria, which has a cubic symmetry, the GDC crystal no longer the cubic symmetry structure-wise. Nevertheless, we found that the deviation from cubic symmetry is negligibly small. Therefore, only the three elastic constants C_{11}, C_{12} and C_{66} representing cubic response are reported here, and their variations with non-stoichiometry are plotted in Figure 4.8 for various temperatures.

Figure 4.8a shows how C_{11} varies with δ at 100, 900, 1173 and 1273 degrees Kelvin for 10GDC. The same is shown in Figure 4.8 b for 20GDC. Similarly, data for C_{66} are shown in Figure 4.8 c – d, and C_{12} in Figure 4.8e – f for 10GDC and 20GDC, respectively. The trend obtained in the variation of the elastic constants with non-

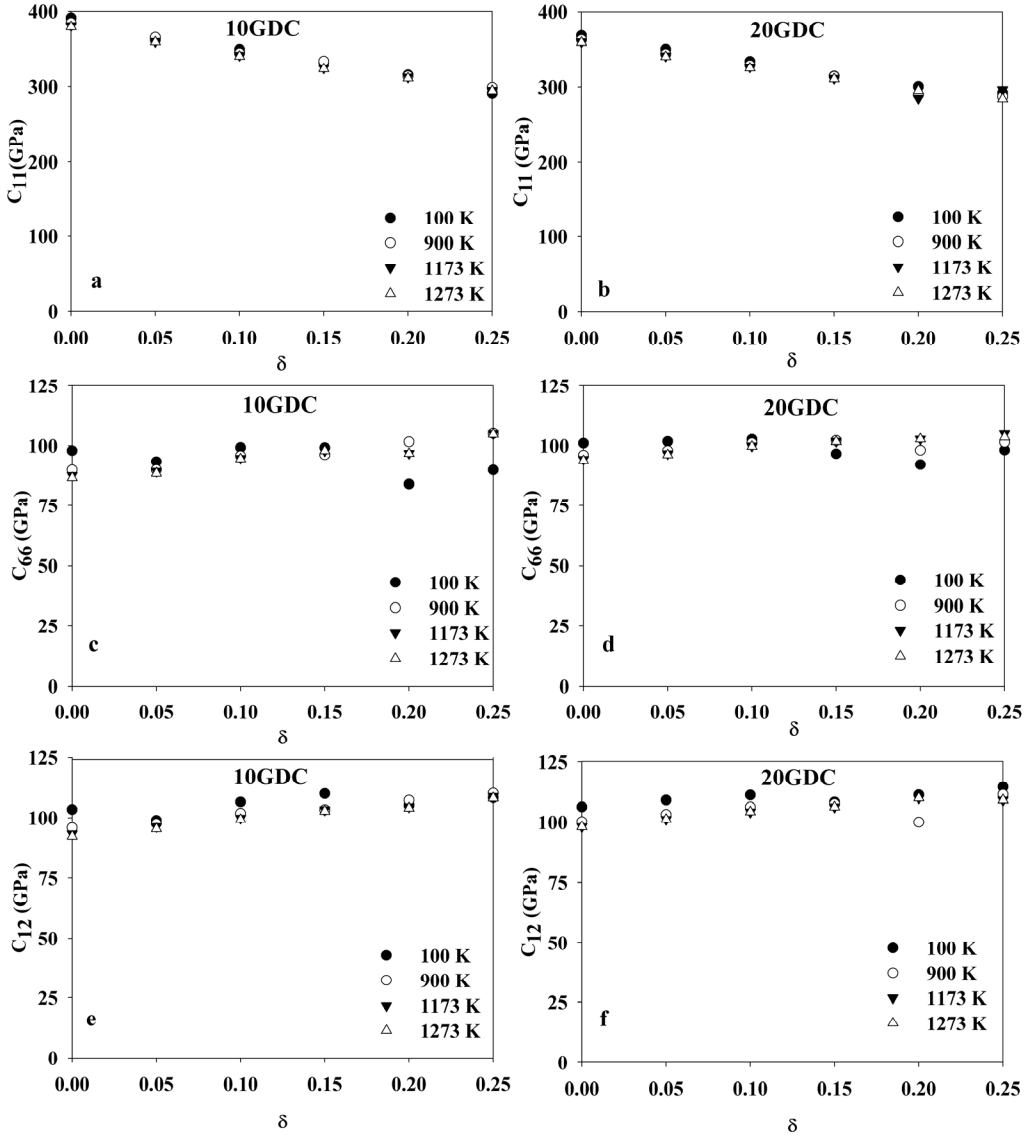

Figure 4.8: (a,b) C_{11}, (c,d) C_{66} and (e,f) C_{12} for 10 and 20GDC

stoichiometry clearly indicates one important point. The variation is higher for C_{11} than for C_{12} and C_{66}. The C_{11} decreases with an average slope of 400 while the others increase with a slope of 45. The former components fall by about 75-100GPa over the entire range of non-stoichiometry examined here while the latter ones do not increase more than 10-

12GPa. Possible reasons for this behavior will be analyzed in the section below, while the contributions of the short range and the long range terms to the elastic tensor will be examined in section 4.6.5

4.6.2 Elastic constants for polycrystalline GDC

The elastic constants obtained using the above approach are valid for a single crystal. However it is well known that the electrolytes are in general polycrystalline. Hence in this section we obtain the elastic constants for polycrystalline GDC using a homogenization method. Consider a polycrystalline solid comprised of numerous

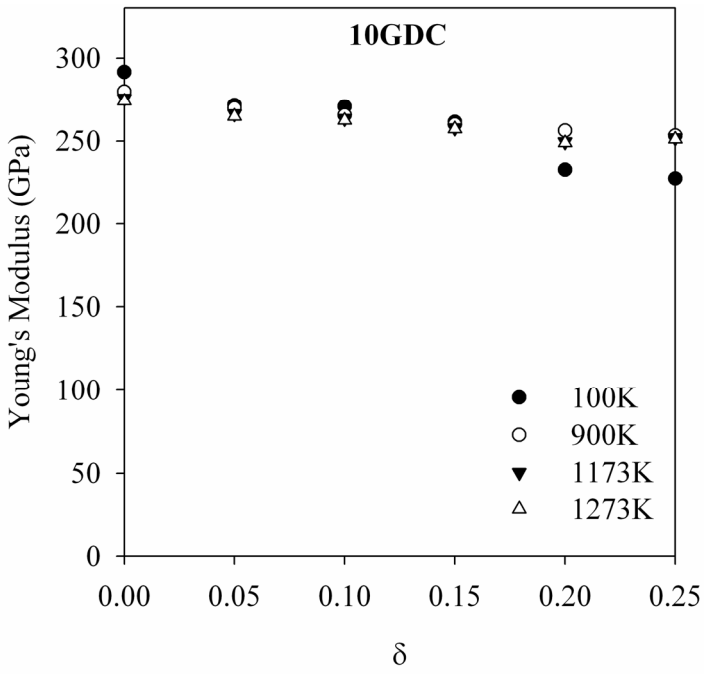

Figure 4.9: Young's Modulus vs. δ for 10GDC

randomly oriented defective single crystal GDC (grains) as analyzed above. The effective elastic constants for the polycrystalline solid can be obtained by a weighted average of the elastic constants of the individual grains [149],

$$\overline{C}_{pqrs} = \frac{1}{8\pi^2}\int_0^{2\pi} d\psi \int_0^{\pi} \sin\theta d\theta \int_0^{2\pi} f(\varphi,\theta,\psi)\alpha_{ip}\alpha_{jq}\alpha_{kr}\alpha_{ls}C_{ijkl}d\varphi \qquad (4.14)$$

where θ, φ and ψ are the Euler angles representing the grain orientation and $f(\varphi,\theta,\psi)$ is the probability distribution of the grain orientation. For random orientation, $f(\varphi,\theta,\psi) = 1$.

Due to the random nature of the grain orientation, the effective elastic constants of the polycrystalline solid are isotropic. Therefore, they can be more conveniently represented by the two more familiar engineering elastic constants, Young's modulus and Poisson's ratio [137, 149]. Results for the Young's modulus are plotted in Figure 4.9 and Figure 4.10 for 10GDC and 20GDC, respectively.

It is again seen that the trend predicted is well approximated by a linear function with a negative slope. Further, it appears from these figures that the Young's modulus by

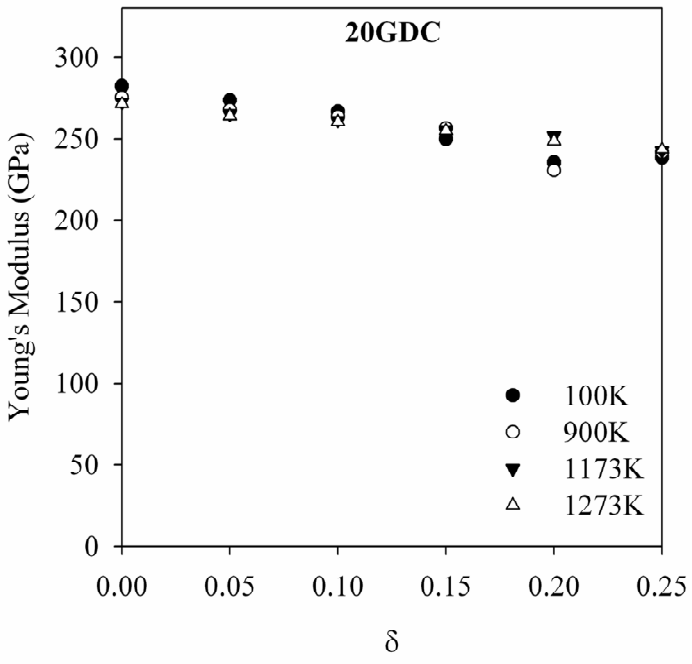

Figure 4.10: Young's Modulus vs. δ for 20GDC

itself and its variation with stoichiometry are not strong functions of temperature.

Although not shown, it was found that the Poisson's ratio is about 0.26, and it does not change by more than 4% over the range of temperature and non-stoichiometry considered here.

To verify the accuracy of the MD simulation estimate, we compare our computed Young's modulus with the experimental data reported in [137] for 10GDC. This is shown in Figure 4.11. Clearly, both experimental data and our numerical computation indicate the near linear variation of Young's modulus versus non-stoichiometry. Our numerical results tend to over predict the modulus at higher vacancy concentrations by about 13%.

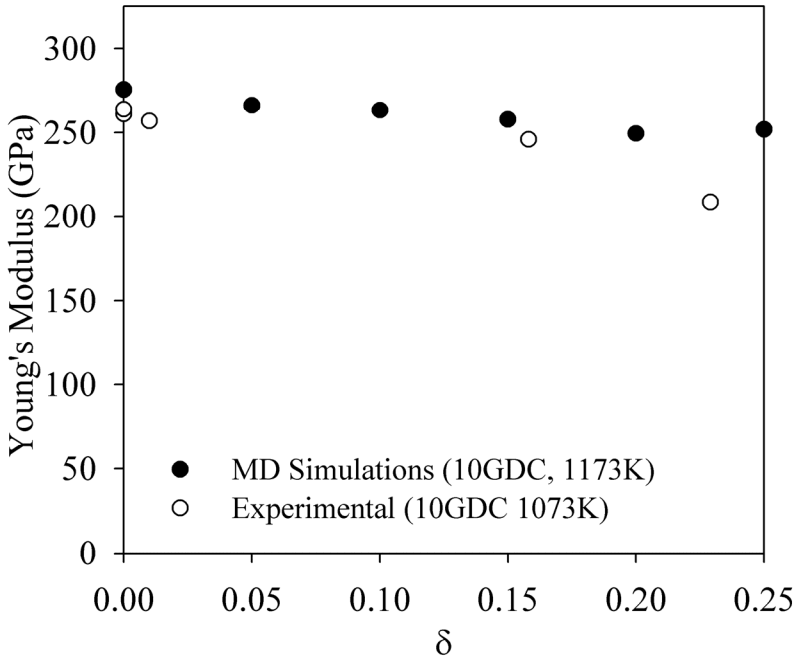

Figure 4.11: Comparison with experiments ref. [15]

It is possible that this deviation occurs because the interatomic potential used here was fit

for stoichiometric GDC. It may not predict the elastic properties of non-stoichiometric compound very accurately, especially at higher vacancy concentrations.

4.6.3 Contribution of inner elastic constants

Intuitively, one would think that that the defective GDC structure, far from being a centro-symmetric, or monatomic Bravais lattice, would not deform homogeneously even under a homogeneous overall deformation. Thus, the inhomogeneous part of the elastic constants ($\tilde{C}_{ijkl}$) would be not negligible. However, our numerical results show that for the ranges of non-stoichiometry and temperature considered here, the contribution from $\tilde{C}_{ijkl}$ is only about 2% for both 10GDC and 20 GDC.

Some authors [145, 150, 151] have suggested that defective fluorite structures may be built from fluorite type modules by different arrangements. In particular 22 different basic fluorite type modules were suggested in [150, 151], which could be used to build defective fluorite based oxides that form a homologous series of the form A_nO_{2n-2m} (A-cation, O-Oxygen). These structures, built from fluorite type modules, are non-primitive and show inner-elastic contribution. The results obtained here seem to indicate that defective ceria structures with several kinds of dopants may not be simply modeled using fluorite type modules. The relaxation of atoms around the vacancies is significant and alters the structure so that the inner elastic contribution becomes negligibly small.

To test this hypothesis, we also computed the elastic constants of the unrelaxed defective GDC structure. Essentially, the unrelaxed structure comprises only fluorite modules as suggested in [150, 151]. By "unrelaxed" we mean the structure as built (before the MD run was performed) where all cations are in the Ce^{4+} positions while all the oxygen ions and vacancies are in the O^{2-} position of a perfect fluorite structure. We

found that for 20GDC at δ = 0.15 and 1173 K, contributions from $\tilde{C}_{ijkl}$ to the total elastic constants can be as much as over 70% for some of the components. Under the same conditions, $\tilde{C}_{ijkl}$ in the relaxed state contributes only a few percent to the overall elastic constants (see Table 4.3).

Table 4.3: Contribution of inner elastic constants

Inner Elastic Constants	Unrelaxed Structure (GPa)	Relaxed Structure (GPa)
$\widetilde{C}_{1111}$	-6.055	-2.63
$\widetilde{C}_{2222}$	-28.17	-1.53
$\widetilde{C}_{3333}$	-22.35	-1.54
$\widetilde{C}_{1122}$	-69.52	0.050
$\widetilde{C}_{1133}$	-75.00	0.18
$\widetilde{C}_{2233}$	-10.53	-0.29
$\widetilde{C}_{2323}$	21.19	-3.40
$\widetilde{C}_{1313}$	-35.46	-4.59
$\widetilde{C}_{1212}$	-53.00	-4.32
$\widetilde{C}_{1123}$	-46.30	-0.010
$\widetilde{C}_{1113}$	21.78	0.156
$\widetilde{C}_{1112}$	14.10	-0.046
$\widetilde{C}_{2223}$	3.11	-0.058
$\widetilde{C}_{2213}$	-5.90	0.076
$\widetilde{C}_{2212}$	-2.05	-0.025
$\widetilde{C}_{3323}$	18.41	-0.12
$\widetilde{C}_{3313}$	-8.80	0.11
$\widetilde{C}_{3312}$	-1.60	-0.06
$\widetilde{C}_{2313}$	-49.61	-0.16
$\widetilde{C}_{2312}$	-0.88	0.12
$\widetilde{C}_{1312}$	4.86	-0.16

Thus, as a conclusion, we believe that the defective ceria structures may not be properly modeled by using fluorite type modules. The relaxed positions that the atoms take are significantly different from the unrelaxed ones in defective structures and must

be accounted for to study the material response. Furthermore, ceria based defective structures (10 and 20GDC), with the vacancy concentrations and dopants examined in the current work, behave more like cubic structures with all the atoms at positions that are either close to or at inversion centers. Therefore there is very little contribution from inner elasticity.

4.6.4 Dependence of elastic constants on initial configuration

Another issue worth mentioning is whether the initial structure created will lead to the global minimum energy state after relaxation. Because of the complex composition of the material, its energy landscape may have a local minimum. An arbitrarily generated initial structure would fall into a local minimum after relaxation, which may then give very different elastic constants each time a new initial structure is used. To verify if this is the case, we generated three different initial structures with $M = 5$ for one specific stoichiometry level and temperature for 10GDC. The OSEC computed from these three initial structures are shown in Table 4.4 in the columns labeled Trial 1 – 3. It is seen that the results from these three very different initial structures differ by less than 1%. This seems to indicate that the computed OSECs are relatively independent of the initial structure of the simulation cell.

A further verification of the above conclusion is conducted by building an initial MD simulation cell in such a way that all vacancies and the replacement of the ions were carried out completely randomly within the entire MD cell itself (i.e. no super cells were constructed) and no inner elasticity was accounted for (i.e. using Eq.). The results are shown in Table 4.4 under the column Trial 4. It is seen that the results differ from those under Trials 1 – 3 by less than 1%. Recall that the results under the columns Trial 1 – 3

were obtained using different initial structures within a super cell and that they accounted for inner elasticity. Data shown in Table 4.4 indicate that the OSEC in the materials considered are independent of both the initial structure and the internal relaxation between different sub-lattices.

Table 4.4: Elastic constants calculations for four trials

	Elastic Constants in 100GPa					% variation from the Average			
Components	**Trial 1**	**Trial 2**	**Trial 3**	**Trial 4**	**Average**	**Trial 1**	**Trial 2**	**Trial 3**	**Trial 4**
C_{11}	3.02	2.92	3.09	3.10	3.03	0.41	0.11	-0.06	-0.07
C_{22}	3.19	3.24	3.14	3.12	3.17	-0.62	-0.06	0.03	0.05
C_{33}	3.20	3.18	3.28	3.12	3.19	-0.20	0.02	-0.09	0.08
C_{12}	1.07	1.08	1.06	1.08	1.08	0.30	-0.01	0.01	-0.01
C_{13}	1.07	1.07	1.06	1.08	1.07	0.20	0.00	0.01	-0.01
C_{23}	1.08	1.06	1.07	1.09	1.07	-0.26	0.01	0.01	-0.01
C_{44}	1.04	1.01	1.00	1.09	1.03	-0.23	0.03	0.03	-0.05
C_{55}	1.00	1.00	0.96	1.08	1.01	0.98	0.01	0.05	-0.07
C_{66}	1.01	0.98	0.97	1.08	1.01	0.27	0.03	0.04	-0.07

4.6.5 Short-range and coulombic contributions

In this section we investigate the relative contributions of the short-range and the

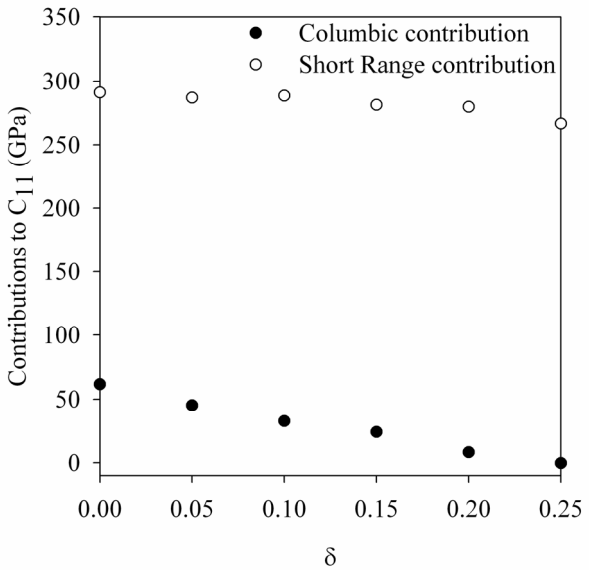

Figure 4.12: Contribution of long and short range parts of the interatomic potential towards C_{11}

long range force fields (coulombic interactions) to the total elastic constants of the compound. All the analyses performed showed a similar trend for the entire range of non-stoichiometry and temperature. Hence, we report the behavior for 1273K, 20GDC only. In Figure 4.12 we show the relative contributions from the coulombic and the short range forces to the elastic constant C_{11}. It can be seen that the contribution of the long range coulombic sum to the elastic constants is relatively small when compared to the

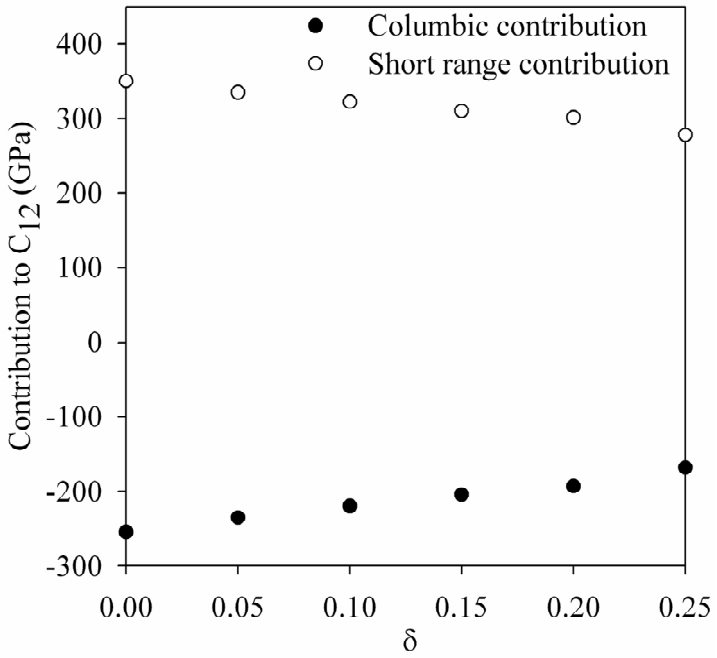

Figure 4.13: Contribution of long and short range parts of the interatomic potential towards C_{12}

contributions from the short range part. Moreover, both contributions, decreased with non-stoichiometry.

The same type of data is shown in Figure 4.13 for C_{12}. From the figure it is clear that the relative magnitudes of the contributions are comparable. Further, with increasing vacancy concentration, the short range contribution decreases while the coulombic contribution increases. From this we can infer that the variation of total C_{12} (Coulombic

+ short range contributions) with the vacancy concentration is small, and this explains the results in Figure 4.8. A similar trend was observed for C_{66} as well (not shown).

4.7 Conclusions

By using a semi-analytical approach in conjunction with MD simulations, the CCE and elastic constants of reduced 10 and 20GDC are determined over a range of non-stoichiometry and temperatures. The MD simulations were conducted on periodic simulation cells of defective 10 and 20GDCs that were constructed using a new approach to allow for the calculation of inner elastic constants. It was shown that the relaxed structure obtained after the simulations was such that the atoms were on, or close to locations which were a center of inversion. Thus the contribution from the inner elastic constants was negligible. This study seems to indicate that the internal relaxation in defective 10 and 20GDC significantly altered the structure to the extent that defective fluorite modules as in [150, 151] may not be used to construct reduced non-stoichiometric ceria.

The numerical results also show that the compositional strain can be approximated as a linear function of non-stoichiometry following Vegard's law, and the corresponding CCE associated with GDC was found to be in the range of 0.069-0.079 for the wide range of temperatures examined.

Over the range of non-stoichiometry examined, the elastic constant C_{11} was found to decrease significantly while C_{12} did not vary as much. Reasons for this behavior were given by examining the contributions from the short range and the coulombic portions to the elastic constants. It was observed that the variations of the contributions to C_{12} was with opposite slopes of almost equal magnitudes and thus did not cause a

significant variation in C_{12} with vacancy concentration. Thus for single crystalline defective GDCs it is sufficient to consider only the variation of C_{11} in order to study the elastic response at varying levels of non-stoichiometry.

The averaged polycrystalline elastic constants were determined by considering an assembly of single crystals with random orientations. The corresponding Young's modulus and Poisson's ratio were tabulated. It was found that for defective GDC structures made of polycrystalline material, it is sufficient to consider only the variation of Young's modulus while modeling the interactions between defect transport and mechanics in GDC.

Finally it is found that neither CCE nor elastic modulus is sensitive to temperature.

CHAPTER 5. STRESSES AND DEFECT TRANSPORT

5.1 Chapter abstract

In this chapter the system of equations introduced in chapter 1 are presented in a one dimensional form. These equations are identified as a modified form of the Nernst-Poisson-Planck system of equations (MNPP). The NPP system has applications in a wide range of physical phenomena ranging from transport in biological membranes [152, 153] to more general electrochemical systems [154]. The numerical issue associated with the classical NPP system is also presented. The presence of a small parameter multiplying the largest derivative in the Poisson equation renders common numerical methods of solutions in the entire domain impossible. This is especially true when the size of the domain is much greater than a characteristic length. This points out the need for a perturbation method requiring the consideration of two length scales, namely the boundary layer and the bulk of the domain.

It is then reiterated that the classical NPP system attains its form on account of two approximations;

1) Neglecting a possible spatial variation of the background elastic energy (usually a part of the standard chemical potential)
2) Assuming a dilute concentration of defects.

Since the main intent of this thesis is to study the effect of stress (elasticity)-defect transport interactions, the first assumption is relaxed, and the elastic contribution to the chemical potential is explicitly considered. For a thin electrolyte (planar or tubular) (10GDC) the MNPP system is solved. The MNPP system contains the effects of chemical

expansion (CCE) and the variation of elastic modulus (OSEC) through two non-dimensional parameters. Since the maximum value of oxygen partial pressure considered is 1atm, the concentration of interstitials and holes was neglected in comparison to the concentration of vacancies and electrons [155] in the analysis performed in this chapter.

Implicit analytical solutions are derived and it is found that the solutions, namely the distribution of vacancies and the electrostatic potential, show non-trivial differences when the effects of elasticity were considered. This showed that elasticity had an effect on the electrochemical fields. Moreover, the stresses induced in the electrolytes were high compared to the strengths of the material suggesting that the material will fail due to induced non-uniform chenmical strains.

Numerical solutions are obtained for the distribution of all the field quantities in the boundary layer by solving the boundary layer differential equation. The main conclusions from the boundary layer solution once again indicated an alteration in the distribution profiles when the effects of elasticity were considered reinforcing the plausibility of interactions. In fact the overall charge density in the boundary layer was found to be enhanced when elasticity was considered. The chapter is then concluded by suggesting that elasticity effects (like applying external loads) can be used over other existing methods which are based on grain boundary engineering, to alter the material's behavior such as its charge storage capacities and conductivities.

5.2 Introduction

In this chapter, we study the effects of stress-defect transport interactions on the distribution of electrochemical field quantities like the distribution of defects, electrostatic potential and mechanical stresses. In order to achieve this objective, we must

solve the MNPP system (introduced in section 3.5.3) of equations subjected to appropriate mechanical and electrochemical boundary conditions. Before discussing the solution procedure directly, it is useful to look at some of the features of the NPP system and examine the literature devoted to solving the NPP system.

5.2.1 The NPP system-Numerical issues

We have seen that the gradient of the electrochemical potential $\widetilde{\mu}_\alpha$ of the defect α forms the "driving force" for defect transport [27]. $\widetilde{\mu}_\alpha$ for the dilute case is given as

$$\widetilde{\mu}_j = \mu_j^* + RT\ln\left(\rho_j\right) + z_j F\phi \tag{5.1}$$

where all the quantities have their usual meanings as in chapter 1, section 1.4. However, we reiterate that μ_α^* is a constant throughout the solid and contains the standard chemical potential μ_α^0 (from the energy for defect formation), and also a constant background elastic energy μ_α^{el} thus enabling the form in Eq. (5.1) for $\widetilde{\mu}_\alpha$ (see ref. [38] for details).

Eq. (5.1) holds, as long as the concentrations are small (dilute regime) [33]. If relation (5.1) is used, then the NPP system for one dimensional isothermal defect transport can be obtained from the phenomenological equations of irreversible thermodynamics under the assumption that the species do not interact [156]. These equations can be obtained from Eq. (3.75) (after setting $\tau_\alpha = 0, \lambda_\alpha = 1$) and Eq. (3.97) in their non-dimensional forms and is given by Eqs. (5.2) and (5.3)

$$\frac{J_\alpha h}{D_\alpha} = -\frac{d\rho_\alpha}{d\bar{x}} - z_\alpha \rho_\alpha \frac{d\bar{\phi}}{d\bar{x}} \tag{5.2}$$

$$-\chi^2 \frac{d^2\bar{\phi}}{d\bar{x}^2} = \left(\sum_{\text{sum over all defects}} z_\alpha \rho_\alpha + z_q Q\right) \tag{5.3}$$

and for sake of simplicity we may say that the differential equations are subjected to Dirichlet boundary conditions as follows,

$$\rho_\alpha(0) = \rho_\alpha^L; \rho_\alpha(1) = \rho_\alpha^R \tag{5.4}$$

and

$$\bar{\phi}(0) = \bar{\phi}_L = 0; \bar{\phi}(1) = \bar{\phi}_R \tag{5.5}$$

where

J_α is the current density of the species α and is a constant for steady state diffusion

h is the length of the domain

$\bar{x}$ is the non-dimensional coordinate $\frac{x}{h}$

$$\chi = \sqrt{\frac{\in V_m RT}{F^2 h^2}} = \frac{\chi_D}{h}$$

χ_D is a characteristic length

Q is the concentration of the immobile defect (moles per mole of the solid) while z_q is its equivalent charge

$\in = \kappa_\varepsilon \varepsilon^0$, is the electrical permittivity of the solid ($C^2 N^{-1} m^{-2}$)

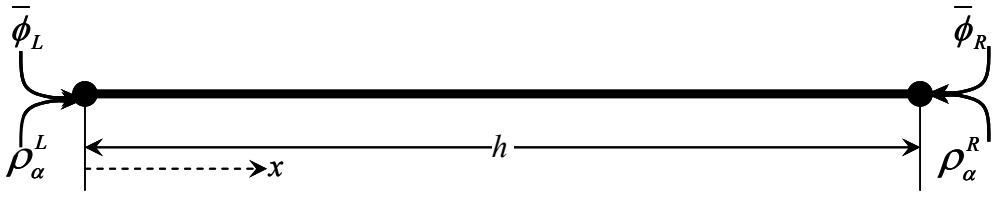

Figure 5.1: One dimensional domain for the NPP system

$\bar{\phi}$ is the non-dimensional electrical potential $\frac{F\phi}{RT}$

ρ_α^L and ρ_α^R are the concentrations of specie α at the **L**eft $\left(\bar{x}=0\right)$ and the **R**ight $\left(\bar{x}=1\right)$ boundaries respectively (see Figure 5.1)

$\bar{\phi}_L$ and $\bar{\phi}_R$ are the non-dimensional electrostatic potentials at the **L**eft $\left(\bar{x}=0\right)$ and the **R**ight $\left(\bar{x}=1\right)$ boundary respectively (see Figure 5.1)

To illustrate the numerical issues arising in the solution to the NPP system we turn our attention to the nondimensional parameter χ^2 which multiplies the highest derivative in the Poisson's equation. For illustration let us assume, $\kappa_\varepsilon = 35$ [157], $V_m = 24\times10^{-6}\,\mathrm{m^3\,mol^{-1}}$, T=1073K. Then

$$\chi = \sqrt{\frac{7.12754\times10^{-21}}{h^2}} = \frac{8.4425\times10^{-11}}{h} \tag{5.6}$$

even if $h = 0.5\times10^{-6}\,\mathrm{m}$, $\chi \approx 169\times10^{-6}$. The small value of χ engenders very large gradients in the values of the primary variables (ρ_α and $\bar{\phi}$) near the boundaries of the domain. Such problems are called boundary layer problems and occur frequently in fluid mechanics. They require a different mathematical treatment called perturbation analysis [158]. Moreover if we were to use finite element or finite difference procedures to solve the system, the domain discretization will have to be in the order of χ_D (at least near the boundaries), which, for the problem at hand is impractical. It is this boundary layer phenomenon which gives rise to a drastic change in the charge storage capacities of nano-crystalline materials and is the motivation for the emerging subject of nano-ionics. In

passing we also notice that if the size of our domain h is comparable to χ_D then the solutions can be obtained by straight forward applications of some numerical method.

For macrosized domains ($\chi_D << h$), the general tendency is to set the LHS of Eq.(5.3) to zero (on account of small value of χ / h) and use the algebraic condition,

$$\left(\sum_{\text{sum over all defects}} z_\alpha \rho_\alpha + z_q Q \right) \approx 0 \tag{5.7}$$

as a governing equation. However, this is not strictly correct, as there could be large gradients near the boundaries of the domain. Equation (5.7) is the so called **Local Electroneutrality** (**LEN**) condition.

Another possibility is a situation where the value of χ is large enough to allow us to set the RHS of Eq. (5.3) to zero and obtain a constant **Electric Field** approximation,

$$\frac{d}{dx}\left(\frac{d\bar{\phi}}{d\bar{x}} \right) = 0 \tag{5.8}$$

Note that $\frac{d\bar{\phi}}{d\bar{x}}$ is the electric field and hence the name constant **Electric Field** approximation.

Thus the numerical issues arising in the solution of the NPP systems prevents the use of a direct numerical procedure like the finite element method, at least for macrosized domains ($\chi_D << h$) as will be our case.

5.2.2 Solution to the NPP system - Review

Several articles have been published showing either numerical [152, 159-162] or analytical methods [163] to solve the system (5.2)-(5.5) . As mentioned, one major obstacle faced in obtaining a numerical solution is due to large gradients in the primary

variables $\left(\rho_i \text{ and } \bar{\phi}\right)$ near the boundaries for a small value of the parameter $\chi\left(\ll 1\right)$ which multiplies the highest derivative in the Poisson's equation (Eq.(5.3)). This requires an asymptotic analysis of the problem [159, 163-167]. In some articles [156, 168] the **LEN** condition or constant field approximation is used to obtain solutions. It can be shown through an asymptotic analysis that LEN and the constant field approximation are only consequences of the zero order term (interior solution) when χ is small (LEN) and when χ is large (constant field) respectively [165, 169], and these are valid only in the bulk of the material. In this work we discuss cases when $\chi \ll 1$ and under such conditions the thickness of the boundary layer is very small when compared to the dimensions of the solid. Under such circumstances a state of Donnan equilibrium exists close to the boundaries due to the thin boundary layer [165]. Donnan equilibrium refers to the phenomenon where the values of the primary variables suffer a "jump" close to the boundaries. This means that the boundary values imposed as in Eqs.(5.4)-(5.5) does not hold for the interior solution (zero order solution) of the NPP system. Even if a complete solution to the boundary layer cannot be obtained, the jump values can be calculated through the method of matched asymptotic expansions, and they can be used as boundary conditions for a complete interior solution. For details on perturbation analysis we refer the reader to references, [158, 170].

The classical form of the NPP system has been revisited, and it is important to note that the system is derived based on certain assumptions regarding the chemical potential (see definition of μ^* and [38]). The material under consideration (GDC) conducts electrons and oxygen ions (or oxygen vacancies). Further as motivated in chapter 1, it also shows a significant volumetric chemical strain due to local deviations

from the stoichiometric vacancy concentration [148]. During functioning, these materials have a non-uniform deviation from stoichiometry, and hence the solid is subjected to inhomogeneous strains throughout their domain. Such strains when not accommodated through appropriate deformation can cause local stresses resulting in mechanical failure of the solid [94, 171]. In addition to stresses being induced, the elastic energy contribution to the chemical potential $\left(\mu^{el}\right)$ can be significant and is no longer a constant throughout the solid. The existence of such effects, where chemical equilibrium is affected due to the presence of stresses, is corroborated by recent works [17, 18, 172], where stress relaxation in a thin GDC sample was related to an association-dissociation reaction. Moreover as pointed out earlier the physical properties of GDC have also been shown to vary with stoichiometry [136-138]. These recent studies point out the need to consider interactions between defect transport and mechanics.

We hence solve the MNPP system and quantify the level of interaction on the electrochemical behavior. The solutions for the interior and the boundary layers are obtained, and the effects of elasticity on solutions, the Donnan equilibrium conditions and on the current voltage relations are discussed. For the sake of simplicity a one dimensional steady state, isothermal (T=800^{o}C) defect transport in 10GDC ($Ce_{0.9}Gd_{0.1}O_{1.95-\delta}$) with a constant concentration of immobile defect (Q=0.1) is considered. Further we assume that only the vacancies contribute to the eigenstrains or cause variations in the elastic properties in the material, hence, $\eta_e = 0$ and $c^e_{ijkl} = 0$. Moreover, in this material it suffices to determine the distributions of the concentrations of vacancies $\left(\rho_v\right)$, electrons $\left(\rho_e\right)$ and the electrical potential $\left(\phi\right)$. It can be assumed that

the interstitials (ρ_O) and the holes (ρ_h) are in negligible quantities when compared to the vacancies and electrons.

5.3 The MNPP system

5.3.1 Basic assumptions and differential equations

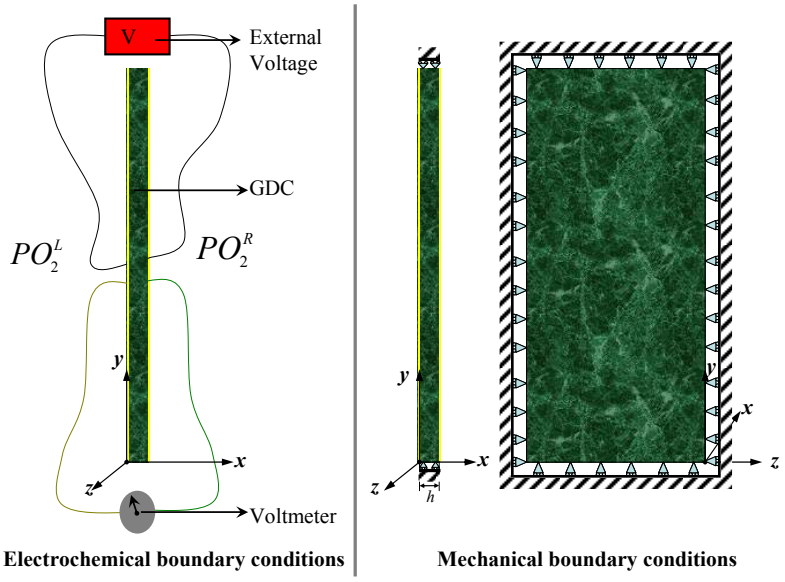

Figure 5.2: Mechanical and electrochemical boundary conditions

5.3.1.1 *Thin planar electrolyte*

Stress dependent defect transport has to be considered when local elastic fields are inhomogeneous and contribute to the non-configurational part of the chemical potential. An Eshelby stress dependent chemical potential was developed in chapter 3. In this section it will be shown that, for a thin electrolyte constrained on all sides as in Figure 5.2 without any externally applied loads, analytical solutions to the MNPP system may be obtained. Under more general conditions, defect transport equations and the equilibrium equations of mechanics have to be solved simultaneously using numerical methods.

Note that the word “thin electrolyte” has been used here with regards to an approximation that will be applied to the mechanical problem, basically to invoke plane stress approximation. The electrolyte is still several orders of magnitude larger than χ_D, requiring a perturbation analysis.

Consider an electrolyte of thickness *h*. The cross-section of the electrolyte is schematically shown in Figure 5.2. It is assumed that the four edges of the electrolyte are all constrained in such a way that it cannot expand in the YZ plane. The only deformation allowed is a change of thickness uniformly. Under such constraints, the strain fields are given as,

$$\varepsilon_{zz} = \varepsilon_{yy} = 0 \tag{5.9}$$

Further, owing to the small value of the gas pressures (which is in the order of a few atms. i.e. 0.101325MPa) on either side of the plate, and the relatively large dimensions of the plate in the lateral (Y and Z) directions, we may assume (Plane stress),

$$\sigma_{xx} = 0 \tag{5.10}$$

Making use of the above approximations, Eqs. (5.9) and (5.10) in the Hooke's law for isotropic materials Eq. (5.11)

$$\sigma_{ij} = \frac{E(\rho_v)}{2(1+\nu)}\left(\varepsilon_{ij} - \delta_{ij}\eta_v\left(\rho_v - \rho_v^0\right)\right) + \frac{E(\rho_v)\nu}{(1+\nu)(1-2\nu)}\left(\varepsilon_{kk} - 3\eta_v\left(\rho_v - \rho_v^0\right)\right) \tag{5.11}$$

it can be easily shown that the following holds,

$$\sigma_{yy} = \sigma_{zz} = -\frac{E(\rho_v)\eta_v\left(\rho_v - \rho_v^0\right)}{(1-\nu)} \tag{5.12}$$

which gives,

$$\sigma_{kk} = -\frac{2E(\rho_v)\eta_v(\rho_v - \rho_v^0)}{(1-\nu)} \tag{5.13}$$

where

$E(\rho_v)$ is the concentration dependent Young's modulus

η_v is the CCE for the vacancies

ρ_v^0 is the stoichiometric vacancy concentration for the GDC (0.05 for 10GDC and 0.1 for 20GDC)

At this point we reiterate that the case under consideration is of self stressed diffusion. Thus, the contribution to the chemical potential from mechanics as given by Eq.(3.71), can be reduced to a simpler form based on the argument in section 3.4.2 .This is given by

$$\mu_v^{el} = V_m \tau_v = -V_m(\sigma_{kk})\eta_v \tag{5.14}$$

which reduces to the following, based on Eqs. (5.10) and (5.13)

$$\mu_v^{el} = V_m 2\eta_v^2 \frac{E(\rho_v)}{(1-\nu)}(\rho_v - \rho_v^0) \tag{5.15}$$

We also agree that the specification of the boundary conditions along *x=0* and *x=h* is invariant in *y*, allowing us to reduce the system of equations (3.95)-(3.97) in their non-dimensional form to a one dimensional case, as follows,

$$\frac{J_v h}{D_v} = -\frac{d\rho_v}{d\bar{x}} - \frac{d\rho_v}{d\bar{x}}(\kappa_1\rho_v + \kappa_2\rho_v^2) - 2\rho_v\frac{d\bar{\phi}}{d\bar{x}} = P \tag{5.16}$$

$$\frac{J_e h}{D_e} = -\frac{d\rho_e}{d\bar{x}} + \rho_e\frac{d\bar{\phi}}{d\bar{x}} = N \tag{5.17}$$

$$\chi^2\frac{d^2\bar{\phi}}{d\bar{x}^2} = -(2\rho_v - \rho_e - Q) \tag{5.18}$$

where $\kappa_1 = \frac{2\eta_v^2 V_m}{(1-\nu)RT}\left(E^0 + 2\beta\rho_v^0\right)$, $\kappa_2 = -\frac{4\eta_v^2 V_m \beta}{(1-\nu)RT}$ and $z_v = +2$, $z_e = -1$ as been used. It is the magnitude of the non-dimensional quantities κ_1 and κ_2 that determines the level of interaction between defect transport and mechanics. Moreover since κ_1 and κ_2 depend on η_v^2, the solution to the system (5.16)-(5.18) is independent of whether the material expands or contracts as a result of deviation from stoichiometry, i.e. it does not matter if $\eta_v > 0$ or if $\eta_v < 0$. However, the stress distribution will show differences on account of its dependence on η_v (see Eq. (5.12)).

Note that, E^0 is the Young's modulus of the material at stoichiometry, while β represents the variation of the Young's modulus with stoichiometry. Based on our analysis in chapter 3 we have used a linear variation for *E* (see Figure 4.11) as follows,

$$E = E^0 + \beta\left(\rho_v^0 - \rho^v\right) \tag{5.19}$$

so that,

$$\beta = -\frac{\partial E}{\partial \rho_v} \tag{5.20}$$

5.3.1.2 ***Thin tubular electrolyte***

Another common form of electrolyte is the tubular electrolyte. Interestingly it is possible to develop the MNPP system for a long electrolyte, by invoking plane strain approximation of elasticity. The mechanical boundary conditions for this configuration are more realistic than the plane stress approximation made for the planar electrolyte. However, we note that the equilibrium equations are not as trivial as for the planar case. To develop the system of equations for the cylindrical configuration, we proceed in the following manner.

Consider a tubular electrolyte with circular a cross section. Let the inner radius be a and the outer radius be b. The wall thickness h is thus given by $h = b - a$. A cross-

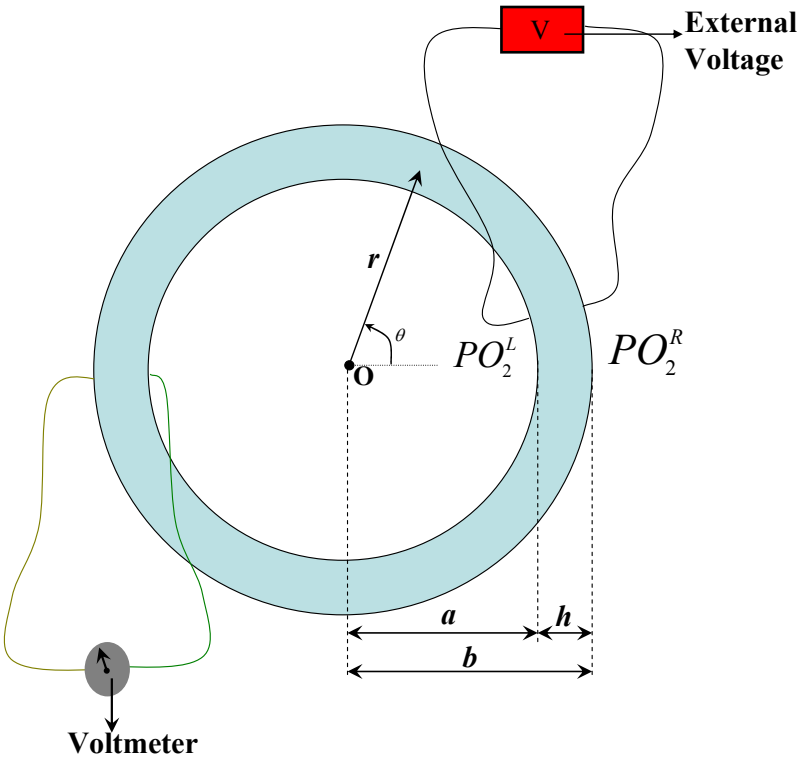

Figure 5.3: Tubular electrolyte

section of the tube is schematically shown in Figure 5.3 where a cylindrical coordinate system attached to the tube is also shown.

It is assumed that the length of the tube is much greater than its diameter so that it can be effectively assumed that the tube is infinitely long. This simplifies the problem into an axisymmetric two dimensional plane strain deformation, i.e., one only needs to consider

$$u_1 = u_r = u(r),\ u_1 = u_r = u(r),\ u_2 = u_\theta = 0,\ u_3 = u_z = 0 \tag{5.21}$$

for the deformation fields, $\rho_\alpha = \rho_\alpha(r)$ for defect concentrations and $\phi = \phi(r)$ for the electrostatic potential.

We begin by considering the mechanical fields. It follows from Eq.(3.13) that the total strain field corresponding to the displacement field described by Eq. (5.21) can be easily computed in the cylindrical coordinate system,

$$\varepsilon_{11} = \varepsilon_r = \frac{du_r(r)}{dr},\ \varepsilon_{11} = \varepsilon_r = \frac{du_r(r)}{dr},\ \varepsilon_{22} = \varepsilon_\theta = \frac{u_r(r)}{r},\ \varepsilon_{33} = 0 \tag{5.22}$$

Making use of the above in the Hooke's law Eq. (5.11), we found that,

$$\sigma_{11} = \sigma_r = K\left(\varepsilon_r(1-\nu) + \varepsilon_\theta\nu - (1+\nu)\eta_v\left(\rho_v - \rho_v^0\right)\right) \tag{5.23}$$

$$\sigma_{22} = \sigma_\theta = K\left(\varepsilon_\theta(1-\nu) + \varepsilon_r\nu - (1+\nu)\eta_v\left(\rho_v - \rho_v^0\right)\right) \tag{5.24}$$

$$\sigma_{33} = \sigma_z = K\left((\varepsilon_r + \varepsilon_\theta)\nu - (1+\nu)\eta_v\left(\rho_v - \rho_v^0\right)\right) \tag{5.25}$$

where

$$K = \frac{E\left(\rho_v\right)}{(1+\nu)(1-2\nu)}$$

All the shear stress components are zero. It is easy to show from Eq. (5.23)-Eq.(5.25) that

$$\sigma_{kk} = K(1+\nu)\left[\left(\frac{du_r}{dr} + \frac{u_r}{r}\right) - 3\eta_v\left(\rho_v - \rho_v^0\right)\right] \tag{5.26}$$

For the axisymmetric problem considered here, the only non-trivial mechanical equilibrium equation from Eq.(3.14) (for cylindrical co-ordinate system) is

$$\frac{d\sigma_r}{dr} + \frac{\sigma_r - \sigma_\theta}{r} = 0 \tag{5.27}$$

Substituting Eqs.(5.23)- (5.25) into Eq.(5.27) in conjunction with Eq. (5.22) yields,

$$\frac{du}{dr}+\frac{u}{r}=\frac{1+\nu}{1-\nu}\eta_v\left(\rho_v-\rho_v^0\right) \tag{5.28}$$

the integration constant is chosen so that the displacement is zero when $\Delta\rho_v=\rho_v-\rho_v^0=0$. Making use of Eq.(5.28) in Eq.(5.26) results in,

$$\sigma_{kk}=-\frac{2E\left(\rho_v\right)}{\left(1-\nu\right)}\eta_v\left(\rho_v-\rho_v^0\right) \tag{5.29}$$

This is identical to Eq. (5.13). Since this is the elastic contribution to the chemical potential we see that the MNPP system for the cylindrical configuration also turns out to be similar to the planar configuration, namely, Eq. (5.16)-Eq. (5.18), where, $\bar{x}=r/h$.

In what is to follow we will show the boundary conditions and the distribution of the vacancy concentration and the electrostatic potential with the planar electrolyte in mind. These solutions are also valid for the tubular system except that the domain now ranges from *a* to *b* rather than from 0 to *h.* The distribution and the nature of stresses within the electrolyte are quite different for the two configurations and are shown in later sections. We now discuss the boundary conditions to which the electrolytes are subjected.

5.3.2 Boundary conditions

The typical boundary conditions to which the system of equations (5.16)-(5.18) may be subjected has been discussed in sections 3.5.2.2 and 3.5.2.3. Some comments are in order, especially with regards to the specification of concentrations at the boundaries. The regions of the electrolyte near the boundaries in which the oxidation-reduction reactions occur as in Eq. (3.87), act as stages for complex multistep reactions [173] and as buffers between the two different phases (P_{O_2} and the electrolyte). These regions contain several atom layers at the most, and the continuum description of stresses cannot

be made without ambiguity. This means that for the boundary reactions we cannot use the stress-dependent electrochemical potentials without reservation. However to mathematically study the consequences of using a stress dependent electrochemical potential in specifying the boundary conditions, we use two methods of specifying the boundary conditions and study the effects on the solutions and the electrochemical behavior.

5.3.2.1 ***Method 1***

First, we use expression (3.88) (restated below) to specify the concentrations at each boundary,

$$K = \rho_v^{\mathrm{R/L}} \left(\rho_e^{\mathrm{R/L}}\right)^2 \sqrt{\left(PO_2\right)^{\mathrm{R/L}}} \tag{5.30}$$

where, the superfixes R/L represent the **R**ight or the **L**eft boundary. Hence, at the boundaries, for a known value of K, PO_2 and ρ_v (ρ_v for specific PO_2 can be obtained from Table 2 in ref. [94]), the electron concentration ρ_e is specified. Note that Eq. (5.30) is obtained by equating the stress independent chemical potentials on either side of reaction Eq.(3.87).

5.3.2.2 ***Method 2***

In the second method we use the stress dependent chemical potential to arrive at a mass action law that includes the stress dependent reaction constant as was introduced in APPENDIX C. Let us consider the reactions on the two boundaries,

$$\rho_v^{\mathrm{L}} \left(\rho_e^{\mathrm{L}}\right)^2 \sqrt{\left(PO_2\right)^{\mathrm{L}}} = KK_\sigma^{\mathrm{L}} = K \exp\left(\frac{V_m \eta_v}{RT}\left(\sigma_{kk}^{\mathrm{L}}\right)\right) \tag{5.31}$$

$$\rho_v^{\mathrm{R}} \left(\rho_e^{\mathrm{R}}\right)^2 \sqrt{\left(PO_2\right)^{\mathrm{R}}} = KK_\sigma^{R} = K \exp\left(\frac{V_m \eta_v}{RT}\left(\sigma_{kk}^{\mathrm{R}}\right)\right) \tag{5.32}$$

Using Eq.(5.31) (5.32) and then Eq.(5.13) we get,

$$\frac{\rho_v^{\mathrm{L}}\left(\rho_e^{\mathrm{L}}\right)^2\sqrt{\left(PO_2\right)^{\mathrm{L}}}}{\rho_v^{\mathrm{R}}\left(\rho_e^{\mathrm{R}}\right)^2\sqrt{\left(PO_2\right)^{\mathrm{R}}}}=\exp\left(\kappa_1\left(\rho_v^{\mathrm{R}}-\rho_v^{\mathrm{L}}\right)+\frac{\kappa_2}{2}\left(\left(\rho_v^{\mathrm{L}}\right)^2-\left(\rho_v^{\mathrm{R}}\right)^2\right)\right) \tag{5.33}$$

If we use the LEN condition in the above equation at both the boundaries to represent the electron concentrations there, we arrive at an expression where the only unknowns are the vacancy concentrations (see Eq.(5.34)).

$$\frac{\rho_v^{\mathrm{L}}\left(2\rho_v^{\mathrm{L}}-Q\right)^2\sqrt{\left(PO_2\right)^{\mathrm{L}}}}{\rho_v^{\mathrm{R}}\left(2\rho_v^{\mathrm{R}}-Q\right)^2\sqrt{\left(PO_2\right)^{\mathrm{R}}}}=\exp\left(\kappa_1\left(\rho_v^{\mathrm{R}}-\rho_v^{\mathrm{L}}\right)+\frac{\kappa_2}{2}\left(\left(\rho_v^{\mathrm{L}}\right)^2-\left(\rho_v^{\mathrm{R}}\right)^2\right)\right) \tag{5.34}$$

We may then specify the vacancy concentration at one end and determine the concentrations at the other by solving the nonlinear algebraic equation (Eq.(5.34)), with known values of partial pressures of oxygen on both sides. In what is to follow we will address the situation when Method1 is used as BC1 and BC2 when Method 2 is followed.

Finally we note that the specification of the boundary conditions for the electrostatic potential is given by

$$\phi^{\mathrm{L}}=V+\frac{RT}{F}\ln\left(\frac{\rho_e^{\mathrm{L}}}{\rho_e^{\mathrm{R}}}\right) \tag{5.35}$$

where we have taken the right boundary to be at zero potential.

5.3.3 Solutions- Perturbation Method

5.3.3.1 *Interior Solution*

First, we look for approximate solution to (5.16)-(5.18) in the bulk (interior) of the system after expanding the primary variables in the following form,

$$\overline{\phi}=\Phi^0+\chi\Phi^1+..., \tag{5.36}$$

$$\rho_v = V^0 + \chi V^1 + \ldots \tag{5.37}$$

$$\rho_e = \overline{E}^0 + \chi \overline{E}^1 + \ldots \tag{5.38}$$

Following the standard procedure, we substitute (5.36)-(5.38) in the differential equations-(5.16)-(5.18), hold $\bar{x}$ fixed and let $\chi \to 0$. This gives us the differential equations for the zero order interior solutions,

$$-\frac{dV^0}{d\bar{x}}\left(1+\kappa_1 V^0 + \kappa_2 \left(V^0\right)^2\right) - 2V^0 \frac{d\Phi^0}{d\bar{x}} = \overline{J}_v^0 \tag{5.39}$$

$$-\frac{d\overline{E}^0}{d\bar{x}} + \overline{E}^0 \frac{d\Phi^0}{d\bar{x}} = \overline{J}_e^0 \tag{5.40}$$

$$0 = -\left(2V^0 - \overline{E}^0 - Q\right) \quad \textbf{(LEN condition)} \tag{5.41}$$

After eliminating $\frac{d\Phi^0}{d\bar{x}}$ from (5.39) and (5.40) , using the LEN condition (to substitute for $\overline{E}^0$), and integrating, we obtain an implicit solution for V^0 as follows (See Eq. (5.42))

$$\begin{aligned} 3B^4\bar{x} &= R\ln\left(\frac{A-BV^0}{A-BL_v}\right) + W_2\left(-BV^0 + BL_v\right) + W_1\left[\left(A-BV^0\right)^2 - \left(A-BL_v\right)^2\right] \\ &+ W_3\left[\left(A-BV^0\right)^3 - \left(A-BL_v\right)^3\right] \end{aligned} \tag{5.42}$$

In the above equation,

$$\begin{aligned} &A = \left(T^0 + S^0\right)Q, B = 4T^0, C = 2Q, D = 2Q\kappa_1, E = 4\kappa_1, L = 2\kappa_2 Q, W_3 = M = 4\kappa_2 \\ &R = 3B^4\left[\frac{C}{B} - \frac{(12-D)A}{B^2} - \frac{(E-L)A^2}{B^3} - \frac{MA^3}{B^4}\right] \\ &W_2 = 3B^4\left[\frac{(12-D)}{B^2} + \frac{(E-L)2A}{B^3} + \frac{3A^2M}{B^3}\right], W_1 = 3B^4\left[\frac{-(E-L)}{2B^3} - \frac{3AM}{2B^4}\right] \\ &T^0 = \overline{J}_v^0 + \overline{J}_e^0, S^0 = \overline{J}_v^0 - \overline{J}_e^0 \end{aligned} \tag{5.43}$$

The integration constant is determined by a limiting process as follows,

$$\lim_{\bar{x}\to 0} V^0 = L_v \tag{5.44}$$

L_v is the value of the vacancy concentration close to the left boundary. At this point we hasten to emphasize that the values of the interior solution "close to the boundaries" $\left(\bar{x}=0,\bar{x}=1\right)$ are not the values "at the boundary" $\left(\rho_v^L \text{ and } \rho_v^R\right)$ owing to the existence of Donnan equilibrium conditions. This will be clear when the boundary layer solutions are obtained.

At this point we also define,

$$\lim_{\bar{x}\to 0} \overline{E}^0 = L_e, \lim_{\bar{x}\to 0} \Phi^0 = L_\phi, \lim_{\bar{x}\to 1} V^0 = R_v, \lim_{\bar{x}\to 1} \overline{E}^0 = R_e, \lim_{\bar{x}\to 1} \Phi^0 = R_\phi \tag{5.45}$$

Further we see that on account of Eq. (5.41),

$$2L_v - L_e - Q = 0 \text{ and } 2R_v - R_e - Q = 0 \tag{5.46}$$

An explicit solution for Φ^0, in terms of V^0 can be obtained by eliminating $d\bar{x}$ from (5.39)-(5.40), and integrating. The solution is given by,

$$2B^3\Phi^0 = 2B^3 L_\phi - \frac{R}{6Q}\ln\left(\frac{A-BV^0}{A-BL_v}\right) + \overline{W}_2\left[-BV^0 + BL_v\right] + \overline{W}_1\left[\left(A-BV^0\right)^2 - \left(A-BL_v\right)^2\right] \tag{5.47}$$

where,

$$\begin{aligned} \overline{W}_2 &= 2\left[\left(S^0 - T^0\right)\left(-B\kappa_1 - 2\kappa_2 A\right)\right] \\ \overline{W}_1 &= \kappa_2\left(S^0 - T^0\right) \end{aligned} \tag{5.48}$$

The integration constant in this case is obtained by using both Eq.(5.44) and the second limit in Eq.(5.45).

Eq.(5.42) gives an implicit relation for the distribution of V^0. The solution is obtained by converging onto a value of V^0 for a given $\bar{x}$. However, to obtain the solution, T^0 and S^0 must be found. This was done by first evaluating equations (5.42) and (5.47) in

the limit as $\bar{x} \to 1$ and then eliminating the ln(…) term, between the resulting equations. In doing so we obtain the following expression for T^0,

$$T^0 = -Q\left(R_\phi - L_\phi\right) - 3\left(R_v - L_v\right) - \frac{\kappa_1}{2}\left(R_p^2 - L_p^2\right) - \frac{\kappa_2}{3}\left(R_p^3 - L_p^3\right) \tag{5.49}$$

Thus we see that the sum of the non-dimensional current densities T^0 is completely determined by the values of the primary variables close to the boundaries. Relation (5.49) along with the definition of A can be used in (5.42) to obtain the value of current densities. However the values of L_v, R_v, L_ϕ and R_ϕ are still unknown and can only be obtained by considering the solution to the boundary layers at the two ends. This we show in the next section.

5.3.3.2 ***Boundary layer solution***

Let us consider the left hand boundary close to $\bar{x} = 0$. We introduce the stretched coordinate,

$$\bar{x} = \chi\zeta \tag{5.50}$$

and write the field variables as,

$$\rho_v\left(\chi\zeta;\chi\right) = \tilde{v}^0 + \chi\tilde{v}^1 + \ldots \tag{5.51}$$

$$\rho_e\left(\chi\zeta;\chi\right) = \tilde{e}^0 + \chi\tilde{e}^1 + \ldots \tag{5.52}$$

$$\bar{\phi}\left(\chi\zeta;\chi\right) = \tilde{\phi}^0 + \chi\tilde{\phi}^1 + \ldots \tag{5.53}$$

Using (5.51)-(5.53) in the differential equations (5.16)-(5.18) and performing the limiting process $\chi \to 0$ we get the governing equations for the zero order boundary layers at the left end,

$$0 = -\frac{d\tilde{v}^0}{d\zeta}\left(1+\kappa_1\tilde{v}^0+\kappa_2\tilde{v}^0\right)-2\tilde{v}^0\,\frac{d\tilde{\phi}^0}{d\zeta} \tag{5.54}$$

$$0 = -\frac{d\tilde{e}^0}{d\zeta}+\tilde{e}^0\,\frac{d\tilde{\phi}^0}{d\zeta} \tag{5.55}$$

$$\frac{d^2\tilde{\phi}}{d\zeta^2} = -\left(2\tilde{v}^0-\tilde{e}^0-Q\right) \tag{5.56}$$

The first two equations (5.54) and (5.55) can be readily integrated to obtain,

$$\tilde{\phi}^0 = \frac{1}{2}\left(\ln\frac{\rho_v^{\mathrm{L}}}{\tilde{v}^0}+\kappa_1\left(\rho_v^{\mathrm{L}}-\tilde{v}^0\right)+\frac{\kappa_2}{2}\left(\left(\rho_v^{\mathrm{L}}\right)^2-\left(\tilde{v}^0\right)^2\right)\right)+\overline{\phi}_L \tag{5.57}$$

$$\ln\left(\frac{\tilde{e}^0}{\rho_e^{\mathrm{L}}}\right)+\overline{\phi}_L = \tilde{\phi}^0 \tag{5.58}$$

In obtaining the above two relations we have used (see Eq. (5.5)),

$$\tilde{v}^0\left(0\right)=\rho_v^{\mathrm{L}},\tilde{e}^0\left(0\right)=\rho_e^{\mathrm{L}} \text{ and } \tilde{\phi}^0\left(0\right)=\overline{\phi}_L \tag{5.59}$$

Now we may take the following limits on Eqs. (5.57) and (5.58) to see that,

$$\lim_{\zeta\to\infty}\tilde{\phi}^0 = L_\phi = \frac{1}{2}\left(\ln\frac{\rho_v^{\mathrm{L}}}{L_v}+\kappa_1\left(\rho_v^{\mathrm{L}}-L_v\right)+\frac{\kappa_2}{2}\left(\left(\rho_v^{\mathrm{L}}\right)^2-\left(L_v\right)^2\right)\right)+\overline{\phi}_L \tag{5.60}$$

$$\lim_{\zeta\to\infty}\tilde{e}^0 = L_e = \rho_e^L\exp\left(L_\phi-\overline{\phi}_L\right) \tag{5.61}$$

as the following relations hold,

$$\lim_{\zeta\to\infty}\tilde{\phi}^0 = \lim_{\bar{x}\to 0}\Phi^0 = L_\phi \tag{5.62}$$

$$\lim_{\zeta\to\infty}\tilde{v}^0 = \lim_{\bar{x}\to 0}V^0 = L_v \tag{5.63}$$

$$\lim_{\zeta\to\infty}\tilde{e}^0 = \lim_{\bar{x}\to 0}\overline{E}^0 = L_e \tag{5.64}$$

By using Eqs. (5.60),(5.61) and the first equation of (5.46) we obtain,

$$2L_v - \rho_e^L \exp\left[\frac{1}{2}\left(\ln\frac{\rho_v^{\mathrm{L}}}{L_v} + \kappa_1\left(\rho_v^{\mathrm{L}} - L_v\right) + \frac{\kappa_2}{2}\left(\left(\rho_v^{\mathrm{L}}\right)^2 - \left(L_v\right)^2\right)\right)\right] - Q = 0 \qquad (5.65)$$

The above equation may be solved for L_v using an iteration procedure. L_v can then be used to obtain L_ϕ and L_e from Eqs. (5.60) and (5.61) respectively. Thus we have the "jumps" in the values of the primary variables close to the boundary ($L_\phi - \phi_L, L_v - \rho_v^{\mathrm{L}}$ and $L_v - \rho_e^{\mathrm{L}}$) that depend on the values at the boundary, κ_1 and κ_2. For clarity the various regions in the domain and the variables valid at the boundaries of these

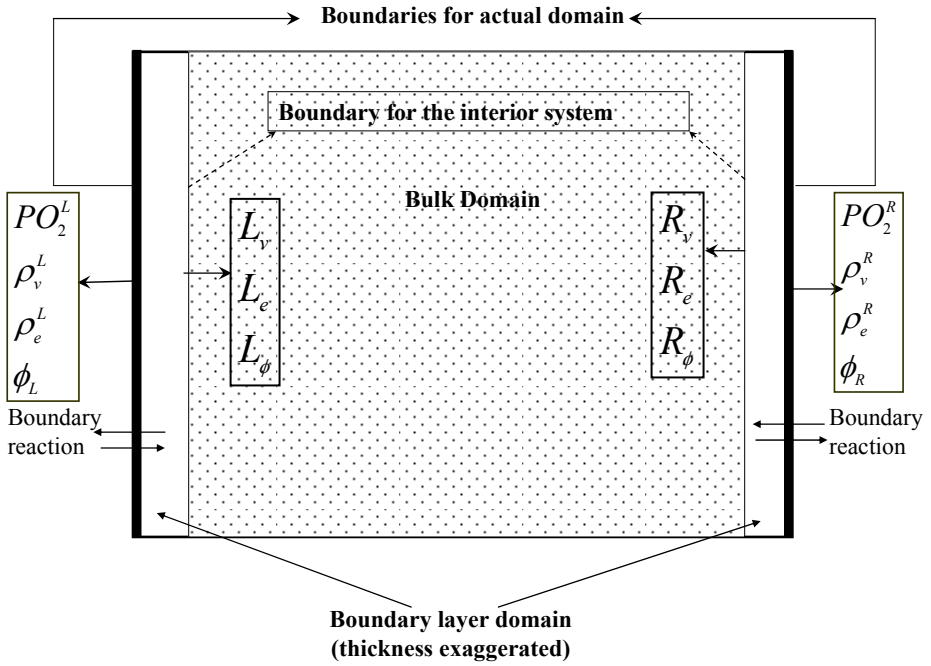

Figure 5.4: Regions within the domain and boundary variables

domains are shown in Figure 5.4.

At this point we note that, if the values of the primary variables satisfy the local electroneutrality condition at the boundary,

$$\left(2\rho_v^L - \rho_e^L - Q\right) = \left(2\rho_v^R - \rho_e^R - Q\right) = 0 \qquad (5.66)$$

then it is easy to verify from Eq. (5.65) and Eq. (5.61) that this is possible only if , $\rho_v^L = L_v, \rho_v^R = R_v, \rho_e^L = L_e \ , \rho_e^R = R_e$ and $\phi_L = L_\phi, \phi_R = R_\phi$. This means that there is no boundary layer if the values of the concentrations satisfy LEN at the boundary and the values of the variables "close to the boundary" can be replaced with those "at the boundary" in Eqs. (5.42) and (5.47). The Method2 (BC2) of prescribing the boundary conditions described in section 5.3.2.2 belongs to this case.

Now proceeding further, a differential equation governing the distribution of $\tilde{v}^0$ can be obtained by differentiating (5.57) twice with respect to ζ and using the result in Eq. (5.56). We get,

$$\left(\frac{1}{\left(\tilde{v}^0\right)^2} - \kappa_2\right)\left(\frac{d\tilde{v}^0}{d\zeta}\right)^2 - \left(\frac{1}{\tilde{v}^0} + \kappa_1 + \kappa_2 \tilde{v}^0\right)\frac{d^2\tilde{v}^0}{d\zeta^2} = -2\left(2\tilde{v}^0 - \Lambda\frac{\exp\left(-\frac{\tilde{v}^0}{2}\left(\kappa_1 + \frac{\kappa_2\tilde{v}^0}{2}\right)\right)}{\sqrt{\tilde{v}^0}} - Q\right) \quad (5.67)$$

where $\Lambda = \rho_e^L\sqrt{\rho_v^L}\exp\left(\frac{\rho_v^L}{2}\left(\kappa_1 + \frac{\rho_v^L\kappa_2}{2}\right)\right)$. The non-linear differential equation (5.67) is subjected to the semi-infinite boundary conditions,

$$\tilde{v}^0\left(\zeta = 0\right) = \rho_v^L \text{ and } \lim_{\zeta\to\infty}\tilde{v}^0\left(\zeta\right) = L_v \quad (5.68)$$

In this work use a shooting method available in MATLAB to solve (5.67)-(5.68). In this method the boundary condition at infinity is specified at a finite value of ζ to first obtain a guess for the solution. This is then used as a guess for larger values of ζ until the value of the function at infinity converges so as to gain confidence that the infinity is large enough. For details please see [174]. The details of the solution profiles for the interior and the boundary layers are given in the following sections. At this point we mention that

the right boundary layer can also be analyzed in an entirely analogous manner by introducing the stretched coordinate

$$\overline{\zeta} = \frac{-1+\overline{x}}{\chi} \tag{5.69}$$

and writing the various fields as,

$$\rho_v\left(1+\overline{\zeta}\chi;\chi\right) = \overline{v}^0 + \chi\overline{v}^1 + \ldots \tag{5.70}$$

$$\rho_e\left(1+\chi\overline{\zeta};\chi\right) = \overline{e}^0 + \chi\overline{e}^1 + \ldots \tag{5.71}$$

$$\overline{\phi}\left(1+\chi\overline{\zeta};\chi\right) = \psi^0 + \chi\psi^1 + \ldots \tag{5.72}$$

From this analysis we obtain R_v, R_e, R_ϕ and the corresponding differential equation for $\overline{v}^0$ after noting that the following limiting conditions hold

$$\lim_{\overline{\zeta}\to-\infty}\psi^0 = \lim_{\overline{x}\to 1}\Phi^0 = R_\phi \tag{5.73}$$

$$\lim_{\overline{\zeta}\to-\infty}\overline{v}^0 = \lim_{\overline{x}\to 1}V^0 = R_v \tag{5.74}$$

$$\lim_{\overline{\zeta}\to-\infty}\overline{e}^0 = \lim_{\overline{x}\to 1}\overline{E}^0 = R_e \tag{5.75}$$

5.4 Distribution of field quantities and interactions

5.4.1 Vacancies and electrostatic potential (Interior Solution)

Table 5.1: Material properties and other constants of the problem

PO_2^R (atm)	PO_2^L (atm)	ρ_v^L	ρ_v^R	E^0 (GPa)	ν	m_v	m_e	h *(cm)*	K 10^{-14} $atm^{1/2}$	β GPa	V_m cm^3/mol
						$mol\ m^2\ J^{-1}\ s^{-1}$					
10^{-21}	1	0.05	0.15	275	0.3	10^{-13}	10^{-10}	0.1	8.2251	200	24

In this section we show the numerical results obtained from expressions (5.42) and (5.47). The electron concentration distribution in the interior ($\overline{E}^0$) can be obtained from the LEN condition (5.41). We particularly examine the results (distribution of vacancies V^0 and the electrostatic potential Φ^0) for three values of applied voltages (V=0, 0.75, 1.5V).

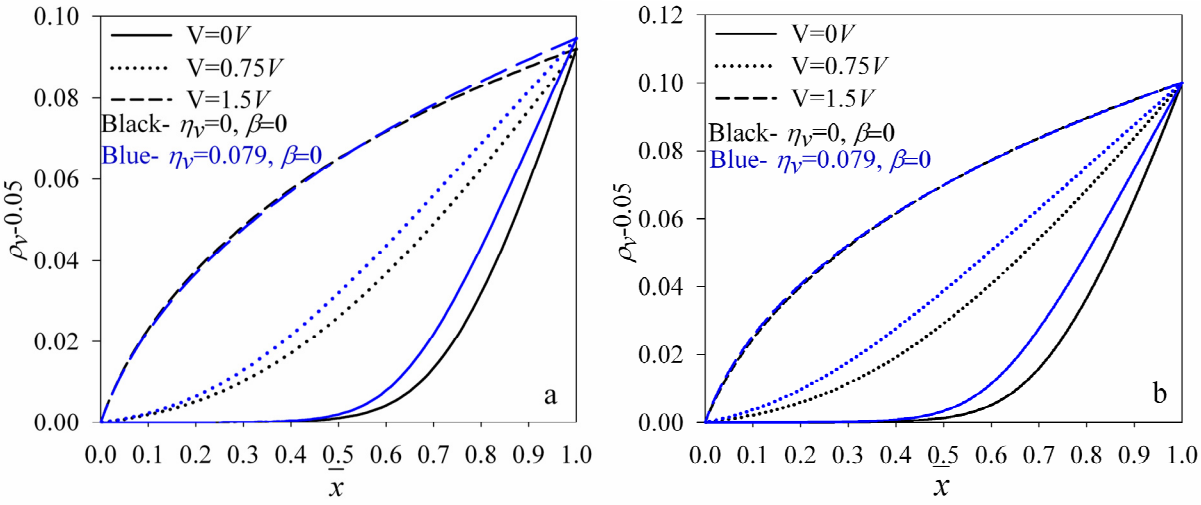

Figure 5.5: Distribution of deviation in vacancy concentration a) BC1 b) BC2

Two values of η_v (0and0.079) and β (0 and 200GPa) are considered to examine the effects of elasticity (that includes the effects of chemical expansion and the variation of Young's Modulus) on the distributions. We further note that, if $\eta_v = 0$ then both κ_1 and κ_2 vanish. The boundary values and other material properties considered for this problem are shown in Table 5.1.

Both the methods of specifying the boundary conditions are used and the results are plotted together for comparison. While using BC2, the vacancy concentration on the

right end was taken as in Table 5.1 while the left boundary concentration was determined as described in section 5.3.2.2, Eq. (5.34).

Figure 5.5 shows the distribution of the deviation in vacancy concentration from its stoichiometric value (0.05 for 10GDC) in the bulk of the material. Clearly, the non-

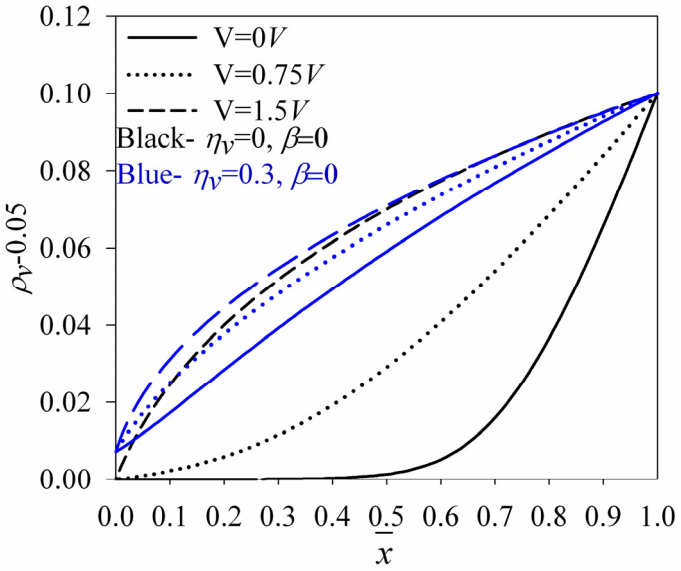

Figure 5.6: Deviation in vacancy concentration for a large value of η_v

trivial differences in the distributions show that the effects of elasticity are noticeable. Further, we see that, at larger values of applied voltages, the influence of elasticity is weaker, and this is true for both the cases in Figure 5.6.

From Figure 5.5a we can notice that close to the right boundary ($\bar{x}=1$) $P_{O_2}^{R}=10^{-21}$ atm and the deviation in vacancy concentration here $\left(\rho_v-0.05\right)$ must be 0.1. But from the figure we observe that this is not the case. This is due to the "jumps" in the values of the variables $\left(R_v-\rho_v^{R}\right)$ as explained in section 5.3.3.2 due to the existence of the boundary layer. Further we note that, at this boundary, the value of the deviation depends on the local elasticity. With the elasticity effect the value is 0.94 while without

it, the value is observed to be 0.92. Thus when elasticity effects are considered, the jumps from the boundary value of 0.1 are slightly lesser than without it. We also see that close to the left end, ($\bar{x}=0$), with or without the elasticity effects, $P_{O_2}^{\mathrm{L}}=1\mathrm{atm}$, the vacancy concentration has its stoichiometric value of 0.05 and the deviation is zero. Thus, when the boundary conditions are specified in such a way that they already satisfy LEN, no jump in the values at the boundary are observed or as mentioned earlier there is no boundary layer here.

In Figure 5.5b we notice that at the right end the deviation is 0.1 as the electron concentration here is specified using the LEN condition (see Eq.(5.34)). Hence, there is

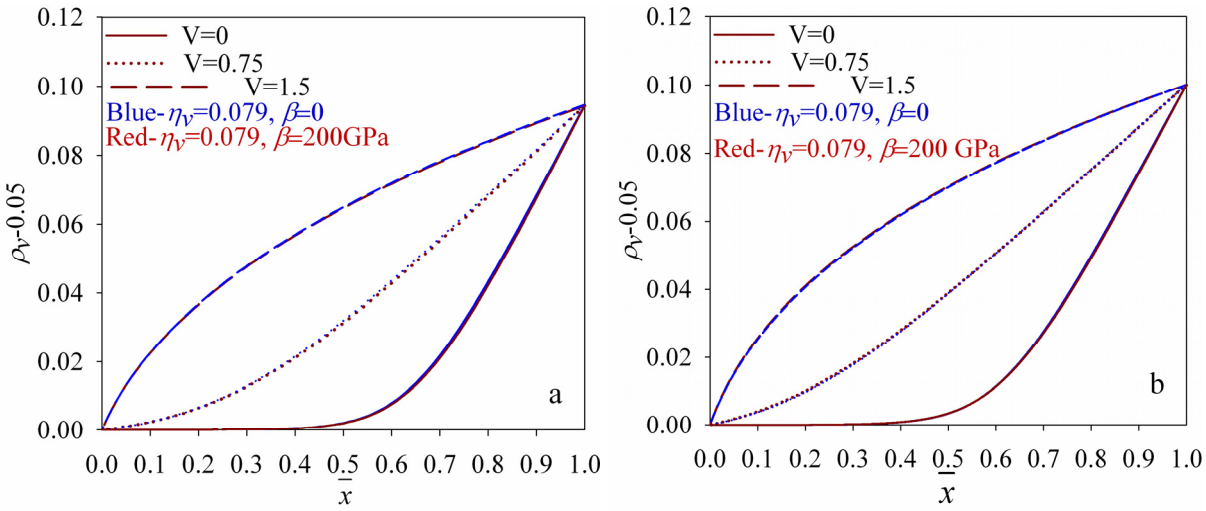

Figure 5.7: Distribution of the deviation with β=200GPa a) BC1 b) BC2

no boundary layer here at the right end as per the discussion in section 5.3.3.2. On the left end, while $\rho_v^L-0.05=0$ for the case with $\eta_v=0$, this is not true for $\eta_v=0.079$. Although this is difficult to see in Figure 5.5b, the use of Eq.(5.34) to specify the concentration at the left end engenders a slightly larger value for the concentration at the left end for non-

zero η_v. This is more clearly seen in Figure 5.6 for a larger value of $\eta_v = 0.3$. Although such a large value of η_v is not typical for ionic solids like GDC, we have used it here only to illustrate the effect of specifying the boundary condition using BC2 and to convey what might be expected for larger values of η_v (or more generally larger values of non-dimensional parameter, κ_1).

Figure 5.7 compares the distribution in the deviation of vacancy concentration

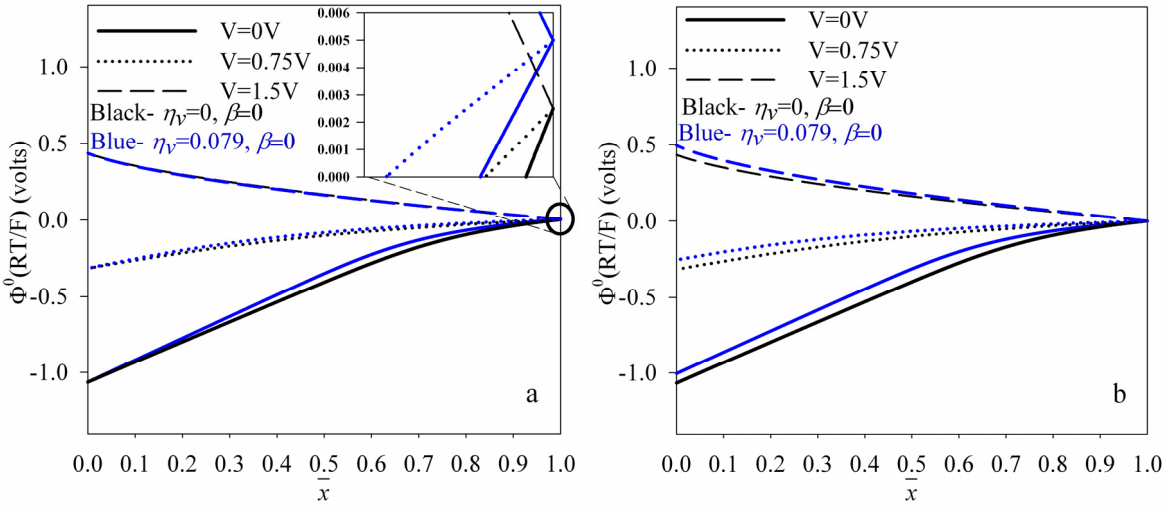

Figure 5.8: Distribution of electrostatic potential a) BC1 b) BC2

when both κ_1 and κ_2 are non zero (i.e. $\eta_v = 0.079$ and $\beta = 200\text{GPa}$), to the case with $\kappa_1 \neq 0$ but $\kappa_2 = 0$ (i.e. $\eta_v = 0.079$ and $\beta = 0$). Clearly, there is no difference in the distribution. This shows that the variation of elastic modulus with stoichiometry does not significantly affect the distribution within the bulk of the material. This is true no matter how the boundary conditions are specified. Since β has no effect, from now on we examine cases for only non-zero κ_1 values and let $\beta = 0$.

Figure 5.8 compares the distribution of $\Phi^0\left(\frac{RT}{F}\right)$. Clearly the distributions are different when stress effects are considered, although this is true to a lesser extent when compared to the differences in the distribution of deviation in vacancy concentration. In this case, for Figure 5.8a the jumps suffered by the boundary values close to the right end are very small. The magnified view of the circled portion is shown as an inset. The jump values are $0.0025V$ for the case in which elasticity effects are neglected, while the jump values are $0.005V$ for the case that takes into account the elasticity effects. We can also notice that similar to the vacancy distribution we see that the electrostatic potential becomes less sensitive to the effects of elasticity at higher voltages. The jumps close to the boundaries (from the boundary value of 0V) are larger with elasticity effects considered than without them.

From Figure 5.8b we see that at the right end the potential is at the specified boundary value of 0V, while at the left end the values are different when elasticity effects are taken into account. This is due to the fact that the electron concentration (from LEN condition) determining the potential here through Eq. (5.35) has different values with and without elasticity being considered due to Eq. (5.34).

5.4.2 Effect on current-voltage relationships

We have seen that the distributions of the defects and the electrostatic potential are affected by elasticity. In order to gauge the overall performance we look into the current voltage relationships. In Figure 5.9 the current densities vs. voltage plot is shown for the cases $\eta_v = 0$ and $\eta_v = 0.079$ for both the methods of specifying the boundary condition. Firstly we see that when the applied voltage is zero, electronic current

vanishes. The applied voltage for which the total current density vanishes within the MIEC is the open circuit voltage (V_{OC}).

Figure 5.9a shows that when stresses are considered in the formulation and the boundary conditions are prescribed as in Method1 the V_{OC} does not change. However, we note that the voltage at which the ionic current vanishes (V_I) increases by about 0.05V. This implies that the ionic current, for a given applied voltage is higher when stress effects are considered as can be observed in Figure 5.9a. Further we also notice that the total current density remains higher when elasticity is considered, at least until the V_{OC}. The ratio of the total to the ionic current is called the current efficiency (η_I) and is defined as follows,

$$\eta_I = \frac{J_v D_v + J_e D_e}{J_v D_v} \tag{5.76}$$

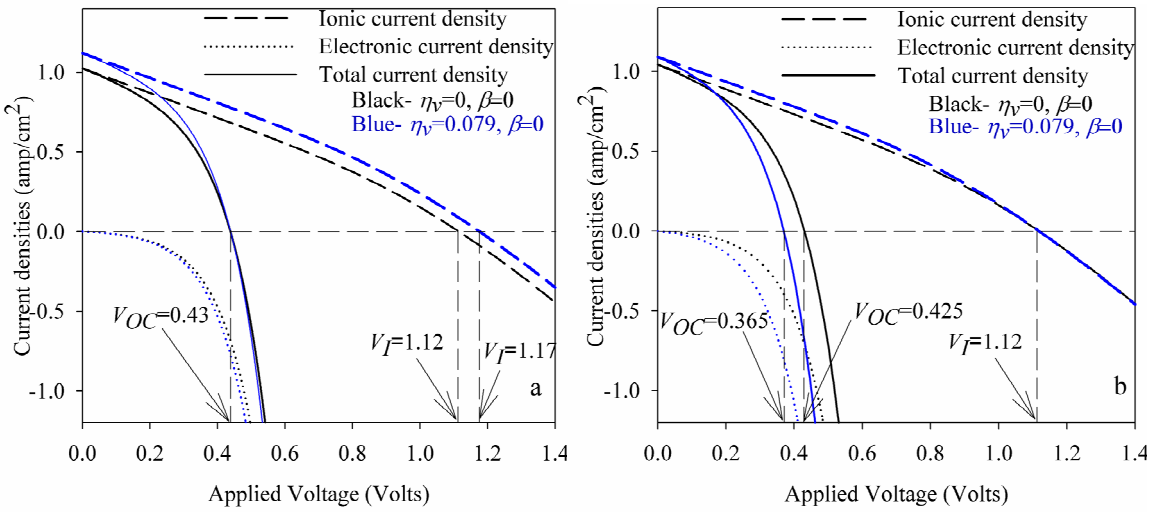

Figure 5.9: Current voltage relationships with boundary conditions a) BC1 b) BC2

The variation of η_I for various applied voltages for both methods of applying the boundary conditions is shown in Figure 5.10. Clearly we see that there is no reduction for the case with BC1 as both the ionic and electronic currents increase more or less proportionally.

Now we turn our attention to Figure 5.9b. In this case, we notice that V_I remains the same whether or not stresses are considered. It can in fact be derived that, when the boundary conditions satisfy LEN condition, the voltage at which the ionic current vanishes is independent of elasticity effects [175]. This can be done by setting J_v=0 in Eq. (5.47) and then using Eq. (5.34) and (5.35). We also notice that the ionic current density, is higher when elasticity effects are considered. The total current density remains larger

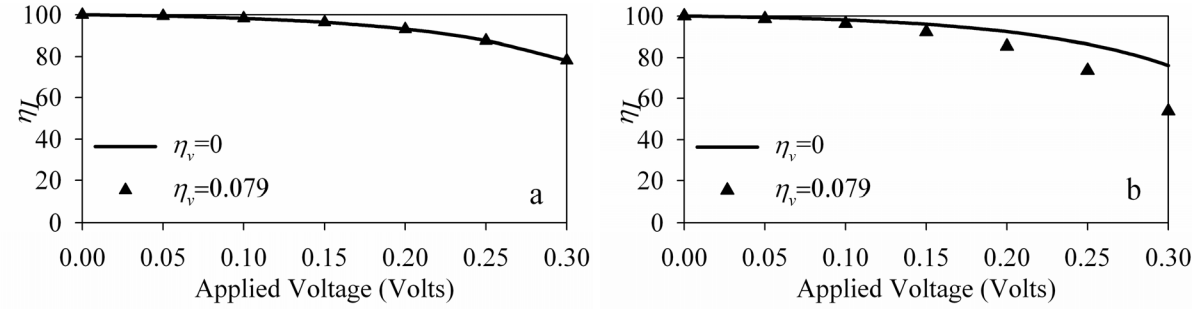

Figure 5.10: Current efficiency for various applied voltages <V_{OC} a) BC1 and b) BC2

for non-zero η_v for low applied voltages, and then begins to decrease. This results in a reduction of the current efficiency when stresses are considered (see Figure 5.10).

The V_{OC}, clearly decreases by about 14% when stresses are considered (Figure 5.9b). Again, for cases when the boundary values satisfy the LEN condition, it can be shown that[175],

$$V_{OC} = \hat{t}_v V_I \tag{5.77}$$

where,

$$\hat{t}_v = 4\left[\frac{-m\kappa_1}{1+2m}\left(\rho_v^R - \rho_v^L\right) - \left(\frac{m-1}{1+2m} + \frac{mQ}{2(1+2m)^2}\right)\ln\left(\frac{\rho_e^R + 4m\rho_v^R}{\rho_e^L + 4m\rho_v^L}\right) - \log\left(\frac{\rho_e^R}{\rho_e^L}\right)\right] \Bigg/ \ln\left(\frac{PO_2^R}{PO_2^L}\right)$$

$$m = -\frac{D_v}{2D_e}$$

Thus a decrease in V_{OC} and η_I is an indication of a poor electrochemical performance of the ionic solid when the effects of elasticity are considered.

In concluding this section we point out that local stresses indeed affect the distribution of the electrostatic potential and the vacancy distributions for lower values of applied voltages. For higher voltages the effects of elasticity are small, as shown in Figure 5.6 and Figure 5.8. This behavior is seen irrespective of how the boundary conditions are applied to solve the MNPP system of equations. However when considering performance measures of the MIEC as a whole, it appears that the manner in which the boundary conditions are specified plays a vital role in determining whether stress effects are important or not. When Method 1 is used neither the current efficiency nor the open circuit voltage are affected. However, on using method 2 we notice that both the current efficiency and the open circuit voltage reduce, showing a decrease in the performance. Thus it might be important to consider the effects of elasticity in electrochemical modeling.

5.4.3 Stress distributions

As mentioned previously the distribution of the electrochemical fields (the vacancy concentration and the electrostatic potential) are identical for both the planar and the tubular configuration. The stress distributions are however quite different.

For the planar case, the stresses are given by, Eq. (5.12) and are plotted in Figure 5.11 for three values of applied voltages. The distributions obtained by specifying the boundary conditions using method 1 (BC1) is used here.

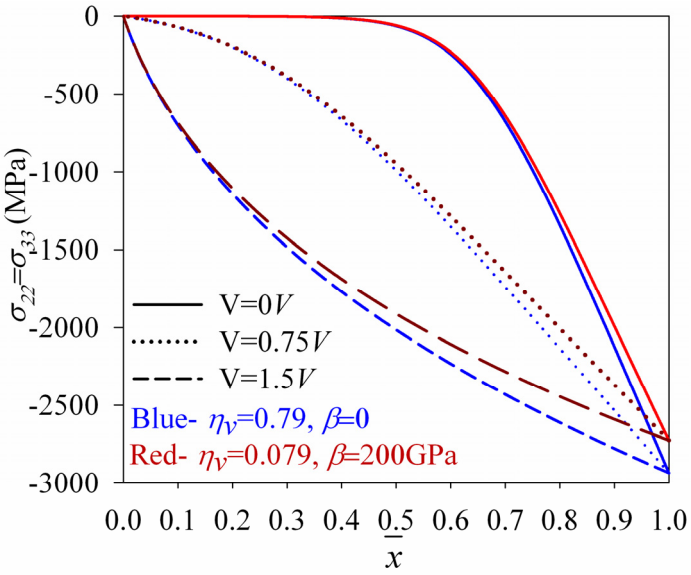

Figure 5.11: Stress distributions for the planar case

It can be seen that at the right end the deviation is maximum and the stresses are highest there. The stresses are close to -2.75GPa which are very high. This is on account of constraining the planar electrolyte as done shown in Figure 5.2. If the constrained are placed such that the electrolyte can bend about the XY plane, then the stresses will not be as high.

For the tubular electrolyte, the expressions for the stresses cannot be obtained without solving the equilibrium equation given by Eq. (5.28). The solution can be easily obtained once the vacancy distribution is calculated; the displacement field solved from Eq. (5.28) is given by,

$$u(x) = C_1 x + \frac{1}{x}\left(C_2 + \frac{1+\nu}{1-\nu}\eta_v h \int_{\hat{a}}^{x} \xi \Delta\rho_v(\xi) d\xi \right) \tag{5.78}$$

where $\Delta\rho_v$ is the vacancy deviation from stoichiometry, and C_1 and C_2 are integration constants to be determined from the boundary conditions. To this end, we calculate the stress components from Eqs. (5.23)-(5.25) as,

$$\sigma_r = K\left(C_1 - \frac{C_2}{x^2}(1-2\nu) \right) - \frac{E^0 \eta_v}{(1-\nu)x^2} \int_{\hat{a}}^{x} \xi \Delta\rho_v(\xi) d\xi \tag{5.79}$$

$$\sigma_\theta = K\left(C_1 + \frac{C_2}{x^2}(1-2\nu) - \eta_v \Delta\rho_v \frac{(1+\nu)(1-2\nu)}{(1-\nu)} \right) + \frac{E^0 \eta_v}{(1-\nu)x^2} \int_{\hat{a}}^{x} \xi \Delta\rho_v(\xi) d\xi \tag{5.80}$$

$$\sigma_z = 2C_1 \nu K - \frac{E^0}{(1-\nu)} \eta_v \Delta\rho_v \tag{5.81}$$

Enforcing zero traction on the inner and the outer ends we obtain

$$C_1 = \frac{E^0 \eta_v \overline{\rho}_v}{(1-\nu)K(\hat{b}^2 - \hat{a}^2)},\ C_2 = \frac{E^0 \eta_v \overline{\rho}_v \hat{a}^2}{(1-\nu)K(\hat{b}^2 - \hat{a}^2)(1-2\nu)} \tag{5.82}$$

where

$$\overline{\rho}_v = \int_{\hat{a}}^{\hat{b}} \xi \Delta\rho_v(\xi) d\xi \tag{5.83}$$

Substituting Eq.(5.82) back to Eqs. (5.79) - (5.81) yields the stresses in terms of the vacancy concentration,

$$\sigma_r = \frac{E^0}{(1-\nu)}\left[\frac{\eta_v \overline{\rho}_v}{(\hat{b}^2 - \hat{a}^2)}\left(1 - \frac{\hat{a}^2}{x^2} \right) - \frac{\eta_v}{x^2} \int_{\hat{a}}^{x} \xi \Delta\rho_v(\xi) d\xi \right] \tag{5.84}$$

$$\sigma_\theta = \frac{E^0}{(1-\nu)}\left[\frac{\eta_v \overline{\rho}_v}{(\hat{b}^2 - \hat{a}^2)}\left(1 + \frac{\hat{a}^2}{x^2} \right) - \eta_v \Delta\rho_v + \frac{\eta_v}{x^2} \int_{\hat{a}}^{x} \xi \Delta\rho_v(\xi) d\xi \right] \tag{5.85}$$

$$\sigma_z = \frac{E^0}{(1-\nu)}\left[\frac{2\nu \eta_v \overline{\rho}_v}{(\hat{b}^2 - \hat{a}^2)} - \eta_v \Delta\rho_v \right] \tag{5.86}$$

Note that the stoichiometry independent Young's modulus has been used here. Further, the non-dimensional limits of integration, are given as, $\hat{a} = a/h, \hat{b} = b/h$.

The radial stresses are negligibly small (in the order of few tens of MPa) and is not shown. The hoop stresses $\sigma_{\theta\theta}$ is however significant and is shown in Figure 5.12. The

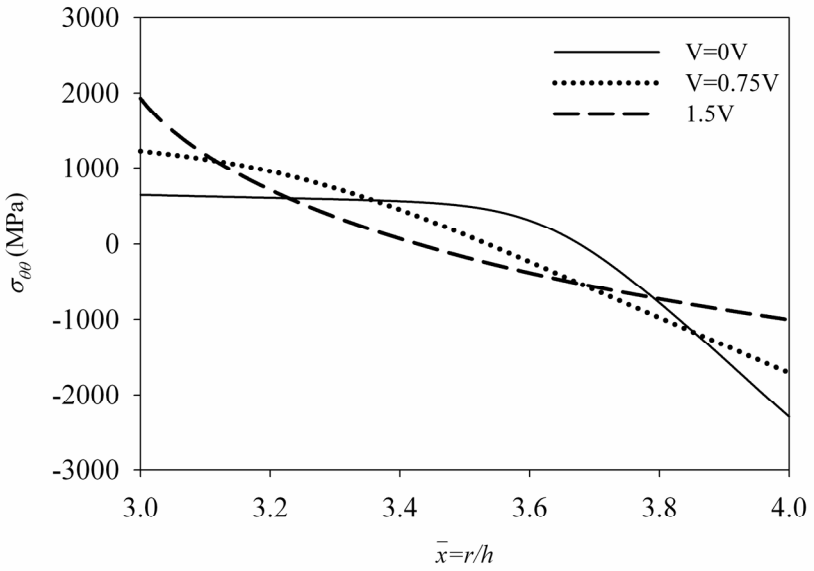

Figure 5.12: Hoop stresses for various values of applied voltages.

calculations were performed for the electrolyte with *a=0.3cm and b=0.4cm* with the boundary conditions once again specified using method I (BC1).

The stresses are still very high and in the order of a few GPa. The interesting aspect of the stress distributions for the tubular electrolyte is that the stresses change from being tensile in the inner radius (cathode) to being completely compressive at the outer radius (anode). This behavior was not seen in the planar case (where stresses where only compressive throughout). High tensile stresses at the inner radius suggest that the radial

cracks which may exist as a result of manufacturing processes may grow and cause the electrolyte to fail during the functioning.

To have a better appreciation for the magnitude of the oxygen vacancy induced stresses, the hoop stress induced in the electrolyte by the thermal mismatch between the cathode, anode and electrolyte of a typical tubular solid oxide fuel cell is shown in Figure 5.13 . For this computation we have considered the electrolyte to be of the same dimensions and material (10GDC) as was done earlier. For the anode, Ni-GDC is considered with 26% porosity having a 50% volume fraction of Ni [176] and with an inner and outer radii of 0.2 and 0.3 cm respectively. The cathode is assumed to be made of Lanthanum manganite with 40% porosity [177] with inner and outer radii of 0.4 and 0.6 cm respectively. Their thermomechanical properties are shown in Table 5.2. A uniform temperature increase of 775^0C is considered to compute the thermal mismatch

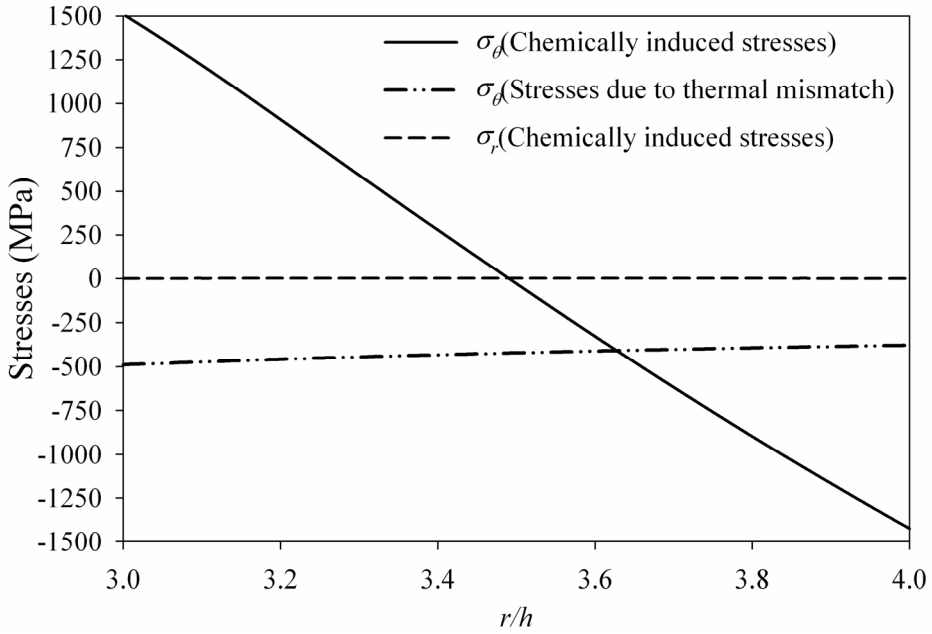

Figure 5.13: Comparing chemically induced and thermally induced stresses

stresses.

Table 5.2: Thermomechanical properties of the electrodes

E_{eff} (Cathode) GPa	$E_{\text{eff(Anode)}}$ GPa	$\nu_{Cathode}$	$\nu_{Cathode}$	$TCE_{Cathode}$ $10^{-6}\,K^{-1}$	TCE_{Anode} $10^{-6}\,K^{-1}$
116	168.35	0.3	0.3	9.36	10

We see from Figure 5.13 that the stresses induced by oxygen vacancy are in the same order or even larger magnitude as those induced by thermal mismatch. Thus it is important that both stresses should be considered in the design and reliability analysis of tubular fuel cells. Unfortunately, only the thermal mismatch stresses are considered in current cell designs. This inevitably leads to significant error and can cause the failure of the electrolyte.

From the results of this section, one can conclude that non-stoichiometric vacancy concentration generates significant mechanical stresses in a tubular cell. In return, these stresses affect adversely the electrochemical field quantities. Therefore, it is important to consider the effects of coupling between the electrochemical and mechanical fields in designing tubular solid oxide fuel cells, when the electrolyte has a high CCE such as GDC.

In the next section we plot the boundary layer solutions of the MNPP system. Once gain the ensuing solutions are the same for both the tubular and the planar cases.

5.5 Boundary layer distribution and charge layers

In the previous section the solutions in the bulk of the ionic solid were discussed. We now discuss the boundary layers which are solutions to the system (5.67) subjected to the boundary conditions given by(5.68). This gives the distribution of vacancy concentration. The potential and the electron concentration distributions can be obtained

from Eqs. (5.57) and (5.58) respectively. As we mentioned earlier, there are no boundary layers close to the left end when BC1 is used, and at both the ends when BC2 is used, as the values of the concentrations at these boundaries satisfy the LEN condition. The distribution of the vacancy concentration, electron concentration and the potential close to the right boundary is shown in Figure 5.14a b and c respectively. The quantities are

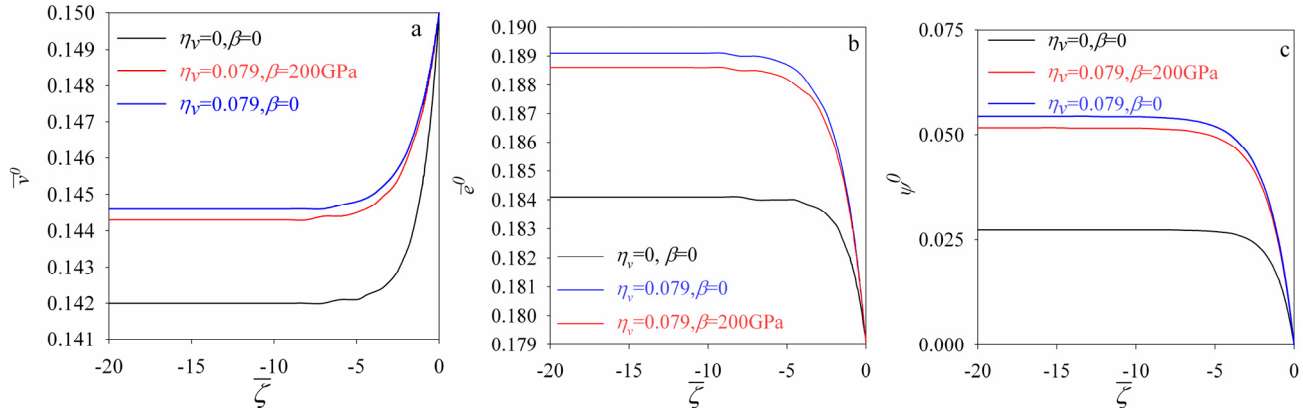

Figure 5.14: Boundary layer solutions of a) Vacancy concentration b) Electron concentrations c) Electrostatic potential

plotted vs. the non-dimensional parameter $\bar{\zeta}$ and the physical dimensions may be obtained from Eq. (5.69). We clearly see that the effects of considering elasticity in the formulations play a role in altering the value of the primary variables in the bulk of the material. As observed before, the effect of considering the variation of elastic modulus with stoichiometry (β) does not affect the results as much as considering chemical expansion does.

To look at the net charge distribution in the boundary layer, the equivalent charge is plotted in Figure 5.15 With a dielectric constant of 35 [157] the characteristic length

χ_D is $8.44\times10^{-11}m$. We see that for the stress independent case $(\eta_v = 0)$, at about $7\chi_D$ ≈0.6 *nm* from the right boundary the equivalent charge is zero and the LEN condition

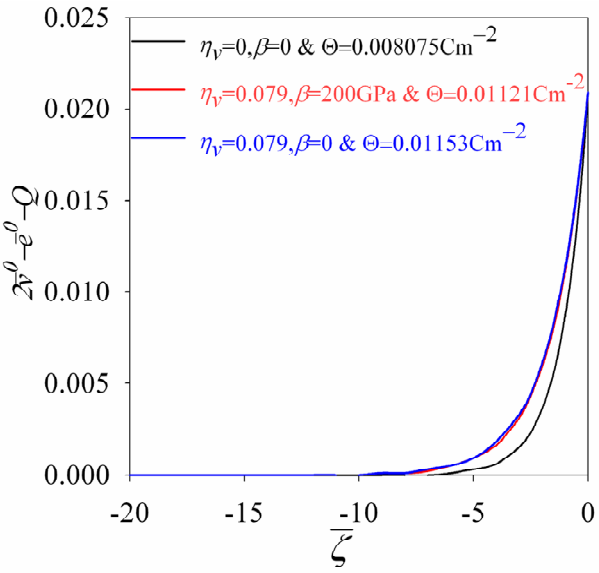

Figure 5.15: Equivalent charge distribution in the boundary layer

begins to be valid. For the case when stress effects are considered ($\eta_v = 0.079$ and $\beta = 0$) this happens at about $10\chi_D$ ≈0.844 *nm* and finally when even the elastic modulus varies with stoichiometry ($\eta_v = 0.079$ and $\beta = 200GPa$) the distance is still about 0.844 *nm*.

We can see from Figure 5.15 that there is a penetration of the charge layer into the material. This is in fact more pronounced if elasticity effects are considered. The surface charge per unit area (Θ) in this region can be obtained by performing the following integral,

$$\Theta = \frac{F\chi_D}{V_m}\int_{-\infty}^{0}\left(2\bar{v}^0 - \bar{e}^0 - Q\right)d\bar{\zeta} \tag{5.87}$$

For the three cases the value of Θ is shown in the figure. Although the absolute magnitude of the surface charge densities is rather small we can see that there is a

substantial enhancement in the charge storing capacity among the three cases. Although the small extent of penetration of the charge layer is not of much consequence for macro sized domains, we can ascertain that at smaller sizes these effects can be significant and can lead to larger charge storing capacities of the ionic solids thus finding useful applications in capacitors.

Recently there have been several efforts to develop new materials with larger charge storage capacities when compared to existing ones[178]. Other studies focus on altering the properties of the material itself, like for example the ionic conductivity [179]. These ideas are almost always addressed in light of grain boundary engineering as a means to alter the material's behavior, either by modifying grain sizes and reducing them to the nano-regime or by altering the chemical behavior of the grain boundaries by doping or sometimes both. The current work, we believe motivates the consideration of elasticity as a means to alter material behavior. We have shown that the self stresses induced in the material due to chemical eigenstrains can alter the electrochemical behavior by affecting the distribution of the field quantities or by affecting the performance itself. It may be possible that the presence of external stimuli in the form of applied loads, the behavior of the material can be improved or deteriorated.

Another area where the ideas presented here can be useful is in considering coherency strains (which are also eigenstrains) occurring between adjacent grains of nano-crystalline materials. An analogous treatment of the problem may be possible. This can be important when the excess energy associated with the interfacial elasticity arising as a result of incoherency, spatially varies and contributes to the non-configurational part

of the chemical potential [180]. This effect will probably be more pronounced for materials with larger values of η_v (CCE) and β values.

5.6 Conclusions

Stress dependent MNPP equations have been introduced and solved using a combination of analytical and numerical methods. 10GDC was considered as the material of interest. The analytical method mainly involved solving the differential system by asymptotic expansion and using the method of matched asymptotes due to the existence of boundary layers. Implicit analytical expressions are obtained for the interior solutions while a differential equation is presented and solved numerically for the boundary layer.

The results of this study indicate mainly two important results with regards to the bulk. Firstly, the distribution of primary variables when stress effects are considered shows a significant difference when compared to the stress independent case. Secondly, the stresses induced are very high that can lead to the failure of the electrolyte. In particular, the tubular case showed tensile hoop stresses at the high partial pressure side which can cause the cracks to grow radially causing the failure of the electrolyte.

With respect to the boundary layer we see that there is a greater penetration of the space charge into the material when stress effects are included. These effects clearly motivate the use of elasticity to enhance the charge storage capacities of ionic solids in addition to other existing methods that use grain boundary engineering.

CHAPTER 6. EFFECT OF INTERACTION ON MECHANICS

6.1 Chapter abstract

In this chapter, the interior 2-D MNPP system is solved using the finite element method through a **U**ser **EL**ement subroutine for the ABAQUS commercial finite element code. 10GDC with flaws (cracks and voids) of various configurations subjected to electrochemical boundary conditions is studied. Two specific crack configurations are considered, namely vertical and horizontal crack in the center of the domain.

The results from the solutions are then post-processed for the stresses and the strain energy release rates. The material force approach is used for determining the strain energy release rate, which is a generalization of the conventional J-integral. These calculations are based on the occurrence of other conservation laws in mechanics in addition to the equilibrium equations.

The main conclusions for the vertical crack configurations suggest that the stress distributions in the vicinity of the crack are very high, leading to possible failure of the electrolyte. Further, the crack always opened for all the values of applied voltages. The variation of the strain energy release rate with applied voltage shows a maxima for an applied voltage of about 0.6V. The strain energy release rates are also plotted as a function of the difference in electrostatic potential rather than the applied voltage. This is done to allow the development of an expression for the strain energy release rate as a function of the applied electrochemical boundary conditions (partial pressure and applied voltage). This expression can be used by designers for specifying limits on safe operating voltages if vertical crack configurations are unavoidable as a result of manufacturing.

For the horizontal crack configurations the results also suggested higher values of stresses at the crack tip. However, in this case, the stresses are tensile only when the applied voltage is less that 1V. For voltages greater than 1V the stresses were compressive, thus closing the crack. The strain energy release rate is plotted against the electrostatic potential at the boundary. These plots reveal that the right crack tip (Crack tip that is closer to the anode or low partial pressure side) is the most sensitive region indicating that the crack would grow into the material towards the anode. Similar to the vertical crack configuration, an expression is obtained for the strain energy release rate as a function of the applied electrochemical boundary conditions for use in design specifications.

6.2 Introduction

In this chapter we discuss the role of interactions between stresses and defect transport on mechanical behavior. In particular, we examine two kinds of flaws that are common in electrolytes, namely cracks and voids. We examine the stress distributions near the crack tip and the void. We also calculate the strain energy release rates for the cracked electrolyte sample that is subjected to electrochemical boundary conditions. Three different crack lengths and two configurations for each length are analyzed. The issue of stress-defect transport interactions will be handled using the framework developed in chapter 3. Unlike the previous chapter, no simplifications with regard to the form of μ_α^{el} will be made. Under such conditions defect transport and elasticity are completely coupled. Analytical solutions as in the previous chapter become impossible due to the coupled nature of the differential equations. To be precise, the defect transport equations and the mechanical equilibrium equations must be solved simultaneously to

obtain a solution for the displacement field, the concentrations of the defects and the electrostatic potential. The main objective of this chapter is to numerically study the effects of such interactions on the strain energy release rates (for the cracks) and stress distributions (for both void and cracks) in a GDC specimen.

6.2.1 Review of pertinent literature

Some of the articles mentioned in this section have probably been cited previously in this thesis, especially in the previous chapter. Here, we cite them again for the sake of completeness and to provide a smooth transition in to the subject. Many studies have been performed to numerically predict the distribution of defects [99, 168, 181, 182] and electrostatic potentials in ionic solids. Separate studies have also been conducted to analyze stresses arising as a result of temperature gradients [19] and non-stoichiometry [94, 171]. In [85] non-stoichiometry generated stresses was considered by neglecting the drift component of diffusion because of which the electrostatic potential does not enter the formulation. As a result, electrical behavior and coupling between electrical and mechanical behavior cannot be studied. All the above mentioned works while providing significant insight into the defect transport or the mechanics problem, neglect coupling, which can be important especially for a material showing large chemical expansion. In addition it is also crucial to realize that some of these works deal with one dimensional defect transport. While this may be appropriate for systems without geometric singularities, it is not for those that have cracks due to the complicated nature of the stresses in the vicinity of the crack tip.

6.2.2 Contribution in this work

To the best of the author's knowledge, no study has been performed to assess the fracture severity under defect transport conditions, nor have studies been performed to analyze the consequences of interactions occurring between defect transport and elasticity on the strain energy release rate. It is well known that ionic solids in solid state devices will have manufacturing flaws or other flaws that arise as a result of stresses generated from thermal mismatch between the electrolyte and the electrodes. Thus it is crucial to understand and also quantify the mechanical response when a solid with a flaw like a crack or a void is subjected to electrochemical loading.

Calculation of strain energy release rates in this work is based on the material force approach and is founded on the concept of forces on elastic singularities first introduced by Eshelby [67]. The problem at hand has three types of elastic singularities [183]. Firstly, point defects or vacancies which cause local eigen expansions, secondly variation of Young's modulus with defect concentration causes material inhomogeneities and thirdly a geometric singularity due to the presence of the crack tip. The advantages of using the material force approach in this problem over the more common J integral [184] or the virtual crack extension approach [185] is that one need not know a-priori the crack growth direction or perform multiple finite element analyses [186] for each crack length in order to determine the strain energy release rates. Also, the presence of material inhomogeneities causes the J integral to be path dependent [187]. In analyses such as those performed in this work, the stress distribution in the vicinity of the crack tip is complicated, and knowledge of the crack growth direction can be difficult to assume. The material force approach requires post processing of the finite element solutions [188-190]

and gives a vectorial representation of forces on the crack tip [191]. The strain energy release rate is then the magnitude of this vector, while the ratio of its components gives the direction of crack growth.

6.3 Differential equations and boundary conditions

6.3.1 Differential equations – Interior equations

The differential equations used in this chapter have been stated in chapter 3, section 3.5.3 and the Eshelby stress dependent chemical potential as in Eq. (3.68) is used. However, owing to the complicated nature of the problem we make several assumptions in solving the coupled set of equations in a two dimensional domain.

1) Firstly as in the previous chapter, we neglect the presence of any interstitials or holes (the point defect) in the system. This has been shown to be a valid approximation in ceria if the partial pressure of oxygen is not more than 1atm [155]. Therefore in Eq. (3.95) and Eq. (3.96) we may set, $\nabla\tilde{\mu}_O = \nabla\tilde{\mu}_h = 0$ and obtain,

$$0 = \frac{-1}{2FRT}\nabla\bullet\left(\rho_v D_v \nabla\tilde{\mu}_v\right) \tag{6.1}$$

$$0 = \frac{-1}{2FRT}\nabla\bullet\left(\rho_e D_e \nabla\tilde{\mu}_e\right) \tag{6.2}$$

On using the expressions for $\tilde{\mu}_v$ and $\tilde{\mu}_e$ from Eq. (3.61)-(3.64), allowing the dilute approximation (λ_α=1) and assuming that only vacancies cause chemical expansion $\left(\eta_e = c^e_{ijkl} = 0\right)$ we obtain the 2-D defect transport equations as,

$$\nabla\bullet\left(\overline{J}_{vx}\vec{i} + \overline{J}_{vy}\vec{j}\right) = -D_v\begin{bmatrix}\dfrac{\partial}{\partial x}\left(\dfrac{\partial\rho_v}{\partial x} + \dfrac{V_m\rho_v}{RT}\dfrac{\partial\tau_v}{\partial x} + \dfrac{2\rho_v F}{RT}\dfrac{\partial\phi}{\partial x}\right) + \\ \dfrac{\partial}{\partial y}\left(\dfrac{\partial\rho_v}{\partial y} + \dfrac{V_m\rho_v}{RT}\dfrac{\partial\tau_v}{\partial y} + \dfrac{2\rho_v F}{RT}\dfrac{\partial\phi}{\partial y}\right)\end{bmatrix} = 0 \tag{6.3}$$

$$\nabla \bullet \left(\overline{J}_{ex} \vec{i} + \overline{J}_{ey} \vec{j} \right) = -D_e \left[\frac{\partial}{\partial x} \left(\frac{\partial \rho_e}{\partial x} - \frac{\rho_e F}{RT} \frac{\partial \phi}{\partial x} \right) + \frac{\partial}{\partial y} \left(\frac{\partial \rho_e}{\partial y} - \frac{\rho_e F}{RT} \frac{\partial \phi}{\partial y} \right) \right] = 0 \qquad (6.4)$$

where

$$\tau_v = \frac{1}{2} c^v_{ijkl} \varepsilon^E_{ij} \varepsilon^E_{kl} + \left(\frac{3}{2} C^0_{ijkl} \varepsilon^E_{ij} \varepsilon^E_{kl} - \sigma_{kk} - \sigma_{km} u_{m,k} \right) \eta_v \qquad (6.5)$$

Note that, for an isotropic material we have,

$$C_{ijkl} = \frac{\nu E(\rho_v) \delta_{ij} \delta_{kl}}{(1+\nu)(1-2\nu)} + \frac{E(\rho_v)}{2(1+\nu)} \left(\delta_{ik} \delta_{jl} + \delta_{il} \delta_{jk} \right) \qquad (6.6)$$

$$c^\alpha_{ijkl} = J^c \left. \frac{\partial C_{ijkl}}{\partial \rho} \right|_{\rho = \rho^0} \qquad (6.7)$$

E is given by Eq. (5.19) and J^c by Eq. (3.26) and Eq. (3.27).

2) We solve the system of equations Eq. (6.3)-(6.4) only in the bulk/interior of the domain. Thus the Poisson's equation (Eq. (3.97)) is replaced by the LEN condition introduced in the previous chapter (see Eq. (5.7)). In other words we have in Eq. (6.3)-(6.4), $\rho_v = V^0$ and $\rho_e = \overline{E}^0 = 2V^0 - Q$ as in section 5.3.3. In this manner the requirement to modify numerical schemes to capture the steep gradients in the field variables near the boundaries is avoided.

6.3.2 Boundary conditions

The mechanical boundary conditions will be clear from the next section. The manner of specifying boundary conditions for concentrations of vacancies and the electrostatic potentials requires some comments.

As mentioned in chapter 5 (BC1), "at the boundaries", for the boundary reactions, continuum quantities are difficult to describe. However, "close to the boundaries", in the differential equations for the boundary layer (Eq. (5.65)) we were able to bring in the

stress dependence due to the simple form of the stress dependent chemical potential. Not only were we able to specify the boundary conditions to solve the interior problem $\left(L_v, L_\phi, R_{v,} R_\phi\right)$, we were also able to solve for the boundary layer distributions (see Eq.(5.67)). In this chapter since we use the complete form of the stress dependent chemical potential (Eq. (6.5)) we are unable to obtain any analytical expression to specify the boundary values to solve for the interior system. To handle this we make the following assumption. Since we are interested in a crack that is located far away from the boundary region, we first assume that close to the boundaries (where we have to specify the concentrations and the potentials) all fields are one dimensional. We also neglect the effect the stresses have on the boundary layer equation (i.e. $\kappa_1 = \kappa_2 = 0$ for Eq. (5.54)). In essence we use the method described in section 5.3.3.2 (Eq.(5.65)) with $\kappa_1 = \kappa_2 = 0$ and its analogue for the right end) in conjunction with BC1 to specify the boundary values for the interior system.

6.4 Geometrical considerations and finite elements

6.4.1 Geometry, flaw configurations & boundary conditions

6.4.1.1 *Electrolyte and crack geometries*

As a first step in an effort to study fully coupled defect transport and mechanics in a MIEC, we consider a stand alone GDC (without the accompanying electrodes) for the study. Under the applied electrochemical boundary conditions the steady state defect distribution, electrostatic potential distribution, stress distributions are governed by Eqs. (6.3), (6.4), **LEN** and the equilibrium equations of mechanics (Eq. (3.14)).Then the strain energy release rates for specific crack configurations can be post processed from the

resulting solutions. We show how variation of crack length and applied external voltage bias affects the values of the strain energy release rates. Then, the stress distributions in the vicinity of the void are studied for various values of applied voltages.

Several configurations of cracks and of the electrolyte itself can be considered. In this work we primarily deal with configurations of the electrolyte used in planar Solid

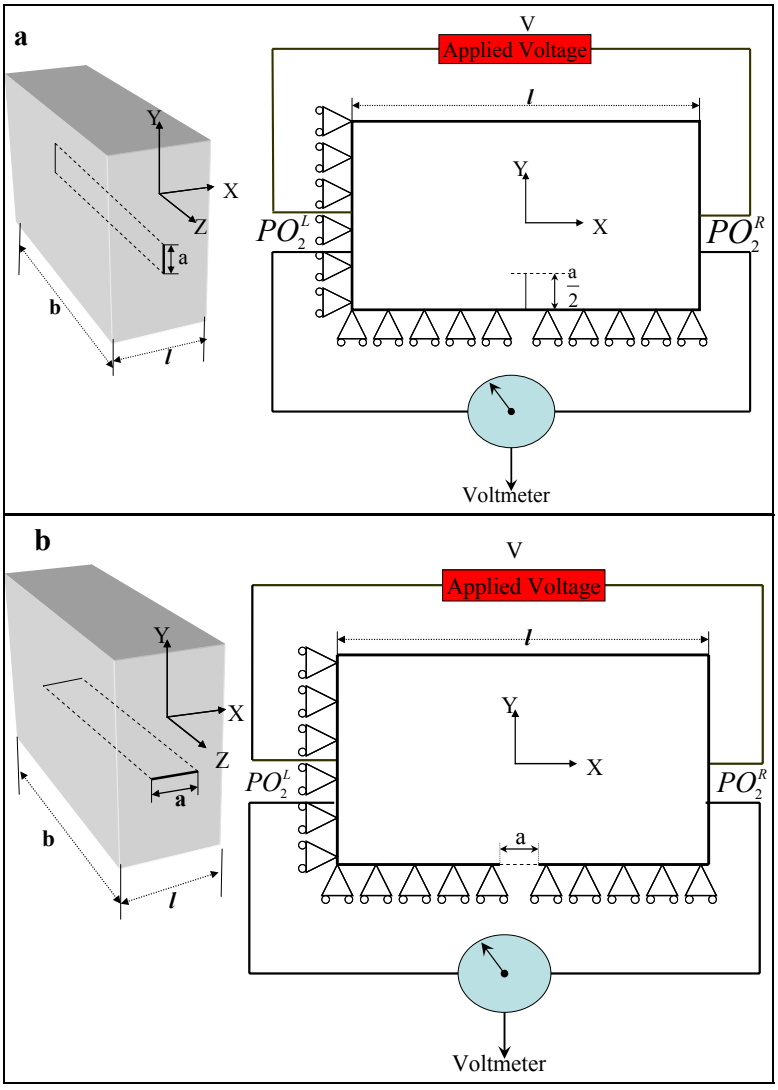

Figure 6.1: Crack configurations and boundary conditions (a) Vertical (b) Horizontal cracks

Oxide Fuel cells (i.e. the planar electrolyte). Cracks in such configurations mainly occur at the interfaces between the electrodes and the electrolyte due to thermal mismatch effects [19] (also see Figure 7.2). Other cracks or voids may be present within the material and may form as a result of manufacturing chemical strains or other loadings. We will study only the latter in this work. The former type of flaws may also be studied by extending the methods developed in this work.

Figure 6.1a and b shows the geometry, boundary conditions and the crack configurations while Figure 6.2 shows the configuration with the void. Further, it is assumed that thickness of the sample (l) is 0.001m, and the cracks and the void penetrate

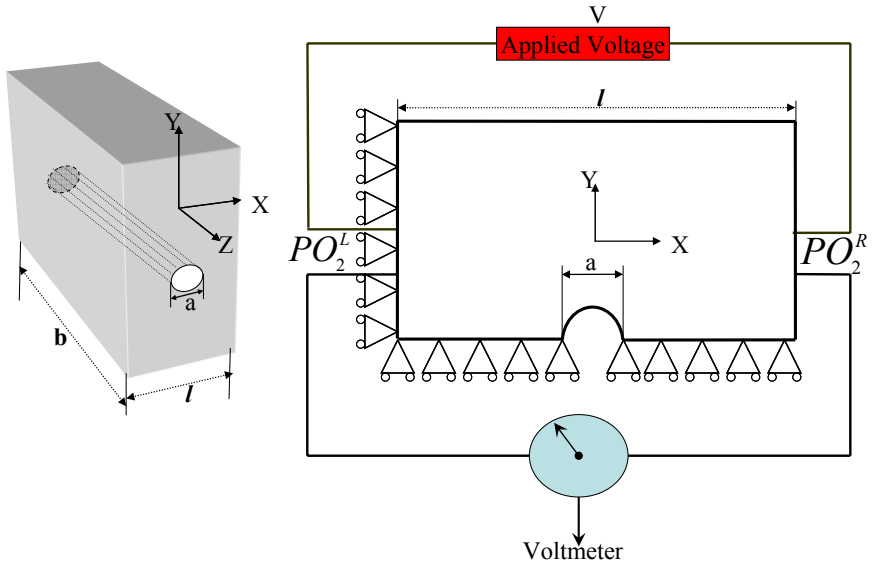

Figure 6.2: Void configuration and boundary conditions

the entire width (b) of the sample. Since in general $b \gg l$, a state of plane strain is assumed $(\varepsilon_{zz} = 0)$ reducing our analysis to the XY plane. We have further taken the height of the sample to be $2l$ (not shown in the figure). Vertical and horizontal cracks of

total lengths $0.4\times10^{-4}\,\text{m}, 0.8\times10^{-4}\,\text{m}$ and $1.0\times10^{-4}\,\text{m}$ are considered to study the effect of varying crack lengths while the applied voltage is varied between -3V and +3V. The void is considered to have a diameter of $1.0\times10^{-4}\,\text{m}$ as shown in Figure 6.2.

6.4.1.2 ***Boundary conditions***

Mechanical

The mechanical boundary conditions are evident from Figure 6.1 and Figure 6.2. The left end is roller-supported so that $u_x = 0$ there. The bottom end is such that $u_y = 0$. The other surfaces including the crack faces and the void surfaces are traction free.

Electrochemical

GDC is subjected to differential partial pressures on either side as shown with, $PO_2^R \ll PO_2^L$ (where the super scripts **L** and **R** denote **L**eft and **R**ight) and external voltage is applied. The concentrations at the boundaries are specified using BC1 (section 5.3.2.1) in conjunction with the arguments presented in section 6.3.2. The other two sides, the crack faces and the void surface are considered, so that the component of the currents normal to these faces is zero (insulating), allowing us to use symmetry as shown in the figures.

6.4.2 Finite element considerations

The governing differential equations are solved using the finite element method [192] through an isoparametric user element subroutine for the ABAQUS commercial finite element code [193]. ABAQUS requires the element's contribution to the Jacobian of the resulting algebraic equations resulting from the finite element discretization. Although quadratic and linear, quadrilateral and triangular element libraries are

developed, we have used quadratic, quadrilateral elements for all the simulations to achieve higher accuracy. The mathematical details of the finite element model and the Jacobian are shown in APPENDIX E. A sample input file that can be used with the user element is provided in APPENDIX F.

The vertical cracks are modeled as a seam so that different nodes with the same coordinates are created on the crack faces (see Figure 6.3). By this method the continuity of the primary variables is not enforced across the crack faces, and the crack opening can be modeled. However, if the cracks close, contact between the disjointed crack faces must be enforced. In this analysis, we have mostly considered cases where the deformation results in opening the vertical crack, and no contact modeling is needed.

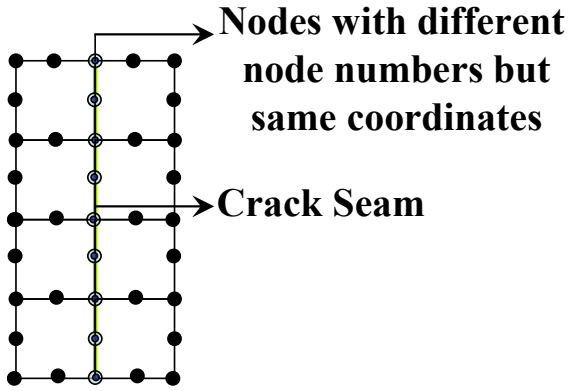

Figure 6.3: Vertical crack modeled as a seam

The modeling of the horizontal crack is straightforward and simply involves specifying a traction free surface as mentioned in section 6.4.1.2. As will be mentioned later, we found that there were values of applied voltages for which the horizontal cracks closed. Since we have not modeled the entire geometry (but used symmetry), the contact that might occur between the two faces of the horizontal crack is not captured. Hence

after the analysis, the reports of the strain energy release rates are given only for those values of applied voltages for which the cracks remained open.

The primary nodal unknowns in the problem are, the concentration of vacancies (V^0), the electrostatic potentials ϕ and the two displacements fields u_x and u_y. Once the finite element equations are solved, the obtained primary unknowns are post-processed for the secondary variables (stresses, strain, currents, material forces etc.) using MATLAB. At this point we note that we are aware of crack tip singular elements that are used to capture the $1/\sqrt{r}$ singularity existing at the crack tip exactly [194, 195]. However, we found on using these elements that the analyses had difficulty in converging to a solution, which we attribute the high degree of non-linearity due to the coupling in the problem. To this end we have used a fine mesh in the vicinity of the crack tip to capture the gradients in the solutions as accurately as possible.

6.4.3 One way vs. two way interactions

As indicated, the purpose of this chapter is to study the effect of stress defect transport interactions on the stress distributions and the strain energy release rate of cracked ionic solids that are subjected to electrochemical driving forces. Two methods of performing the coupled analysis must be detailed. In one method, we may first solve the defect transport equations, completely independent of elasticity (i.e. independent of the equilibrium equations of mechanics). The resulting defect distributions (and hence the resulting eigenstrain distributions) can be used as an input to the constitutive equations of linear elasticity. The mechanical equilibrium equations can then be solved to predict the ensuing mechanical fields and responses. Clearly in this case, the differential equations governing defect transport are solved independently of the mechanics equations and may

be said to represent a "one way" coupling. This is the solution methodology that is currently being followed to perform stress analysis of ionic solids while still considering the effect of chemical strains. However, we have seen that elasticity can have a contribution to the non-configurational part of the chemical potential, and in this case both the governing differential equations (defect transport and mechanics) are fully coupled and will be referred to as the "two way " coupling. In this chapter the effect of performing a "one way" interaction is studied and the results are compared to those from a "two way" interaction.

6.5 Material forces and strain energy release rates

6.5.1 The concept of material forces

A detailed introduction to material forces is beyond the scope of our current discussion. For this, the reader is referred to the fundamental works of Eshelby [67, 89]. Here, we give a very brief description of the material forces approach and the use of the finite element method to calculate these forces. We begin by stating that several conservation laws appear in mechanics [183]. Conservation laws are divergence expressions occurring naturally in an associated physical problem. In mechanics, under static deformation one encounters the most common conservation law, which is the vanishing of the divergence of the second order stress tensor or (equilibrium) when there are no body forces acting. If body forces are present, then the divergence equals the negative of the body force [88] (also see Eq. (3.18)).

$$\nabla \bullet \boldsymbol{\sigma}^{0} + \mathbf{f} = \mathbf{0} \tag{6.8}$$

In the above expression, $\boldsymbol{\sigma}^{0}$ is the first Piola-Kirchhoff stress tensor, while $\mathbf{f}$ is the body force. The choice of the stress tensor (Cauchy or Piola Kirchhoff) depends on the

problem at hand. Here, we use this choice for convenience, as the expressions are more condensed. Other conservation laws also emerge from elastostatics but are however obtained only if (6.8) is satisfied. (This is so because Eq. (6.8) is also the Euler-Lagrange equation of the system, see, [183] for details).

The relevant conservation law in our case is the vanishing of the divergence of the material stress or Eshelby stress tensor $\boldsymbol{\Sigma}$ introduced in chapter 3.

$$\nabla \bullet \Sigma = 0 \tag{6.9}$$

However, similar to $\boldsymbol{\sigma}^0$, Eq. (6.9) holds only as long as there are no material body forces. Material body forces are caused by singularities such as inclusion, defects, cracks, material inhomogeneities etc. Hence, when such singularities are present, we have,

$$\nabla \bullet \Sigma = \mathbf{M} \tag{6.10}$$

where in Eq. (6.10), $\mathbf{M}$ is the material body force vector.

The Eshelby stress $\boldsymbol{\Sigma}$ is a function of $\boldsymbol{\sigma}^0$ and the deformation gradient $\mathbf{F}$ through the relation,

$$\boldsymbol{\Sigma} = W\mathbf{I} - \mathbf{F}^T\boldsymbol{\sigma}^0 \tag{6.11}$$

where W is the strain energy density per unit volume of the reference configuration, and $\mathbf{I}$ the identity tensor. Note that the Eshelby stress as introduced in chapter 3, (Eq. (3.61)) has a slightly different form owing to the approximations involved in Eq. (3.33) i.e. expansion of the elastic strain energy about stoichiometric concentrations and neglecting higher order terms in the concentrations. Thus the derived Eshelby stress in chapter 3 may be viewed as that for dilute defect concentration. If we do not make this approximation then, the form attained for Eshelby stress is given by Eq. (6.11). Eq. (6.9) or Eq. (6.10) may be viewed as additional conditions that the deformation and stresses

need to satisfy if Eq. (6.8) holds. Therefore, in a typical mechanics problem, once we have solved for the stress field by solving equation Eq. (6.8), we may check if Eq. (6.9) is satisfied. If it does, then we may conclude that no singularities exist in the material. Otherwise, the resulting vector **M** is the body force caused due to the singularity, and integrating the components of **M** around a singularity (a crack tip for example) gives the actual material force.

For infinitesimal strain theory, the difference between the reference and the current configuration is not important, and we may approximate $\boldsymbol{\sigma}^0$ as the Cauchy's stress $\boldsymbol{\sigma}$. Thus we may write, when no body forces are acting, Eq.(6.8) and Eq.(6.11) as

$$\nabla \bullet \boldsymbol{\sigma} = \mathbf{0} \tag{6.12}$$

$$\boldsymbol{\Sigma} = \mathbf{W}\mathbf{I} - \left(\mathbf{I} + \nabla \mathbf{u}\right)^T \boldsymbol{\sigma} \tag{6.13}$$

where **u** is the displacement field. Using Eq. (6.12) and Eq. (6.13) in Eq. (6.10) we have,

$$\nabla \bullet \left(\mathbf{W}\mathbf{I} - \nabla \mathbf{u}^T \boldsymbol{\sigma}\right) = \mathbf{M} \tag{6.14}$$

To see how **M** can be related to the Rice's J integral or the strain energy release rate, see APPENDIX G. In general the strain energy release rate is given as,

$$G = \frac{\left|\mathbf{F}^{\mathbf{M}}\right|}{b} \tag{6.15}$$

where,

$$F_i^M = \int_V M_i dV = \int_V \Sigma_{ij,j} dV \tag{6.16}$$

and the direction of crack growth will be opposite to that pointed by $\mathbf{F}^{\mathbf{M}}$ (see [187]).

6.5.2 Finite elements and material forces

For 2-D, Eq.(6.16) reduces to,

$$F_i^M = b\int_A \Sigma_{ij,j}\, dA \tag{6.17}$$

The integral on the RHS of Eq. (6.17) may be easily computed using the common gauss quadrature procedure often used in the finite element method. Basically, the integral is computed over each finite element to obtain the nodal material forces. This is then assembled to obtain the global material force vector at all the nodes. This process is represented as [186],

$$F_i^{M,NODES} = \bigcup_{e=1}^{N_e} \sum_{n=1}^{N_n} \sum_i \sum_j b\Sigma_{ij}\psi_{,j} w_i w_j \det(\bar{\mathrm{J}}) \tag{6.18}$$

where,

$\bigcup$ denotes the assembly procedure

N_n is the number of nodes per element

N_e is the total number of elements

w_i and w_j are the Gaussian weights

$\psi_{,j}$ is the derivative of the shape function evaluated at the Gauss points of the finite element

$\det(\bar{\mathrm{J}})$ is the determinant of the Jacobian that transforms the integral from the master to the actual finite element.

Thus, once $\mathbf{F}^M$ is calculated at the nodes, G is calculated at the crack tip from Eq. (6.15).

At this point a few comments related to the materials force approach and finite elements is in order. As noted earlier in the introduction, the problem has several kinds of singularities. Hence, whether or not a crack is present, material forces will always exist in the problem under consideration. We will use this method only in light of the crack tip in

the domain. Forces due to other singularities are calculated but do not have a physical interpretation like the crack tip forces. All they indicate is that the material is inhomogeneous and that point defects are present.

Spurious material forces are also known to occur when the finite element method (FEM) is used to solve the differential equations [190]. This is because FEM only approximates the solution. This fact has been used for structural optimization and adaptive remeshing procedures [188, 196]. In this work, no adaptive mesh refinement is performed, as it is impossible to separate the spurious material forces from the actual ones due to the various singularities.

We hence conclude this section by reiterating that the material force analysis is only a post processing routine and can be easily performed after the direct problem is solved.

6.6 Results and discussion- Crack configurations

The field equations introduced in section 6.3 subjected to boundary conditions as described in section 6.4.1.2 were solved using the FEM. The material properties used are similar to those in Table 5.1. First we discuss the distribution of the various field quantities like defect concentration and stresses for three values of applied voltages (3,-1, +3V) to describe general features of the problem. The electrostatic distributions are not shown, as they do not directly affect the mechanical behavior. Moreover, the behavior of the strain energy release rate curves for various applied voltages is more intuitive by examining the distribution of the vacancies for the applied voltages. For the distribution of the field quantities we show the results only for the crack length $1.0\times10^{-4}m$. Other

crack lengths showed a qualitatively similar behavior. Then the strain energy release rate values for the various cracked configurations for all the applied voltages are shown.

6.6.1 Vacancy concentration & crack tip stresses

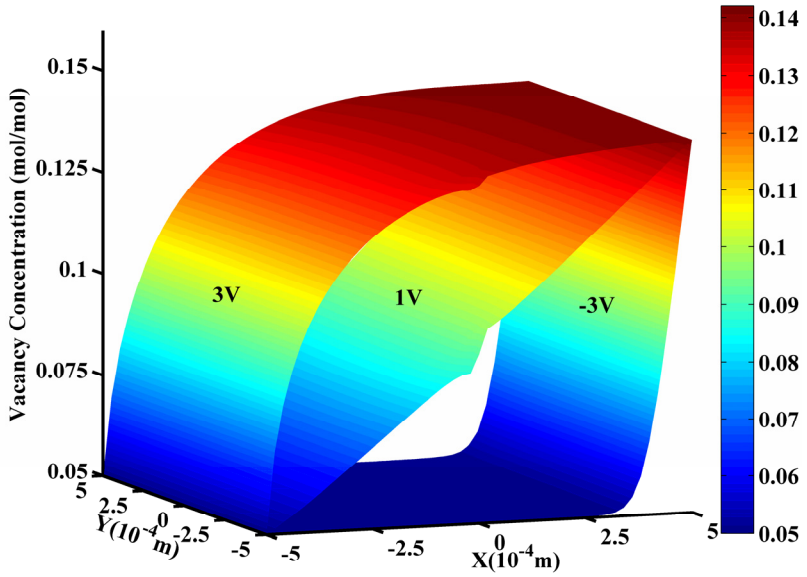

Figure 6.4: Distribution of vacancy concentration for three values of applied voltages

6.6.1.1 *Vertical crack configuration*

Figure 6.4 shows the distribution of vacancies for three values of the applied voltages (+3, -1 and -3V) for the vertical crack (Figure 6.1a) configuration. This figure is to give an idea as to how the distribution actually looks. First, one can observe that the concentration distribution varies monotonically with applied voltage just like the 1D case analyzed in the previous chapter. For large negative voltages, the distribution in most of the domain is uniform, and it attains higher gradients only in the vicinity of the low partial pressure side (Anode side for a fuel cell). For large positive voltages the exact opposite seems to be happening, where larger gradients are found in the higher partial

pressure side (Cathode in a fuel cell). For intermediate voltages, the distributions are in between the two extremes.

A discontinuity in vacancy concentration appears due to zero current conditions at the crack faces. This manifests as the disturbances in the contour plot (Figure 6.5) very close to the crack tips as shown. Far away from the cracks, the vacancy concentrations reaches the far field values and can be analyzed more or less using a 1-D approximation. All three plots show the same region ($-1\times10^{-5} < X < 1\times10^{-5}$ m and $-5\times10^{-4} < Y < -1\times10^{-4}$ m) very close to the crack.

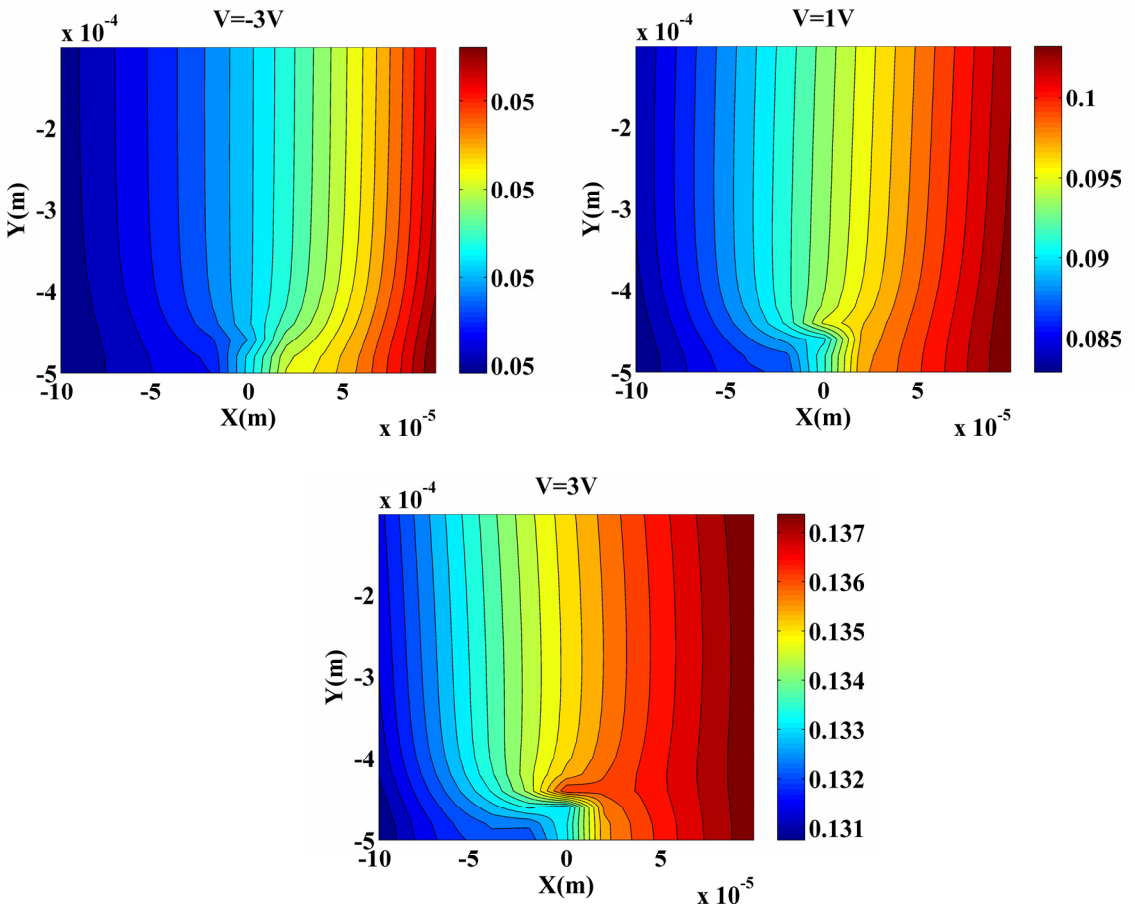

Figure 6.5: Filled contour plots of vacancy concentration near the crack

Figure 6.6 shows the stress distributions. We observed that the magnitudes of the stresses were high when the applied voltage was 1V. For other voltages the stresses showed qualitatively a similar behavior, although the magnitudes of the stresses were smaller. For this reason only the stress distributions for an applied voltage of 1V are

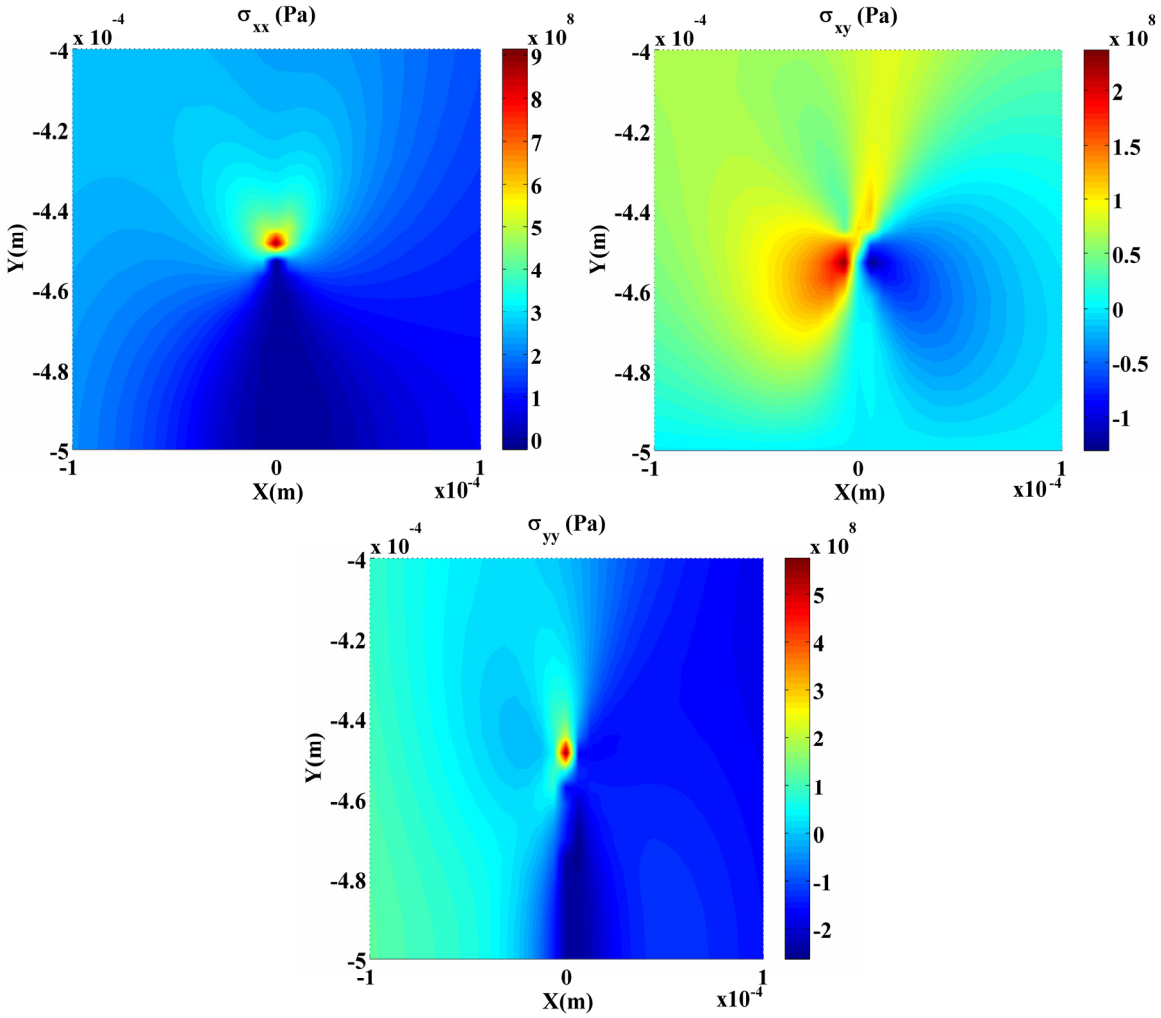

Figure 6.6: Stress distributions near the crack when applied voltage is 1V

shown. We can see that the most important component is the σ_{xx} component. It has a value as high as 900MPa in the vicinity of the crack tip. The other components, although

of a smaller magnitude in comparison to σ_{xx} are still quite high (especially σ_{yy}). Further, for the vertical crack configuration, the stress component σ_{xx} was always positive for all the values of the applied voltages. This meant that the cracks always opened in this case. This was not true for the horizontal crack configuration, as will be shown in the next section.

6.6.1.2 ***Horizontal crack configuration***

The vacancy distribution profiles for the three values of applied voltages are shown in Figure 6.7. The profiles are very similar to the vertical crack configuration

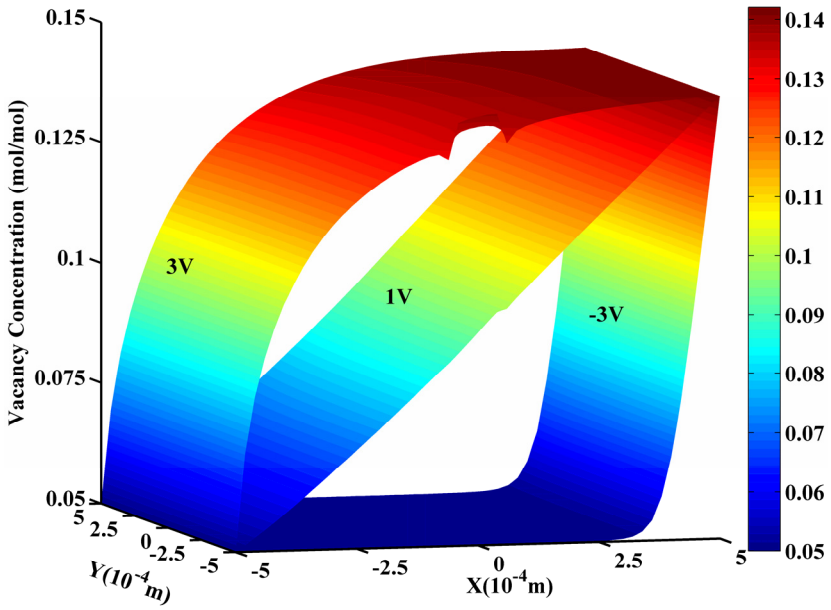

Figure 6.7: Vacancy distribution for three values of applied voltages

except near the crack. Due to the zero current conditions in the face of the crack, there are discontinuities in the vacancy profile. The disturbances that manifest as a result are shown in Figure 6.8.

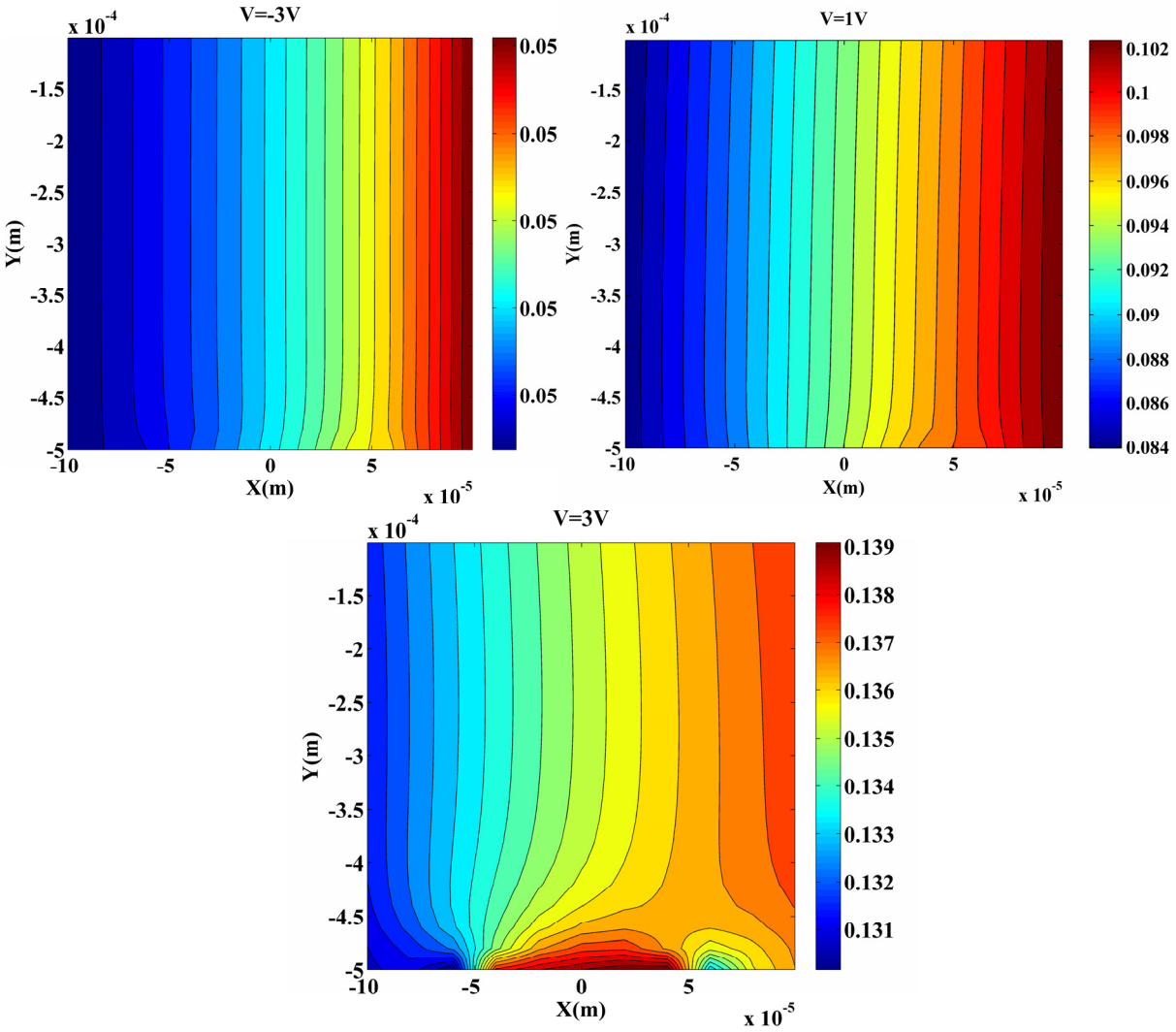

Figure 6.8: Filled contour plots of vacancy concentration near the crack

Clearly we see that the disturbance in the contours is not severe for the -3V and 1V cases. However, it is quite high for the 3V case. Although a direct analysis for this behavior is difficult owing to the coupled nature of the problem, it could be said that at high voltages the deviations in the vacancy concentrations are large and that creates higher stresses which in turn alter the vacancy concentrations even more significantly near the crack tips.

Further, for this crack configuration, the crack remained open when the applied voltages were between -3 and 1V. For higher values of applied voltages the crack closed. This can be seen from the distributions of σ_{yy} in Figure 6.9 near the crack tips for the three values of the applied voltages. Clearly when the applied voltage is -3V, the stresses

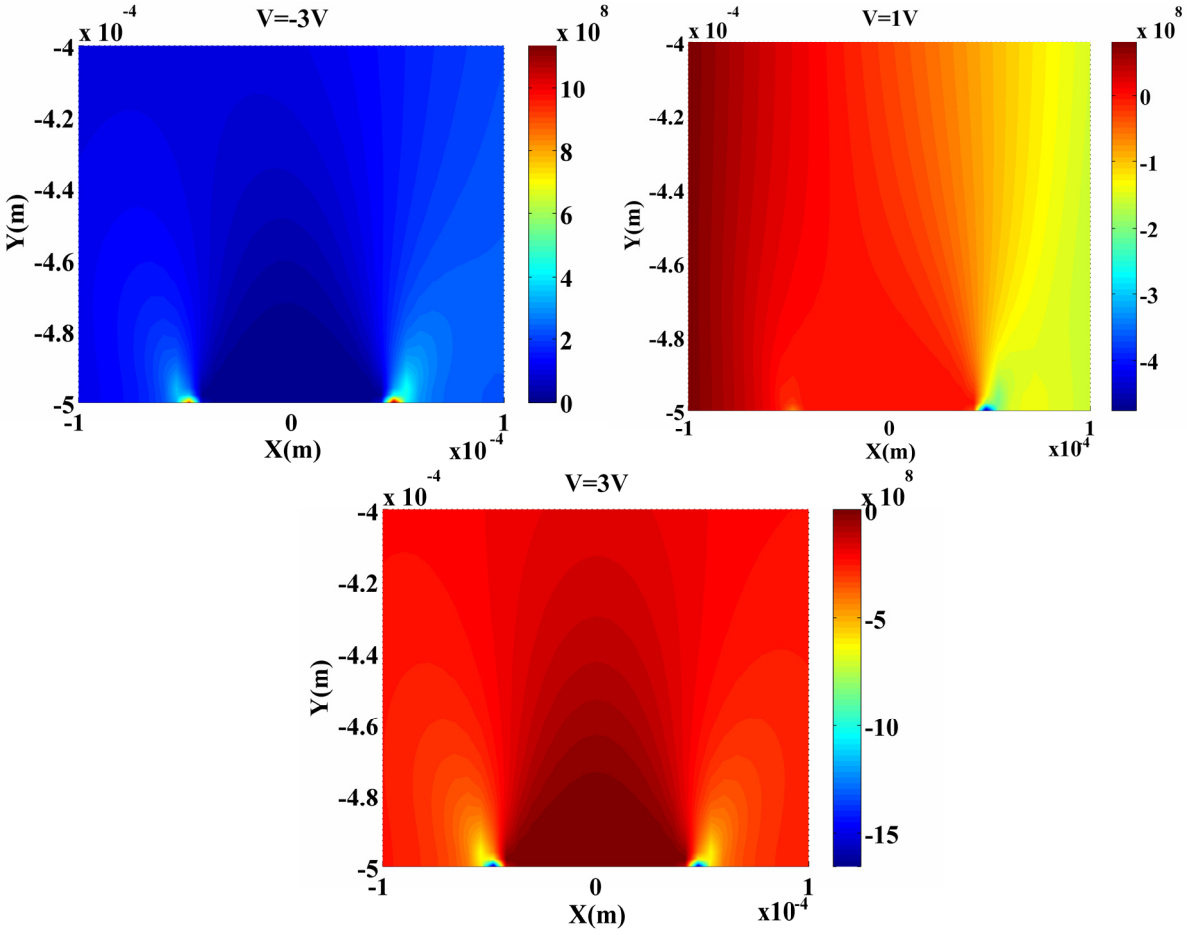

Figure 6.9: Distribution of σ_{yy} (Pa) for three values of applied voltages

are close to 1GPa, especially near the right crack tip. When the voltage is 1V, the stresses are compressive in the right tip, while negligibly small in the left tip. For 3V, the stresses are compressive on both the crack tips. These results basically point out that if a solid electrolyte has a central horizontal crack as considered, then under applied

electrochemical conditions, the crack is more likely to grow towards the anode or the low partial pressure side. This will also be clear when we examine the strain energy release rate results for the horizontal crack configuration.

6.6.2 Strain energy release rates (*G*)

The material forces at the crack tips and the strain energy release rates were calculated for each of the crack lengths and the various applied voltages, using the method described in section 6.5.2. For both the crack configurations we show the G vs. ϕ^L (see Eq. (5.35)) instead of the more intuitive G vs. V (applied voltage) curve. Note that ϕ^L is the dimensional (physical) electrostatic potential on the left end and $\phi^R = 0$. Once the function is fit in this manner, we may use the relation given by Eq. (5.35) along with the mass action law (Eq. (5.30)) to arrive at an expression for G completely in terms of the applied boundary conditions. This is done with the same idea as is usually done in traditional fracture mechanics where, for example, G is related to remote loading and geometry. The expression so developed can then be used directly by designers while building fuel cell components in order to specify safe working conditions for known crack geometries. It can also be used to assess mechanical reliability with the knowledge of just the crack length, location and the boundary conditions (applied partial pressure and external voltage).

In the next sub-section the strain energy release rate values are plotted and the results are discussed. As mentioned earlier (see section 6.4.3), we compare the results obtained using a two way interaction with that obtained from performing just a one way analysis. The error is plotted against various values of applied voltages for both crack configurations.

6.6.3 Vertical crack

The G vs. ϕ^L curve for the vertical crack configuration is shown in Figure 6.10. In the figure the dots indicate the results obtained using the two way interaction, while the triangles from considering only one way interactions. The lines represent the fitted curve (to two way interaction). We clearly see that the strain energy release rate curve shows a

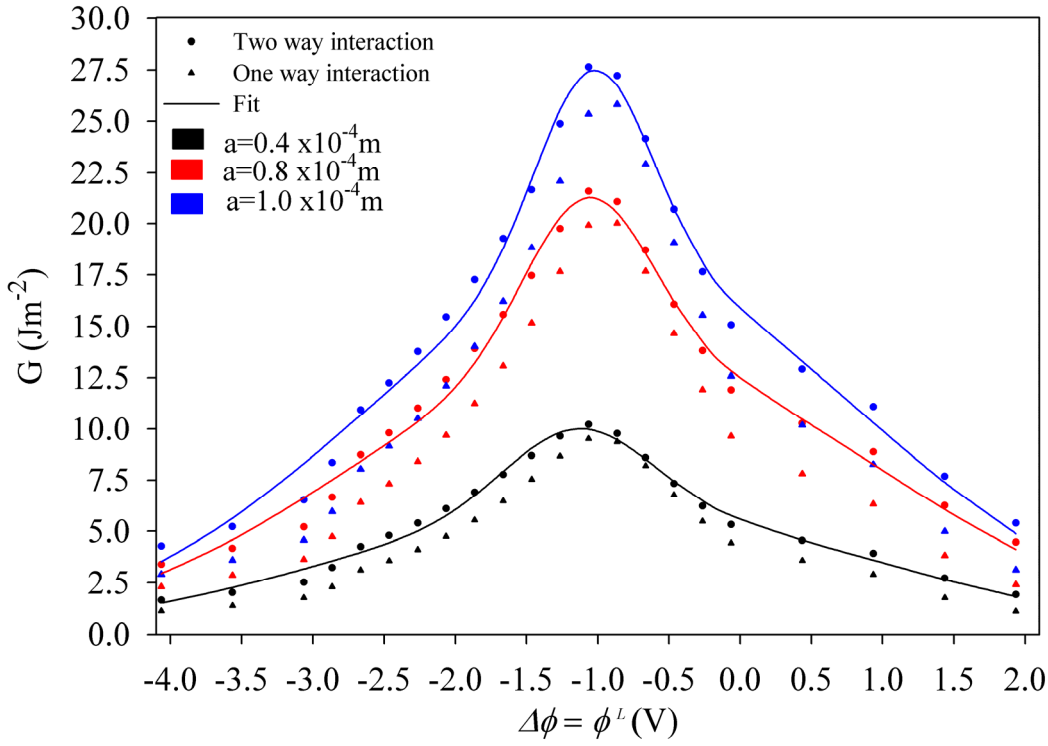

Figure 6.10: Strain energy release rate curves (Vertical crack configuration)

maxima, at approximately $\phi^L \approx -1.06V$ (which corresponds to an applied voltage of 0.6V) for all the three crack lengths. For large negative or positive values of applied voltages, G seems to decrease to zero. This behavior may be explained on the basis of the observed nature of the variation of the distribution of the vacancy concentrations with applied voltages. We have seen that, for large positive or negative voltages the vacancy

concentration attains higher gradients only close to either end (cathode/anode) and is more or less uniform in the central domain where the crack is present. Due to this, the strains and hence stress magnitudes are small near the crack tip for large positive/negative voltages. For certain voltages the distribution is such that the gradients are large (see V=1V case) resulting in large stresses. This is the reason for the bell shaped curve that is observed. We also observe that for a given applied chemical boundary condition, G increases with crack length.

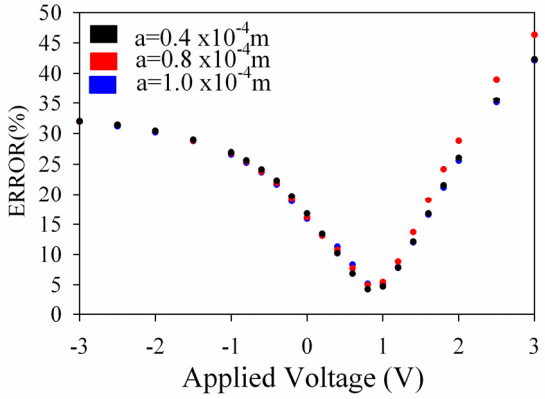

Figure 6.11: Error incurred in performing a one way analysis

The results obtained from one way interactions (the triangles) consistently lie below the results which are obtained using the two way interaction. The error incurred in calculating G using only; a one way interaction for the three crack lengths is plotted in Figure 6.11. The error is as high as 45% and as low as 5% in the voltage range studied. Clearly, this indicates that, the two way interaction, (in other words the stress-defect transport interactions) has a significant effect on G. It also means that the design of the ionic solid with a vertical crack configuration subjected to electrochemical loading as in this study would be safer if the design analysis was performed using the two way coupled theory rather than the routinely performed one way analysis.

Figure 6.12 shows the material force at the crack tips for the applied voltage of 0.6V (note that the arrows have been exaggerated for clarity). We observe that the crack does not necessarily grow along the Y axis ($\theta=90^o$), but has a component in the X direction, although small. The variation of the angle θ for different applied voltages and crack lengths is plotted below in Figure 6.13. It can be seen that the angle of crack growth can be as high as 115^o for the larger crack at 0.6V. However for most of the cases we see that it is close to 90^o.

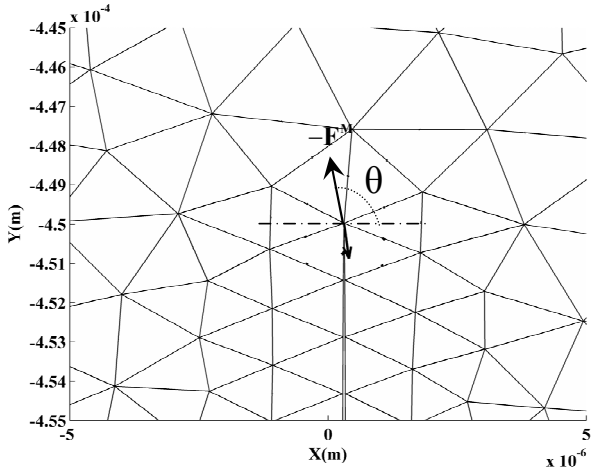

Figure 6.12: Crack tip material force and possible direction of crack growth

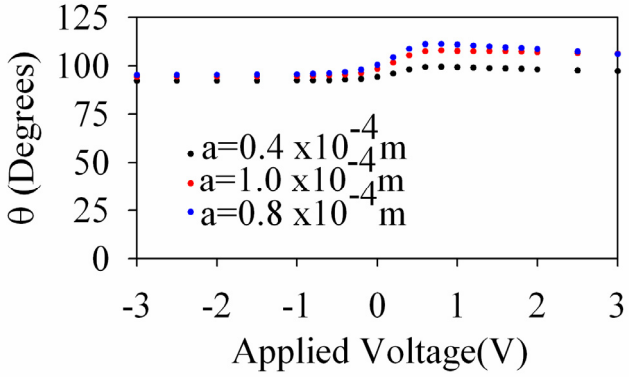

Figure 6.13: Variation of direction of crack growth with applied voltage

As mentioned earlier in this section, a mathematical relationship was obtained for the dependence of strain energy release rate on electrochemical boundary conditions. This was done by first fitting the obtained values of G (for the two way interaction) vs. ϕ^L, to the Gaussian type function (Eq. (6.19)),

$$G = a_1 \exp\left(-\left(\frac{\phi^L - b_1}{c_1}\right)^2\right) + a_2 \exp\left(-\left(\frac{\phi^L - b_2}{c_2}\right)^2\right) \tag{6.19}$$

where, a_1, b_1, c_1, a_2, b_2, c_2 are constants depending on the crack lengths and are shown in Table 6.1.

Table 6.1 Fitting parameters for the expression (6.19)

a (10^{-4}m)	a_1	a_2	b_1	b_2	c_1	c_2
0.4	4.073	5.971	-1.138	-0.9523	0.7121	2.654
0.8	7.77	13.58	-1.069	-0.8804	0.6175	2.577
1	9.917	17.63	-1.028	-0.8956	0.5627	2.499

Expression (6.19) may easily be modified to so as to obtain G completely in terms of the boundary conditions by first using Eq. (5.35) to substitute for ϕ^L. Then using mass action law (Eq. (5.30) or even (5.33) we obtain a formula for G that contains the partial pressure, vacancy concentrations at the boundaries and the applied voltage. When the vacancy concentration can in general be expressed as a function of the partial pressure of oxygen, then the expression for G can be given completely in terms of just the partial pressure and the applied voltage.

6.6.4 Horizontal crack

The G vs. ϕ^L curve for horizontal crack configurations is plotted in Figure 6.14. We have shown earlier that the cracks closed when the applied voltage is greater than 1V

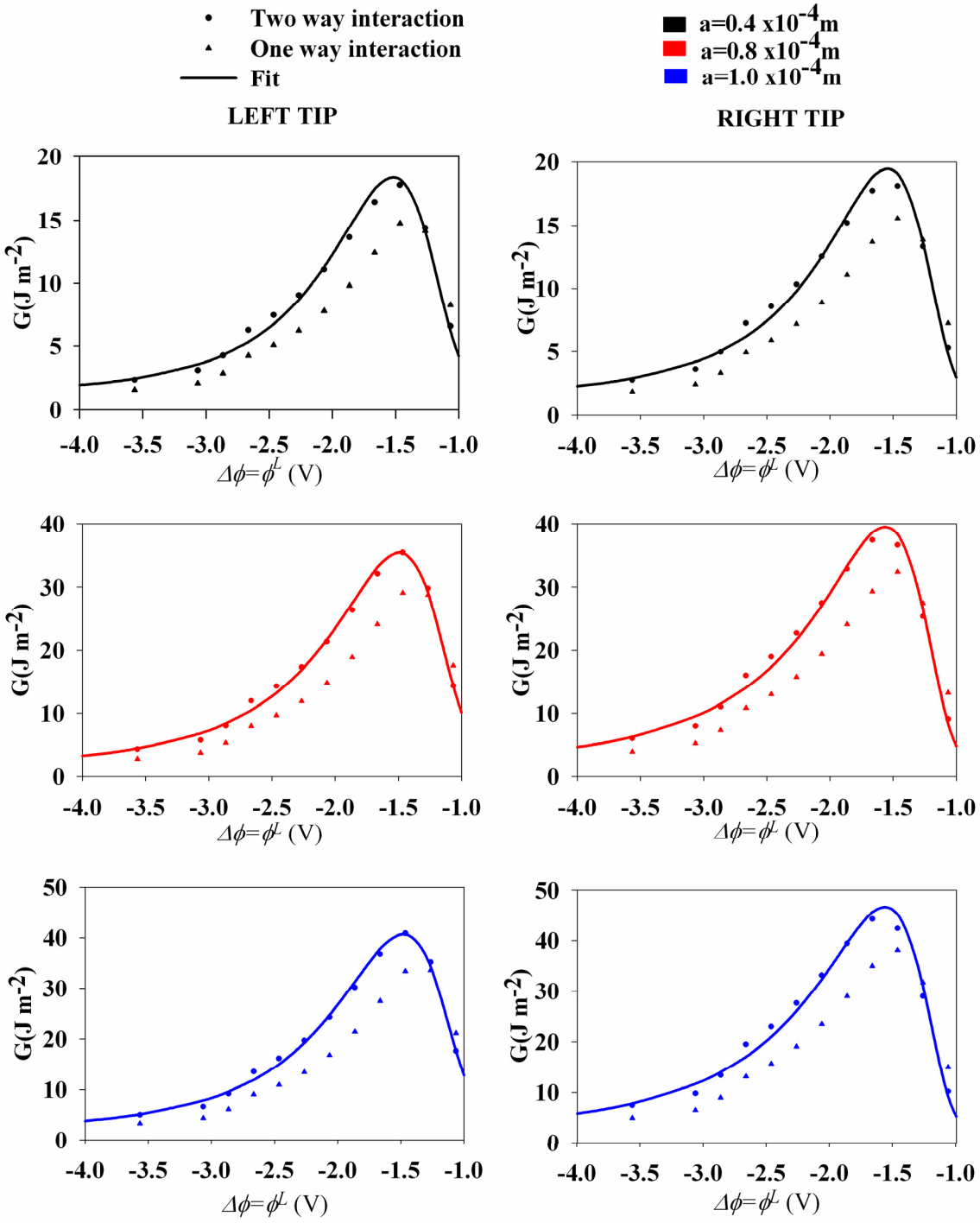

Figure 6.14: G vs. ϕ^L curves for horizontal crack configuration at both tips

(See section 6.6.1.2); therefore we plot the curves only for values of ϕ^L which corresponds to an applied voltage less than 1V. The plots are shown for both the left and the right crack tips in Figure 6.14 . In all cases G exhibits single maxima at around 0.2V and approaches zero for values less than 0.2V. As the crack lengths are increased the values of G also increase for a given voltage. We also notice that the differences in the G values between the left and right crack tips increase with crack lengths. Clearly, the values of G for the right tip are higher than those obtained for the left for most of the applied voltages. Hence it can be said that the right tip will grow towards the anode side (low partial pressure side) for the considered voltage range. Also it can be noted that, similar to the vertical crack configuration, the G values predicted from one way interaction are lower than those predicted from the two way case. This once again means that safer standards can only be set if design analyses are performed using a two way response rather than a one way response.

The error incurred in using only a one way interaction to predict G is plotted in

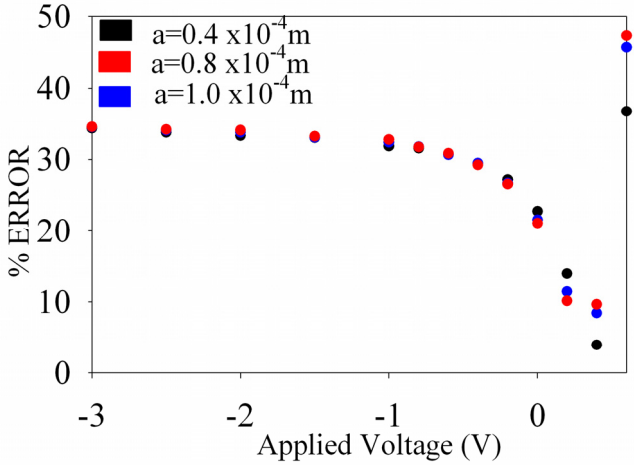

Figure 6.15: Error incurred in performing a one way analysis

Figure 6.15. It can be seen that the error remains around 35% when the applied voltage is between -3 and -1V. Then, there is a steep decrease to a minima at about 0.6V, after which a precipitous increase is observed. These results once again indicate that the two way interaction affects the values of G significantly.

The direction of crack growth for this case was analyzed similar to the vertical crack configuration. It was found that the crack will grow into the material at both the tips horizontally. The vertical components of the material force vectors were found to be one order of magnitude smaller than the horizontal components.

A curve was fit to obtain G as a function of the applied electrochemical boundary conditions. The best fit for all crack lengths was obtained for the function of the following form given by Eq. (6.20).

$$G = \exp\left(-a_1 \exp\left(-b_1 \phi^L\right) - a_2 \exp\left(-b_2 \phi^L\right)\right) \tag{6.20}$$

where, a_1, b_1, a_2 and b_2 are all functions of crack lengths and are shown in Table 6.2.

Table 6.2: Fitting parameters for the expression (6.20)

LEFT TIP $10^{-4} m$	a_1	b_1	a_2	b_2
4	71.94	-2.801	-11.86	-0.7266
8	73.77	-3.147	-8.929	-0.4988
10	69.36	-3.145	-8.802	-0.4735
RIGHT TIP $10^{-4} m$	a_1	b_1	a_2	b_2
4	114.8	-3.329	-9.38	-0.6127
8	167.6	-3.814	-7.671	-0.3993
10	204.8	-4.017	-7.441	-0.3615

As done previously for the vertical crack configuration, the expression Eq.(6.20) can be easily modified into a form that is entirely in terms of the boundary conditions.

6.7 Results and discussion- Void configurations

Voids can be other common forms of flaws that occur in manufacturing processes. Voids may be present at several locations in the domain and can lead to premature failure due to stress concentrations occurring as a result of chemically induced stresses. In this work the void is considered to be located in the central domain of the material just like the crack configurations.

This section is to very briefly analyze the magnitudes of the stresses near the void and compare it to a case which does not have a void, for the same electrochemical boundary conditions. Further, the most important component of the stresses in this case is the hoop component about the void's surface. The variation of these stresses along the surface is shown and compared to the case when no void is present. We also show the variation of the maximum value of the hoop stresses induced, as a function of the applied voltage.

Results from the previous analysis for the crack configurations clearly indicate that two-way interactions predict larger values of the strain energy release rates when compared to that predicted by the one way interaction. This meant that the designs would be safer if analysis were performed by considering a two way interaction. Thus, for the void configurations only the results from the two way analysis are presented.

6.7.1 Hoop stresses

Figure 6.16 shows the variation of hoop stress for various values of applied voltages. Figure 6.16a shows the result for the case with the void while Figure 6.16b shows the same results at exactly the same radial coordinate (0.00005m) for the case

without the void (the shaded semi circle indicates the presence of material there). The results are shown for four values of applied voltages (0, 1, 3 and -3V).

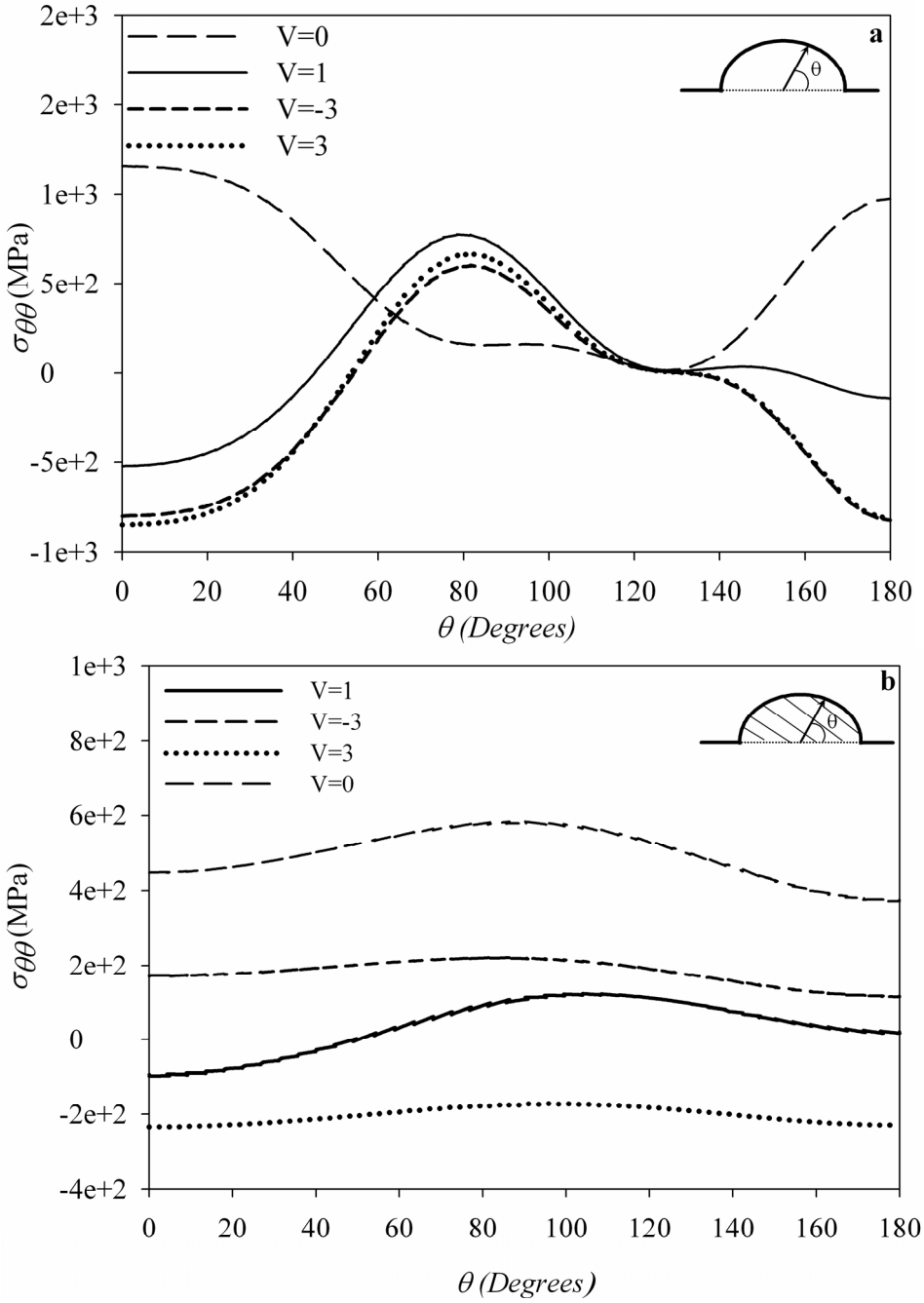

Figure 6.16: Variation of $\sigma_{\theta\theta}$ with θ for various values of applied voltages

Clearly, the hoop stresses are very high for the case with the void, which is expected due to stress concentration. The stresses are as high as 1GPa when the void is present, while only a few hundred MPa when there is no void for the same values of applied voltages. When there is no void we see that the stress distributions vary monotonically with the applied voltage. For large negative voltages, the stresses are tensile and gradually change to being completely compressive at larger positive voltages. As observed they all show maxima at almost the same value of θ. For the case with the void, the stress distribution shows maxima for three different values of θ (0, 180 and 80^o).

Figure 6.17 compares the maximum values of hoop stresses occurring at the void with that obtained for the case without the void at the same radial coordinate (0.00005m). Clearly when there is no applied voltage (electrolyte is functioning purely as a fuel cell), the stresses are highest in both the cases. The stresses are as high as 1.2GPa if void is

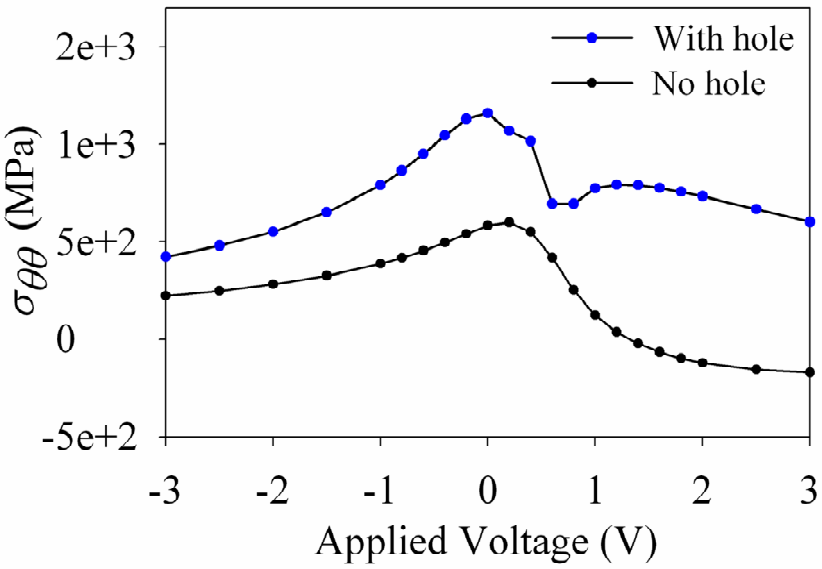

Figure 6.17: Variation of maximum hoop stress with applied voltage

present when compared to about 600Mpa without the void.

Recent studies [197] show that the fracture strength of oxide ceramics can depend on several factors including method of manufacture, dopant concentrations and sintering temperatures. For 10GDC they report the values of fracture strength between 180MPa and 300MPa. The analyses in this section clearly indicate that the hoop stresses arising due to chemical expansion is high even when flaws like voids are not present in the electrolyte (>500MPa) and even higher when voids are present (>1GPa). These high stresses can nucleate cracks or propagate existing radial cracks from the flaw and lead to a failure of the electrolyte. Thus, it is important to consider the chemical stresses in GDC or in other materials showing significant chemical expansion.

6.8 Conclusions

The interior MNPP system of equations that was introduced in chapter 3 was solved in conjunction with the mechanical equilibrium equations. The stresses, vacancy concentrations were obtained under two way interactions existing between defect transport and elasticity. The results were presented in light of the mechanical response of the ionic solid. It was found that stresses have a significant effect on the distribution by studying both the distribution of vacancy concentrations and the strain energy release rates for two configurations of cracks of various lengths and for several applied voltages. The strain energy release rate (G) was determined using the material force approach, and its advantages in this particular problem were mentioned. The finite element solution was developed through a user element subroutine for ABAQUS. The user element can serve as a useful tool to predict mechanical and electrochemical behavior under stress-defect transport interactions in ionic solids.

It was found that the stresses for the vertical crack can be as high as 900MPa near the tip and can result in failure of the ionic solid. Further, it was seen that the crack always experiences a tensile stress, resulting in the opening of the crack for all values of applied voltages. To study the effect of stresses on the values of G, both one way and two way interaction studies were carried out. It was seen that the error incurred in carrying out only a one way interaction was as high as 50%. Furthermore, cracks were found to grow at an angle due to complex stresses at the tip.

The strain energy release rates for both the horizontal and the vertical crack configurations exhibited maxima at specific applied voltages. For other voltages, G was shown to display an asymptotic behavior decreasing to zero. This was related to the behavior of the variation in distribution of vacancies with the applied voltages. The values of G are reported to be consistently lower when only one way interaction is considered. As a consequence of this, safer design of the electrolyte for mechanical reliability is possible if a two way interaction is considered. Thus, while modeling solid state components showing significant chemical expansion for mechanical stability, a two way interaction must be considered.

Simple mathematical expressions are shown to predict G accurately. These expressions can be directly used by designers to assess the failure behavior of solid electrolytes. Basically, if critical values of G are known, then it would be possible to specify safer operating voltages and partial pressures using the expressions developed in this work. Thus the expressions developed prove to be a useful tool to predict the failure propensity of ionic materials or to give bounds of the safe operating voltages if the critical strain energy release rate values and the crack configurations are known.

Finally, the stresses in the vicinity of a small void were analyzed. It was seen that the stresses there can be as high as 1GPa and can potentially lead to crack nucleation or crack growth. In particular, the highest values of the stresses occur when no voltage is applied, i.e. when the electrolyte is functioning in a typical fuel cell environment.

CHAPTER 7. SUMMARY AND RECOMMENDATIONS FOR FUTURE RESEARCH

7.1 Overview and findings

7.1.1 Introduction

This thesis addresses the issue of interaction between elasticity and transport of charged point defects in ionic solids. The material GDC was chosen for this study for its prospective role as an electrolyte in low temperature solid oxide fuel cells and for two of its interesting traits that make the interaction possible; 1) Large chemical coefficient of expansion and 2) Variation of elastic properties with vacancy concentration. The main part of this thesis begins with the definition of chemical potential of point defects in ionic solids and a very brief introduction to molecular simulations in chapter 2. The remainder of this thesis builds on these fundamentals to develop continuum framework (chapter 3), to determine material properties using MD (chapter 4), to solve a system of differential equations (chapters 5 &6) and finally to post process the results from the solutions to numerically quantify the extent of the interactions (chapters 5 & 6). Before we give a detailed summary for each chapter the major findings of this work are listed.

7.1.1.1 *Findings*

1) Stresses and defect transport indeed interact significantly in materials with large CCE like GDC.
2) The magnitude of the stresses induced in both the planar and the tubular electrolytes are high. In particular, the tubular electrolyte shows tensile stresses at the cathode side due to chemical strains, and these are in the order of

stresses generated as a result of thermal mismatch with the electrodes. These may cause cracks to grow radially along the thickness of the ionic solid while functioning as an electrolyte. This means that along with thermal mismatch effects, the chemically induced stresses must also be considered while designing these electrolytes.

3) Stresses in the vicinity of flaws are also large when compared to the tensile strengths of the material. These stresses are functions of the applied electrochemical loadings like voltage and partial pressures. Hence, in the regular design of ionic solids or during their reliability analysis, the thermal and chemically induced stresses must be taken into account.
4) The effect of interaction between stresses and defect transport also affects the strain energy release rates of the cracked electrolyte significantly. The error incurred in estimating the values of the strain energy release rates using the regular methods can be as high as 50%. This hence reinforces the need to consider stress-defect transport interactions while designing ionic solids for their applications.

7.2 Chapter summaries

7.2.1 Chapter 3- Continuum framework

This chapter provides the necessary framework to couple defect-transport and mechanics in a typical oxide ceramic. The Eshelby stress dependent chemical potential is derived and is used to develop the framework which essentially consist of differential/algebraic equations and associated boundary conditions. The solution to this boundary value problem enables us to study the interactions. Unlike the existing theories,

the equations developed here provide a fully coupled framework for investigating the interactions between mechanical and electrochemical fields. In all other previous studies, the electrochemical potentials depend on only the hydrostatic stress or explicitly on the Cauchy's stress.

As discussed, the quantities of significance in this chapter are the Eshelby stress and two material properties, namely the CCE and OSEC which make the interaction possible. All stress components are involved in the electrochemical potentials, making the problem fully coupled. This requires the diffusion equations to be solved simultaneously with the equilibrium equations of mechanics, even when small strain deformation is assumed.

7.2.2 Chapter 4 – Atomistic simulations for material properties

The material properties introduced in chapter 3 (CCE & OSEC) were determined using a combination of analytical and MD simulations. This was done by relaxing MD simulation cells of defective GDC at various temperatures. While the determination of the CCE was straightforward, this was not the case for the OSEC on account of possible inner elastic contributions due to the non-primitive nature of defective GDC lattices. On examining the elastic constants it was found that only C_{11} varied with non-stoichiomtery. A possible reason for this was given by examining the contribution of the short range and the long range parts of the interatomic potential to the elastic constants.

The numerical values of the CCE and the Young's modulus were found to be reasonably close to existing experimental data. It was found that the CCE was in the range of 0.069-0.079 for a wide range of temperatures for both 10 & 20GDC and the polycrystalline Young's modulus varied with a clope of about -200GPa with

stoichiometry. The Poisson's ratio was found to be insensitive to stoichioemetry. Further both CCE and the OSEC were found to be insensitive to temperature.

These values of CCE and stoichiometry dependent Young's modulus were then used in the subsequent chapters to solve the differential equations introduced in chapter 3.

7.2.3 Chapter 5- The 1D MNPP system –Interactions on defect transport

In chapter 5 a modified form of the NPP system was introduced and solved for two common configurations of the electrolyte, namely planar and tubular. The singular nature of the Possion equation rendered numerical solutions in the entire domain impossible when the size of the domain was much greater than a characteristic length. This pointed out the need for a singular perturbation method using the method of matched asymptotic expansions.

Implicit solutions were possible for the interior system because the stress dependent chemical potential possessed a simple form due to the condition of plane self-stress. The solutions were examined for two methods of applying boundary conditions. It was found that the solutions, namely the distribution of vacancies and the electrostatic potential, showed non-trivial differences when the effects of elasticity were considered. This showed that elasticity had an effect on the electrochemical fields. The stress distributions were also examined and it was found that these were in the same order or even higher than stresses induced as a result of thermal mismatch between the electrodes and the electrolyte. This suggested that both thermal and chemically induced stresses must be taken into account while designing ionic solids for applications.

Numerical solutions were obtained for the distribution of all the field quantities in the boundary layer by solving the boundary layer differential equation. The boundary

layer solution once again indicated an alteration in the distribution profiles when the effects of elasticity were considered. In fact it is found that the overall charge density in the boundary layer was found to be enhanced when elasticity was considered. The chapter was then concluded by suggesting that elasticity effects (like applying external loads) can be used over other existing methods, based on grain boundary engineering, to alter the material's behavior.

7.2.4 Chapter 6 – The 2D MNPP system -Interactions on mechanics

The interior 2-D MNPP system was solved using the finite element method. The specification of the boundary conditions was based on a one dimensional approximation of the boundary layer equations without the effects of elasticity being considered. 2-D domains of electrolytes with commonly occurring manufacturing flaws were used for the study. 10GDC with two different crack configurations (vertical and horizontal) and a void was subjected to electrochemical boundary conditions for the study. The GDC electrolyte was subjected to a wide range of applied voltages in order to determine the deformation, stresses and the strain energy release rates for the cracked configurations. It was indicated that the complexity of the stresses in the vicinity of the crack tip required the material force approach, which is a generalization of the conventional J-integral.

The main conclusions in this chapter were that the stresses in the vicinity of the flaws were very high in comparison to the strengths of these materials. While the vertical crack showed variations in the crack growth direction, the horizontal cracks were always found to grow horizontally into the domain towards the anode side for certain voltages.

For both the vertical and the horizontal crack configurations, the strain energy release rates were determined using both the "two way interaction" and a "one way

interaction" analyses. The "one way" interaction refers to an analysis that does not involve the use of stress dependent chemical potential, but that which considers the effect of chemical strains generated as a result of deviation from non-stoichiometry on elasticity. The comparison of these results showed that the one-way interaction consistently predicted lower values of the strain energy release rates, suggesting that safer designs would require two way interactions to be considered.

7.2.5 Contributions

The major contributions of this work are:

1) Development of the Eshelby stress dependent chemical potential for point defects in ionic solids within the dilute approximation.
2) Development of an MD simulation based methodology to calculate CCE and elastic constants in defective lattice structures.
3) Introduction and solution of a new form of the NPP system that accounts for the effects of elasticity.
4) Development of a user element subroutine for ABAQUS to solve coupled stress-defect transport problems in ionic solids.
5) Development of expressions for the strain energy release rates as a function of applied electrochemical boundary conditions to specify safer operating voltages in ionic solids functioning under fuel cell environment.

Although the various contributions were discussed with GDC as an example, the methodologies developed can be easily extended to other materials of interest.

7.3 Recommendations for future research

7.3.1 Introduction

This thesis consists of several broad areas like continuum thermodynamic modeling, molecular simulations, defect chemistry and solid state ionics. All these areas have been useful in laying the fundamental foundations for studying the multiphysics problem of stress defect transport interaction. There are several points where this thesis can branch out leading to interesting research topics which may be of both practical and academic importance. Some of these obviously originate in relaxing some of the assumptions made in this thesis. The various branches are described and some references that can be useful starting points are recommended for further reading.

7.3.2 Relaxation of the requirement of dilute approximation

In this work it has been consistently assumed that the concentrations of defects are small. This causes the chemical potential to have a Boltzmann type distribution (see Eq.(2.15)). While this is true for most of the materials, interesting features of stress-chemistry interaction have been reported in materials with large concentration of defects in [17, 18]. Under such circumstances a Fermi-Dirac type statistics is required (see. Eq. (2.14)). It will be of considerable interest to see how the differential equations governing defect transport turn out and what solutions may predict, especially on using the coupled formulation.

In addition to acquiring a Fermi-Dirac distribution, the large concentration of defects can result in defect-defect interaction forming clusters. Theoretical modeling of the chemical potential of defects that interact by forming complex clusters remain limited to date and some them can be found in [44, 51, 52]. However, it has been shown that the

effects of these clusters have a pronounced effect on the ionic conductivity of electrolytes used in fuel cells [198].This occurs because, the otherwise mobile point defect like a vacancy is trapped by the cations, especially when their concentrations are high. Even molecular simulations have been able to show the presence and the effect of these clusters [47, 48].

Thus modeling, by relaxing the dilute approximation can open up at least two branches in the theoretical modeling aspect of defect transport/thermodynamics of ionic solids.

7.3.3 The intermediate configuration & differential geometry

In chapter 3, the intermediate configuration was introduced to develop the Eshelby stress dependent chemical potential. For several years, this differential manifold has been treated like any other using the Kronecker delta as the metric. However, [199] points out that such a manifold might not be as straightforward to deal with as other usual spaces encountered in elasticity, due to its non-Euclidean nature. This topic addresses the deeper philosophical discussions pertaining to differential geometry which completely branches out from the theme of investigation followed in this work. To gain better appreciation for ideas on this aspect of the problem the reader is referred to [200] and references therein.

7.3.4 Alternate materials and MD related recommendations

GDC is the material of interest in the current work. Other materials like doped Lanthanum (LSC- $La_{1-x}Sr_xCoO_{3-\delta}$) and Barium oxides (BSCF- $Ba_{0.5}Sr_{0.5}Co_{0.8}Fe_{0.2}O_{3-\delta}$) are also known to be of use in solid oxide fuel cell electrodes. While LSC is used as anodes BSCF is used as a cathode material. Similar to GDC, they also undergo,

significant, chemical expansion (see [12, 201] and [11] for more information). The theoretical frame work developed in chapter 3 and the methodologies developed in chapter 4, can be easily extended to study these material systems as well.

While it was shown that the contribution of inner elasticity towards the elastic constants was small for GDC, it may not be the case for other materials due to complicated crystal structure. The methodologies and the codes written for GDC can also be used for the material systems introduced in this section.

Determination of CCE was based on the simple methodology of comparing the relaxed MD cell volumes. Some recent works use micromechanics concepts to more rigorously compute the formation volume of the defects in Silicon based materials. For details the reader is referred to [121, 202, 203]. These techniques, while requiring knowledge of micromechanics [149] may lead to more elegant homogenization procedures for atomistic- continuum coupling, in contrast to the simple but "brute force" approached employed in this work.

It was mentioned in passing, in section 1.4 that in addition to the formation volume, the migration volume of the defect may also be affected by stresses. The migration volume is related to the physical change in the volume as the atom squeezes through the lattice to reach another lattice point having a minimum energy. This has not received much attention with defect transport in ionic solids. It would be interesting to perform molecular calculations based on MD by examining the energy land scape in the vicinity of point defects in order to measure the extent of stress dependence on the migration volume of the defects. The Nudged Elastic band method (NEB) is used to find minimum energy path ways for chemical reactions. The details of this relatively new

approach can be found in [204] and references therein. The migration volume is directly related to the diffusion coefficient (or more generally the Onsager coefficients). Once the stress dependence of these coefficients is determined, they can be used in the theoretical framework developed in this work to solve fully coupled stress defect transport problems.

7.3.5 Size effects

In this work a macroscopic solid with point defects was considered in most part (except in chapter 4, where a polycrystalline aggregate was used to determine the homogenized Young's modulus). With the advent of nano-technology, smaller sized structures have shown different properties when compared to their macroscopic counterparts. The effect of sizes is pronounced, not only on the mechanical properties like stiffness [139, 205] or yield strength [206, 207] of the material but also on the conductivity values, conductivity type, mass and charge storage capabilities [29] of

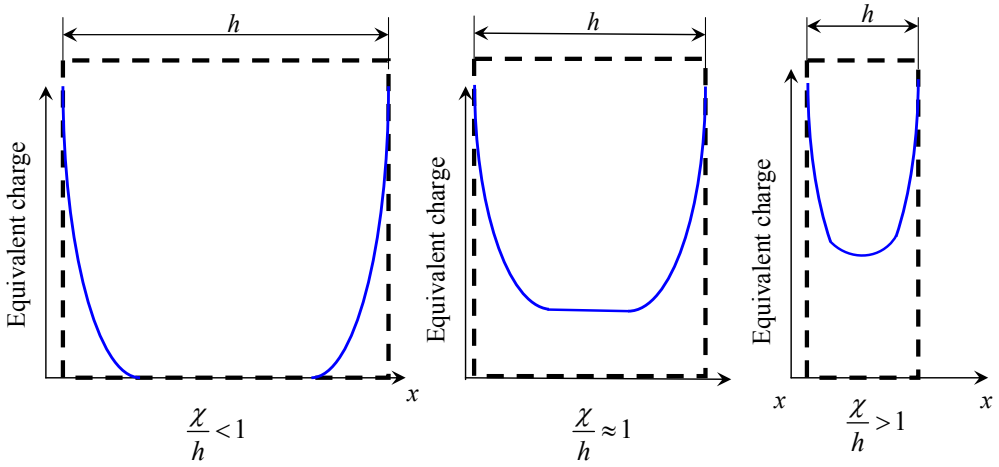

Figure 7.1: Size effect on charge storage

solids. The effects of surfaces dominate in nano-crystalline materials and hence the contributions of elasticity to interesting phenomenon in these confined systems cannot be ruled out.

In addition to the so called “trivial size” effect just discussed (augmentation of altered property due to the size of grains in the material) a “true size” effect can occur [33]. Chapter 5 contains a hidden motivation for this topic, although it does not explicitly deal with nano-sized/nano-crystalline material. To look at this aspect in a simple yet detailed manner we refer the reader to Figure 5.15. Here the regions close to the surface are charged while the interior or the bulk is not. This is the case because charge neutrality holds in the bulk of the material owing to the fact that, the material was of macroscopic size, making the perturbation analysis possible. The perturbation approach enables delineation of the domain clearly into **The bulk** where (LEN is valid) and **The boundary layer** which is charged. If our material and domain were such that $\chi / h \approx 1$ or even $\chi / h > 1$ then the perturbation method and the semi-infinite conditions as in Eq. (5.68) would cease to be valid. A sketch of what happens as the sizes are reduced is shown in Figure 7.1. Clearly as we see, the reduction in size causes the charge of the bulk of the domain to deviate from the LEN condition. This clearly means that the charge density (charge per unit volume) can be enhanced if the size is made smaller. Consequently, in materials with nano-sized grains the size effect just explained can occur in all the grains enhancing the overall charge storage capacity. In addition the surfaces /interfaces of the grains in the material start to perceive each other, leading to the true size effect.

The effects of elasticity can also be significant in ionic solids with nano-sized grains due to structural interference effects. The adjacent grains on account of their misorientation, are subjected to structural misfit (eigen) strains. In this case the formation energy of the defect varies spatially from the grain boundary to the interior of the grain, resulting in a contribution to the non-configurational part of the chemical potential. Thus

we see that in polycrystalline materials the effects of size and of elasticity can have an influence in altering the over all material properties.

The effects of size described in this section are all motivated based on the discussions in chapter 5. Chapter 5 provides some of the fundamentals and ideas associated with the size effect; however, the extension to treat size effect issues cannot be achieved without solving the complete NPP or the MNPP, system which can be numerically challenging.

7.3.6 Other crack configurations in electrolytes

In chapter 6 a user element was written and the governing differential equations were solved over a domain with a vertical and horizontal crack whose existence was attributed to manufacturing flaws. As mentioned in section 6.4.1 other crack configurations may exist. As shown in Figure 7.2 vertical cracks and delamination cracks can occur near the electrolyte-electrode interface.

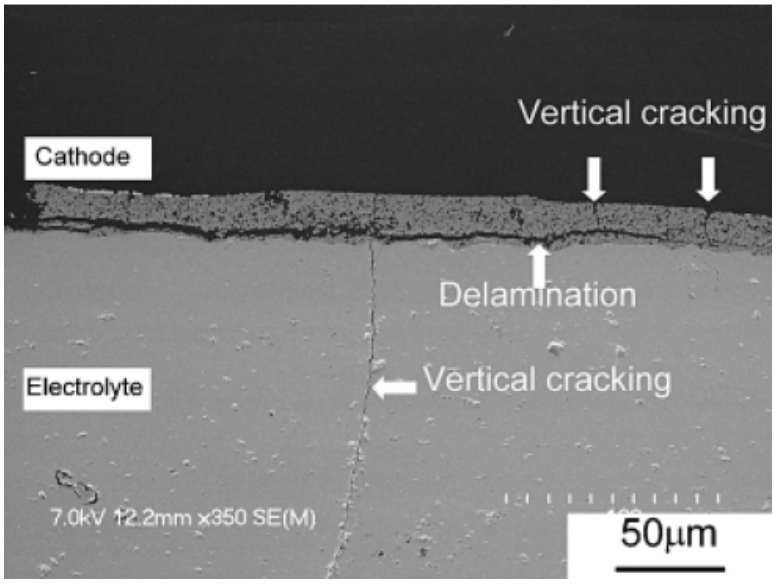

Figure 7.2: Showing various types of cracks in the electrolytes [208]

The extension of the analyses performed in this work to consider these kinds of cracks is straightforward. The only difference lies in specifying the concentration and the electrostatic potential at the crack faces instead of specifying a zero current condition. However, the issue of a boundary layer still exists while specifying Dirichlet type boundary conditions (specification of concentrations and potentials). This may be handled in the same manner as done in this work for the left and right boundaries (see section 6.3.2 for details). Similar to what was done in chapter 6, strain energy release rate curves for applied voltages may yield useful results suggesting safer operating voltages or design modifications for extended life of the ionic solid.

7.3.7 Recommendations for experimental verifications

This thesis is entirely theoretical with motivations of possible stress-chemistry interactions drawn from experiments conducted in [17, 18, 22, 209]. In order to complement and verify the phenomena of stress-defect transport interactions in ionic solids, some suggestions are given below. In this regard, we would like to state that the experimental methods of electrochemistry are not completely familiar to the author and hence we cautiously mention a few approaches that seem possible. Moreover, it seems quite a challenge to develop experimental methods to verify the problems exactly as they appear in chapter 5 or chapter 6. For this reason, the methodology is provided only to verify if stress has an effect. The quantitative values of the various measures might still be different from the ones obtained numerically in this work on account of the different mechanical boundary conditions.

7.3.7.1 ***Measuring the voltage-Indirect load method***

The set up that may be used in order to perform an experiment to determine the effect of stresses on transport of defects in ionic solids is shown in Figure 7.3. The

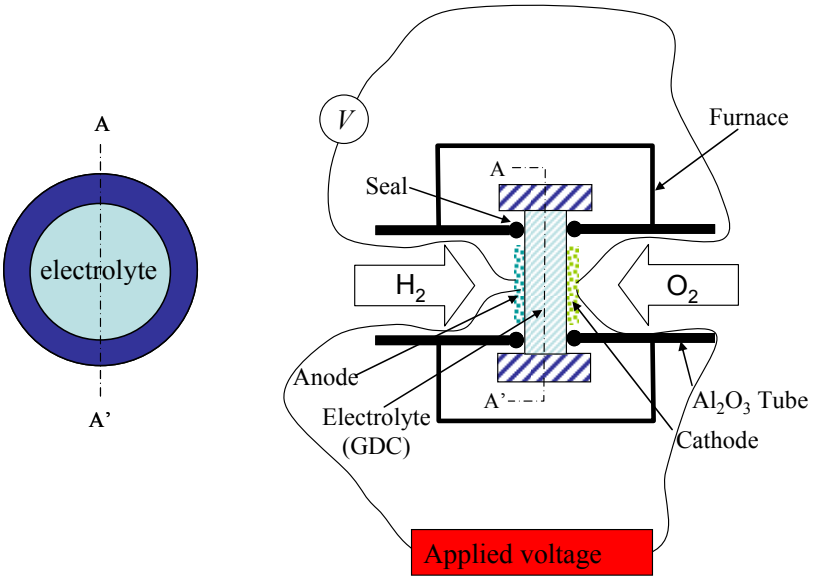

Figure 7.3: Experimental set up for the indirect load method

experiment involves inserting a planar electrolyte (with a large CCE) of circular shape into a hollow tube made of a low TCE, high modulus material. During operation at high temperature, the tube exerts a compressive stress on the electrolyte due to thermal strains. The amount of compressive stress can be controlled by varying the wall thickness of the tube. The voltage reading may be observed and compared to the values when no alumina ring is used (or when a high TCE material is used). Any variation in the reading (with and without the alumina ring) indicates that stresses and defect transport interact. It might also be possible to use an ammeter to measure the current for various values of the applied voltages. The value of the voltage at which the current is zero is the open circuit

voltage (V_{OC}). The comparison of this quantity with and without the alumina ring can also indicate the effects of stresses on the electrochemical performance.

7.3.7.2 ***Measuring the voltage-Direct load method***

Alternatively instead of using thermal stresses to load the electrolyte, we may

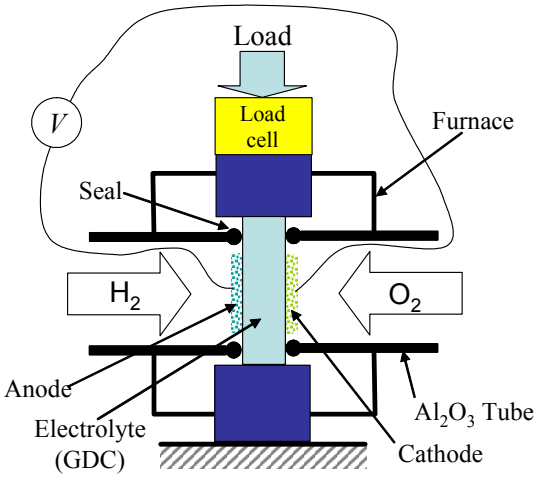

Figure 7.4: Experimental set up for the direct load method

directly apply forces similar to the procedure followed in [209] and measure the voltage. The set up is shown below in Figure 7.4.

As opposed to the previous method, this method more easily establishes a quantitative relation between the applied load and the resulting voltage. Note however that the stresses induced in the electrolyte are a combination of loads due to eigenstrains from chemical expansion, thermal expansion and the applied forces.

Using these methods, the effects of stresses on the electrochemical performance may be at least qualified. However, it must be kept in mind that the elastic energy induced, must alter the defect transport rather than cause failure of the material. Thus the extent of interaction is contingent upon how the elastic energy in the material dissipates.

The presence of minor flaws may cause failure of the electrolyte by growth of cracks resulting in the failure of experiment. Thus the material must be defect free as far as possible.

APPENDIX A. DERIVATION OF ESHELBY STRESS

In this appendix the expression for the Eshelby stress (second equality in Eq. (3.60)) is derived. The following two matrix identities come in handy while performing the derivation,

$$\frac{\partial J}{\partial F_{iJ}} = J f_{Ji}\,, \frac{\partial f_{Ji}}{\partial F_{kL}} = -f_{Jk} f_{Li} \tag{A.1}$$

where

$J = \mathrm{Det}[F_{iJ}]$.

First compute

$$\frac{\partial \left[J^c w_0(\mathbf{E}^E) \right]}{\partial F^c_{\hat{I}J}} = w_0(\mathbf{E}^E) \frac{\partial J^c}{\partial F^c_{\hat{I}J}} + J^c \frac{\partial w_0(\mathbf{E}^E)}{\partial F^c_{\hat{I}J}} = J^c f^c_{J\hat{I}} w_0(\mathbf{E}^E) + J^c \frac{\partial w_0(\mathbf{E}^E)}{\partial F^c_{\hat{I}J}} \tag{A.2}$$

It follows from the second of (A.1) that

$$\frac{\partial F^E_{m\hat{N}}}{\partial F^c_{\hat{I}J}} = \frac{\partial \left(F_{mK} f^c_{K\hat{N}} \right)}{\partial F^c_{\hat{I}J}} = F_{mK} \frac{\partial f^c_{K\hat{N}}}{\partial F^c_{\hat{I}J}} = -F_{mK} f^c_{K\hat{I}} f^c_{J\hat{N}} \tag{A.3}$$

Thus,

$$J^c \frac{\partial w_0(\mathbf{E}^E)}{\partial F^c_{\hat{I}J}} = J^c \frac{\partial w_0(\mathbf{E}^E)}{\partial E^E_{\hat{K}\hat{L}}} \frac{\partial E^E_{\hat{K}\hat{L}}}{\partial F^E_{m\hat{N}}} \frac{\partial F^E_{m\hat{N}}}{\partial F^c_{\hat{I}J}} = -J^c \tilde{\sigma}^E_{\hat{K}\hat{L}} \frac{\partial E^E_{\hat{K}\hat{L}}}{\partial F^E_{m\hat{N}}} F_{mK} f^c_{K\hat{I}} f^c_{J\hat{N}} \tag{A.4}$$

where

$$\tilde{\sigma}^E_{\hat{K}\hat{L}} = \frac{\partial w_0(\mathbf{E}^E)}{\partial E^E_{\hat{K}\hat{L}}} \tag{A.5}$$

is the second Piola-Kirchhoff stress written in the intermediate configuration. Furthermore, making use of Eq. (3.24), we obtain

$$\tilde{\sigma}^{E}_{\hat{K}\hat{L}} \frac{\partial E^{E}_{\hat{K}\hat{L}}}{\partial F^{E}_{m\hat{N}}} = \tilde{\sigma}^{E}_{\hat{K}\hat{L}} \frac{\partial}{\partial F^{E}_{m\hat{N}}} \left[\frac{1}{2} \left(F^{E}_{n\hat{K}} F^{E}_{n\hat{L}} - \delta_{\hat{K}\hat{L}} \right) \right] = \tilde{\sigma}^{E}_{\hat{N}\hat{L}} F^{E}_{m\hat{L}} = \hat{\sigma}^{0}_{\hat{N}m} \tag{A.6}$$

where the third equality follows from Eq. (3.16) and $\hat{\sigma}^{0}_{\hat{N}m}$ is the first Piola-Kirchhoff stress written in the intermediate configuration. It is expressed in the natural configuration by Eq. (3.17),

$$\sigma^{0}_{Jm} = J^{c} f^{c}_{J\hat{N}} \hat{\sigma}^{0}_{\hat{N}m} \tag{A.7}$$

Making use of (A.6)-(A.7) in (A.4) yields

$$J^{c} \frac{\partial w_0(\mathbf{E}^{E})}{\partial F^{c}_{\hat{I}J}} = -\sigma^{0}_{Jm} F_{mK} f^{c}_{K\hat{I}} \tag{A.8}$$

Substituting (A.8) into (A.2) leads to

$$\frac{\partial \left[J^{c} w_0(\mathbf{E}^{E}) \right]}{\partial F^{c}_{\hat{I}J}} = \left(J^{c} w_0(\mathbf{E}^{E}) \delta_{KJ} - \sigma^{0}_{Jm} F_{mK} \right) f^{c}_{K\hat{I}} = \Sigma_{JK} f^{c}_{K\hat{I}} \tag{A.9}$$

This completes the proof.

APPENDIX B. GIBB'S APPROACH TO DERIVE MASS ACTION LAWS

In this appendix the relation between the electrochemical potential of various species in the solid and also between an external gas and the solid is derived based on the variational principle. These relations transform to mass action laws (Eq. (3.88), Eq.(3.90) and Eqs. (3.99)).

According to Gibbs [210], *For the equilibrium of any isolated system it is necessary and sufficient that in all possible variations of the state of the system which do not alter its energy, the variation of its entropy shall either vanish or be negative.*

Consider an isolated system comprising an oxide in contact with oxygen gas. Let the internal energy density of the solid π_s be a state function of the deformation gradient F_{iJ}, entropy density *s*, concentrations (in mole fractions) of oxygen ions $\rho_{O_o^x}$, charged vacancies $\rho_{V_O^{\bullet\bullet}}$, interstitial vacancies $\rho_{V_i^x}$, charged interstitial oxygen ions $\rho_{O_i^{''}}$, electrons ρ_e and holes ρ_h.The internal energy of the gas phase π_g is assumed to be a state function of the molar volume V_g, the entropy density s_g and the composition, e.g., oxygen concentration ρ_{O_2}. Let the solid-gas interface be denoted by *S*. The total internal energy of the solid-gas system can be written as

$$\Pi_T = \int_{V_s} \pi_s(F_{iJ}, s_s, \rho_{O_o^x}, \rho_{V_O^{\bullet\bullet}}, \rho_{V_i^x}, \rho_{O_i^{''}}, \rho_e, \rho_h)dv + \int_{V_g} \pi_g(V_g, s_g, \rho_{o_2})dv \qquad \text{(B.1)}$$

Strictly speaking, a surface integral containing the excess energy associated with the interface should also be included in the total internal energy expression (B.1). However,

inclusion of the surface energy term has no effect on the interfacial conditions we are trying to derive [54]. Therefore, for simplicity, it is not included here.

According to the Gibbs variational principle, the equilibrium state minimizes the internal energy subject to the following constraints:

Constant number of oxygen lattice sites throughout the solid

$$\int_{V_s}\left(\rho_{O_o^X}+\rho_{V_O^{\cdot\cdot}}\right)dv = K_1 \tag{B.2}$$

Constant number of interstitial lattice sites through the solid

$$\int_{V_s}\left(\rho_{V_i^X}+\rho_{O_i^{''}}\right)dv = K_2 \tag{B.3}$$

Electroneutrality condition under equilibrium

$$\int_{V_s}\left(2\rho_{V_O^{\cdot\cdot}}-2\rho_{O_i^{''}}-\rho_e+\rho_h\right)dv = 0 \tag{B.4}$$

Constant number of oxygen ions in the entire system (solid and gas)

$$\int_{V_g} 2\rho_{o_2}dv+\int_{V_s}\left(\rho_{O_i^{''}}+\rho_{O_o^X}\right)dv = K_4 \tag{B.5}$$

Constant total entropy of the system,

$$\int_{V_s} s_s dv+\int_{V_g} s_g dv = \Xi \tag{B.6}$$

These constraints can be relaxed by using the Lagrange multipliers, λ_i (i = 1 to 5), i.e.

$$\begin{aligned}\int_{V_s}\Big[\,&\delta\pi_s-\lambda_1(\delta\rho_{O_o^X}+\delta\rho_{V_O^{\cdot\cdot}})-\lambda_2(\delta\rho_{V_i^X}+\delta\rho_{O_i^{''}})-\lambda_5\delta s_s\\&-\lambda_3(2\delta\rho_{V_O^{\cdot\cdot}}-2\delta\rho_{O_i^{''}}-\delta\rho_e+\delta\rho_h)-\lambda_4(\delta\rho_{O_i^{''}}+\delta\rho_{O_o^X})\Big]dV\\&+\int_{V_g}\Big[\,\delta\pi_g-2\lambda_4\delta\rho_{o_2}-\lambda_5\delta s_g\Big]dV=0\end{aligned} \tag{B.7}$$

Note that

$$\delta\pi_s = \sigma^0_{Ji}\delta F_{iJ} + T_s\delta s_s + \tilde{\mu}_{O_o^X}\delta\rho_{O_o^X} + \tilde{\mu}_{V_o^{\bullet\bullet}}\delta\rho_{V_o^{\bullet\bullet}} + \tilde{\mu}_{V_i^X}\delta\rho_{V_i^X} + \tilde{\mu}_{O_i^{''}}\delta\rho_{O_i^{''}} + \tilde{\mu}_e\delta\rho_e + \tilde{\mu}_h\delta\rho_h \tag{B.8}$$

$$\delta\pi_g = -p\delta V_g + T_g\delta s_g + \tilde{\mu}_{O_2}\delta\rho_{O_2} \tag{B.9}$$

where σ^0_{Ji} is the first Piola-Kirchhoff stress, T_s is the absolute temperature, $\tilde{\mu}_\alpha$ ($\alpha = O_o^X, V_o^{\bullet\bullet}$ etc.) are the electrochemical potentials of various species, in the solid phase, while p is the pressure, T_s is the absolute temperature and $\tilde{\mu}_{O_2}$ is the oxygen electrochemical potential, in the gas phase.

Substituting (B.8) - (B.9) into (B.7) and collecting like terms yield

$$\tilde{\mu}_{O_o^X} = \lambda_1 + \lambda_4,\ \tilde{\mu}_{V_o^{\bullet\bullet}} = \lambda_1 + 2\lambda_3,\ \tilde{\mu}_{V_i^X} = \lambda_2,\ \tilde{\mu}_{O_i^{''}} = \lambda_2 - 2\lambda_3 + \lambda_4 \tag{B.10}$$

$$\tilde{\mu}_e = -\lambda_3,\ \tilde{\mu}_h = \lambda_3,\ \mu_{o_2} = 2\lambda_4,\ T_s = \lambda_5,\ T_g = \lambda_5 \tag{B.11}$$

There are nine equations in (B.10) - (B.11) containing five Lagrange multipliers. Eliminating the Lagrange multipliers in these equations, we arrive at the following four relations among the electrochemical potentials,

$$\tilde{\mu}_{V_i^X} + \tilde{\mu}_{O_o^X} = \tilde{\mu}_{V_o^{\bullet\bullet}} + \tilde{\mu}_{O_i^{''}},\ \tilde{\mu}_e + \tilde{\mu}_h = 0 \tag{B.12}$$

$$T_s = T_g,\ \tilde{\mu}_{O_o^X} = \tilde{\mu}_{V_o^{\bullet\bullet}} + 2\tilde{\mu}_e + \frac{1}{2}\tilde{\mu}_{O_2} \tag{B.13}$$

The relations in Eq.(B.12) involve electrochemical potentials in the solid only. Utilizing the expressions of chemical potentials, the two equations in Eq. (B.12) lead directly to the two equations in Eq.(3.99); these equations represent the mass action laws for the Frenkel equilibrium and electron-hole condition, respectively.

The first of Eq. (B.13) gives the thermal equilibrium of the solid-gas interface, i.e., the temperature across the interface must be continuous at equilibrium. The second of Eq. (B.13) describes the solid-gas interaction at the interface. Making use of the

expressions of chemical potentials, one can easily show that (B.13) leads to the interfacial condition as shown in Eq.(3.88).

It should be mentioned that, in the above formulation, it has been assumed that electrochemical reactions are relatively much faster than the diffusion of species so that at any given instance, an instantaneous state of quasi-equilibrium can be achieved for diffusion analysis.

APPENDIX C. STRESS DEPENDENT EQUILIBRIUM CONSTANT

We now derive stress dependent equilibrium constant for the defect reactions. We do this using the boundary reaction (gas solid reaction) as an example. For simplicity, we assume that the effect of compositional change on the elastic compliance is negligible ($s_{ijkl}^{\alpha} \approx 0$), and all the stresses are generated by defect deviation from stoichiometry ($S_{ijkl}^{0}\sigma_{ij}\sigma_{kl} \approx 0$).Therefore, it follows from Eq. (3.73) that the stress dependent electrochemical potential for a species α can be written as,

$$\tilde{\mu}_{\alpha} = \mu_{\alpha}^{0} + RT\ln\left(\gamma_{\alpha}\rho_{\alpha}\right) - V_{m}\eta_{\alpha}\sigma_{kk} + z_{\alpha}F\phi \tag{C.1}$$

where μ_{α}^{0} is the chemical potential at some standard state. The activity coefficient takes into account the interaction among the defects and is considered a unity for a dilute solution where such interactions are negligible. Substituting (C.1) into the second of Eq.(B.13) yields,

$$\mu_{O_O^x}^{0} - \mu_{V_O^{\bullet\bullet}}^{0} - 2\mu_{e}^{0} - \frac{1}{2}\mu_{O_2}^{0} + V_m\eta_v\sigma_{kk} = RT\ln\left[\frac{\rho_{v_O^{\bullet\bullet}}\rho_e^2\sqrt{P_{O_2}}}{\rho_{O_O^x}}\right] \tag{C.2}$$

Eq. (C.2) also be written in terms of the equilibrium constant K_{S1},

$$\frac{\rho_{v_O^{\bullet\bullet}}\rho_e^2\sqrt{P_{O_2}}}{\rho_{O_O^x}} = K_{S1} = k_0 K_{\sigma} \tag{C.3}$$

where

$$k_0 = \exp\left(\frac{\mu^0_{O_o^x} - \mu^0_{V_o^{\cdot\cdot}} - 2\mu^0_e - \frac{1}{2}\mu^0_{O_2}}{RT} \right) \tag{C.4}$$

is the stress-independent part of the equilibrium constant and

$$K_\sigma = \exp\left(\frac{V_m \eta_v}{RT} \sigma_{kk} \right) \tag{C.5}$$

is the stress-dependent part of the equilibrium constant.

The above derivation may also be carried out for the Frenkel and Schottky equilibrium reactions in order to establish relations among the various defects. Since we have considered only two kinds of defects in this work, these reactions are not required.

APPENDIX D. INNER ELASTICITY

D.1 Derivation of Inner Elastic Constants

In this section we derive the expressions for the elastic constants in a concise manner. We follow the derivation in [130] closely. Consider a crystal system with N different sub-lattices. The site of the atoms in different sub-lattices may or may not have the inversion center as one of its symmetry elements. As explained earlier, in those crystals that are primitive it is not necessary to consider inner elasticity as there will be no preferential displacement of the sub-lattices with respect to each other. In cases where the crystal is non-primitive, inner elasticity has to be accounted for as the sub-lattices move on application of a homogenous strain as shown in Figure 4.4, for two kinds of sub-lattices.

On subjecting a primitive crystal (all atoms have inversion as a symmetry element), with N sub-lattices to a homogenous Lagrange strain (**E**), any vector $\mathbf{r^0}$, joining two atoms in the undeformed state, transforms to the deformed state of **r** through the relation,

$$r=\mathbf{F}r^{o} \tag{D.1}$$

where,

F is the deformation gradient

r^{o} is the position vector between two atoms before deformation

r is the position vector after deformation

The homogenous Lagrange strain is given by,

$$\mathbf{E}=\frac{\mathbf{1}}{\mathbf{2}}\left[\mathbf{F}^{T}\mathbf{F}-\mathbf{I}\right] \tag{D.2}$$

where, **I** is the identity tensor

If the system is governed by a central kind of interatomic potential (interaction between atoms depends only on the magnitude of distances between the atoms), then the total energy density (u) is given as,

$$u = \frac{1}{2\Omega} \sum_{p=1}^{N} \sum_{\substack{q=1 \\ q \neq p}}^{N} e(r^{pq}) \tag{D.3}$$

where,

$e(r^{pq})$ is the potential energy due to the interaction between atom p and q due to both the short range and the Coulombic forces.

r^{pq} is the magnitude of the distance between atom p and q

Ω is the MD cell volume

The contribution from the long range coulombic interaction to the energy $e(r^{pq})$ and its derivatives for the calculation of elastic constants, is evaluated using Wolf sum [211]. This method is used here as it can be applied even to highly disordered ionic systems.

The elastic constants C_{ijmn} for the primitive lattice system are given using the formulae,

$$C_{ijmn} = \left. \frac{\partial^2 u}{\partial E_{ij} \partial E_{mn}} \right|_{E_{ij}=0} = \frac{1}{4\Omega} \sum_{p=1}^{N} \sum_{\substack{q=1 \\ q \neq p}}^{N} \frac{\partial}{\partial s^{pq}} \left(\frac{1}{r^{pq}} \frac{\partial e(r^{pq})}{\partial r^{pq}} \frac{\partial s^{pq}}{\partial E_{ij}} \right) \left. \frac{\partial s^{pq}}{\partial E_{mn}} \right|_{E_{ij}=0} \tag{D.4}$$

$$C_{ijmn} = \frac{1}{2\Omega} \sum_{p=1}^{N} \sum_{\substack{q=1 \\ p \neq q}}^{N} \left[\frac{1}{\left(r^{pq}\right)^2} \left\{ \frac{\partial^2 e(r^{pq})}{\partial \left(r^{pq}\right)^2} - \frac{1}{r^{pq}} \frac{\partial e(r^{pq})}{\partial r^{pq}} \right\} \right|_{r=r^o} r_i^{o[pq]} r_j^{o[pq]} r_m^{o[pq]} r_n^{o[pq]} \Bigg] \tag{D.5}$$

where

$r_i^{o[pq]}$ refers to the i^{th} component of the position vector from atom p to q at zero strain and

$$s^{ab} = \left[2E_{mn} + I_{mn} \right] r_m^{o[ab]} r_n^{o[ab]} \tag{D.6}$$

is the square of the magnitude of the distance between atom a and b.

Eq. (D.5) is the common expression used to determine elastic constants, directly from the interatomic potential, when inner elasticity can be neglected. For a non-primitive crystal, preferential displacement of sub-lattices is allowed and Eq. (D.1) is no longer correct and the following relation must hold (see Figure 4.4),

$$\mathrm{r}^{[ab]} = \mathrm{F}\mathrm{r}^{o[ab]} + \delta^{s_a} - \delta^{s_b} \tag{D.7}$$

Where, δ^{s_a} is read as the relative displacement of sub-lattice to which atom 'a' belongs. The relative displacements are always taken with respect to the reference atom in the N^{th} sub-lattice. We also note that $\delta^{s_a}=0$ if the sub-lattice to which '*a*' belongs is the same as the one to which N belongs. This is true because the atoms belonging to a particular sub-lattice suffer a rigid body preferential displacement with respect to the reference atom. Now, the square of the magnitude of the distance between the two atoms is given by,

$$s^{ab} = \left[2E_{mn} + I_{mn}\right] r_m^{o[ab]} r_n^{o[ab]} + 2\left[\xi_m^{s_a} - \xi_m^{s_b}\right] r_m^{o[ab]} + \left[\xi_p^{s_a} - \xi_p^{s_b}\right] [2E_{pr} + I_{pr}]^{-1} \left[\xi_r^{s_a} - \xi_r^{s_b}\right] \tag{D.8}$$

where,

$$F_{ij}\delta_i^{s_a} = \xi_j^{s_a} \tag{D.9}$$

In using the above relation a new set of inner displacement variables, $\xi_j^{s_a}$, is introduced to ensure that the strain energy/strain energy density is rotationally invariant [130].

Let the internal energy density *u*, be a function of the applied homogenous Lagrange strain (**E**) and the 3(N-1) rotationally invariant inner displacement variables ξ_i^k k=1, 2, 3, 4, 5,…..N-1. We have dropped the s_a superscript on the $\xi's$ for notational simplicity. Hence we obtain,

$$u = u\left(E_{ij}, \xi^1, \xi^2, \xi^3 .....\xi^{N-1}\right) \tag{D.10}$$

where

ξ^k is a vector with three components ξ_1^k, ξ_2^k and ξ_3^k

Expanding (D.10) using Taylor's series, we can write,

$$u - u^o = T_{ij}E_{ij} + A_\alpha^k \xi_\alpha^k + \frac{1}{2}C_{ijmn}E_{ij}E_{mn} + \frac{1}{2}B_{\alpha\beta}^{kl}\xi_\alpha^k \xi_\beta^l + D_{ij\alpha}^k E_{ij}\xi_\alpha^k + ...higher\ order\ terms \quad (D.11)$$

Summation convention is used for both the super script (identifying the sub-lattice index) and also the subscript (identifying components of Cartesian coordinates). Greek letters are used to denote the components of the vectors and tensors arising from differentiating with respect to the components of ξ^k. Clearly in Eq. (D.11), **T** would be the stress while **C** is the stiffness for primitive crystals. Although no geometric relation exists between the ξ^k's and E_{ij}, both strive to minimize the energy at equilibrium. So, for an applied strain **E**, ξ takes a value that minimizes the energy, or we may write,

$$\xi_\alpha^k = \varphi_\alpha^k \left(E_{mn}\right) \ for\ k = 1,2,3,4...N\text{-}1 \quad (D.12)$$

Implying that the equilibrium values of the inner displacement variables, ξ's, are functions of a given applied homogenous strain. Expanding Eq.(D.12) in Taylor's series we get,

$$\xi_\alpha^k = P_{\alpha mn}^k E_{mn} + G_{\alpha mnpq}^k E_{mn}E_{pq} + ...higher\ order\ terms \quad (D.13)$$

P is called the internal strain tensor. When a crystal is subjected to a homogenous strain **E**, the components of the internal displacements ξ_α^k can be obtained from Eq.(D.13) uptown terms linear in the strain (sufficient for small strain where, $E_{mn}E_{pq} \approx 0$). Since ξ minimizes u at equilibrium, we have by differentiating u in Eq.(D.11) with respect to each of ξ_λ^h (h=1,2,3,4…..N-1, while λ=1,2,3),

$$A_\lambda^h + \left[B_{\lambda\beta}^{hl}P_{\beta mn}^l + D_{mn\lambda}^h\right]E_{mn} + B_{\lambda\beta}^{hl}G_{\beta mnrs}^l E_{mn}E_{rs} = 0 \quad (D.14)$$

Since the coefficient of each power of **E** must be zero we have, to the first order in strain, ($E_{mn}E_{pq} \approx 0$),

$$\begin{aligned} A^h_\lambda &= 0 \\ B^{hl}_{\lambda\beta}P^l_{\beta mn} + D^h_{mn\lambda} &= 0 \end{aligned} \tag{D.15}$$

From the first of Eq.(D.15) we can see that the stress **T** is unaffected by inner elasticity. Let us now define an inverse of **B** and call it **g**, then

$$g^{th}_{\kappa\lambda}B^{hl}_{\lambda\beta} = I_{\kappa\beta}I^{tl} \tag{D.16}$$

$I^{pc} = 1$ if p and c belong to the same sub-lattice, zero otherwise

$I_{\alpha\beta}$ is equal to 1 if $\alpha=\beta$, zero otherwise

We may obtain **P** as,

$$P^l_{\kappa mn} = -D^h_{mn\lambda}g^{hl}_{\kappa\lambda} \tag{D.17}$$

Using Eqs. (D.13),(D.15) and (D.17) we can write (D.11) as,

$$u - u^o = T_{ij}E_{ij} + \frac{1}{2}\left[C_{ijmn} - D^k_{ij\alpha}g^{kr}_{\alpha\beta}D^r_{\beta mn}\right]E_{ij}E_{mn} \tag{D.18}$$

The Brugger's **T**otal elastic constants ($\mathbf{C}^{\mathbf{T}}$) are given as,

$$C^{\mathrm{T}}_{ijmn} = C_{ijmn} - D^k_{ij\alpha}g^{kr}_{\alpha\beta}D^r_{\beta mn} \tag{D.19}$$

If u is of the form given by Eq. (D.3), then it can easily be shown that, **C** is given by Eq.(4.8) while **D** and **B** are given by,

$$\frac{\partial^2 u}{\partial\xi^b_\alpha\partial E_{uv}} = \frac{1}{2\Omega}\sum_{p=1}^{N}\sum_{\substack{q=1\\q\neq p}}^{N}\frac{1}{\left(r^{pq}\right)^2}\left[\frac{\partial^2 e(r^{pq})}{\partial\left(r^{pq}\right)^2} - \frac{1}{\left(r^{pq}\right)}\frac{\partial e(r^{pq})}{\partial r^{pq}}\right]r_u^{o[pq]}r_v^{o[pq]}r_\alpha^{o[pq]}\left[I^{pb} - I^{qb}\right] = D^b_{uv\alpha} \tag{D.20}$$

$$\begin{aligned} &\frac{\partial u}{\partial\xi^b_\alpha\partial\xi^c_\beta} = \frac{1}{2\Omega}\sum_{p=1}^{N}\sum_{\substack{q=1\\p\neq q}}^{N}\frac{1}{\left(r^{pq}\right)^2}\left[\frac{\partial^2 e(r^{pq})}{\partial\left(r^{pq}\right)^2} - \frac{1}{\left(r^{pq}\right)}\frac{\partial e(r^{pq})}{\partial r^{pq}}\right]\left[I^{pb} - I^{qb}\right]\left[I^{pc} - I^{qc}\right]r_\alpha^{o[pq]}r_\beta^{o[pq]} \\ &+\frac{1}{r^{pq}}\frac{\partial e(r^{pq})}{\partial r^{pq}}I_{\alpha\beta}\left[I^{pb} - I^{qb}\right]\left[I^{pc} - I^{qc}\right] = B^{bc}_{\alpha\beta} \end{aligned} \tag{D.21}$$

As mentioned previously, crystals that are defective must be considered as being non-primitive and in the calculation of elastic constants must include possible contributions from inner elasticity. Thus, Eq. (D.19) must be used to evaluate the elastic constants of the crystal.

Next, in order to verify the codes written to perform the computations we compare the internal strains **P**, of pure fluorite structure (CaF_2). We show that internal strains suffered by the two oxygen sub-lattices are equal and opposite as required by the fluorite structure [134]. We also compare the values of the internal strains of the oxygen sub-lattices, to data from literature, validating our codes both qualitatively and quantitatively.

D.2 Validation of codes

CaF_2 belongs to space group $Fm\bar{3}m$ just like CeO_2 (see section 4.4.1) with Ca in Wyckoff position (4a) while the two oxygen ions in positions (8c). The lattice constant of CaF_2 is 5.44Å. The symmetry of inner strain tensor, **P** is directly related to the point group of the Wyckoff position [128, 131]. Position (4a) belongs to the point group $m\bar{3}m$ while (8c) to $\bar{4}3m$. Clearly, since (4a) contains an inversion center $\left(\bar{3}=3+\bar{1}\right)$ [129] , this sub-lattice (Ca^{4+}) does not show any inner displacement. However, the position (8c) does not posses the inversion center and hence undergoes preferential displacement when the crystal is subjected to a homogenous strain. On referring to Table 2.2 of reference [127] it can be noticed that, for this site the nonzero components of the internal strain are 14=25=36.

To validate our codes, CaF_2 was relaxed at 300K in an NST ensemble. The Buckingham interatomic potential was used. The potential parameters were taken from

ref. [212] and are given in Table D.1. The potential predicts the elastic properties of CaF_2 with good accuracy [212].

Table D.1: Potential parameters for CaF_2

Ion-Pair	A(eV)	ρ(Å)	C(eV Å^6)
Ca-F	1272.80	0.299700	0.00
F-F	99731834	0.120130	17.02

The internal strains $\mathbf{P^n}$, calculated for the two oxygen sub-lattices (n=1, 2) is shown below,

$$P^1 = \begin{bmatrix} 0 & 0 & 0 & -0.165 & 0 & 0 \\ 0 & 0 & 0 & 0 & -0.165 & 0 \\ 0 & 0 & 0 & 0 & 0 & -0.165 \end{bmatrix} \tag{D.22}$$

$$P^2 = \begin{bmatrix} 0 & 0 & 0 & 0.165 & 0 & 0 \\ 0 & 0 & 0 & 0 & 0.165 & 0 \\ 0 & 0 & 0 & 0 & 0 & 0.165 \end{bmatrix} \tag{D.23}$$

where Voigt notation [88] has been used to represent the tensor. Clearly the only non-zero components are 14=25=36. Also, it is easily verified that for a given applied strain, inner displacements as predicted by Eq. (D.17), up to terms linear in strain, are equal and opposite for the two sub-lattices as required by the fluorite structure. This qualitatively validates our codes. Further, results from [134] show that the inner displacements of the two sub-lattices are in the range 0.031 ± 0.024 (in units of lattice constant). Assuming a lattice constant of 5.44Å the range can be given as 0.1684 ± 0.024. Clearly the obtained values here are close to what was obtained in literature thus validating our codes quantitatively as well.

D.3 Why not label all atoms in the MD cell as a sub-lattice?

In computationally determining the contribution of the inner elastic constants, several matrices must be populated. One of the major hassles faced in this particular problem is the inversion procedure in Eq. (D.16) to determine the tensor **g.** The matrix **B**

Table D.2: Form of the B matrix

$$\mathbf{B}=\begin{bmatrix}
B_{11}^{11} & B_{12}^{11} & B_{13}^{11} & B_{11}^{12} & B_{12}^{12} & B_{13}^{12} & & B_{11}^{1(N-1)} & B_{12}^{1(N-1)} & B_{13}^{1(N-1)} \\
B_{21}^{11} & B_{22}^{11} & B_{23}^{11} & B_{21}^{12} & B_{22}^{12} & B_{23}^{12} & \cdots\cdots & B_{21}^{1(N-1)} & B_{22}^{1(N-1)} & B_{23}^{1(N-1)} \\
B_{31}^{11} & B_{32}^{11} & B_{31}^{11} & B_{31}^{12} & B_{32}^{12} & B_{31}^{12} & & B_{31}^{1(N-1)} & B_{32}^{1(N-1)} & B_{31}^{1(N-1)} \\
 & & & & & & & & & \\
B_{11}^{21} & B_{12}^{21} & B_{13}^{21} & B_{11}^{22} & B_{12}^{22} & B_{13}^{22} & & B_{11}^{2(N-1)} & B_{12}^{2(N-1)} & B_{13}^{2(N-1)} \\
B_{21}^{21} & B_{22}^{21} & B_{23}^{21} & B_{21}^{22} & B_{22}^{22} & B_{23}^{22} & \cdots\cdots & B_{21}^{2(N-1)} & B_{22}^{2(N-1)} & B_{23}^{2(N-1)} \\
B_{31}^{21} & B_{32}^{21} & B_{31}^{21} & B_{31}^{22} & B_{32}^{22} & B_{31}^{22} & & B_{31}^{2(N-1)} & B_{32}^{1(N-1)} & B_{31}^{2(N-1)} \\
. & & & & & & . & & & \\
 & & & & & & . & & & \\
. & & & & & & . & & & \\
B_{11}^{(N-1)1} & B_{12}^{(N-1)1} & B_{13}^{(N-1)1} & & & & & B_{11}^{(N-1)(N-1)} & B_{12}^{(N-1)(N-1)} & B_{13}^{(N-1)(N-1)} \\
B_{21}^{(N-1)1} & B_{22}^{(N-1)1} & B_{23}^{(N-1)1} & & & & \cdots\cdots & B_{21}^{(N-1)(N-1)} & B_{22}^{(N-1)(N-1)} & B_{23}^{(N-1)(N-1)} \\
B_{31}^{(N-1)1} & B_{32}^{(N-1)1} & B_{31}^{(N-1)1} & & & & & B_{31}^{(N-1)(N-1)} & B_{32}^{(N-1)(N-1)} & B_{31}^{(N-1)(N-1)}
\end{bmatrix}$$

which is inverted to obtain **g** is of the following form (Table D.2)

where *N* is the number of sub-lattices in the system. If we had all the atoms in the system as a sub-lattice, then clearly the size of this matrix would be very large and computationally more demanding than if we construct periodically repeating defective unit cells (**D-unit cells**) in the manner constructed for this work (maximum of only 60 sub lattices pure ceria is needed).

APPENDIX E. FINITE ELEMENT FORMULATIONS

In this appendix we formulate the finite element model for the system of equations given by Eqs.(6.3) and (6.4). Note that we will also need the equilibrium equations of mechanics (its plane strain formulation) to solve the coupled problem. The finite element formulation and the Jacobian are given only for the defect transport equations. The development for the plane strain mechanics problem can be found in any standard text like [192].

Let use first take the defect transport equations (Eq.(6.3)-(6.4)) and let v and e be the weight functions for the two equations. Then, for a finite element domain Ω^e the weak form reads,

$$\begin{aligned} &D_v \int_{\Omega^e} \left[\frac{\partial v}{\partial x}\left(\frac{\partial V^0}{\partial x} + V^0 \frac{\partial \bar{\tau}}{\partial x} + 2V^0 \frac{\partial \bar{\phi}}{\partial x} \right) + \frac{\partial V}{\partial y}\left(\frac{\partial V^0}{\partial y} + V^0 \frac{\partial \bar{\tau}}{\partial y} + 2V^0 \frac{\partial \bar{\phi}}{\partial y} \right) \right] dxdy = \\ &D_v \int_{\Gamma^e} v \left[\left(\frac{\partial V^0}{\partial x} + V^0 \frac{\partial \bar{\tau}}{\partial x} + z_p V^0 \frac{\partial \bar{\phi}}{\partial x} \right) n_x + \left(\frac{\partial V^0}{\partial y} + V^0 \frac{\partial \bar{\tau}}{\partial y} + 2V^0 \frac{\partial \bar{\phi}}{\partial y} \right) n_y \right] ds \end{aligned} \tag{E.1}$$

and

$$\begin{aligned} &D_e \int_{\Omega^e} \left[\frac{\partial e}{\partial x}\left(\frac{\partial \overline{E}^0}{\partial x} - \overline{E}^0 \frac{\partial \bar{\phi}}{\partial x} \right) + \frac{\partial e}{\partial y}\left(\frac{\partial \overline{E}^0}{\partial y} - \overline{E}^0 \frac{\partial \bar{\phi}}{\partial y} \right) \right] dxdy = \\ &D_e \int_{\Gamma^e} e \left[\left(\frac{\partial \overline{E}^0}{\partial x} - \overline{E}^0 \frac{\partial \bar{\phi}}{\partial x} \right) n_x + \left(\frac{\partial \overline{E}^0}{\partial y} - \overline{E}^0 \frac{\partial \bar{\phi}}{\partial y} \right) n_y \right] ds \end{aligned} \tag{E.2}$$

Note that in the above two equations $\bar{\tau} = \frac{V_m \tau_v}{RT}$, $\bar{\phi} = \frac{F\phi}{RT}$ and $\bar{\tau} = \bar{\tau}\left(u_x, u_y, V^0\right)$.

Clearly we can see that,

$$D_v \left(\frac{\partial V^0}{\partial x} + V^0 \frac{\partial \bar{\tau}}{\partial x} + 2V^0 \frac{\partial \bar{\phi}}{\partial x} \right) n_x + D_v \left(\frac{\partial V^0}{\partial y} + V^0 \frac{\partial \bar{\tau}}{\partial y} + 2V^0 \frac{\partial \bar{\phi}}{\partial y} \right) n_y = \vec{\mathbf{J}}_v \tag{E.3}$$

$$D_e\left(\frac{\partial \overline{E}^0}{\partial x}-\overline{E}^0\frac{\partial \overline{\phi}}{\partial x}\right)n_x+D_e\left(\frac{\partial \overline{E}^0}{\partial y}-\overline{E}^0\frac{\partial \overline{\phi}}{\partial y}\right)n_y=\vec{\mathbf{J}}_e \tag{E.4}$$

Examining the LHS of equations (E.1) and (E.2). These contribute to the stiffness matrix. We interpolate the primary variables of the above two equations, (V^0 and ϕ) using their nodal values as follows,

$$\begin{aligned} V^0&=\psi_i V_i^0\\ \phi&=\psi_i\phi_i \end{aligned} \tag{E.5}$$

Also note that due to electroneutrality condition we will have,

$$\overline{E}^0=2V^0-Q=2\psi_i V_i^0-Q \tag{E.6}$$

The LHS of the i[th] algebraic equation (the finite element model) corresponding to just the two differential equations (Eq. (E.1) and Eq.(E.2)) are given by,

$$E_i^{V^0}=D_v\int_{\Omega^e}\begin{bmatrix}\dfrac{\partial\psi_i}{\partial x}\left(\dfrac{\partial\psi_j}{\partial x}V_j^0+\left(\psi_j V_j^0\right)\dfrac{\partial\overline{\tau}}{\partial x}+2\left(\psi_j V_j^0\right)\dfrac{\partial\psi_m}{\partial x}\overline{\phi}_m\right)+\\ \dfrac{\partial\psi_i}{\partial y}\left(\dfrac{\partial\psi_j}{\partial y}V_j^0+\left(\psi_j V_j^0\right)\dfrac{\partial\overline{\tau}}{\partial y}+2\left(\psi_j V_j^0\right)\dfrac{\partial\psi_m}{\partial y}\overline{\phi}_m\right)\end{bmatrix}dxdy \tag{E.7}$$

$$E_i^{\phi}=D_e\int_{\Omega^e}\begin{bmatrix}\dfrac{\partial\psi_i}{\partial x}\left(2\dfrac{\partial\psi_j}{\partial x}V_j^0-\left(2\psi_j V_j^0-Q\right)\dfrac{\partial\psi_m}{\partial x}\overline{\phi}_m\right)+\\ \dfrac{\partial\psi_i}{\partial y}\left(2\dfrac{\partial\psi_j}{\partial y}V_j^0-\left(2\psi_j V_j^0-Q\right)\dfrac{\partial\psi_m}{\partial y}\overline{\phi}_m\right)\end{bmatrix}dxdy \tag{E.8}$$

Now let us derive the Jacobian of the algebraic equations. At each node we have four degrees of freedom, they are, $u_x=u,u_y=v,V^0,\phi$. Interpolating *u* and *v* similar to Eq.(E.5) at the nodes, the Jacobian (**JJ**) of the various degrees of freedom from just the above two equations (E.7) and (E.8) are given as,

$$^{V^0}JJ^{u}_{ik} = D_v \int_{\Omega^e} \left[\frac{\partial \psi_i}{\partial x} \left(\left(\psi_j V^0_j \right) \frac{\partial}{\partial u_k} \left(\frac{\partial \bar{\tau}}{\partial x} \right) \right) + \frac{\partial \psi_i}{\partial y} \left(\left(\psi_j V^0_j \right) \frac{\partial}{\partial u_k} \left(\frac{\partial \bar{\tau}}{\partial y} \right) \right) \right] dxdy \qquad \text{(E.9)}$$

$$^{V^0}JJ^{v}_{ik} = D_v \int_{\Omega^e} \left[\frac{\partial \psi_i}{\partial x} \left(\left(\psi_j V^0_j \right) \frac{\partial}{\partial v_k} \left(\frac{\partial \bar{\tau}}{\partial x} \right) \right) + \frac{\partial \psi_i}{\partial y} \left(\left(\psi_j V^0_j \right) \frac{\partial}{\partial v_k} \left(\frac{\partial \bar{\tau}}{\partial y} \right) \right) \right] dxdy \qquad \text{(E.10)}$$

$$^{V^0}JJ^{V^0}_{ik} = D_v \int_{\Omega^e} \begin{bmatrix} \frac{\partial \psi_i}{\partial x} \left(\frac{\partial \psi_k}{\partial x} + \psi_k \frac{\partial \bar{\tau}}{\partial x} + \left(\psi_j V^0_j \right) \frac{\partial}{V^0_k} \left(\frac{\partial \bar{\tau}}{\partial x} \right) + 2\psi_k \frac{\partial \psi_j}{\partial x} \bar{\phi}_j \right) + \\ \frac{\partial \psi_i}{\partial y} \left(\frac{\partial \psi_k}{\partial y} + \psi_k \frac{\partial \bar{\tau}}{\partial y} + \left(\psi_j V^0_j \right) \frac{\partial}{V^0_k} \left(\frac{\partial \bar{\tau}}{\partial y} \right) + 2\psi_k \frac{\partial \psi_j}{\partial y} \bar{\phi}_j \right) \end{bmatrix} dxdy \qquad \text{(E.11)}$$

$$^{V^0}JJ^{\phi}_{ik} = D_v \int_{\Omega^e} \left[\frac{\partial \psi_i}{\partial x} \left(2 \left(\psi_j V^0_j \right) \frac{\partial \psi_k}{\partial x} \right) + \frac{\partial \psi_i}{\partial y} \left(2 \left(\psi_j V^0_j \right) \frac{\partial \psi_k}{\partial y} \right) \right] dxdy \qquad \text{(E.12)}$$

where,

$$^{V^0}JJ^{q}_{ik} = \frac{\partial E^{V^0}_i}{\partial q_k} \qquad \text{(E.13)}$$

Note that in the above equation, the superfixes V^0 indicate that the Jacobian is obtained from the equations governing vacancy defect transport equations i.e. Eq. (E.7) and q is the degree of freedom $u_x = u, u_y = v, V^0$ or ϕ.

In a similar manner we obtain for the other equation (governing the electrostatic potential),

$$^{\phi}JJ^{u}_{ik} = 0 \qquad \text{(E.14)}$$

$$^{\phi}JJ^{v}_{ik} = 0 \qquad \text{(E.15)}$$

$$^{\phi}JJ^{V^0}_{ik} = D_e \int_{\Omega^e} \left[\frac{\partial \psi_i}{\partial x} \left(2 \frac{\partial \psi_k}{\partial x} - 2 \frac{\partial \psi_p}{\partial x} \bar{\phi}_p \right) + \frac{\partial \psi_j}{\partial y} \left(2 \frac{\partial \psi_k}{\partial y} - 2 \frac{\partial \psi_p}{\partial y} \bar{\phi}_p \right) \right] dxdy \qquad \text{(E.16)}$$

$$^{\phi}JJ^{\phi}_{ik} = D_e \int_{\Omega^e} \left[\frac{\partial \psi_i}{\partial x} \left(-\left(2\psi_j V^0_j - Q \right) \frac{\partial \psi_k}{\partial x} \right) + \frac{\partial \psi_j}{\partial y} \left(-\left(2\psi_j V^0_j - Q \right) \frac{\partial \psi_k}{\partial y} \right) \right] dxdy \qquad \text{(E.17)}$$

Where we again have,

$$ {}^{\phi}JJ^{q}_{ik} = \frac{\partial E^{\phi}_{i}}{\partial q_{k}} \tag{E.18} $$

indicating that the Jacobian elements $\left({}^{\phi}JJ^{q}_{ik}\right)$ correspond to equations governing the electrostatic potential.

APPENDIX F. SAMPLE INPUT FILE FOR ABAQUS

In this appendix a sample input file that can be used with the user element is given. The input file is for a vertical crack configuration. Note that a basic knowledge of ABAQUS finite element code is assumed. For details the reader is referred to the ABAQUS user manuals [193].

```
*HEADING
**Two Dimensional Elasticity-Defect Transport Coupling
**DOF -1 U-DISP, DOF -2 V-DISP, DOF -3 Normalized Vacancy Concentration (Normalized with
**the concentration of immobile defect Q, DOF-9 Normalized Potential (Normalized with the
**thermal voltage (F/RT))
*NODE, NSET=OUT,INPUT=NODES.inp
*USER
ELEMENT,NODES=8,TYPE=U1002,PROPERTIES=10,COORDINATES=2,VARIABLES=41,UN
SYMM
1,2,3,9
*ELEMENT,TYPE=U1002,ELSET=EALL,INPUT=ELEM_Q.inp
*USER
ELEMENT,NODES=6,TYPE=U3002,PROPERTIES=10,COORDINATES=2,VARIABLES=31,UN
SYMM
1,2,3,9
*ELEMENT,TYPE=U3002,ELSET=EALL,INPUT=ELEM_T.inp
**NODE SETS (FOR SPECIFYING BOUNDARY CONDITIONS)
*Nset, nset=BOTTOM
** NODE NUMBERS CORRESPONDNG TO BOTTOM BOUNDARY
*Nset, nset=LEFT
** NODE NUMBERS CORRESPONDNG TO LEFT BOUNDARY
*Nset, nset=RIGHT
** NODE NUMBERS CORRESPONDNG TO RIGHT BOUNDARY
*Nset, nset=TOP
** NODE NUMBERS CORRESPONDNG TO TOP BOUNDARY
**END NODE SETS
**ASSIGN ALL ELEMENT PROPERTIES
** abs indicates “absolute”
** BETA is the change of the Young’s Modulus with vacancy concentration
*UEL PROPERTY,ELSET=EALL
**abs(Equivalent charge on vacancy), abs(Equivalent charge on electron),abs(Equivalent charge
**on the immobile defect),Concentration of immobile defect,CCE,BETA,Temperature (K)
2.0,1.0,1.0,0.1,0.079,0.05,0.0,1073.0
** Young’s Modulus at stoichiometry, Poisson’s ratio
275.0e+9,0.3
*BOUNDARY
**CONSTRAIN DOF 1, 3, 9 for LEFT NODES
**CONTRAIN DOF 2 for BOTTOM
LEFT,1,1
LEFT,3,3
LEFT,9,9
```

```
BOTTOM,2,2
*STEP,INC=10000,NAME=PART1,EXTRAPOLATION=PARABOLIC
*STATIC
0.000001,1,0.000001,0.1
*BOUNDARY,TYPE=DISPLACEMENT
RIGHT,3,3,0.9203
** NOTE THAT THE RIGHT POTENTIAL IS GIVEN WITH RESPECT TO THE LEFT
RIGHT,9,9,11.54024
*OUTPUT,FIELD
*NODE OUTPUT,NSET=OUT,VARIABLE=ALL
*OUTPUT,HISTORY
*ENERGY OUTPUT,ELSET=EALL,VARIABLE=ALL
** DAT FILE
*ENERGY PRINT,ELSET=EALL
ALLSE
**MESSAGE FILES
*PRINT,FREQUENCY=1000,SOLVE=YES
*EL PRINT,FREQUENCY=1000
SDV
*CONTROLS,PARAMETERS=TIME INCREMENTATION
10,20,15,20
*END STEP
```

APPENDIX G. J-INTEGRAL FROM MATERIAL FORCES

To see how, **M** in Eq.(6.14) can be related to the Rice's J integral or the strain energy release rate we write Eq.(6.14) in indicial form as,

$$M_i = W_{,i} - \left(u_{p,i}\sigma_{pj}\right)_{,j} \tag{G.1}$$

Explicitly M_1 is written as,

$$M_1 = W_{,1} - \left(u_{p,1}\sigma_{pj}\right)_{,j} \tag{G.2}$$

On integrating M_1 about the tip of the crack (Figure G.1), we have,

$$F_1^M = b\int_A \left[W_{,1} - \left(u_{p,1}\sigma_{pj}\right)_{,j} \right] dA \tag{G.3}$$

where b is the thickness of the specimen. Using divergence theorem, we can rewrite Eq. (G.3) as,

$$F_1^M = b\oint_\Gamma W n_1 - \left(u_{p,1}\sigma_{pj}\right)_{,j} n_j d\Gamma \tag{G.4}$$

$$F_1^M = b\oint_\Gamma \left(W n_1 - u_{p,1,j} t_p\right) d\Gamma \tag{G.5}$$

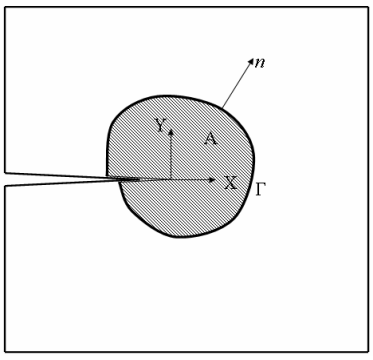

Figure G.1: Contour integral about the crack tip

The Cauchy relation, $\sigma_{ij} n_j = t_i$ and Eq. (6.12) are used to arrive at Eq.(G.5). Here, t_i is the traction vector. Clearly F_1^M / b in Eq. (G.5) is nothing but the conventional *J*-integral [213]. This happens to be a scalar quantity only because we have considered M_1 component from Eq.(G.1). For a crack that is known to propagate only along the X axis, M_2=0 and hence it suffices to use the J-integral alone. In general, for an arbitrary crack we may state that the material force is a more generalized *J*- integral and its components $\left(F_i^M\right)$ give us a measure of the crack tip forces. The strain energy release rate *G*, is then given by,

$$G = \frac{\left|\mathbf{F^M}\right|}{b} \tag{G.6}$$

REFERENCES

[1] Knauth P, Tuller HL. Solid-state ionics: Roots, status, and future prospects. Journal of the American Ceramic Society 2002;85:1654.

[2] Singhal SC, Kendall K. High Temperature Solid Oxide Fuel Cells. Fundamentals, Design and Applications: Elsevier, 2003.

[3] Fouletier J, Siebert E. Potentiometric solid-state oxygen sensors. Ion-Selective Electrode Review 1986;8:133.

[4] Tuller HL. Defect engineering: Design tools for solid state electrochemical devices. Electrochimica Acta 2003;48:2879.

[5] Merkle R, Maier J. How is Oxygen Incorporated into Oxides? A Comprehensive Kinetic Study of a Simple Solid -State Reaction with $SrTiO_3$ as a Model Material. Angewandte Chemie 2008;47:3874.

[6] Montross CS, Yokokawa H, Dokiya M. Thermal stresses in planar solid oxide fuel cells due to thermal expansion differences. British Ceramic Transactions 2002;101:85.

[7] Zheng K, Steele BCH, Sahibzada M, Metcalfe IS. Solid oxide fuel cells based on $Ce(Gd)O_{2-x}$ electrolytes. Solid State Ionics 1996;86-88:1241.

[8] Yasuda I, Hishinuma M. Electrical conductivity, dimensional instability and internal stressesof CeO_2-Gd_2O_3. Electro Chem Soc, vol. 97, 1998. p.178.

[9] Mogensen M, Lindegaard T, Hansen UR. Physical Properties of mixed conductor solid oxide fuel cell anodes of doped CeO2. J. Electrochem. Soc 1994;141:2122.

[10] Armstrong TR, Stevenson JW, Pederson LR, Raney PE. Dimensional Instability of doped Lanthanum Chromite. J. Electrochem. Soc 1996;143:2919.

[11] Montross CS. Stress in alkali earth doped lanthanum chromites from oxygen potential gradients. British Ceramic Transactions 1996;95:1.

[12] Adler SB. Chemical expansivity of electrochemical ceramics. Journal of the American Ceramic Society 2001;84:2117.

[13] Park CY, Jacobson AJ. Thermal and chemical expansion properties of $La_{0.2}Sr_{0.8}Fe_{0.55}Ti_{0.45}O_{3-x}$. Solid State Ionics 2005;176:2671.

[14] Bishop SR, Duncan K, Wachsman ED. Thermochemical expansion of SOFC materials. 29th International conference on advanced ceramics and composites, ACerS, Cocoa beach, Florida, Jan 23-28, 2005, 2005.

[15] Wang YL, Duncan K, Wachsman ED, Ebrahimi F. The effect of oxygen vacancy concentration on the elastic modulus of fluorite-structured oxides. Solid State Ionics 2007;178:53.

[16] Wang Y, Duncan KL, Wachsman ED, Ebrahimi F. Effects of Reduction Treatment on Fracture Properties of Cerium Oxide. J. Am. Ceram. Soc 2007;12:3908.

[17] Greenberg M, Wachtel E, Lubomirsky I, Fleig J, Maier J. Elasticity of Solids with a Large Concentration of Point Defects. Advanced Functional Materials 2006;16:48.

[18] Kossoy A, Feldman Y, Wachtel E, Lubomirsky I, Maier J. Elasticity of solids with a large concentration of point defects II. The chemical strain effect in Ce0.8Gd0.2O1.9. Advanced Functional Materials 2007;17:2393.

[19] Johnson J, Qu J. A numerical simulation tool for fracture analysis in solid oxide fuel cells. Ceramic Engineering and Science Proceedings 2005;26:307.

[20] Singh R, Jacob KT. Solution of transport equations in a mixed conductor - A generic approach. International Journal of Engineering Science 2004;42:1587.

[21] Chung C-Y, Chung Y-C. Performance characteristics of micro single-chamber solid oxide fuel cell: Computational analysis. Journal of Power Sources 2006;154:35.

[22] Barbashov VI, Komysa YA. Mechanoelectric effect in solid electrolytes. Fizika Tverdogo Tela 2005;47:229.

[23] Lubomirsky I. Mechanical properties and defect chemistry. Solid State Ionics 2006.

[24] Samara GA. High pressure studies of ionic conductivity in solids. Solid State Physics: Advances in Research and Applications 1984;38:1.

[25] Barsoum MW. Fundamentals of ceramics. Bristol ; Philadelphia, PA: McGraw-Hill, 2003.

[26] Larche FC, Voorhees PW. Diffusion and Stresses: Basic Thermodynamics. Diffusion and Defect Data. Pt A Defect and Diffusion Forum 1996:31.

[27] Haase R. Thermodynamics of Irreversible Processes: Addison Wesley, 1963.

[28] Maier J. Nano-ionics: More than just a fashionable slogan. Journal of Electroceramics 2004;13:593.

[29] Maier J. Nanoionics: ion transport and electrochemical storage in confined systems. Nature Materials 2005;4:805.

[30] Maier J. Point-defect thermodynamics and size effects. Solid State Ionics 2000;131:13.

[31] Maier J. Nano-sized mixed conductors (Aspects of nano-ionics. Part III). Solid State Ionics 2002;148:367.

[32] Maier J. Defect chemistry and ion transport in nanostructured materials: Part II. Aspects of nanoionics. vol. 157. Cracow, Poland: Elsevier Science B.V., 2003. p.327.

[33] Maier J. Nano-Ionics:Trivial and non-Trivial Size Effects on Ion Conduction in Solids. Z. Phys. Chem 2003;217:415.

[34] Maier J. Transport in electroceramics: Micro- and nano-structural aspects. Journal of the European Ceramic Society 2004;24:1251.

[35] Maier J. "Inner Chemical Life" of Solids. Chemistry International 2006;28.

[36] Wagner C, Schottky W. Theory of regular mixed phases. Zeitschrift fur Physikalische Chemie 1930;11:163.

[37] Wagner C. Theory of the tarnishing process. Zeitschrift fur Physikalische Chemie 1936;32:447.

[38] Maier J. Physical Chemistry of Ionic Materials, Ions and Electrons in Solids. England: John Wiley & Sons, 2004.

[39] Schottky W. Halbleiterprobleme. Braunschweig:Vieweg 1958;IV.

[40] Krèoger FA. The chemistry of imperfect crystals. Amsterdam, New York,: North-Holland Pub. Co.;Interscience, 1964.

[41] Schottky W. Statistik und Thermodynamik der Unordnungs Zustande in Kristallen, Insbesondere bei Geringer Fehlordnung. Z. Elektrochem 1939;45.

[42] Rickert H. Electrochemistry of Solids: Springer-Verlag, 1982.

[43] Maier J. Defect Chemistry: Composition, Transport, and Reactions in the Solid State; Part I: Thermodynamics. Angewandte Chemie (International Edition in English) 1993;32:313.

[44] Allnatt AR, Lidiard AB. Atomic Transport in Solids: Cambridge University Press, 1993.

[45] Fergus JW. Doping and defect association in oxides for use in oxygen sensors. Journal of Materials Science 2003;38:4259.

[46] Wang Z, Chen ZQ, Zhu J, Wang SJ, Guo X. Evidence of defect associates in yttrium-stabilized zirconia. Radiation Physics and Chemistry 2000;58:697.

[47] Zacate MO, Minervini L, Bradfield DJ, Grimes RW, Sickafus KE. Defect cluster formation in M_2O_3-doped cubic ZrO_2. Solid State Ionics 2000;128:243.

[48] Minervini L, Zacate MO, Grimes RW. Defect cluster formation in M_2O_3-doped CeO_2. Solid State Ionics 1999;116:339.

[49] Schmalzried H. Chemical Kinetics of Solids, 1995.

[50] Girifalco LA. Statistical Mechanics of Solids. USA: Oxford University Press, 2000.

[51] Ling S. High-concentration point-defect chemistry: statistical-thermodynamic approach applied to nonstoichiometric cerium dioxides. Physical Review B (Condensed Matter) 1994;49:864.

[52] Ling S. Statistical thermodynamic formulation of high concentration point defect chemistry in perovskite crystalline systems: Application to Strontium doped Lanthanum Chromite. J. Phys. Chem. Solids. 1994;55:1445.

[53] Agren J. Diffusion in phases with several components and sublattices. J. Phys. Chen. Solids. 1982;43:421.

[54] Voorhees PW, Johnson WC. The thermodynamics of elastically stressed crystals. In: Enrenreich H, Spaepen F, editors. Solid State Physics- Advances in Research and Applications, vol. 59. Elsevier. Inc, 2004.

[55] Kroger FA. Chemistry of Imperfect Crystals. Amsterdam: North-Holland, 1964.

[56] Kroger FA, Stieljes FH, Vink HJ. Thermodynamics and Formulations of Reactions involving Imperfections in Solids. Philips. Res. Rep. 1959;14:557.

[57] Kroger FA, Vink HJ. Relations between the Concentrations of Imperfections in Crystalline Solids. New York: Academic Press, 1956.

[58] Callen HB. Thermodynamics. New York: Wiley, 1960.

[59] Lankhorst MHR, Bowmeester HJM, Verweij H. Thermodynamics and Transport of Ionic and Electronic Defects in Crystalline Oxides. J. Am. CEram. Soc 1997;80:2175.

[60] Ziegler H. An introduction to thermomechanics, 1983.

[61] Murray AD, Murch GE, Catlow CRA. A new hybrid scheme of computer simulation based on Hades and Monte Carlo: Application to ionic conductivity in Y3+ doped CeO2. Solid State Ionics 1986;18-19:196.

[62] Ruiz-Salvador AR, Garcia-Sanchez MF, O'Reilly-Lukin M, Lewis DW, Gomez A. Approaching the structure of heavily defective ionic oxides through atomistic modelling. Phys. Stat. Sol(c) 2005;2:3521.

[63] Stapper G, Bernasconi M, Parrinello NNaM. Ab initio study of structural and electronic propoerties of yttria-stabilized cubic zirconia. Physical Review B (Condensed Matter and Materials Physics) 1999;59:797.

[64] Haile JM. Molecular Dynamics Simulation: Wiley, 1992.

[65] Weiner JH. Statistical Mechanics of Elasticity. Mineola, NY: Dover Publications, 2002.

[66] Leach AR. Molecular Modelling: Principles and Applications. Dorchester, Dorset, Great Britain: Prentice Hall, 2001.

[67] Eshelby JD. The Force on an Elastic Singularity. Philosophical Transactions of the Royal Society of London Series a-Mathematical and Physical Sciences 1951;244:87.

[68] Wu CH. The role of Eshelby stress in composition-generated and stress-assisted diffusion. Journal of the Mechanics and Physics of Solids 2001;49:1771.

[69] Li JCM, Oriani RA, Darken LS. The thermodynamics of stressed solids. Zeitschrift fur Physikalische Chemie 1966;49:271.

[70] Guggenheim EA. Thermodynamics. New York Interscience Publishers, Inc, 1949.

[71] Koehler JS. Diffusion of lattice defects in a stress field. Physical Review 1969;181:1015.

[72] Johnson H. Defect Transport in Heterogeneous Stress Fields. Scripta Metallurgica 1970;4:771.

[73] Philibert J. Diffusion and Stresses. Diffusion and Defect Data. Pt A Defect and Diffusion Forum 1996:3.

[74] Aziz MJ. Pressure and stress effects on diffusion in Si. Defect and Diffusion Forum 1998;153-155:1.

[75] Olmsted DL, Phillips R, Curtin WA. Modelling diffusion in crystals under high internal stress gradients. Modelling and Simulation in Materials Science and Engineering 2004:781.

[76] Li JCM, Nolfi FV, Johnson CA. Diffusional equilibrium of substitutional atoms in a stressed solid. Acta Metallurgica 1971;19:749.

[77] Larche FC, Cahn JW. The interactions of composition and stress in crystalline solids. Acta Metallurgica 1985;33:331.

[78] Larche F, Cahn JW. Linear theory of thermochemical equilibrium of solids under stress. 1973;21:1051.

[79] Denton AR, Ashcroft NW. Vegard's law. Physical Review A 1991;43:3161.

[80] Larche F, Cahn JW. Non-linear theory of thermomechanical equilibrium of solids under stress. 1978;26:53.

[81] Johnson WC. Phenomenological thermodynamic treatment of elastically stressed ionic crystals. Journal of the American Ceramic Society 1993;76:1713.

[82] Johnson WC. Thermodynamic equilibria in two-phase, elastically stressed ionic crystals. Journal of the American Ceramic Society 1994;77:1581.

[83] Johnson WC, Huh JY. Thermodynamics of stress-induced interstitial redistribution in body-centered cubic metals. Metallurgical and materials transactions 2003;34A.

[84] Krlshnamurthy R, Srolovitz DJ. A general solution for two-dimensional stress distributions in thin films. Journal of Applied Mechanics, Transactions ASME 2004;71:691.

[85] Krishnamurthy R, Sheldon BW. Stresses due to oxygen potential gradients in non-stoichiometric oxides. Acta Materialia 2004;52:1807.

[86] Dimos D, Wolfenstine J, Kohlstedt DL. Kinetic demixing and decomposition of multicomponent oxides due to a nonhydrostatic stress. Acta Metallurgica 1987;36:1543.

[87] Larche FC, Cahn JW. The effect of self-stress on diffusion in solids. Acta Metallurgica 1982;30:1835.

[88] Malvern LE. Introduction to the Mechanics of a continuous medium: Prentice-Hall, Inc, 1969.

[89] Maugin G. Material Inhomogenities in Elasticity. Bury, St. Edmunds, Great Britain: Chapman & Hall, 1993.

[90] Clayton JD, Bammann DJ, McDowell DL. Anholonomic configuration spaces and metric tensors in finite elastoplasticity. International Journal of Non-Linear Mechanics 2004;39:1039.

[91] Wu CH, Liu P. The nonlinear interplays of mechanical and chemical strains in diffusion. Diffusion and Defect Data. Pt A Defect and Diffusion Forum 2005;237-240:95.

[92] Denton AR, Ashcroft NW. Vegard's law. Physical Review A 1990;43:3161.

[93] Wang. Y, Duncan KL, Wachsman ED. The effect of lattice vacancy concentration on mechanical properties of fluorite related oxides. 29th International Conference on Advanced Ceramics and Composites, ACerS, Cocoa Beach, FL, 2005.

[94] Atkinson A, Ramos TMGM. Chemically-induced stresses in ceramic oxygen ion-conducting membranes. Solid State Ionics, Diffusion & Reactions 2000;129:259.

[95] Gillan MJ. The long-range distortion caused by point defects. Philosophical Magazine A (Physics of Condensed Matter, Defects and Mechanical Properties) 1983;48:903.

[96] Gillan MJ. The elastic dipole tensor for point defects in ionic crystals. Journal of Physics C (Solid State Physics) 1984;17:1473.

[97] Schober HR, Ingle KW. Calculation of relaxation volumes, dipole tensors and Kanzaki forces for point defects. Journal of Physics F (Metal Physics) 1980;10:575.

[98] Lee DK, Yoo HI. Measurement of the Onsager coefficients of mixed ionic-electronic conduction in oxides. Phys. Rev. B 2007;75.

[99] Liu M, Winnick J. Fundamental issues in modeling of mixed ionic-electronic conductors (MIECs). Solid State Ionics, Diffusion & Reactions 1999;118:11.

[100] Bard AJ, Faulkner LR. Electrochemical Methods Fundamentals and Applications. Noida, India: Bribasi Art Press Ltd., 2000.

[101] Fleig J. On the current-voltage characteristics of charge transfer reactions at mixed conducting electrodes on solid electrolytes
Phycal Chemistry Chemical Physics 2005;7:2027.

[102] Leeuw SWd, Gillan MJ. Calculation of the free energy of vacancy formation in solids. J. Phys. C. Solid state physics 1982;15:5161.

[103] Fisher CAJ, Matsubara H. Oxide ion diffusion along grain boundaries in zirconia: a molecular dynamics study. Solid State Ionics, Diffusion & Reactions 1998;113-115:311.

[104] Gillan MJ, Harding JH, Tarento R-J. Calculation of defect migration rates by molecular dynamics simulation. J. Phys. C. Solid state physics 1987;20:2331.

[105] Kilo M, Argirusis C, Borchardt G, Jackson RA. Oxygen diffusion in yttria stabilised zirconia-experimental results and molecular dynamics calculations. Phys. Chem. Chem Phys 2003;5:2219.

[106] Yamamura Y, Kawasaki S, Sakai H. Molecular dynamics analysis of ionic conduction mechanism in yttria-stabilized zirconia. Solid State Ionics, Diffusion & Reactions 1999;126:181.

[107] Islam MS. Computer modelling of defects and transport in perovskite oxides. Solid State Ionics 2002;154-155:75.

[108] Kulkarni AJ, Zhou M, Ke FJ. Orientation and size dependence of the elastic properties of zinc oxide nanobelts. Nanotechnology 2005;16:2749.

[109] Muller-Plathe F. A simple nonequilibrium molecular dynamics method for calculating the thermal conductivity. The Journal of Chemical Physics 1997;106:6082.

[110] Harding JH. Computer simulation of defects in ionic solids. Reports on Progress in Physics 1990;53:1403.

[111] Naumovich EN, Patrakeev MV, Kharton VV, Islam MS. Defect Interactions in $La_{0.3}Sr_{0.7}Fe(M')O_{3-\delta}$ (M'=Al,Ga) perovskite: Atomistic simulations and analysis of $P(O_2)$-T-δ diagrams. Solid State Ionics 2006;177:457.

[112] F.Zimmer, Ballone P, Maier J, Parrinello M. Defect-defect interactions in ionic conductors: A classical MD and MC study. Berichte der Bunsengesellschaft fuer Physikalische Chemie 1997;101:1333.

[113] Dwivedi A, Cormack AN. A computer simulation study of the defect structure of calcia-stabilized zirconia. Philosophical Magazine A (Physics of Condensed Matter, Defects and Mechanical Properties) 1990;61:1.

[114] Shimojo F, Okazaki H. Molecular dynamics studies of yttria stabilized zirconia. II. Microscopic mechanism of oxygen diffusion. Journal of the Physical Society of Japan 1992;61:4106.

[115] Shimojo F, Okabe T, Tachibana F, Kobayashi M, Okazaki H. Molecular dynamics studies of yttria stabilized zirconia. I. Structure and oxygen diffusion. Journal of the Physical Society of Japan 1992;61:2848.

[116] Kilo M, Jackson RA, Borchardt G. Computer modelling of ion migration in zirconia. Philosophical Magazine 2003;83:3309.

[117] Inaba H, Sagawa R, Hayashi H, Kawamura K. Molecular dynamics simulation of gadolinia-doped ceria. Solid State Ionics, Diffusion & Reactions 1999;122:95.

[118] Hayashi H, Sagawa R, Inaba H, Kawamura K. Molecular dynamics calculations on ceria-based solid electrolytes with different radius dopants. Solid State Ionics 2000;131:281.

[119] Catlow CRA. Transport in doped fluorite oxides. Solid State Ionics 1984;12:67.

[120] Ye F, Mori T, Ou DR, Cormack AN, Lewis RJ, Drennan J. Simulation of ordering in large defect clusters in gadolinium-doped ceria. Solid State Ionics;In Press, Corrected Proof.

[121] Puchala B, Falk ML, Garikipati K. Elastic effects on relaxation volume tensor calculations. Phys. Rev. B 2008;77.

[122] Born M, Huang K. Dynamical Theory of Crystal Lattices. New York: Clarendon Press . Oxford, 1954.

[123] Tosi MP. Cohesion of Ionic Solids in the Born Model. Solid State Physics-Advances in Research and Applications 1964;16:1.

[124] Zhou ZC, Joos B. Fluctuation formulas for the elastic constants of an arbitrary system. Phys. Rev. B 2002;66.

[125] Yoshimoto K, Papakonstantopoulos GJ, Lutsko JF, de Pablo JJ. Statistical calculation of elastic moduli for atomistic models. Phys. Rev. B 2005;71.

[126] Alber I, Bassani JL, Khantha M, Viter V, Wang GJ. Grain boundaries as heterogeneous systems: atomic and continuum elastic properties. Philosophical Transactions of the Royal Society, Series A (Physical Sciences and Engineering) 1992;339:555.

[127] Cousins CSG. Inner Elasticity and the Higher-Order Elasticity of some Diamond and Graphite Allotropes. Physics, vol. Doctor of Philosophy: University of Exeter, 2001. p.190.

[128] Cousins CSG. Inner Elasticity. Journal of Physics C-Solid State Physics 1978;11:4867.

[129] Borchardt-Ott W. Crystallography. Germany: Springer, 1995.

[130] Martin JW. Many-body forces in solids and the Brugger elastic constants. II. Inner elastic constants. Journal of Physics C (Solid State Physics) 1975;8:2858.

[131] Cousins CSG. The symmetry of inner elastic constants. J. Phys. C: Solid State Phys 1978;11:4881.

[132] Gratias D, Portier R, Fayard M. Crystallographic Description of Coincidence-Site Lattice Interfaces in Homogenous Crystals. Acta. Cryst 1979;A35:885.

[133] Wang ZL, Kang ZC. Functional and Smart Materials. *Structural Evolution and Structure Analysis*. New York: Plenum Press. New York, 1998.

[134] Pooke DM, Devine SD. Inner displacement and the internal strain tensor in the fluorite structure. Journal of Physics C (Solid State Physics) 1984;17:3531.

[135] Dasgupta S, Sengupta S. Homogeneous deformation theory for noncentrosymmetric ionic crystals in quadratic response regime: antipiezoelectricity. Physics Letters A 1985;107A:266.

[136] Ebrahimi F, Yanli W, Duncan K, Wachsman ED. The effect of oxygen vacancy concentration on the elastic modulus of fluorite-structured oxides. Solid State Ionics, Diffusion & Reactions 2007;178:53.

[137] Duncan KL, Yanli W, Bishop SR, Ebrahimi F, Wachsman ED. Role of point defects in the physical properties of fluorite oxides. Journal of the American Ceramic Society 2006;89:3162.

[138] Duncan KL, Wang Y, Bishop SR, Ebrahimi F, Wachsman ED. The role of point defects in the physical properties of nonstoichiometric ceria. Journal of Applied Physics 2007;101:044906.

[139] Dingreville R, Qu J. A semi-analytical method to compute surface elastic properties. Acta Materialia 2007;55:141.

[140] Smith W, Forester TR. DL_POLY_2.0: A general-purpose parallel molecular dynamics simulation package. Journal of Molecular Graphics 1996;14:136.

[141] Vyas S, Grimes RW, Gay DH, Rohl AL. Structure, stability and morphology of stoichiometris ceria crystallites. J. Chem. Soc., Faraday Trans 1998;94:427.

[142] Gotte A, Spanberg D, Hermansson K, Baudin M. Molecular Dynamics study of oxygen self diffusion in reduced CeO_2. Solid State Ionics 2007;178:1421.

[143] Guttman L. Order-Disorder Phenomena in Metals. Solid State Physics-Advances in Research and Applications 1956;3:145.

[144] Martin RL. Structural Theory for Nonstoicheiometry .1. Defect Fluorite-Type Structures - Lanthanoid Oxides Mox with 1.7 Less Than X Less Than 2.0. Journal of the Chemical Society-Dalton Transactions 1974:1335.

[145] Kang ZC, Eyring L. A compositional and structural rationalization of the higher oxides of Ce, Pr, and Tb. Journal of Alloys and Compounds 1997;249:206.

[146] Martin JW. Many-body forces in metals and the Brugger elastic constants. Journal of Physics C (Solid State Physics) 1975;8:2837.

[147] Wachsman ED. Effect of oxygen sublattice order on conductivity in highly defective fluorite oxides. Journal of the European Ceramic Society 2004;24:1281.

[148] Li YP, Maxey ER, Richardson JW, Ma BH, Lee TH, Song SJ. Oxygen non-stoichiometry and thermal-chemical expansion of $Ce_{0.8}Y_{0.2}O_{1.9-\delta}$ electrolytes by neutron diffraction. Journal of the American Ceramic Society 2007;90:1208.

[149] Jianmin Q, Cherkaoui M. Fundamentals of micromechanics of solids: John Wiley & Sons, Inc, 2006.

[150] Krivovichev SV. Systematics of fluorite-related structures. II. Structural diversity. Solid State Sciences 1999;1:221.

[151] Krivovichev SV. Systematics of fluorite-related structures. I. General principles. Solid State Sciences 1999;1:211.

[152] Brumleve TR, Buck RP. Numerical solution of the Nernst-Planck and Poisson equation with applications to membrane electrochemistry and solid state physics. J. Electroanal. Chem 1978;90:1.

[153] Cardenas AE, Coalson RD, Kurnikova MG. Three-Dimensional Poisson-Nernst-Planck Theory Studies: Influence of Membrane Electrostatic on Gramicidn A Channel Conductance. Biophysical Journal 2000;79:80.

[154] Bazant MZ, Thorton K, Ajdari A. Diffuse -charge dynamics in electrochemical systems. Physical Review E 2004;70:1.

[155] Tuller HL. Nonstoichiometric Oxides: Academic Press Newyork, 1981.

[156] Liu M. Distributions of charged defects in mixed ionic-electronic conductors. I. General equations for homogeneous mixed ionic-electronic conductors. Journal of the Electrochemical Society 1997;144:1813.

[157] Kim S, Maier J. On the conductivity mechanism of nanocrystalline ceria. Journal of the Electrochemical Society 2002;149:73.

[158] Nayfeh AH. Introduction to Perturbation Techniques. New York: John Wiley & Sons, 1981.

[159] Kato M. Numerical Analysis of the Nernst-Planck-Poisson system. J. theor. biol 1995;177:299.

[160] Samson E, Marchand J. Numerical Solution of the Extended Nernst-Planck Model. Journal of Colloid and Interface Science 1999;215:1.

[161] Samson E, Marchand J, Robert JL, Bournazel JP. Modelling ion diffusion mechanisms in porous media. Int. J. Numer. Meth. Engng 1999;46:2043.

[162] Urtenov MA-K, Kirillova EV, Seidova NM, Nikonenko VV. Decoupling of the Nernt-Planck and the Poisson Equations. Application to a Membrane system at Overlimiting Currents. J. Phys. Chem. B 2007;111:14208.

[163] Barcilon V, chen DP, Eisenberg RS, Jerome JW. Qualitative Properties of Steady-State Poisson-Nerns-Planck Systems: Perturbation and Simulation Study. SIAM Journal on Applied Mathematics 1997;57:631.

[164] Eisenberg B, Liu W. Poissoin-Nernst-Planck systems for ion channels with permanent charges. SIAM J. Math. Anal 2007;38:1932.

[165] MacGillivray AD. Nernst-Planck equations and the electro-neutrality and donnan equilibrium assumptions. Journal of Chemical Physics 1968;48:2007.

[166] Park JH, Jerome JW. Qualitative Properties of Steady-State Poisson-Nernst-Planck Systems: Mathematical Study. SIAM Journal on Applied Mathematics 1997;57:609.

[167] MacGillivray AD. Asymptotic Solutions of the Time-Dependent Nernst-Planck Equations. The Journal of Chemical Physics 1969;52:3126.

[168] Chen Z. Comparison of the Mobile Charge Distribution Models in Mixed Ionic-Electronic Conductors. Journal of the electrochemical society 2004;151:A1576.

[169] MacGillivray AD, Hare D. Applicability of Goldman's Constant Field Assumption to Biological Systems. J. theor. biol 1969;25:113.

[170] Kevorkian J, Cole JD. Perturbation Methods in Applied Mathematics: Springer, 1981.

[171] Atkinson A. Chemically-induced stresses in gadolinium-doped ceria solid oxide fuel cell electrolytes. Solid State Ionics, Diffusion & Reactions 1997;95:249.

[172] Lubomirsky I. Mechanical properties and defect chemistry. Solid State Ionics 2006;177:1639.

[173] Jamnik J, Maier J. Transport across Boundary Layers in Ionic Crystals Part I: General Formalism and Conception. Ber. Bunsenges. Phys. Chem 1997;101:23.

[174] Kirrzenka J, Shampine LF. A BVP Solver based on Residual Control and the MATLAB PSE. ACM TOMS 2001;27:299.

[175] Swaminathan N, Qu J, Sun Y. An electrochemomechanical theory of defects in ionic solids. Part II. Examples. Philosophical Magazine 2007;87:1723.

[176] Jaiswal A, Wachsman E. Fabrication of anode supported thick film ceria electrolytes for IT-SOFCs. Ionics 2005;11:161.

[177] Laurencin J, Morel B, Bultel Y, Lefebvre-Joud F. Thermo-mechanical aspects of SOFC operations. vol. P 2005-07. Quebec, Canada: Electrochemical Society Inc., Pennington, NJ 08534-2896, United States, 2005. p.903.

[178] Arico AS, Bruce P, Scrosati B, Tarascon J-M, Schalwijk WV. Nanostructures materials for advanced energy conversion and storage devices. Nature 2005;4:366.

[179] Bellino MG, Lamas DG, Reca NEWd. Enhanced Ionic Conductivity in Nanostructured, Heavily Doped Ceria Ceramics. Advanced Functional Ceramics 2006;16:107.

[180] Maier J. Thermodynamic aspects and morphology of nano-structured ion conductors: Aspects of nano-ionics Part I. Solid State Ionics 2002;154-155:291.

[181] Riess I. Theoretical treatment of the transport equations for electrons and ions in a mixed conductor. Journal of the Electrochemical Society 1981;128:2077.

[182] Riess I. Current-voltage relation and charge distribution in mixed ionic electronic solid conductors. Journal of the Physics and Chemistry of Solids 1986;47:129.

[183] Kienzler R, Herrmann G. Mechanics in Material Space with Applications to Defect and Fracture Mechanics. Germany: Springer-Verlag, 2000.

[184] Rice JR. A Path Independent Integral and the Approximate Analysis of Strain Concentration by Notches and Cracks. ASME Journal of Applied Mechanics 1968;35:379.

[185] Parks DM. A stiffness derivatve finite element technique for the determination of crack tip stress intensity factors. International Journal of Fracture 1974;10:487.

[186] Steinmenn P, Ackermann D, Barth FJ. Application of material forces to hyperelastistatic fracture mechanics. II. Computational setting. International Journal of Solids and Structures 2001;38:5509.

[187] Simha NK, Fischer FD, Shan GX, Chen SR, Kolednik O. J-intergral and crack driving force in elastic-plastic materials. Journal of the Mechanics and Physics of Solids 2008.

[188] R.Mueller, Kolling S, Gross D. On configurational forces in the context of the finite element method. International Journal for Numerical Methods in Engineering 2002;53:1557.

[189] Mueller R, Maugin GA. On material forces and finite element discretizations. Computational Mechanics 2002;29:52.

[190] Braun M. Configurational forces induced by finite element discretization. Poc. Estonian. acad. Sci. Phys. Math 1997;46:24.

[191] Adden S, Merzbacher M, Forst P. Material forces as a simple criterion for the description of crack-turning problems. Aerospace Science and Technology 2006;10:519.

[192] Reddy JN. An Introduction to the Finite Element Method. Singapore: Mc Graw-Hill International Editions, 1993.

[193] Abaqus/Standard User Manuals. Dassault SystemesSimulia Corporation.

[194] Barsoum RS. On the use of isoparametic finite elements in linear fracture mechanics. Int. J. Numer. Meth. Eng. 1974;10:25.

[195] Henshell RD, Shaw KG. Crack tip finite elements are unnecessary. Int. J. Numer. Meth. Eng. 1975;9:495.

[196] Gross D, Kolling S, Mueller R, Schmidt I. Configurational forces and their application in solid mechanics. European Journal of Mechanics A/Solids 2003;22:669.

[197] Ishida T, Iguchi F, Sato K, Hashida T, Yugami H. Fracture properties of $(CeO_2)_{1-x}(RO_{1.5})_x$ (R-Y, Gd, and Sm; x=0.02-0.2) ceramics. Solid State Ionics 2005;176:2417.

[198] Cole M, Catlow CRA, Dragun JP. Exafs Studies of Doped-Zro2 Systems. J. Phys. Chem. Solids 1990;51:507.

[199] Clayton JD, Bammann DJ, McDowell DL. Anholonomic configuration spaces and metric tensors in finite elastoplasticity. International Journal of Non-Linear Mechanics 2004;39:1039.

[200] Clayton JD, Bammann DJ, McDowell DL. A geometric framework for the kinematics of crystals with defects. Philosophical Magazine 2005;85:3983.

[201] Chen X, Yu J, Adler SB. Thermal and Chemical Expansion of Sr-Doped Lanthanum Oxide ($La_{1-x}Sr_xCoO_{3-\delta}$). Chem. mater 2005;17:4537.

[202] Garikipati K, Bassman L, Deal M. A lattice-based micromechanical continuum formulation for stress-driven mass transport in polycrystalline solids. Journal of the Mechanics and Physics of Solids 2001;49:1209.

[203] Garikipati K, Bassman LC. Atomically-based field formulations for coupled problems of composition and mechanics. Boston, MA, USA: Mater. Res. Soc, 2001. p.9.

[204] Sheppard D, Terrell R, Henkelman G. Optimization methods for finding minimum energy paths. The Journal of Chemical Physics 2008;128:1.

[205] Dingreville R, Qu J, Mohammed C. Surface free energy and its effect on the elastic behavior of nano-sized particles, wires and films. Journal of the Mechanics and Physics of Solids 2005;53:1827.

[206] Malygin GA. Effect of grain size dispersion on the strength and plasticity of nanocrystalline metals. Physics of the Solid State 2008;50:1056.

[207] Gutkin MY, Ovid'ko IA. Homogeneous nucleation of glide dislocation loops in nanoceramics. Physics of the Solid State 2008;50:655.

[208] Sato K, Hashida T, Yashiro K, Yugami H, Kawada T, Mizusaki J. Mechanical damage evaluation of solid oxide fuel cells under simulated operating conditions. Journal of the Ceramic Society of Japan 2005;113:562.

[209] Pannikkat AK, Raj R. Measurement of an electrical potential induced by normal stress applied to the interface of an ionic material at elevated temperatures. Acta Materialia 1999;47:3423.

[210] Gibbs JW. The Collected Works of J. Willard Gibbs. United States of America: Yale University Press, 1948.

[211] Wolf D, Keblinski P, Phillpot SR, Eggebrecht J. Exact method for the simulation of Coulombic systems by spherically truncated parwise r^{-1} summation. Journal of Chemical Physics 1999;110:8254.

[212] Rabone.J.A.L, De LH. Interatomic potential models for natural apatite crystals:Incorporating Strontium and the Lanthanides. J Comput Chem. 2006;27:23.

[213] Bazant ZP, Planas K. Fracture and Size Effect in Concrete and Other Quasibrittle Materials. Florida, USA: CRC Press, 1998.